A Multiscale FEM Approach for Rubber Friction on Rough Surfaces

Von der Fakultät für Maschinenbau
der Gottfried Wilhelm Leibniz Universität Hannover

zur Erlangung des akademischen Grades
Doktor-Ingenieur

genehmigte Dissertation
von

Dipl.-Ing. Paul Wagner

geboren am 18.08.1987 in Ziegenhals, Polen

2018

Herausgeber:
Prof. Dr.-Ing. habil. Dr. h.c. mult. Dr.-Ing. E.h. Peter Wriggers

Verwaltung:
Institut für Kontinuumsmechanik
Gottfried Wilhelm Leibniz Universität Hannover
Appelstraße 11
30167 Hannover

Tel: +49 511 762 3220
Fax: +49 511 762 5496
Web: www.ikm.uni-hannover.de

© Dipl.-Ing. Paul Wagner
Institut für Kontinuumsmechanik
Gottfried Wilhelm Leibniz Universität Hannover
Appelstraße 11
30167 Hannover

Alle Rechte, insbesondere das der Übersetzung in fremde Sprachen, vorbehalten. Ohne Genehmigung des Autors ist es nicht gestattet, dieses Heft ganz oder teilweise auf photomechanischem, elektronischem oder sonstigem Wege zu vervielfältigen.

ISBN 978-3-941302-23-5

1. Referent: Prof. Dr.-Ing. habil. Dr. h.c. mult. Dr.-Ing. E.h. Peter Wriggers
2. Referent: Prof. Stanislaw Stupkiewicz

Tag der Promotion: 07.12.2017

Zusammenfassung

Die Erforschung von Gummireibung auf rauen Oberflächen ist für das Verständnis des Reifen-Fahrbahn-Kontaktes und die Verbesserung der Gripeigenschaften zukünftiger Reifen von fundamentalem Interesse. Ein Ziel der Arbeit ist es, relevante physikalische Effekte mit einem Finite Elemente Modell abzubilden und somit die Vorhersage der Reibverhältnisse bestimmter Gummi-Straßenoberflächen-Kombinationen unter verschiedenen globalen Bedingungen zu ermöglichen. Desweiteren soll die numerische Methode genutzt werden, um durch die Trennung der physikalischen Effekte und durch die Zugänglichkeit zu nicht messbaren Größen wertvolles Verständnis zu Gummireibung zu generieren.

Raue Oberflächen erzeugen beim Reibprozess eine zyklische Anregung der viskoelastischen Gummimischungen, die zu Energiedissipation und damit zu einer als Hysteresereibung bezeichneten Reibkraft führt. Die Modellierung von Hysteresereibung wird durch die direkte Verwendung von rauen Oberflächenprofilen in Kombination mit einem viskoelastischen Materialmodell realisiert und bildet gleichzeitig Verzahnungseffekte ab. Um alle relevanten Oberflächenasperitäten abbilden zu können, wird in dieser Arbeit eine Multiskalenmethode vorgestellt, die auf Kontakt-Homogenisierung und einer Betrachtung der Oberfläche auf mehreren Längen-Skalen beruht. Der makroskopische Druck wird über Homogenisierung von mehreren Oberflächenprofilen auf die unteren Skalen weitergegeben und die resultierende Hysteresereibung in Form von homogenisierten Reibkoeffizienten zurück gegeben.

Zusätzlich zu Hysterese wird in dieser Arbeit Adhäsion modelliert. Dazu wird die Kontaktfläche durch die Berücksichtigung aller Längen-Skalen abgeschätzt. Adhäsion wird als Interaktion von Gummimolekülketten mit Atomen der rauen Oberfläche betrachtet. Der Multiskalen-Ansatz wird um ein makrosopisches phänomenologisches Adhäsionsgesetz erweitert.

Beim Reibprozess mit hohen Geschwindigkeiten erwärmt sich der Gummiblock in der Kontaktfläche zudem stark, was zu einer Änderung der Reibantwort führt. Deshalb wird der Multiskalen-Ansatz um Temperatureffekte erweitert. Auf der obersten Skala wird eine thermo-mechanisch gekoppelte Simulation durchgeführt. Die resultierenden Temperaturen und die damit geänderten Materialeigenschaften werden auf allen Skalen berücksichtigt, um den Einfluss der Temperatur auf die Hysteresereibung abzubilden.

Der numerische Multiskalen-Ansatz wird für die einzelnen physikalischen Effekte zunächst ausführlich erläutert. Anschließend werden einige wichtige methodische Fragestellungen anhand von numerischen Studien beleuchtet. Im weiteren Verlauf wird der Ansatz mit experimentellen Ergebnissen validiert und aufgezeigt, welche ausgewählten physikalischen Effekte und globalen Parameteränderungen sich mit der vorgestellten Methode abbilden lassen.

Schlagworte: Kontakt Homogenisierung, Multiskalen-Ansatz, Gummireibung, Hysteresereibung, Adhäsion, Kontakttemperatur

Abstract

Studying rubber friction on rough surfaces provides an essential part for understanding the tire-road-interaction and the improvement of grip properties for future tire development. One goal of this work is to include relevant physical effects in a finite element model in order to be able to predict friction responses of certain rubber-road surface-combinations under different global conditions. Furthermore, the numerical method could be used to generate additional valuable knowledge about rubber friction since physical effects are divided and access to quantities that are not reachable in experiments is provided.

Rough surfaces generate a cyclic excitation of sliding viscoelastic rubber materials leading to energy dissipation and consequently to a frictional force known as hysteretic friction. Modelling of hysteretic friction is realized directly using rough surface profiles in combination with a viscoelastic material model. Simultaneously, interlocking effects are included. In order to consider relevant surface asperities, a multiscale framework is presented in this work which is based on contact-homogenization and consideration of the rough surface on several length-scales. The macroscopic pressure is transferred by homogenization over several rough surface samples and the resulting hysteretic friction is passed back via a homogenized coefficient of friction.

In addition to hysteresis, adhesion is modelled in this work. For that reason, the contact area resulting from consideration of all length scales is estimated. Adhesion is considered as the interaction of rubber molecule chains with atoms of the rough counter surface. A phenomenological adhesion model is integrated into the multiscale approach.

Furthermore, during a sliding process with high velocities, a strong heating of the rubber block at the contact interface is observed providing a change of the frictional response. Hence, temperature effects are included into the multiscale approach. A thermomechanically coupled simulation is realized on the largest length scale. Based on the calculated temperatures the material properties are changed on all lower scales. Consequently, the influence of thermal effects on hysteretic friction is demonstrated.

The numerical multiscale approach is described for individual physical effects in detail and some relevant numerical studies with respect to the methodology are performed. Thereafter, the approach is validated with experimental results and the capability of the proposed method to predict the influence of different physical effects and global parameter changes is demonstrated.

Keywords: Contact homogenization, Multiscale approach, Rubber friction, Hysteretic friction, Adhesion, Contact temperature

Danksagung

Diese Arbeit ist im Rahmen meiner Forschungstätigkeit am Institut für Kontinuumsmechanik der Leibniz Universität Hannover innerhalb eines Kooperationsprojektes mit der Continental Reifen Deutschland GmbH entstanden. Ich bedanke mich bei Continental für die finanzielle Unterstützung, die mir diese Arbeit ermöglicht hat.
Ich möchte mich herzlich bei meinem Doktorvater Prof. Peter Wriggers bedanken. Dank seiner Unterstützung und Förderung war es mir möglich das Thema gezielt zu bearbeiten und von seinem Wissen zu profitieren. Die gute Arbeitsatmosphäre und von ihm eröffneten Möglichkeiten werde ich stets in positiver Erinnerung behalten. Ein großer Dank gilt Prof. Burkhard Wies, der mit seiner positiven Art und dem Interesse an der Arbeit wesentlich zum Erfolg des Projektes beigetragen hat. Desweiteren möchte ich mich herzlich bei Prof. Stanislaw Stupkiewicz für die Übernahme des zweiten Referates und für seine wertvollen Kommentare zur Arbeit bedanken. Prof. Ludger Overmeyer danke ich für die Übernahme des Prüfungsvorsitzes.
Ich möchte mich für die Unterstützung der „Contact and Friction Physics“-Gruppe um Thiemo Kessel, Stefan Torbrügge und Rene van-der-Steen bedanken. Ein großer Dank für die wertvollen Hinweise und Anmerkungen während des Projektes gilt dem Review Team um Christoph Bederna, Dong Zheng, Pavel Ignatyev, Thomas Schulze, Rafal Nojek und Klaus Wiese. Großer Dank gilt drei Personen, die mich in verschiedenen Projektphasen intensiv unterstützt haben: Corinna Klapproth, Corinna Prange und Heiko Clasen. Die Unterstützung war vorbildlich und es hat viel Spaß gemacht mit ihnen zu arbeiten.
Ich bedanke mich bei allen Studenten, die ihre studentischen Arbeiten bei mir absolviert haben. Insbesondere auf Lennart Veltmaat konnte ich mich stets verlassen und er hat großartige Arbeit geleistet. Ich konnte während der Arbeit auf hervorragende experimentelle Ergebnisse zurückgreifen und möchte mich bei allen Personen bedanken, die daran mitgewirkt haben. Insbesondere gilt mein Dank den Kollegen vom IDS, DIK, Hagen Lind, Matthias Wangenheim und Stefan Ripka.
Ich möchte mich bei allen Kollegen des Institutes bedanken, die mir organisatorisch geholfen haben oder Spaß mit mir hatten. Insbesondere die gemeinsame Zeit auf dem Fußballfeld beim Betriebssport wird mir immer positiv in Erinnerung bleiben. Sebastian, Tobias und Artsem danke ich für alles, was ich gemeinsam mit ihnen am Institut und außerhalb erleben durfte. Man kann sich auf sie verlassen.
Ich bedanke mich bei meiner Familie und meinen Freunden für das Verständnis, dass ich während meiner Promotionszeit nicht immer überall dabei sein konnte. Umso intensiver habe ich die gemeinsamen Stunden genossen. Bei meiner Frau Anna möchte ich mich für die großartige Unterstützung während aller Promotionsphasen und darüberhinaus bedanken. Mit ihrem Verständnis sind selbst sehr schwierige Phasen nur halb so wild.

Hannover, Januar 2018 Paul Wagner

Contents

Chapter 1

Introduction

1.1 Motivation

Tire manufacturers face a lot of challenging tasks in the development process of new tires. The superior aim is to optimize characteristics like rolling resistance, handling, noise, wear or braking performance among others. These aims partly contradict themselves leading to complex relationships and target conflicts during the development process, see figure 1.1 a). In order to understand and improve all targets field studies with real tires (see figure 1.1 b)), experimental tests in laboratory and simulation techniques are widely used.

For further improvement of the complex grip behaviour of tires, containing multiple physical phenomena, more sophisticated and improved simulation tools in combination with new experimental approaches are demanded, see figure 1.1 c). This work concentrates on modelling the safety-relevant aspect of grip performance on wet and dry surfaces with the aim to improve it later on. A massive improvement of the car

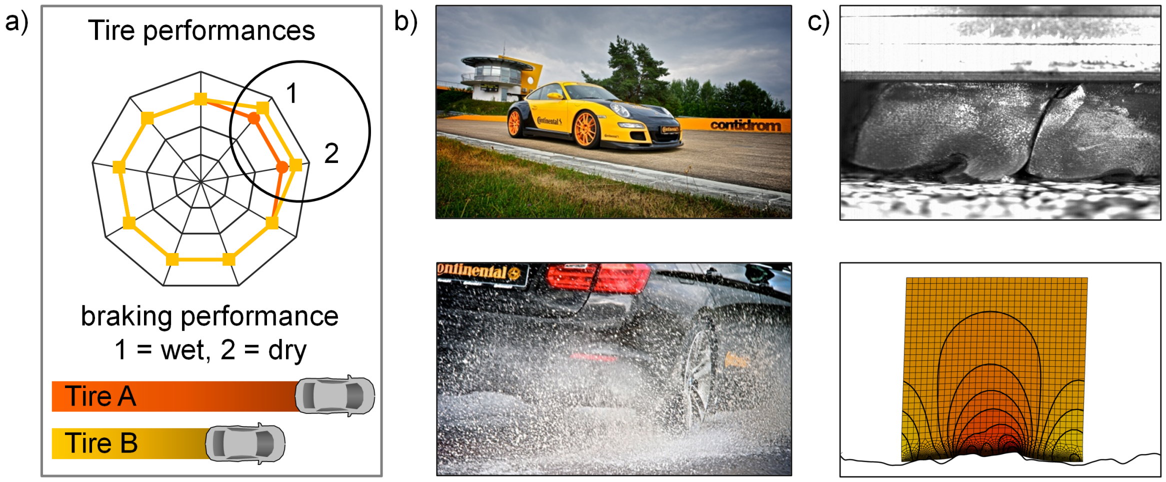

Figure 1.1: a) Tire performances with exemplary braking performance of two tires. b) Dry and wet braking (pictures taken by bluestudios GmbH / Volker Warning, courtesy of Continental). c) Fundamental studies: experiments (Courtesy of Continental) and numerical modelling of sliding rubber blocks.

braking performance was achieved over the last decades by introducing for example anti-lock braking systems (ABS) or compounds with an improved grip level. Reduced braking distances by improved tire performances will help to reduce the number of traffic fatalities in the future, contributing to the desirable goal of zero fatalities and accidents, called vision zero.

One goal of this work is to gain more knowledge of the physical processes of rubber friction, taking place on a large range of length scales. In order to achieve this goal, the work concentrates on effects of a macroscopic rubber block with the size of a few centimeters down to the smallest relevant length scales of some micrometers excluding the analysis of tire mechanics. The method is validated with experimental results and generates a deeper understanding of the process, providing additional useful information that is inaccessible in experimental studies. With this valuable knowledge, tire engineers can further improve the grip performance of new innovative tires.

1.2 State of the Art

In order to understand the process of rubber friction, a lot of experimental and modelling studies were performed, starting with the early works of SCHALLAMACH (1952, 1953) and GROSCH (1963). Based on the performed measurements and observations, fundamental statements regarding the physical mechanisms of rubber friction are derived in SCHALLAMACH (1971), see also ROBERTS & THOMAS (1975); ROBERTS (1976); BARQUINS & ROBERTS (1986). Summarizing, a complex behaviour under a lot of macroscopic parameters such as load, velocity, temperature, rubber material and state of the counter surface is noticed and linked to the physical phenomena of hysteretic friction, adhesion, and other effects. However, contemporary experimental studies show still the necessity of further investigations, see LAHAYNE & EBERHARDSTEINER (2007); RIPKA ET AL. (2009); RIPKA (2013); WALLASCHEK & WIES (2013).

The mechanism of hysteretic friction originates from the energy dissipation inside the viscoelastic rubber material during sliding, leading to a different response of rubber in contrast to non-viscoelastic materials like metals for example. The origin of adhesion and its influence on the frictional response of sliding rubber is a topic under controversial discussion. Adhesion is, contrary to the bulk phenomenon hysteresis, a surface effect described from a macroscopic point of view as the sticking of the rubber to the counter surface. This observation is a direct result of interactions between rubber molecules and surface atoms on a nanometer length scale. Additionally, rubber samples heat up during sliding and thus change the properties of hysteretic and adhesive effects, especially for large sliding velocities. A lot of valuable results are provided by the cited experimental studies and various questions about rubber friction are answered. Nevertheless, certain effects at the contact interface, the complex interaction of different mechanisms, and prediction of frictional responses remain an open question.

In order to predict the frictional response of rubber and to gain some additional understanding and information, multiple modelling approaches are developed. Starting with KLÜPPEL & HEINRICH (2000) and PERSSON & TOSATTI (2000); PERSSON (2001), analytical approaches were proposed first for hysteretic friction and then extended by models for adhesion and thermomechanical interaction, see Persson (2002); Persson et al. (2005); Le Gal et al. (2005); Le Gal & Klüppel (2008); Lorenz et al. (2015) and Persson (2006, 2014); Fortunato et al. (2015). In addition to the mentioned experimental studies, these analytical approaches revealed further valuable insights of rubber friction and its mechanisms. Nonetheless, those analytical approaches contain certain assumptions, uncertain input parameters or simplifications. Within the analytical models, sub-models for e.g. calculating the current contact area are necessary. Numerical modelling of the contact interaction with the help of finite element technology can replace those sub-models and improve the prediction quality. Also, more complex material models i.e. nonlinear instead of linear theories could be used within a finite element framework, getting closer to the vision described in the previous section 1.1.

Therefore, rubber friction is modelled with finite elements in this thesis trying to generate more knowledge about the process of a sliding rubber block besides the available knowledge from experimental and analytical studies. A single numerical model with all rough surface details would be hard to handle and very expensive from a computational point of view, because a very fine resolution in space and time has to be provided for sliding rubber samples on a rough surface. As a consequence, complex contact problems with microscopic details are often solved with multiscale approaches dividing the original problem into separate calculations. In contrast to single scale approaches like Hofstetter et al. (2006b), multiscale approaches reveal the chance to model hysteresis directly. Hence, multiscale approaches are used as a basis of the developed method in this thesis including hysteresis, adhesion and temperature effects at the contact interface.

A popular finite element approach is based on a contact homogenization procedure reducing the amount of information that has to be transferred between the scales, see Temizer & Wriggers (2008); Wriggers & Reinelt (2009). With this approach a very complex communication between the scales is omitted, see for example Nitsche (2011). Macroscopic contact values (pressure, velocity) are passed as boundary conditions to the microscopic length scales. The response of the microscopic sub-model is used to compute a resulting coefficient of friction. This coefficient of friction is averaged in time in order to be reduced to a time-independent value enhancing the macroscopic contact formulation by microscopic interactions in a next step. These contact homogenization approaches, see also Wagner et al. (2015) and Wagner et al. (2017), proved to be a powerful and useful tool for the simulation of complex contact problems consisting of details on a large range of length scales, especially rubber friction on rough road surfaces.

In Wriggers & Reinelt (2009); Falk et al. (2016), also adhesive interactions on the lowest length scale are introduced. Extensions to thermal interactions of rubber on a rough surface can be found in Temizer & Wriggers (2010b); Temizer (2011, 2014, 2016). In addition to the general multiscale framework, a lot of numerical studies on the microscopic length scale were performed to study the properties and outcome of homogenization, see for example Temizer & Wriggers (2010a), de Lorenzis & Wriggers (2013), Temizer (2013), Stupkiewicz et al. (2014) and Temizer

(2014).

1.3 Structure of the Thesis

An overview of rubber friction physics including experimental studies, contributing effects and modelling approaches is provided in chapter 2. Afterwards, the continuum mechanical fundamentals and basic equations for the solution of contact problems including rough surfaces and viscoelastic rubber materials in a geometrically nonlinear setting are presented in chapter 3 and 4, respectively. The governing equations are solved with the finite element method and therefore the background of finite elements for solid mechanics and contact problems is explained in chapter 5. The developed multiscale approach for rubber friction is divided into physical effects that are modelled and explained in chapters 6, 7 and 8. First of all, the approach for hysteretic friction and the main features of contact homogenization are derived in chapter 6 starting with an overview of known approaches and main results. Secondly, the multiscale method is extended for adhesive interactions in chapter 7. Finally, a modification of the multiscale approach in order to include thermomechanical interactions is proposed in chapter 8. Implementation details are provided in each chapter and certain important aspects are examined with numerical studies. The results of the multiscale method and single aspects are validated with experimental results at the end of chapters 6, 7 and 8 in order to reveal the prediction quality of the multiscale method. The results are summarized in chapter 9 and an outlook is given.

Chapter 2

Elastomer Friction Physics

For an appropriate modelling of rubber friction, a deep understanding of the experimental observations and underlying physical processes is essential. Thus, the results of the most important fundamental experimental studies are summarized in this chapter, completed by a short review on contemporary experimental techniques. After an illustration of the physical effects contributing to the frictional response of sliding rubber samples, a brief overview on modelling approaches is given. Analytical approaches are roughly summarized since some aspects of the later proposed multiscale approach and results are compared to these approaches. The chapter is completed with a classification of numerical studies on rubber friction.

2.1 Experimental Investigations

The fundamental studies of SCHALLAMACH and GROSCH are summarized and as an example for contemporary experiments, the test setups used for validation in later chapters are explained. Details of the test results together with certain details of the measurement techniques are explained during the validation studies in chapters 6, 7 and 8.

2.1.1 Fundamental Studies

Studies of friction between solid bodies started a few hundred years ago with the pioneering works of DA VINCI, AMONTONS and COULOMB using simple experimental setups. The latter developed a mathematical description summarizing the early experimental results. The proportional connection between normal force F_z and the perpendicular friction force F_x during sliding, described by the friction coefficient μ, depends mainly on the material pairing and is called COLOUMB friction law

$$F_x = \mu F_z. \tag{2.1}$$

In POPOVA & POPOV (2015) an overview of the early works by AMONTONS and COULOMB is given, summarizing their experimental observations and formulated laws

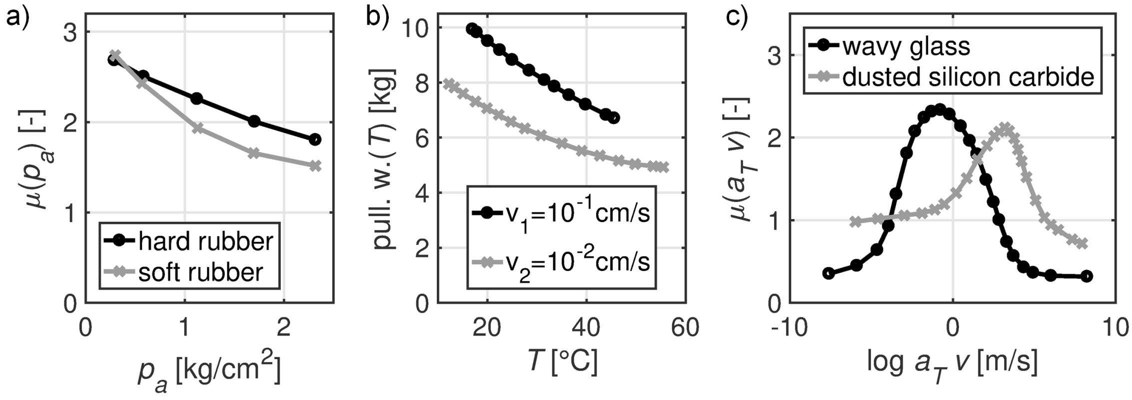

Figure 2.1: a) Measured coefficient of friction over apparent pressure $p_a = m/A$ (mass divided by area) for two rubber compounds, extracted from Schallamach (1952). b) Measured pulling weight (pull. w.) over temperature T (controlled via the surface track) for two velocities, extracted from Schallamach (1953). c) Coefficient of friction over velocity v shifted with a constant factor a_T for two surfaces, extracted from Grosch (1963).

of friction. Coulomb investigated for example already several dependencies on friction like weight, surface conditions or contact area and more.

The fundamental studies in Schallamach (1952, 1953) observe that rubber friction depends significantly on the applied macroscopic pressure p, velocity v and temperature T, see figure 2.3 for a schematic rubber block with applied loads. The well-known dependence on the used materials is confirmed by experimental studies using different sliding rubber materials and counter surfaces. As a consequence of the significant influence of the macroscopic variables, a friction law with a constant coefficient of friction does not hold for rubber friction: $\mu(p, v, T)$.

Besides the mentioned dependencies, the coefficient of friction is time- and history-dependent for sliding rubber samples induced by viscoelastic effects, local temperature changes and different states of the rough counter surface. The time-dependency of a single measurement is removed in most experimental results considering the kinetic coefficient of friction by averaging over time, cf. equation (2.2). Thereby the dynamic start of the sliding process with a force peak (also referred to as the static coefficient of friction) as well as local fluctuations over time are excluded.

In Schallamach (1952) the load-dependency of the coefficient of friction of different rubber materials is measured on a dry glass plate, displayed in figure 2.1 a). The results show a decreasing coefficient of friction for increasing pressure values. All experiments are performed with a velocity of $2.16 \cdot 10^{-3}$cm/s and are repeated for different vulcanizates of natural rubber showing different responses.

The velocity- and temperature-dependency of an unloaded vulcanizate of natural rubber on a silicon-carbide surface is investigated in Schallamach (1953). For the used setup a decrease of frictional force (less pulling weight in this experimental setup) with increasing temperature at constant velocity is observed in Schallamach (1953), see figure 2.1 b). This observation is assigned to the strong temperature dependency of the viscoelastic material properties, details are explained in section 3.3.1. The additional variation of the applied velocity indicates a higher measured pulling weight for a higher velocity. Nevertheless, this effect may change its direction for different velocity values. In Grosch (1963), the velocity-dependency of rubber friction is investigated in more detail observing that a strong connection between the loss modulus and the frictional behaviour of different rubber materials exists. A typical bell-curve for the coefficient of friction over velocity is measured in Grosch (1963) on wavy glass and dusted silicone carbide surface, shown in figure 2.1 c). The curves are not directly measured over the large velocity-range but mastered (shifting the single curves by a constant factor a_T) from various measurements at different temperatures and low velocities. For this purpose, the concept of frequency-temperature-equivalence derived by Williams, Landel, and Ferry in Williams et al. (1955) (cf. subsection 3.3.1) is transferred to rubber friction.

The fundamental friction properties of elastomers with respect to changing macroscopic variables p, v, T are displayed in this section for a rough overview. They may change for different experimental input parameters and are studied in detail together with numerical results in chapters 6, 7 and 8. First links of the experimental observations to the underlying physical effects hysteresis and adhesion are provided in Grosch (1963), see section 2.2 for a detailed description.

In later decades further experimental studies were conducted that helped to understand more about the mechanisms of rubber friction. The fundamental studies with the main findings were summarized above and just an extract of further experimental works is mentioned here. In Schallamach (1971) visual observations through transparent, sliding rubber samples show waves of detachment at the interface. Furthermore, in Roberts & Thomas (1975) the adhesion mechanism of smooth rubber surfaces is studied more in detail. In Barquins & Roberts (1986) various rubber friction measurements for different velocities, temperatures, loads, and geometries are carried out, revealing a strong connection of frictional force to the area of contact and small contributions of viscoelastic properties on smooth surfaces. The reader is referred to Zeng (2013) for a larger review of experimental studies of rubber friction.

2.1.2 Contemporary Studies

Starting with friction test rigs for investigations of rubber friction in Schallamach (1952, 1953) and Grosch (1963) a couple of test rigs with increasing complexity were developed over the decades. Friction experiments are often performed on test rigs with a linear movement of the rubber block or the counter surface. Rotational test rigs are rather used for wear studies since larger sliding distances can be captured with such setups, see Gäbel (2009) for an overview.

The numerical results of this work are compared at the end of chapters 6, 7 and 8 to results measured at different linear test rigs. A machine used at Continental Reifen Deutschland GmbH is named high speed linear friction tester (HSLFT). Furthermore, a similar test rig (named HiLiTe) is used and developed at the Institute of Dynamics and Vibration Research (IDS) in Hanover. The relevant macroscopic parameter range for braking tires is assumed to be $0.1 < p < 0.5$MPa and $0.1 < v < 3$m/s. The

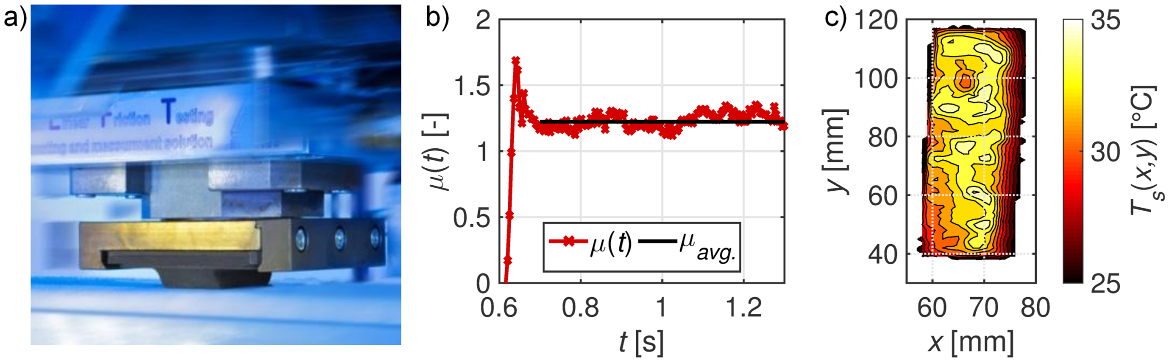

Figure 2.2: a) High speed linear friction tester (HSLFT) with a sliding rubber sample (pictures taken by bluestudios GmbH / Volker Warning, courtesy of Continental). b) Measured coefficient of friction, c) temperature of the rubber sample bottom after sliding.

HSLFT and HiLiTe are able to apply such relevant loads and velocities on top of fixed rubber blocks. Additionally, the whole test setups are placed in climate boxes ensuring a constant ambient temperature, see figure 2.2 a). Materials and counter surfaces can be exchanged easily, providing also the possibility to test winter conditions with an ice surface. Some details and pictures of the linear friction test rigs can be found in Hofstetter et al. (2006a,b) or in Ignatyev et al. (2015). Further descriptions of the HiLiTe and the developments of the machine can be found in Ripka et al. (2009); Ripka (2013) and Wallaschek & Wies (2013). Linear test rigs used in other elastomer friction studies differentiate mainly in the possible pressure- and velocity-ranges. Often, velocities below $v = 0.01$m/s and pressures of a low magnitude ($p = 0.01$MPa for example) are applied, see described setups in Lorenz et al. (2011) or Le Gal & Klüppel (2008).
During the experiment, the sum of the forces in x-(horizontal) $F_x(t)$ and z-(vertical) direction $F_z(t)$ are measured on top of the rubber block. These quantities are used to calculate the time-dependent coefficient of friction $\mu(t)$

$$\mu(t) = \frac{\sum F_x(t)}{\sum F_z(t)}, \quad \mu_{avg.} = \frac{1}{t_{end} - t_{start}} \int\limits_{t_{start}}^{t_{end}} \mu(t)\,\mathrm{d}t, \tag{2.2}$$

In order to reduce the amount of information for a p, v, T-parameter-set the steady state coefficient of friction $\mu_{avg.}$ is evaluated by averaging over a time interval $t_{start} - t_{end}$, see also figure 2.2 b). Additionally, further quantities like the temperature of the road track or the temperature of the rubber sample (displayed in figure 2.2 c)) can be measured with modern test rigs, see Lindner (2005); Lahayne & Eberhardsteiner (2007); Linke et al. (2014).

2.2 Contributions to Elastomer Friction

A first distinction and classification of the relevant physical effects for rubber friction can be found in Kummer (1966). Figure 2.3 shows a schematic overview of all known physical effects for a sliding rubber block on a partly wet rough surface. A complex interaction in the contact layer between hysteresis, adhesion, viscous friction, cohesion, and interlocking effects is observed. The total measured tangential force (F_x) in experiments is the result of the interaction of all contributing effects:

$$F_x(F_H, F_A, F_V, F_C, F_I). \tag{2.3}$$

All quantities depend heavily on the applied load and the surface conditions. The single effects are explained in detail in the following subsections. For a general overview of different friction mechanisms for rubber and other materials, the reader is referred to Persson (2000).

2.2.1 Hysteresis and Adhesion

The surface asperities of a rough surface enforce a cyclic loading and unloading of the sliding rubber material. Due to viscoelastic properties of rubber materials, an internal energy dissipation is generated, leading to a horizontal resistance force during the sliding process, named hysteresis or hysteretic friction, cf. subsection 2.3.2 for a mathematical description. In figure 2.3, two dissipation areas are displayed. Large energy dissipation because of large local deformations (small bright red areas) is assumed to be induced by the small surface asperities. Furthermore, less energy dissipation by the larger surface asperities is expected (light red area), see also Persson & Tosatti (2000) and Persson (2001). The reported velocity-dependency of rubber friction is strongly linked to this effect since the rubber material is excited with different frequencies for different sliding velocities. The frequency-dependent response of rubber materials under cyclic loading can be measured in laboratories providing a basis for modelling the effect of hysteretic friction.
The dissipated energy is transferred into heat causing a temperature rise of the rubber during sliding, indicated in figure 2.3 in the hysteresis frame. Since the viscoelastic rubber properties are temperature-dependent as well, a rising temperature causes a

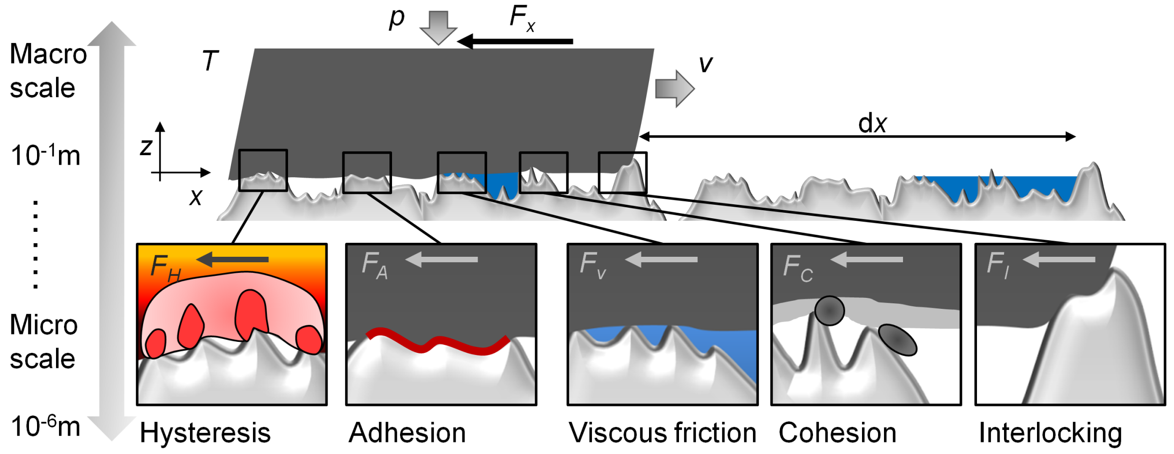

Figure 2.3: Macroscopic rubber block with microscopic details showing relevant physical effects for rubber friction.

significant change of these properties. The change of the viscoelastic properties influences in turn the frictional response. Especially for high sliding velocities, this effect is observed in experiments and has to be addressed in analytical or numerical models.

Intermolecular forces act in the close contact layer between rubber material and the road surface on a nanometer length scale. This surface phenomenon is called adhesion, for a general overview see Pocius (2002). On the macroscopic length scale, an occurring sticking of the rubber to the rough surface can be observed and certain forces are necessary to overcome the bonding of the bodies. There exist plenty of possible explanations for the origin of this phenomenon like van-der-Waals forces or an interaction of rubber molecules and rough surface atoms. The latter effect is assumed to be the prevailing mechanism for rough surfaces and will be addressed in detail together with some model assumptions in section 7.2. Further possibilities for the adhesion mechanism would be interfacial crack propagation, an interaction between rubber filler particles or wear effects, see Lorenz et al. (2015) for an overview.

Different frictional responses of rubber samples are measured for the same rough surface under dry, partly wet and wet surface conditions. This observation is linked to the assumption of different shares of hysteresis and adhesion for changing surface conditions and a complex interaction of these effects. A loss of adhesive bonds for lubricated surfaces is assumed, leading to a suppressed adhesional contribution. Consequently, a lower frictional response for wet surfaces is expected.

2.2.2 Further Physical Effects

During the interaction with a rough road surface, the rubber material wears down. This process (also called cohesion) leads to a significant change of the rubber contact layer and contributes to the frictional behaviour of the material. Material is removed from the rubber block and can create a complex interaction with the remaining rubber material, shown in figure 2.3. The micro structure of rubber consisting of free rubber and hard agglomerates influences the detachment of rubber particles at the microscopic scale. Additionally, the worn surface can consist of different microscopic fractions (free rubber or hard agglomerates) which may again significantly influence adhesion.

In contrast to the above described phenomena, viscous friction is only relevant for wet surfaces. Small road cavities could be filled with water and contribute no longer to hysteretic friction. Moreover, the frictional behaviour is changed because water fills the space between rubber and road leading to a contribution to the overall friction force resulting from shearing of the water film.

Another contribution to the frictional force are interlocking effects. The rubber block hits with its edges asperities of the rough road surface causing a horizontal resistance force. This effect is especially expected at the leading edge of the rubber block and increases with the surface roughness.

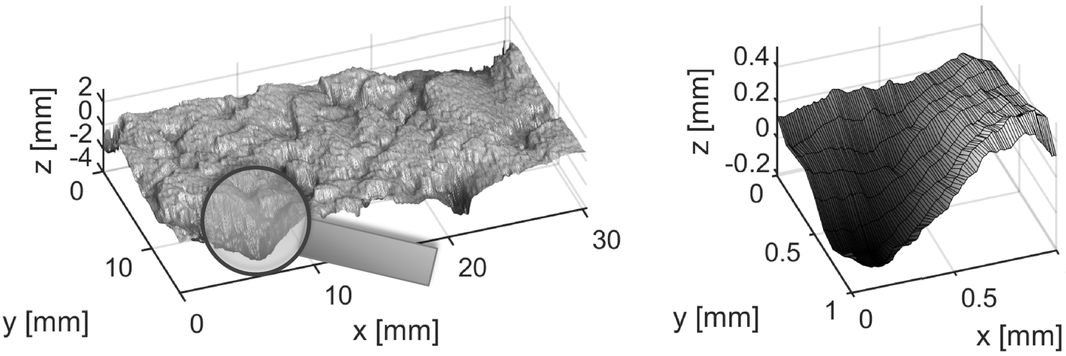

Figure 2.4: Exemplary rough road surface with microscopic details.

2.3 Modelling Elastomer Friction

After an introduction to mathematical descriptions of rough surfaces, a short overview and classification of existing analytical and numerical models for rubber friction is provided. Important results of pioneering works are summarized. Advantages and disadvantages of the methods are discussed in order to demonstrate the necessity for a numerical multiscale approach for elastomer friction on rough surfaces, introduced later in chapters 6, 7 and 8.

2.3.1 Surface Description

Rough road surfaces usually made of asphalt or concrete are rough over many length scales and exhibit the self-affine character of fractal surfaces. An overview of fractal geometry is given in Mandelbrot (1983). An example of a rough road surface is given in figure 2.4. By definition self-affine surfaces show statistical invariance under anisotropic dilation in a certain surface-wavelength (λ) range ($\lambda_{min} - \lambda_{max}$), meaning a rough surface shows the same statistical properties and morphology under a scaling α in cross section direction and α^H in the perpendicular direction. The so-called Hurst-exponent H is introduced as a measure for surface irregularity and is linked to the fractal dimension by $D = 3 - H$ for three-dimensional surfaces.
One way to describe rough surfaces mathematically is to calculate the height difference

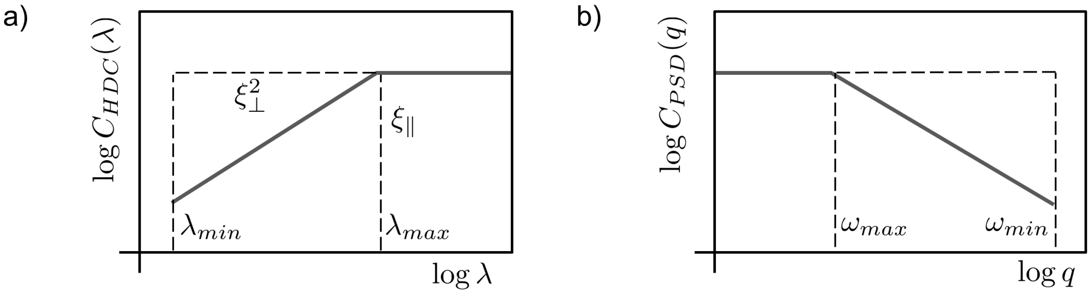

Figure 2.5: a) Exemplary schematic height difference correlation function (HDC) of a rough road surface. b) Exemplary schematic power spectral density function (PSD) of a rough road surface.

correlation (HDC)

$$C_{HDC}(\lambda) = \langle (z(x+\lambda) - z(x))^2 \rangle. \tag{2.4}$$

This function evaluates the average ($\langle ... \rangle$) square height difference of the height profile $z(x)$ for different horizontal wavelengths λ in x-direction. For self-affine surfaces, the function C_{HDC} is described by the power law

$$C_{HDC}(\lambda) = \xi_\perp^2 \left(\frac{\lambda}{\xi_\parallel} \right)^{2H}, \tag{2.5}$$

for $\lambda < \xi_\parallel$ with $2H$ representing the slope. The cutoff-point is defined by the values $\xi_\parallel$ and $\xi_\perp^2$, see figure 2.5 a) for a schematic example of a HDC function. Beyond the cutoff-point, the HDC shows a characteristic plateau for a rough surface since the height differences are determined by the surface envelope.

The description of a rough surface by the power spectral density (PSD) is in the context of elastomer friction introduced in Persson et al. (2005) and reads

$$C_{PSD}(q) = \frac{1}{(2\pi)^2} \int \langle z(\boldsymbol{x}) z(\boldsymbol{0}) \rangle e^{-i\boldsymbol{q}\cdot\boldsymbol{x}} \mathrm{d}^2 x, \tag{2.6}$$

with the spatial vector $\boldsymbol{x}$, the wave vector $\boldsymbol{q}$, and the mean height of the profile $z(\boldsymbol{0})$. Under the assumption that the statistical properties of the considered surface are translationally invariant and isotropic, the magnitude of the wave vector $q = |\boldsymbol{q}|$ is used to evaluate C_{PSD}. A schematic example of a PSD function of a rough surface is given in figure 2.5 b). The PSD function and HDC function can be used equally to describe the characteristics of a self-affine, rough surface and can be transformed to each other.

2.3.2 Analytical Models

Two well known analytical approaches for the description of rubber friction are the ones from Persson & Tosatti (2000); Persson (2001) and from Klüppel & Heinrich (2000). The energy dissipation inside the rubber volume V_r during a certain time Δt is the origin of hysteretic friction (cf. section 2.2) and can be calculated by the product of stress $\boldsymbol{\sigma}$ and the time derivative of strain $\dot{\boldsymbol{\varepsilon}}$:

$$\Delta E_{diss} = \int_0^{\Delta t} \int_0^{V_r} \boldsymbol{\sigma} : \dot{\boldsymbol{\varepsilon}} \, \mathrm{d}V \, \mathrm{d}t. \tag{2.7}$$

Transformations (see Klüppel & Heinrich (2000) or Persson (2001)) of the equation lead to a description including the frequency-dependent loss modulus $E''(\omega)$ of the rubber material and the power spectral density $C_{PSD}(q)$ of the rough surface introduced in the previous subsection. Furthermore, the dissipated energy during the sliding interval T has to be equal to the product of the hysteretic friction force F_H and the applied velocity v

$$\Delta E_{diss}/T = F_H v. \tag{2.8}$$

Using this equation and integrating over all excitation wavelengths leads to equations for the hysteretic friction coefficient with some differences for the mentioned approaches. In Klüppel & Heinrich (2000), μ_H is calculated with the applied macroscopic pressure σ_0 and the macroscopic velocity v

$$\mu_H = \frac{1}{2(2\pi)^2} \frac{\langle z_P \rangle}{\sigma_0 v} \int E''(\omega) \cdot S(\omega)\omega \, \mathrm{d}\omega, \tag{2.9}$$

using a frequency-dependent description of the power spectral density $S(\omega)$ based on the quantities $(\xi_\parallel, \xi_\perp^2, H)$ of the height difference correlation. The quantity $\langle z_P \rangle$ represents the mean penetration depth of the rubber into the rough surface. Klüppel & Heinrich (2000) use an extension of the well-known theory of Greenwood & Williamson (1966) for self-affine surfaces to determine $\langle z_P \rangle$.

In contrast to the the theory of Klüppel & Heinrich (2000); Persson (2001) uses a function $P(q)$ describing the interaction of the rubber block and the road surface on each length scale, obtaining different results. The latest formulation for the coefficient of friction by Persson (2014) reads

$$\mu_H = \frac{1}{2} \int\limits_{q_{min}}^{q_{max}} C_{PSD}(q) S(q) P(q) q^3 \, \mathrm{d}q \int\limits_{0}^{2\pi} \cos\phi \frac{E^*(qv\cos\phi, T_q)}{(1-\nu^2)\sigma_0} \, \mathrm{d}\phi. \tag{2.10}$$

with the magnitude of the wave vector q, a reduction factor $S(q)$, the complex viscoelastic rubber modulus E^*, the Poisson ratio ν, the surface angle ϕ and the temperature T_q. The detailed theory for the incorporation of flash temperature effects can be found in Persson (2006, 2014) and Fortunato et al. (2015).

An additional important mechanism contributing to rubber friction is adhesion. Extensions of the friction theory including adhesive effects are presented in Persson (2002); Persson et al. (2005); Le Gal et al. (2005) and Le Gal & Klüppel (2008). In Lorenz et al. (2015), the adhesive contribution is modelled with a frictional shear stress τ_A and the contact area $A_1 = P(q_{max})A_0$:

$$\mu_A = \frac{\tau_A}{\sigma_0}\frac{A_1}{A_0} = \frac{\tau_A}{\sigma_0} P(q_{max}). \tag{2.11}$$

The used assumptions and the adhesion law which are applied in the later proposed multiscale setup are explained in chapter 7.

2.3.3 Numerical Models

In order two provide an overview of numerical models for rubber friction using the finite element method, the approaches are divided into two main categories and some subcategories. An overview and details of single scale approaches are provided in this subsection whereas the overview of multiscale approaches is postponed to section 6.1.

- Single scale approaches

  - Elastic or viscoelastic continuum on flat or rough surface without microscopic details
  - Viscoelastic continuum on rough surface with all surface details

- Multiscale approaches
  - Contact homogenization
  - Projection methods

Pure elastic or viscoelastic rubber models without modelling complex contact interactions between the rubber and a flat or rough surface without microscopic details belong to the first category. These models concentrate on the macroscopic modelling of rubber friction predicting for example contact pressures or temperatures, see HOFSTETTER ET AL. (2006a). Furthermore, such models are also used to compare different rubber block geometries on the macroscopic length scale. A drawback regarding multiple rubber-surface combinations is that for such approaches a complex friction experiment is needed to incorporate a friction law in the contact simulation. Thus, for slight changes in material or surface properties, a completely new measurement has to be performed. A prediction of the hysteretic contribution is thus not achievable.

Another way to model rubber friction is the direct modelling of the viscoelastic material properties and the involved rough surface with all details. Predictions and detailed studies of the contact interaction are possible with such approaches using friction experiments for validation of the model. Consequently, no experimental data from friction experiments are necessary as a model input. The viscoelastic material properties are gained from well-known laboratory experiments. The rubber material is considered to be homogeneous in most numerical studies of rubber friction. An extension to complex heterogeneous rubber micro structures is possible and probably necessary for detailed wear and adhesion studies. Nevertheless, modelling the surface roughness with all asperity details directly makes a single scale calculation too expensive for today's computer technology.

Therefore, complex contact interactions with rough surfaces can be modelled with numerical multiscale approaches in an efficient way. The two subcategories including relevant literature about multiscale approaches for rubber friction are discussed at the beginning of chapter 6 and 8.

Chapter 3

Continuum Mechanics

With the theory of continuum mechanics, three-dimensional thermomechanical problems can be described with a set of mathematical equations. The kinematical relations and an adequate strain measure are the basis for the description. The universally valid balance equations provide a system of differential equations for the considered continua. Each material reacts differently to an applied load. Therefore, a proper constitutive law has to capture the relationship between independent variables (displacement, temperature) and dependent variables (e.g. stresses) for the considered material correctly. Fundamental introductions and further continuum mechanical aspects can be found in ALTENBACH (2012); CHADWICK (1999); HAUPT (2000); HOLZAPFEL (2000); MARSDEN & HUGHES (1994); OGDEN (1984); TRUESDELL ET AL. (2004). In order to apply a solution with the finite element method, the weak formulations of the balance laws are stated at the end of this chapter.

3.1 Kinematics

This section introduces the fundamental quantities for a body undergoing large deformations. In a large deformation setting, it is necessary to distinguish between the initial and the current configuration. Following the common literature, capital letters are used for quantities defined in the initial configuration and small letters for quantities defined in the current configuration.

By definition, a solid body $\mathcal{B}$ consists of a certain number of connected particles P. During a deformation process no change in the amount of particles is assumed. The position vector of a particle or material point is denoted with $\boldsymbol{X}$ in the initial configuration at time $t = 0$ and with $\boldsymbol{x}$ at the current configuration, see figure 3.1. The used basis system of unit vectors $\boldsymbol{E}_i, \boldsymbol{e}_i$ is denoted utilizing the EINSTEIN summation convention for both configurations

$$\boldsymbol{X} = X_i \boldsymbol{E}_i \quad , \quad \boldsymbol{x} = x_i \boldsymbol{e}_i. \tag{3.1}$$

A common notation for the deformation process is given by the mapping operator φ

$$\boldsymbol{x} = \varphi \left(\boldsymbol{X}, t \right). \tag{3.2}$$

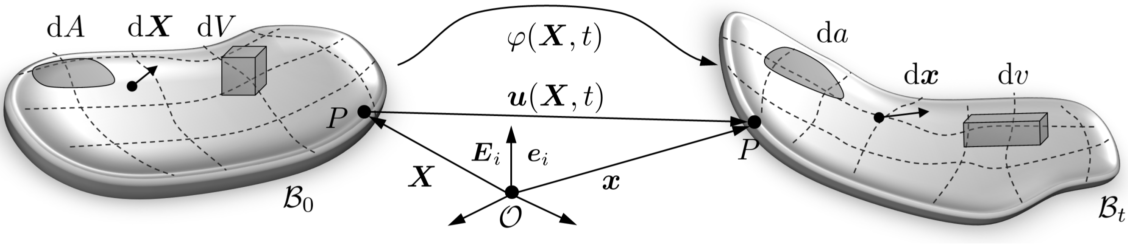

Figure 3.1: Kinematics of a solid body including surface, line and volume elements.

The displacement vector $\boldsymbol{u}$ of a given point is the difference between the position in the current and the initial configuration

$$\boldsymbol{u}\left(\boldsymbol{X},t\right)=\boldsymbol{x}\left(\boldsymbol{X},t\right)-\boldsymbol{X}. \tag{3.3}$$

The time derivative of the position vector describes the velocity $\boldsymbol{v}$ and the second time derivative describes the acceleration $\boldsymbol{a}$

$$\boldsymbol{v}=\frac{\mathrm{d}\boldsymbol{u}}{\mathrm{d}t}=\frac{\mathrm{d}\boldsymbol{x}}{\mathrm{d}t}=\dot{\boldsymbol{x}},\quad \boldsymbol{a}=\frac{\mathrm{d}^2\boldsymbol{x}}{\mathrm{d}t^2}=\frac{\mathrm{d}\boldsymbol{v}}{\mathrm{d}t}=\dot{\boldsymbol{v}}=\ddot{\boldsymbol{x}}. \tag{3.4}$$

The deformation gradient $\boldsymbol{F}$ maps a line element from the initial configuration $\mathrm{d}\boldsymbol{X}$ to the current configuration $\mathrm{d}\boldsymbol{x}$ during a deformation process

$$\mathrm{d}\boldsymbol{x}=\boldsymbol{F}\cdot\,\mathrm{d}\boldsymbol{X}\quad,\ \boldsymbol{F}=\frac{\partial\boldsymbol{x}}{\partial\boldsymbol{X}}. \tag{3.5}$$

From a physical point of view, no points are allowed to vanish or to appear suddenly. Thus, the inverse $\boldsymbol{F}^{-1}$ mapping has to exist. This is ensured by a condition for the determinant

$$\det\boldsymbol{F}=J>0. \tag{3.6}$$

This quantity is also called JACOBIAN J, mapping infinitesimal volume elements:

$$\mathrm{d}v=J\,\mathrm{d}V. \tag{3.7}$$

After a transformation surface elements can be mapped with the so-called NANSON's formula

$$\boldsymbol{n}\,\mathrm{d}a=J\boldsymbol{F}^{-T}\cdot\boldsymbol{N}\,\mathrm{d}A, \tag{3.8}$$

with $\boldsymbol{n},\boldsymbol{N}$ being the normal vector of the considered surface element in current and initial configuration. In order to describe deformations, strain measures have to be introduced. The deformation gradient is not suitable for this purpose since it also includes rigid body motions. To circumvent this drawback, the GREEN-LAGRANGE tensor $\boldsymbol{E}$ and the EULER-ALMANSI tensor $\boldsymbol{e}$ are defined in the following way

$$\boldsymbol{E}=\frac{1}{2}\left(\boldsymbol{C}-\boldsymbol{1}\right),\quad \boldsymbol{e}=\frac{1}{2}\left(\boldsymbol{1}-\boldsymbol{b}^{-1}\right), \tag{3.9}$$

with the right Cauchy-Green tensor $\boldsymbol{C}$ in the initial configuration and the left Cauchy-Green tensor $\boldsymbol{b}$ in the current configuration, given by the following equations:

$$\boldsymbol{C} = \boldsymbol{F}^T \cdot \boldsymbol{F}, \quad \boldsymbol{b} = \boldsymbol{F} \cdot \boldsymbol{F}^T. \tag{3.10}$$

The time derivative of the deformation gradient $\boldsymbol{F}$ is often called material deformation velocity gradient. A mapping to the current configuration leads to the spatial velocity gradient $\boldsymbol{l}$ and its symmetric representation $\boldsymbol{d}$

$$\dot{\boldsymbol{F}} = \frac{\partial \dot{\boldsymbol{x}}}{\partial \boldsymbol{X}} = \frac{\partial \boldsymbol{v}}{\partial \boldsymbol{X}}, \quad \boldsymbol{l} = \dot{\boldsymbol{F}} \cdot \boldsymbol{F}^{-1} = \frac{\partial \dot{\boldsymbol{x}}}{\partial \boldsymbol{x}}, \quad \boldsymbol{d} = \frac{1}{2}\left(\boldsymbol{l} + \boldsymbol{l}^T\right). \tag{3.11}$$

3.2 Balance Equations

In this section, all principle balance laws of continuum mechanics are derived that are used for the weak formulations in section 3.4.

Conservation of Mass

During a deformation process, the mass m remains constant and does not change in time for a closed system. This means that no mass, also expressed by the density ρ integrated over the volume of a body, is added to the system or removed from it.

$$\frac{\mathrm{d}}{\mathrm{d}t} m = \frac{\mathrm{d}}{\mathrm{d}t} \int\limits_{\mathcal{B}_t} \rho \,\mathrm{d}v = \frac{\mathrm{d}}{\mathrm{d}t} \int\limits_{\mathcal{B}_0} \rho_0 \,\mathrm{d}V = \frac{\mathrm{d}}{\mathrm{d}t} \int\limits_{\mathcal{B}_0} \rho J \,\mathrm{d}V = 0. \tag{3.12}$$

With (3.7) the equation can be reformulated in the initial configuration. The time derivate can be applied on the inner part of the integral, leading to

$$\dot{m} = \int\limits_{\mathcal{B}_0} \frac{\mathrm{d}}{\mathrm{d}t} (\rho J) \,\mathrm{d}V = \int\limits_{\mathcal{B}_0} (\dot{\rho} + \rho \,\mathrm{div}\, \dot{\boldsymbol{x}}) \, J \,\mathrm{d}V = \int\limits_{\mathcal{B}_t} (\dot{\rho} + \rho \,\mathrm{div}\, \dot{\boldsymbol{x}}) \,\mathrm{d}v = 0. \tag{3.13}$$

The local form of the continuity equation with the mass density field $\rho = \rho(\boldsymbol{x}, t)$ can be written as

$$\dot{\rho} + \rho \,\mathrm{div}\, \dot{\boldsymbol{x}} = 0. \tag{3.14}$$

Balance of Linear and Angular Momentum

The time derivative of the linear momentum $\boldsymbol{L}$ of a body $\mathcal{B}_t$ in the current configuration equals the sum of the applied external forces forming the balance equation

$$\frac{\mathrm{d}}{\mathrm{d}t} \boldsymbol{L} = \frac{\mathrm{d}}{\mathrm{d}t} \int\limits_{\mathcal{B}_t} \rho \dot{\boldsymbol{x}} \,\mathrm{d}v = \int\limits_{\mathcal{B}_t} \rho \boldsymbol{b} \,\mathrm{d}v + \int\limits_{\partial \mathcal{B}_t} \boldsymbol{t} \,\mathrm{d}a. \tag{3.15}$$

The external forces include mass forces $\boldsymbol{b}$ and surface tractions $\boldsymbol{t}$. The Cauchy theorem defines the traction as the product of the stress tensor $\boldsymbol{\sigma}$ and the outward normal vector $\boldsymbol{n}$. With the use of the Gauss theorem the surface integral can be exchanged by a volume integral

$$\int\limits_{\partial\mathcal{B}_t} \boldsymbol{t}\,\mathrm{d}a = \int\limits_{\partial\mathcal{B}_t} \boldsymbol{\sigma}\cdot\boldsymbol{n}\,\mathrm{d}a = \int\limits_{\mathcal{B}_t} \operatorname{div}\boldsymbol{\sigma}\,\mathrm{d}v. \tag{3.16}$$

Equation (3.15) can be rewritten as

$$\int\limits_{\mathcal{B}_t} \operatorname{div}\boldsymbol{\sigma}\,\mathrm{d}v + \int\limits_{\mathcal{B}_t} \rho\boldsymbol{b}\,\mathrm{d}v = \int\limits_{\mathcal{B}_t} \rho\ddot{\boldsymbol{x}}\,\mathrm{d}v. \tag{3.17}$$

The local form for the balance of linear momentum for an arbitrary volume reads

$$\operatorname{div}\boldsymbol{\sigma} + \rho\boldsymbol{b} = \rho\ddot{\boldsymbol{x}}, \tag{3.18}$$

with a vanishing inertia term $\rho\ddot{\boldsymbol{x}} = 0$ for static problems.
The balance of angular momentum is formulated with respect to a fixed point $\boldsymbol{x}_0$ as a reference point. Thus, the time derivative of angular momentum in the current configuration equals the sum of applied external moments

$$\frac{\mathrm{d}}{\mathrm{d}t}\boldsymbol{J} = \frac{\mathrm{d}}{\mathrm{d}t}\int\limits_{\mathcal{B}_t} (\boldsymbol{x}-\boldsymbol{x}_0)\times\rho\boldsymbol{v}\,\mathrm{d}v = \int\limits_{\mathcal{B}_t} (\boldsymbol{x}-\boldsymbol{x}_0)\times\rho\boldsymbol{b}\,\mathrm{d}v + \int\limits_{\partial\mathcal{B}_t} (\boldsymbol{x}-\boldsymbol{x}_0)\times\boldsymbol{t}\,\mathrm{d}a. \tag{3.19}$$

Using the Gauss theorem, the conservation of mass, and the balance of linear momentum, it can be shown that the Cauchy stress tensor has to be symmetric

$$\boldsymbol{\sigma} = \boldsymbol{\sigma}^T. \tag{3.20}$$

Balance of Energy

The first law of thermodynamics states: The sum of applied mechanical power P and thermal power Q equals the time derivative of the total energy that can be decomposed into a kinetic part K and an internal part U

$$\frac{\mathrm{d}}{\mathrm{d}t}E = \frac{\mathrm{d}}{\mathrm{d}t}(K+U) = P + Q. \tag{3.21}$$

The kinetic energy K is induced by the motion of the body in time and the inner energy U contains the stored heat in the body and the strain energy in consequence of elastic strains with u as the specific internal energy

$$K = \int\limits_{\mathcal{B}_t} \frac{1}{2}\rho\boldsymbol{v}\cdot\boldsymbol{v}\,\mathrm{d}v, \quad U = \int\limits_{\mathcal{B}_t} \rho u\,\mathrm{d}v. \tag{3.22}$$

The origin of the mechanical power are all external forces ($\boldsymbol{t}$ and $\boldsymbol{b}$) acting on the body. The thermal power is decomposed into the internal heat source ρr and a heat flux $\boldsymbol{q}$ across the surface.

$$P = \int\limits_{\mathcal{B}_t} \rho \boldsymbol{v} \cdot \boldsymbol{b} \,\mathrm{d}v + \int\limits_{\partial\mathcal{B}_t} \boldsymbol{v} \cdot \boldsymbol{t} \,\mathrm{d}a, \quad Q = \int\limits_{\mathcal{B}_t} \rho r \,\mathrm{d}v - \int\limits_{\partial\mathcal{B}_t} \boldsymbol{q} \cdot \boldsymbol{n} \,\mathrm{d}a, \tag{3.23}$$

The heat flux vector direction is defined positive when pointing outside the body and vice versa. Together with the normal vector which points outside, a negative contribution for heat fluxes out of the system is ensured and a positive contribution for applying a heat flux. Inserting equations (3.23) and (3.22) in equation (3.21) leads to

$$\frac{\mathrm{d}}{\mathrm{d}t} \int\limits_{\mathcal{B}_t} \rho \left(u + \frac{1}{2} \boldsymbol{v} \cdot \boldsymbol{v} \right) \,\mathrm{d}v = \int\limits_{\mathcal{B}_t} \left(\rho r + \rho \boldsymbol{v} \cdot \boldsymbol{b} \right) \,\mathrm{d}v + \int\limits_{\partial\mathcal{B}_t} \left(\boldsymbol{v} \cdot \boldsymbol{t} - \boldsymbol{q} \cdot \boldsymbol{n} \right) \,\mathrm{d}a. \tag{3.24}$$

By the use of the Gauss theorem and the balance of linear momentum (3.18) the equation is simplified and converted to the local form

$$\rho \dot{u} = \rho r + \boldsymbol{\sigma} : \boldsymbol{d} - \operatorname{div} \boldsymbol{q}. \tag{3.25}$$

Entropy inequality

The second law of thermodynamics provides an inequality including the direction of a thermodynamic process. The measure of entropy S is introduced and defined as the integration of the specific entropy density s. In a thermomechanical process, the transformation of mechanical energy into heat is irreversible and leads to an increase of the entropy. As a consequence, the entropy introduced over the boundaries of the system by thermal power (see equation (3.23)) divided by the temperature θ has to be less than or equal to the time derivative of inner entropy

$$\frac{\mathrm{d}}{\mathrm{d}t} S = \frac{\mathrm{d}}{\mathrm{d}t} \int\limits_{\mathcal{B}_t} \rho s \,\mathrm{d}v \geq \int\limits_{\mathcal{B}_t} \rho \frac{r}{\theta} \,\mathrm{d}v - \int\limits_{\partial\mathcal{B}_t} \frac{1}{\theta} \boldsymbol{q} \cdot \boldsymbol{n} \,\mathrm{d}a. \tag{3.26}$$

The local form is derived by applying the divergence theorem

$$\rho \theta \dot{s} \geq \rho r - \operatorname{div} \boldsymbol{q} + \frac{1}{\theta} \boldsymbol{q} \cdot \operatorname{grad} \theta. \tag{3.27}$$

The Helmholtz free energy density function ψ can be expressed by the Legendre-transformation using the specific internal energy u and the entropy density s

$$\rho \psi = \rho u - \rho \theta s. \tag{3.28}$$

The time derivative of the whole equation excluding mass changes is given by:

$$\rho \theta \dot{s} = \rho \dot{u} - \rho \dot{\psi} - \rho s \dot{\theta}. \tag{3.29}$$

Using the time derivative of the Legendre-transformation, the first law of thermodynamics (3.25), the second law of thermodynamics can be specified in the local form which is often called Clausius-Duhem inequality

$$\boldsymbol{\sigma} : \boldsymbol{d} - \rho \dot{\psi} - \rho s \dot{\theta} - \frac{1}{\theta} \boldsymbol{q} \cdot \operatorname{grad} \theta \geq 0. \tag{3.30}$$

3.3 Constitutive Equations

In a first step, a few material characteristics of rubber are described in order to choose appropriate constitutive laws, completing the already derived set of equations. Afterwards, the thermodynamical theory including internal variables is described and the constitutive relations for hyperelasticity and viscoelasticity are introduced in subsections 3.3.3 and 3.3.4. Two different formulations for the hyperelastic and viscoelastic constitutive equations are used throughout this work within two finite element codes FEAP and ABAQUS. For completeness, both sets of equations are derived and it is indicated which finite element code uses the corresponding formulation.

3.3.1 Rubber Characteristics

This section describes and illustrates the most important physical properties of elastomers, see Röthemeyer & Sommer (2013) and Gent (2012) for an overview. The material model used throughout this thesis is based on the provided qualitative descriptions.

The basic ingredients of an elastomer used for tire applications are natural rubber (also called caoutchouc) and synthetic rubber. Natural rubber is a product of the rubber tree (Hevea brasiliensis), whereas synthetic rubber is manufactured by the use of petroleum byproducts. The raw product consists of long molecular chains of carbon atoms and other ingredients like hydrogen, oxygen, nitrogen and chlorine. In the initial state of maximized entropy, these chains are disordered and wadded. Under an external mechanical loading, the chains are stretched in the direction of loading causing a decrease in entropy. During the release of the external loading the chains entangle again and the system returns into a state of maximized entropy.

One of the most known characteristics of elastomers is their ability to undergo large deformations without material failure. Unfilled elastomers return to their undeformed shape when the load is released. This reversible non-linear stress-strain-behaviour is called hyperelasticity. A deformation up to 400% of the initial dimensions is possible, showing a non-linear behaviour in a stress-strain-curve, see figure 3.2 a). With the same material properties in all directions, the material is called isotropic. Thus, no direction dependency is introduced in this work. In addition to the hyperelastic properties, elastomers behave nearly incompressible under an applied load. This fact has to be considered in material models for elastomers, see e.g. Reese (2001).

The polymer chains of natural or synthetic rubber are cross-linked during a vulcanization process to set up physical properties for technical applications like tires or seals.

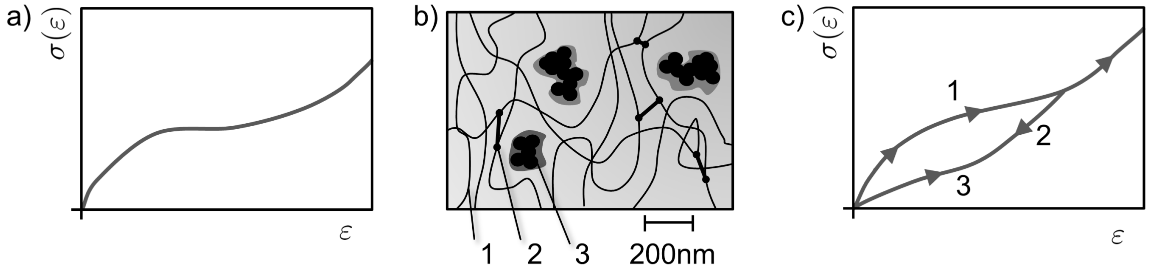

Figure 3.2: a) Exemplary stress-strain curve for an unfilled elastomer. b) Exemplary micro structure of a filled elastomer: 1) Polymer chain, 2) crosslink via sulfur bridges, 3) filler cluster. c) Exemplary path dependency of the stress-strain curve (Mullins effect) for a filled elastomer: 1) Loading, 2) unloading, 3) reloading.

Sulfur and fillers are added to the raw material, adjusting the final material properties. In a next step heat is applied during the vulcanization process. Carbon black or silica is often used in tire industry to increase the strength of the filled elastomer. An exemplary sketch showing a micro structure of a filled elastomer with polymer chains, crosslinks via sulfur bridges, and filler particles forming clusters can be found in figure 3.2 b).

Usually, filled elastomers show a path dependency in their quasi-static stress-strain-curve. It can also be detected for some unfilled elastomers, see Harwood et al. (1965), Harwood & Payne (1966a) and Harwood & Payne (1966b). A previous loading of the rubber material leads to an irreversible softening of the material, see figure 3.2 c). This phenomenon is called Mullins effect, see Mullins (1948). This effect is explained by the micro-mechanical breakage of hard filler clusters. Thus, after unloading a softer behaviour in the next loading path according to the unloading path is observed. In order to exclude the modelling of the Mullins effect in this work, rubber samples are preconditioned before measurements. The stress-strain curves are measured in a quasi-static test, loading rubber samples with tension and compression.

The material behaviour of elastomers under loading shows a time-dependency which is called viscoelasticity and can be assigned to a mixture of solid- and fluid-like properties. The viscous contribution is responsible for the observed energy dissipation under cyclic loading. Phenomena like relaxation or creep of elastomers are observed in experiments. Relaxation represents the decrease of stress under constant strain, whereas creep stands for the increase of strain under constant stress. Elastomer materials used for tires usually undergo deformations in a large frequency range, showing different stress-strain relations at different frequencies.

For an appropriate modelling and characterization of elastomers a dynamical mechanical analysis (DMA) is performed, see figure 3.3 a). A periodic time-dependent strain is applied on a rubber sample and the resulting force is measured resulting in a strain-stress response, including a time delay between both quantities, see figure 3.3 b). The phase lag $\delta(\omega)$ between strain $\varepsilon(t)$ and stress $\sigma(t)$ is a measure for the viscosity of the elastomer at a certain frequency

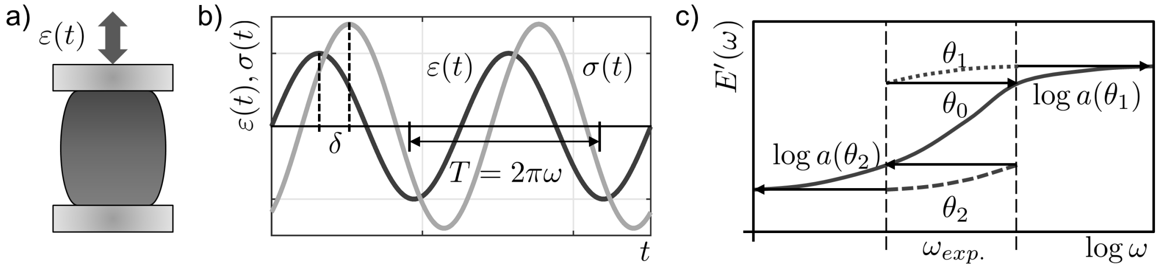

Figure 3.3: a) Test setup of a dynamical mechanical analysis, b) qualitative strain and stress signals, c) exemplary mastering procedure of the storage modulus.

$$\varepsilon(t) = \hat{\varepsilon}\sin(\omega t), \quad \sigma(t) = \hat{\sigma}(\omega)\sin(\omega t + \delta(\omega)). \tag{3.31}$$

The phase lag is used to determine the so-called storage modulus $E'(\omega)$ and loss modulus $E''(\omega)$ of the elastomer by using the applied strain amplitude $\hat{\varepsilon}$ and the measured phase lag and stress amplitude $\hat{\sigma}(\omega)$. The combination of the storage and loss modulus is called complex modulus $E^*(\omega)$:

$$E'(\omega) = \frac{\hat{\sigma}(\omega)}{\hat{\varepsilon}}\cos\delta(\omega), \quad E''(\omega) = \frac{\hat{\sigma}(\omega)}{\hat{\varepsilon}}\sin\delta(\omega), \quad E^*(\omega) = E'(\omega) + iE''(\omega). \tag{3.32}$$

The storage modulus describes the elastic portion of the material whereas the loss modulus stands for the viscous material fraction responsible for the energy dissipation. Since it is quite difficult to measure all possible frequencies with a single test device, a master curve is constructed by the use of a frequency-temperature-equivalent. The illustrated measurement of the storage modulus in figure 3.3 c) is conducted for different temperatures in the experimental frequency window $\omega_{exp.}$. The measured data for different temperatures are then shifted during the so-called mastering process, see figure 3.3 c), generating storage and loss modulus data over a wide range of frequencies. During mastering, the shift factor equation derived in WILLIAMS ET AL. (1955) is used

$$\log a(\theta) = -\frac{c1\,(\theta - \theta_{ref})}{c2 + (\theta - \theta_{ref})}, \tag{3.33}$$

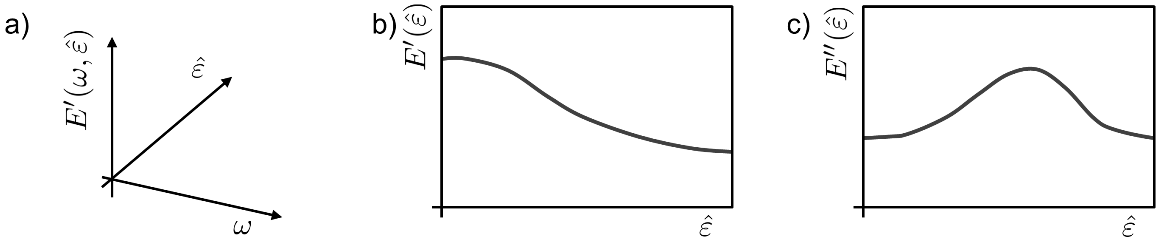

Figure 3.4: a) Exemplary storage and loss modulus dependency on frequency and strain amplitude. b)-c) Examplary storage and loss modulus over increasing strain amplitude (PAYNE effect) for a given frequency.

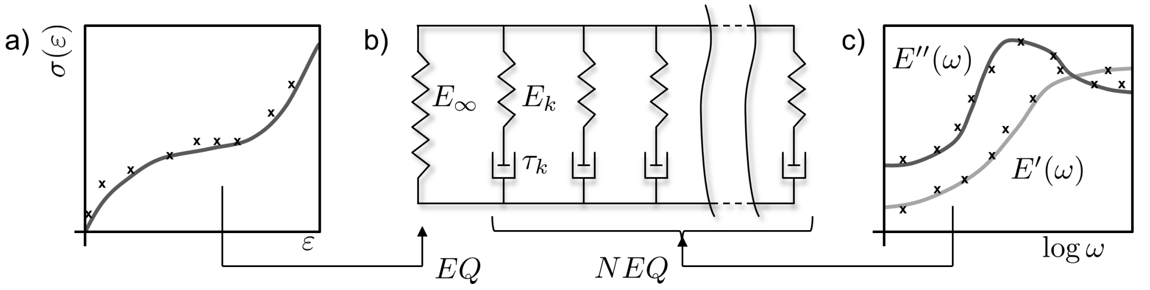

Figure 3.5: a) Fitted hyperelastic response (measurement represented by black crosses), b) rheological model with Maxwell elements, c) Fitted storage and loss modulus over frequency (measurement represented by black crosses).

with θ_{ref} being a reference temperature. The material-dependent constants c_1 and c_2 have to be determined by a fitting procedure, resulting in mastered curves for storage and loss modulus.

The so-called Payne effect is observed for filled elastomers, especially elastomers filled with carbon-black. Measurements show that the storage and the loss moduli depend, in addition to the frequency, on the prescribed strain-amplitude $\hat{\varepsilon}$, see Payne (1962a), Payne (1962b) and Fletcher & Gent (1954). This effect is illustrated exemplarily in 3.4 a), cf. Höfer & Lion (2009) for the shape of the functions. The Payne effect is very significant for low strain amplitudes in the range of $0.1\% - 20\%$ and varies for the volume share of filler material. Usually, a decreasing storage modulus and a bell-shaped curve for the loss modulus can be measured, see figure 3.4 b)-c). Additionally, for increasing filler content this effect increases as well. A common explanation for this phenomenon is the fracture of filler clusters under increasing strains. This theory is not valid for every type of filler and some effects cannot be explained with this theory, see Boehm (2001) for more details. This effect is excluded in this work by using also preconditioned test samples for the dynamical mechanical analysis (DMA). Another observed effect with respect to the applied loads during a dynamical test is the dependency on the preload. For experimental and numerical studies of this effect the reader is referred to Höfer & Lion (2009); Rendek & Lion (2010).

Physical effects like creep and relaxation in one-dimensional stress states of elastomers can be described by simple one-dimensional rheological models containing a combination of one spring and one damper element with the associated relaxation time τ. For the possibility to capture both effects, more complex models with an additional spring element are necessary.

In order to describe the viscoelastic material response, a common rheological model is used in this work. It provides the basis for an extended three-dimensional description considering finite strains in subsection 3.3.4. The rheological model consists of a spring for the equilibrium response (EQ) and parallel Maxwell elements containing a linear spring and a damper each for the non-equilibrium response (NEQ), see figure 3.5 b) and e.g. Reese & Govindjee (1998b) and Rust (2011). The parallel network of Maxwell elements is called Prony series defined by the Prony parameters E_k and τ_k. For the equilibrium part data of a quasi-static test is used and for the non-equilibrium response a dynamic measurement is used, see figure 3.5 a)/c) and above for descriptions of the measurements. The applied loads of the dynamic measurement equipment are limited leading to small deformations of the test sample in the range of $0.1\% - 2\%$ and therefore the spring response is characterized by a linear behaviour with the YOUNG's modulus E_k. The number of elements and values for the desciption of a certain elastomer are determined during a fitting process approaching the measured and mastered storage and loss modulus data, see figure 3.5 c). For the approximation of both moduli, the serial representation of the complex modulus is used

$$E^*(\omega) = \underbrace{E_\infty + \sum_{k=1}^{n} \frac{E_k \tau_k^2 \omega^2}{1 + \tau_k^2 \omega^2}}_{E'(\omega)} + i \underbrace{\sum_{k=1}^{n} \frac{E_k \tau_k \omega}{1 + \tau_k^2 \omega^2}}_{E''(\omega)} . \tag{3.34}$$

The long-term modulus E_∞ and instantaneous modulus E_0 are definied by

$$E_\infty = E^*(\omega \to 0, t \to \infty), \quad E_0 = E^*(\omega \to \infty, t \to 0) = E_\infty + \sum_{k=1}^{n} E_k. \tag{3.35}$$

The opposite notation based on the consideration of the frequency boundary values instead of a time dependent notation is also used in literature. The dimensionless modulus γ_k (also called e_i or g_i in literature) reads

$$\gamma_k = \frac{E_k}{E_0} = \frac{G_k}{G_0}. \tag{3.36}$$

It can also be expressed by the shear modulus G and is used later in subsection 3.3.4 for viscoelastic material models.

In order to describe the thermal behaviour of elastomers, thermal material parameters are determined in experiments. Parameters of interest and necessary for thermomechanical simulations are the specific heat capacity c, the thermal conductivity k and the thermal expansion coefficient α. The viscoelastic material response is influenced by the prevailing temperature inside the rubber material. This fact can be addressed by a shift of the reference relaxation time τ_{ref} with the introduced shift factor a (cf. equation (3.33))

$$\tau(\theta) = a(\theta)\, \tau_{ref}. \tag{3.37}$$

3.3.2 Thermodynamics with State Variables

All derived constitutive models have to fulfill certain principles, avoiding unphysical descriptions. Important principles are:

- Determinism: The thermodynamical behaviour of a material point is described by its past and present states. Future or stochastic processes are not relevant for an appropriate constitutive theory.

- Frame indifference: The derived constitutive relations do not depend on the observer position and are invariant to rigid body motions.
- Local action: The behaviour of a material point is only affected by near points.

Further principles can be found e.g. in HOLZAPFEL (2000); TRUESDELL ET AL. (2004). Thermomechanical processes can be described by a set of state variables $\left\{\boldsymbol{F}, \theta, \operatorname{grad}\theta, \boldsymbol{Q}_i^k\right\}$. In order to be able to describe dissipative processes, like plastic or viscoelastic effects, a set $(k = 1 - n)$ of additional inelastic (i) variables $\boldsymbol{Q}_i^k$ is used. Since this work concentrates on homogeneous continua, the position vector is not introduced as an internal variable. The HELMHOLTZ free energy density function is used for the derivation of a constitutive theory in this section. It is a function of the state variables

$$\psi = \psi(\boldsymbol{F}, \theta, \operatorname{grad}\theta, \boldsymbol{Q}_i^k). \tag{3.38}$$

The time derivative of this function together with the relation

$$\boldsymbol{\sigma} : \boldsymbol{d} = \left(\boldsymbol{\sigma} \cdot \boldsymbol{F}^{-T}\right) : \dot{\boldsymbol{F}} \tag{3.39}$$

are inserted into the local form of the CLAUSIUS-DUHEM inequality (see equation (3.30)), following COLEMAN & NOLL (1963)

$$\begin{aligned}\left(\boldsymbol{\sigma} \cdot \boldsymbol{F}^{-T} - \rho\frac{\partial\psi}{\partial\boldsymbol{F}}\right) : \dot{\boldsymbol{F}} - \rho\left(s + \frac{\partial\psi}{\partial\theta}\right)\dot{\theta} - \rho\frac{\partial\psi}{\partial\operatorname{grad}\theta}\frac{\mathrm{d}}{\mathrm{d}t}\left(\operatorname{grad}\theta\right)& \\ -\sum_{k=1}^{n}\left(\rho\frac{\partial\psi}{\partial\boldsymbol{Q}_i^k} : \dot{\boldsymbol{Q}}_i^k\right) - \frac{1}{\theta}\boldsymbol{q} \cdot \operatorname{grad}\theta \geq 0.&\end{aligned} \tag{3.40}$$

In order to fulfill the inequality, the following expression is assumed for the CAUCHY stress tensor $\boldsymbol{\sigma}$

$$\boldsymbol{\sigma} = \rho\frac{\partial\psi}{\partial\boldsymbol{F}} \cdot \boldsymbol{F}^T. \tag{3.41}$$

Consequently, the stress can be computed from the derivative of the HELMHOLTZ free energy density function. Furthermore, the CAUCHY stress tensor $\boldsymbol{\sigma}$ can also be derived based on the left CAUCHY-GREEN tensor

$$\boldsymbol{\sigma} = 2\rho\boldsymbol{b} \cdot J^{-1}\frac{\partial\psi}{\partial\boldsymbol{b}}. \tag{3.42}$$

In HOLZAPFEL (2000) detailed derivations are stated, including also the expressions for the second PIOLA-KIRCHHOFF stress tensor $\boldsymbol{S}$ in the initial configuration

$$\boldsymbol{S} = \rho_0\frac{\partial\psi}{\partial\boldsymbol{E}} = 2\rho_0\frac{\partial\psi}{\partial\boldsymbol{C}}. \tag{3.43}$$

Another important quantity for constitutive relations is the elasticity tensor, used in this work for the equilibrium part of a viscoelastic material model, see subsection 3.3.1.

Like stress tensors, it can be defined in the initial or in the current configuration by using the second derivative of the free energy density function

$$\mathbb{C} = \rho_0 \frac{\partial^2 \psi}{\partial \boldsymbol{E} \partial \boldsymbol{E}} = 4\rho_0 \frac{\partial^2 \psi}{\partial \boldsymbol{C} \partial \boldsymbol{C}}, \quad \mathbb{c} = 4\rho \boldsymbol{b} \frac{\partial^2 \Psi}{\partial \boldsymbol{b} \partial \boldsymbol{b}}. \tag{3.44}$$

In addition to stress and elasticity tensors, the following equation for the entropy s can be derived from equation (3.40)

$$s = -\frac{\partial \psi}{\partial \theta}. \tag{3.45}$$

Furthermore, the following equations have to hold for the temperature gradient dependency of the free energy density function and the temperature gradient

$$\frac{\partial \psi}{\partial \operatorname{grad} \theta} = \boldsymbol{0}, \quad -\frac{1}{\theta} \boldsymbol{q} \cdot \operatorname{grad} \theta \geq 0. \tag{3.46}$$

The second term states that heat flows from warmer to colder regions at constant deformation. The remaining term of equation (3.40) is named internal dissipation D_{int} and associated with n inelastic variables $\boldsymbol{Q}_i^k$

$$D_{int} = -\sum_{k=1}^{n} \left(\rho \frac{\partial \psi}{\partial \boldsymbol{Q}_i^k} : \dot{\boldsymbol{Q}}_i^k \right) \geq 0. \tag{3.47}$$

The heat flux $\boldsymbol{q}$ through a material at a certain temperature gradient differs for different materials and has to be specified. A constitutive relation based on the temperature gradient with the heat conductivity tensor $\boldsymbol{k}$ is introduced

$$\boldsymbol{q} = -\boldsymbol{k} \cdot \operatorname{grad}(\theta). \tag{3.48}$$

It reduces to a constant parameter k multiplied with the unity tensor for materials with isotropic heat conductance properties and will be used in this thesis.
For a detailed description of the thermal behaviour, the energy balance (3.25) has to be considered. Together with the time derivative of the LEGENDRE-transformation (3.29) it is rewritten as

$$\rho s \dot{\theta} + \rho \dot{s} \theta + \rho \dot{\psi} = \rho r + \boldsymbol{\sigma} : \boldsymbol{d} - \operatorname{div} \boldsymbol{q}. \tag{3.49}$$

Inserting the derived expressions for the derivates leads to

$$\begin{aligned} \rho s \dot{\theta} + \rho \theta \left(-\frac{\partial^2 \psi}{\partial \theta \partial \boldsymbol{F}} : \dot{\boldsymbol{F}} - \sum_{k=1}^{n} \frac{\partial^2 \psi}{\partial \theta \partial \boldsymbol{Q}_i^k} : \dot{\boldsymbol{Q}}_i^k - \frac{\partial^2 \psi}{\partial \theta \partial \theta} : \dot{\theta} \right) + \boldsymbol{\sigma} : \boldsymbol{d} - D_{int} - \rho s \dot{\theta} \\ = \rho r + \boldsymbol{\sigma} : \boldsymbol{d} - \operatorname{div} \boldsymbol{q}. \end{aligned} \tag{3.50}$$

Introducing the heat capacity $c = -\theta \frac{\partial^2 \psi}{\partial \theta^2}$ the equation transforms to

$$\rho c \dot{\theta} + \rho \theta \left(-\frac{\partial^2 \psi}{\partial \theta \partial \boldsymbol{F}} : \dot{\boldsymbol{F}} - \sum_{k=1}^{n} \frac{\partial^2 \psi}{\partial \theta \partial \boldsymbol{Q}_i^k} : \dot{\boldsymbol{Q}}_i^k \right) + \operatorname{div} \boldsymbol{q} - D_{int} - \rho r = 0. \tag{3.51}$$

The expression in brackets contains coupled derivatives describing structural thermo-elastic and thermo-inelastic heating or cooling, cf. HOLZAPFEL (2000). Since this effect is relevant for high deformation rates and is rather small in comparison to the other studied effects in this work, it is neglected in the following sections and chapters.

3.3.3 Isotropic Thermo-Hyperelastic Material Models

Hyperelastic material behaviour of rubber-like materials is described with certain strain energy functions Ψ. The specific strain energy function per unit volume can be identified as the HELMHOLTZ free energy density function from equation (3.38)

$$\Psi = \rho_0 \psi, \quad \Psi_{EQ} = \Psi_{EQ}\left(I_C, II_C, III_C, \theta\right) = \Psi_{EQ}\left(I_b, II_b, III_b, \theta\right). \tag{3.52}$$

For an isotropic material with the same response in all directions, the strain energy function depends on the temperature and the three invariants of the left or right CAUCHY-GREEN-tensor I_*, II_*, III_*. A description with the principal stretches λ_* is also possible and used for example for strain energies based on OGDEN's theory. The invariants are connected to the CAUCHY-GREEN tensors or the principal stretches, see equation (A.1), (A.2) and (A.3) in appendix A. The pure hyperelastic response under small deformation velocities is often called equilibrium (EQ) response and thus used as an index.

A specific representation of the MOONEY-RIVLIN strain energy function (cf. MOONEY (1940) and RIVLIN (1948)) is used for a FEAP element with the material parameters μ_1, μ_2 and λ (LAMÉ constants)

$$\begin{aligned}\Psi_{EQ}^{MR}(J, I_b, II_b) =& \frac{\mu_1}{2}\left(I_b - 3 - 2\ln J\right) - \frac{\mu_2}{2}\left(II_b - 3 - 4\ln J\right) \\ &+ \frac{\lambda}{4}\left(J^2 - 1 - 2\ln J\right).\end{aligned} \tag{3.53}$$

The corresponding CAUCHY stress tensors are derived by the use of equation (3.42) and the derivatives of the invariants of the CAUCHY-GREEN tensors (equation (A.4), (A.5) and (A.6))

$$\boldsymbol{\sigma}_{EQ}^{MR} = \frac{\mu_1}{J}\left(\boldsymbol{b} - \mathbf{1}\right) - \frac{\mu_2}{J}\left(I_b \boldsymbol{b} - \boldsymbol{b}^2 - 2 \cdot \mathbf{1}\right) + \frac{\lambda}{2J}\left(J^2 - 1\right)\mathbf{1}. \tag{3.54}$$

A strain energy function and the corresponding stress vectors for a NEO-HOOKEan material model are listed for completeness in equation (A.10), (A.11) and (A.12).

In the software ABAQUS (see SIMULIA (2014a,c)) a different formulation for modelling hyperelastic material behaviour is used and explained in the following. Since rubber materials show incompressibility, a multiplicative split of the deformation gradient in a volumetric and isochoric part with volume preserving properties is often applied, cf. FLORY (1961),

$$\boldsymbol{F} = J^{1/3}\bar{\boldsymbol{F}}, \quad \bar{\boldsymbol{C}} = \bar{\boldsymbol{F}}^T \cdot \bar{\boldsymbol{F}}, \tag{3.55}$$

defining the corresponding isochoric right CAUCHY-GREEN tensor. The equilibrium part of the specific strain energy function is consequently split in two parts. The volumetric part (VOL) describes volume changes and the isochoric part (ISO) depends on the invariants of the isochoric right CAUCHY-GREEN tensor:

$$\Psi_{EQ}(J, I_{\bar{C}}, II_{\bar{C}}, \theta) = \Psi_{EQ,VOL}(J, \theta) + \bar{\Psi}_{EQ,ISO}(I_{\bar{C}}, II_{\bar{C}}). \tag{3.56}$$

The invariants of the right CAUCHY-GREEN tensor are linked through the following relations:

$$I_{\bar{C}} = J^{-2/3} I_C, \quad II_{\bar{C}} = J^{-4/3} II_C, \quad III_{\bar{C}} = 1. \tag{3.57}$$

A specific strain energy function based on the works of MOONEY and RIVLIN together with a split in volumetric and isochoric parts reads

$$\Psi_{EQ}^{MR}(J, I_{\bar{C}}, II_{\bar{C}}, \theta) = C_{10}\left(I_{\bar{C}} - 3\right) - C_{01}\left(II_{\bar{C}} - 3\right) + \frac{1}{D_1}\left(\frac{J}{J_{th}} - 1\right)^2, \tag{3.58}$$

with the material constants C_{10}, C_{01} and D_1. In order to describe thermal expansion behaviour, the thermal JACOBIAN J_{th} is introduced with the thermal expansion coefficient α

$$J_{th} = \left(1 + \alpha\left(\theta - \theta_0\right)\right)^3. \tag{3.59}$$

Since thermal expansion is a effect of minor importance for the later proposed analysis of the thermomechanical friction process of rubber, it is neglected in this work. Therefore, the last part of the specific strain energy reduces to $\frac{1}{D_1}\left(J-1\right)^2$.
Fittings to the quasi-static stress-strain measurement are performed by an industry partner providing values for the material parameter E, ν and the non-linearity factor f of a BLATZ-KO model, BLATZ & KO (1962). The combination of (A.7), (A.8) and (A.9) leads to the expressions for the used MOONEY-RIVLIN parameters by use of the provided parameters

$$C_{10} = \frac{Ef}{4(1+\nu)}, \quad C_{01} = \frac{E(1-f)}{4(1+\nu)}, \quad D_1 = \frac{6(1-2\nu)}{E}. \tag{3.60}$$

Rubber materials are considered as incompressible materials that enforce the volume constraint $J = 1$. In order to account for this incompressibility constraint, a modified strain energy function is postulated, cf. HOLZAPFEL (2000),

$$\tilde{\Psi} = \Psi(\bar{\boldsymbol{C}}) - p(J-1), \tag{3.61}$$

introducing the LAGRANGE-multiplier p. The LAGRANGE-multiplier is identified as the hydrostatic pressure and has to be identified from equilibrium equations and boundary conditions in a further step. The modified strain energy function provides the basis for a Q1P0 finite element formulation needed for the later executed calculations.

3.3.4 Finite Linear Viscoelasticity

The description of the viscoelastic material behaviour is based on a rheological model (cf. section 3.3.1) for finite strains and is therefore called finite. The strain energy function is split accordingly into a history-independent equilibrium part (EQ) and a history-dependent, dissipative and non-equilibrium part (NEQ). The EQ part is defined by a hyperelastic spring, see figure 3.5. The NEQ part is modelled by n MAXWELL elements connected in parallel to the equilibrium spring. The equilibrium part and particular forms of the strain energy function are described in the previous section.

The specific strain energy functions of the non-equilibrium part are based on the inelastic variables $\boldsymbol{Q}_i^k$ in addition to the inner variables temperature θ and the isochoric right CAUCHY-GREEN tensor

$$\Psi(J, \bar{\boldsymbol{C}}, \theta, \boldsymbol{Q}_i) = \Psi_{EQ}(J, \bar{\boldsymbol{C}}, \theta) + \sum_{k=1}^{n} \Psi_{NEQ}^k(\bar{\boldsymbol{C}}, \theta, \boldsymbol{Q}_i^k). \tag{3.62}$$

The volumetric changes are associated to the hyperelastic equilibrium part and the non-equilibrium part depends only on deviatoric changes. The second PIOLA-KIRCHHOFF stress tensor with a split of the equilibrium part in volumetric and isochoric contributions is derived by using equation (3.43) and equation (3.56)

$$\boldsymbol{S}(J, \bar{\boldsymbol{C}}, \theta, \boldsymbol{Q}_i) = \boldsymbol{S}_{EQ,VOL}(J, \theta) + \boldsymbol{S}_{EQ,ISO}(\bar{\boldsymbol{C}}) + \sum_{k=1}^{n} \boldsymbol{S}_{NEQ,ISO}^k(\bar{\boldsymbol{C}}, \theta, \boldsymbol{Q}_i^k). \tag{3.63}$$

A formulation without a split in volumetric and isochoric parts in the current configuration reads

$$\boldsymbol{\sigma}(\boldsymbol{b}, \theta, \boldsymbol{Q}_i^k) = \boldsymbol{\sigma}_{EQ}(\boldsymbol{b}, \theta) + \sum_{k=1}^{n} \boldsymbol{\sigma}_{NEQ}^k(\boldsymbol{b}, \theta, \boldsymbol{Q}_i^k). \tag{3.64}$$

Furthermore, all temperature dependencies of the strain energy function are neglected since no thermal expansion, no coupling effects and no changes of the non-equilibrium part due to temperature are considered in this work, see chapter 8 for further explanations. The viscoelastic formulation is completed by an evolution equation for the history-dependent inelastic internal variables $\boldsymbol{Q}_i^k$. The first order differential equation is given by

$$\dot{\boldsymbol{Q}}_i^k = \mathcal{F}(\bar{\boldsymbol{C}}, \boldsymbol{Q}_i^k). \tag{3.65}$$

Time-dependency (t) will be highlighted at certain equations which are important for the later used algorithmic treatment in chapter 5 and omitted elsewhere for clarity. Since the evolution equation is defined by a linear dependency of the variables $\bar{\boldsymbol{C}}, \boldsymbol{Q}_i^k$ and the theory is able to capture large deformations, the whole formulation is called finite linear viscoelasticity. It is restricted to small deformation rates and small deviations from the thermomechanical equilibrium, see REESE & GOVINDJEE (1998b), Reese (2001) or Lion (1997) for further details. There exist two common approaches for the choice of the inelastic inner variables and the corresponding evolution equation, a deformation- and stress-based approach.

The deformation-based approach is used in the software FEAP and described henceforth. A multiplicative split of the deformation gradient in elastic (e) and inelastic (i) parts is introduced

$$\boldsymbol{F} = \boldsymbol{F}_e^k \cdot \boldsymbol{F}_i^k. \tag{3.66}$$

Furthermore, the inelastic inner variable equals the inelastic right Cauchy-Green tensor which can be expressed by the inelastic deformation gradient $\boldsymbol{F}_i^k$

$$\boldsymbol{Q}_i^k = \boldsymbol{C}_i^k = \left(\boldsymbol{F}_i^k\right)^T \cdot \boldsymbol{F}_i^k. \tag{3.67}$$

Analogously, the elastic left Cauchy-Green tensor is calculated with the help of the inelastic right Cauchy-Green tensor C_i^k

$$\boldsymbol{b}_e^k = \boldsymbol{F}_e^k \cdot \left(\boldsymbol{F}^k\right)_e^T = \boldsymbol{F} \cdot \left(\boldsymbol{C}_i^k\right)^{-1} \cdot \boldsymbol{F}^T. \tag{3.68}$$

Following Reese & Govindjee (1998b), the linear evolution equation with respect to the time-dependent tensors $\boldsymbol{C}(t), \boldsymbol{C}_i^k(t)$, for finite linear viscoelasticy, is introduced as

$$\dot{\boldsymbol{C}}_i^k(t) = \frac{1}{\tau_k}\left(\boldsymbol{C}(t) - \boldsymbol{C}_i^k(t)\right). \tag{3.69}$$

With the evolution equation, the inelastic right Cauchy-Green tensor $\boldsymbol{C}_i^k(t_{n+1})$ for Maxwell element k with the relaxation time τ_k at the new time step t_{n+1} is calculated using the trapezoid rule

$$\boldsymbol{C}_i^k(t_{n+1}) = \frac{\Delta t}{2\tau_k + \Delta t}\left(\boldsymbol{C}(t_n) + \boldsymbol{C}(t_{n+1}) - \boldsymbol{C}_i^k(t_n)\right) + \frac{2\tau_k}{2\tau_k + \Delta t}\boldsymbol{C}_i^k(t_n). \tag{3.70}$$

In a next step, the inelastic right Cauchy-Green tensor can be transferred to the elastic left Cauchy-Green tensor by using equation (3.68). Consequently, it is possible to derive the Cauchy stress tensor for every Maxwell element by use of equation (3.42) from a Mooney-Rivlin strain energy function with the material parameters μ_1^k, μ_2^k and λ^k

$$\boldsymbol{\sigma}_{NEQ}^{MR,k} = \frac{\mu_1^k}{J}\left(\boldsymbol{b}_e^k - \boldsymbol{1}\right) - \frac{\mu_2^k}{J}\left(I_{b_e}^k \cdot \boldsymbol{b}_e^k - \boldsymbol{b}_e^k \cdot \boldsymbol{b}_e^k - 2 \cdot \boldsymbol{1}\right) + \frac{\lambda^k}{2J}\left(\left(J_e^k\right)^2 - 1\right)\boldsymbol{1}. \tag{3.71}$$

The reader is referred to Reese & Govindjee (1998a); Reese (2001) for further details regarding the exact derivation of stress and elasticity tensors for the Maxwell elements.

The stress-based approach of finite linear viscoelasticity is applied in the software ABAQUS and explained below, see also SIMULIA (2014a). As a basis for the approach, a strain energy function is introduced (cf. Simo (1987))

$$\Psi(J,\bar{\boldsymbol{C}},\boldsymbol{Q}_i^k) = \underbrace{\Psi_{EQ,VOL}(J) + \Psi_{EQ,ISO}(\bar{\boldsymbol{C}})}_{\Psi_{EQ}} \underbrace{- \sum_{k=1}^{n} \frac{1}{2}\bar{\boldsymbol{C}} : \boldsymbol{Q}_i^k + \sum_{k=1}^{n} \Psi_k(\boldsymbol{Q}_i^k)}_{\Psi_{NEQ}}, \tag{3.72}$$

defining an equilibrium part (already described in the previous subsection) and a non-equilibrium part that contains the time-dependent inner variable $\boldsymbol{Q}_i^k$. The evolution equation is given by a linear function, see also Holzapfel & Simo (1996b,a) and Simo & Hughes (1998), with the relaxation time τ_k and dimensionless modulus γ_k (cf. equation (3.36)) for each Maxwell element k

$$\dot{\boldsymbol{Q}}_i^k(t) + \frac{1}{\tau_k}\boldsymbol{Q}_i^k(t) = \frac{\gamma_k}{\tau_k}\mathrm{DEV}\left\{2\frac{\partial\Psi_{EQ,ISO}(\bar{\boldsymbol{C}}(t))}{\partial\bar{\boldsymbol{C}}(t)}\right\}, \quad \lim_{t\to\infty}\boldsymbol{Q}_i^k(t) = 0. \tag{3.73}$$

The operator DEV, also called deviator in literature, is defined as follows

$$\mathrm{DEV}[\bullet] = (\bullet) - \frac{1}{3}[(\bullet) : \boldsymbol{C}]\boldsymbol{C}^{-1}. \tag{3.74}$$

The inner variable approaches a value of zero for an infinite time interval leading to a stress response that is just defined by the equilibrium part. In order to solve the evolution equation within a finite element framework, an algorithmic internal variable $\boldsymbol{H}^k(t)$ is introduced by the use of a convolution integral (see Simo & Hughes (1998) for further details)

$$\boldsymbol{H}^k(t) = \int_{-\infty}^{t} \mathrm{e}^{-\frac{t-s}{\tau_k}} \frac{\mathrm{d}}{\mathrm{d}s}\mathrm{DEV}\left\{2\frac{\partial\Psi_{EQ,ISO}(\bar{\boldsymbol{C}}(s))}{\partial\bar{\boldsymbol{C}}(s)}\right\}\,\mathrm{d}s. \tag{3.75}$$

The time dependent integral can be approached by the use of the midpoint rule in the time interval $[t_n, t_{n+1}]$ leading to an updated algorithmic internal variable

$$\begin{aligned} \boldsymbol{H}^k(t_{n+1}) &= \mathrm{e}^{-\frac{\Delta t}{\tau_k}}\boldsymbol{H}^k(t_n) \\ &+ \mathrm{e}^{-\frac{\Delta t}{2\tau_k}}\left(\mathrm{DEV}\left\{2\frac{\partial\Psi_{EQ,ISO}(\bar{\boldsymbol{C}}(t_{n+1}))}{\partial\bar{\boldsymbol{C}}(t_{n+1})}\right\} - \mathrm{DEV}\left\{2\frac{\partial\Psi_{EQ,ISO}(\bar{\boldsymbol{C}}(t_n))}{\partial\bar{\boldsymbol{C}}(t_n)}\right\}\right). \end{aligned} \tag{3.76}$$

The updated variable is used to determine the whole second Piola-Kirchhoff stress tensor $\boldsymbol{S}(t_{n+1})$ of the current time step

$$\boldsymbol{S}(t_{n+1}) = \boldsymbol{S}_{EQ,VOL}(t_{n+1}) + \gamma_\infty\boldsymbol{S}_{EQ,ISO}(t_{n+1}) + J^{-2/3}\sum_{k=1}^{n}\gamma_k\mathrm{DEV}\left\{\boldsymbol{H}^k(t_{n+1})\right\}, \tag{3.77}$$

with the expressions for the volumetric and isochoric stresses

$$\boldsymbol{S}_{EQ,VOL} = J\frac{\partial\Psi_{EQ,VOL}(J)}{\partial J}\cdot\boldsymbol{C}^{-1}, \quad \boldsymbol{S}_{EQ,ISO} = J^{-2/3}\mathrm{DEV}\left\{2\frac{\partial\Psi_{EQ,ISO}(\bar{\boldsymbol{C}})}{\partial\bar{\boldsymbol{C}}}\right\}. \tag{3.78}$$

This model can be directly linked to PRONY parameters, see subsection 3.3.1. Further details regarding the derivation of the elasticity tensor for the non-equilibrium part can be found in SIMO (1987); SIMO & HUGHES (1998).

3.4 Weak Forms of Equilibrium

In order to solve the partial differential equations from section 3.2, weak forms are derived for the later introduced finite element method in chapter 5. Mechanical and thermal parts are introduced subsequently to calculate the primary variables displacement $\boldsymbol{u}$ and temperature θ.
The balance of linear momentum was derived in section 3.2 and is given for the quasi-static case with applied (marked by the superscript) body forces $\hat{\boldsymbol{b}}$

$$\operatorname{div}\boldsymbol{\sigma} + \rho\hat{\boldsymbol{b}} = 0. \tag{3.79}$$

In order to specify the problem, boundary conditions are introduced for the mechanical problem. DIRICHLET boundary conditions prescribe the displacement $\hat{\boldsymbol{u}}$ on $\partial_u\mathcal{B}_t$ and NEUMANN boundary conditions are used to apply tractions $\hat{\boldsymbol{t}}$ on $\partial_t\mathcal{B}_t$

$$\boldsymbol{u} - \hat{\boldsymbol{u}} = 0 \;\text{ on } \partial_u\mathcal{B}_t, \quad \boldsymbol{t} - \hat{\boldsymbol{t}} = 0 \;\text{ on } \partial_t\mathcal{B}_t, \quad \boldsymbol{u}(t=0) = \boldsymbol{u}_0 \;\text{ in } \mathcal{B}_t. \tag{3.80}$$

The so-called initial boundary value problem (IBVP) is accomplished by the definition of initial conditions, for example an initial displacement $\boldsymbol{u}(t=0)$.
A weak form of a differential equation G is derived by multiplying the differential equation with a test function and integration over the domain. The superscript b indicates that all equations are applied to a solid body, whereas c indicates contact contributions, cf. section 4. The test function can also be seen as a virtual displacement or a weighting function and equals zero at the DIRICHLET boundary. The balance of linear momentum and the NEUMANN boundary condition are multiplied with the test function $\delta\boldsymbol{u}$:

$$\int_{\mathcal{B}_t} \left(\operatorname{div}\boldsymbol{\sigma} + \rho\hat{\boldsymbol{b}}\right) \cdot \delta\boldsymbol{u}\,\mathrm{d}v = \int_{\partial_t\mathcal{B}_t} \left(\boldsymbol{t} - \hat{\boldsymbol{t}}\right) \cdot \delta\boldsymbol{u}\,\mathrm{d}a. \tag{3.81}$$

With the use of the divergence theorem

$$\operatorname{div}\left(\boldsymbol{\sigma}\cdot\delta\boldsymbol{u}\right) = \operatorname{div}\boldsymbol{\sigma}\cdot\delta\boldsymbol{u} + \boldsymbol{\sigma} : \operatorname{grad}\delta\boldsymbol{u}, \tag{3.82}$$

the equation is transferred to

$$G_u^b(\boldsymbol{u},\delta\boldsymbol{u}) = \int_{\mathcal{B}_t} \left(\operatorname{div}\left(\boldsymbol{\sigma}\cdot\delta\boldsymbol{u}\right) - \boldsymbol{\sigma} : \operatorname{grad}\delta\boldsymbol{u} + \rho\hat{\boldsymbol{b}}\cdot\delta\boldsymbol{u}\right)\,\mathrm{d}v - \int_{\partial_t\mathcal{B}_t} \left(\boldsymbol{t} - \hat{\boldsymbol{t}}\right) \cdot \delta\boldsymbol{u}\,\mathrm{d}a = 0. \tag{3.83}$$

Further simplification is achieved by using the GAUSS theorem, leading to

$$G_u^b(\boldsymbol{u}, \delta\boldsymbol{u}) = \int_{\mathcal{B}_t} \boldsymbol{\sigma} : \operatorname{grad}^s \delta\boldsymbol{u}\,\mathrm{d}v - \int_{\mathcal{B}_t} \rho\hat{\boldsymbol{b}} \cdot \delta\boldsymbol{u}\,\mathrm{d}v - \int_{\partial_t\mathcal{B}_t} \hat{\boldsymbol{t}} \cdot \delta\boldsymbol{u}\,\mathrm{d}a = 0. \tag{3.84}$$

The complete weak form derived in the initial configuration with the variation of the Green-Lagrange tensor $\delta\boldsymbol{E}$ reads

$$G_u^b(\boldsymbol{u}, \delta\boldsymbol{u}) = \int_{\mathcal{B}_0} \boldsymbol{S} : \delta\boldsymbol{E}\,\mathrm{d}V - \int_{\mathcal{B}_0} \rho\hat{\boldsymbol{b}}_0 \cdot \delta\boldsymbol{u}\,\mathrm{d}V - \int_{\partial_t\mathcal{B}_0} \hat{\boldsymbol{t}}_0 \cdot \delta\boldsymbol{u}\,\mathrm{d}A = 0. \tag{3.85}$$

In order to calculate the temperature θ of a body the reformulated first law of thermodynamics without heat sources r is used (cf. equation (3.51))

$$\rho c\dot{\theta} + \operatorname{div}\boldsymbol{q} - D_{int} = 0. \tag{3.86}$$

In analogy to the mechanical boundary conditions, the IBVP is set up with Dirichlet boundary conditions for the temperature θ, Neumann boundary conditions for the normal component of the heat flux $\boldsymbol{q}$ and initial temperature values θ_0

$$\theta - \hat{\theta} = 0 \;\text{ on } \partial_\theta\mathcal{B}_t, \quad \boldsymbol{q}\cdot\boldsymbol{n} - \hat{\boldsymbol{q}}\cdot\hat{\boldsymbol{n}} = 0 \;\text{ on } \partial_q\mathcal{B}_t, \quad \theta(t=0) = \theta_0 \;\text{ in } \mathcal{B}_t. \tag{3.87}$$

The weak form of equilibrium is derived by multiplication of equation (3.86) and the heat flux condition (3.87) with the thermal test function $\delta\theta$.

$$\int_{\mathcal{B}_t} \left(\rho c\dot{\theta} + \operatorname{div}\boldsymbol{q} - D_{int}\right) \cdot \delta\theta\,\mathrm{d}v = \int_{\partial_q\mathcal{B}_t} (\boldsymbol{q}\cdot\boldsymbol{n} - \hat{\boldsymbol{q}}\cdot\hat{\boldsymbol{n}}) \cdot \delta\theta\,\mathrm{d}a. \tag{3.88}$$

Similar to the transformations for the mechanical part, the divergence and Gaussian theorems are applied. Additionally, the constitutive relation for the heat flux (equation (3.48)) is inserted, leading to

$$G_\theta^b(\theta, \delta\theta) = \int_{\mathcal{B}_t} \left(\rho c\dot{\theta}\delta\theta + k\operatorname{grad}^T\theta\operatorname{grad}\delta\theta - D_{int}\delta\theta\right)\,\mathrm{d}v + \int_{\partial_q\mathcal{B}_t} \hat{\boldsymbol{q}}\cdot\hat{\boldsymbol{n}}\delta\theta\,\mathrm{d}a = 0. \tag{3.89}$$

Chapter 4

Contact Mechanics

In order to model large sliding distances of a rubber block on a rough surface, a close look on contact mechanics is essential. The kinematical relations in normal and tangential directions of the contact interface are described and used for the formulation of the contact interface constraints. Afterwards, the most common solution methods for mechanical contact problems are presented, introducing the weak forms. In the last section, the contribution of a thermal interface to the weak form is derived since thermomechanical coupling will be considered in chapter 8. Fundamental introductions to contact mechanics can be found in Laursen (2003); Willner (2012); Wriggers (2006). The derived weak forms provide the basis for the discretization of the contact problem with finite elements in chapter 5.

4.1 Contact Kinematics

In figure 4.1 two separated bodies are displayed that might get a common contact surface $\partial_c \mathcal{B}_t$. Following the literature, the upper body is the so-called slave and the lower body is called master. The slave body and all slave quantities are superscripted with 1 and all master quantities with 2. The position vector $\boldsymbol{x}^i$ for each possible contact point on each surface is introduced and a parametrization is provided by the convective coordinates ξ_1 and ξ_2 without the use of the superscript for slave and master, see also figure 4.1. The tangential and normal vectors $\boldsymbol{a}^i_\alpha$ and $\boldsymbol{n}^i$ can be calculated for each surface-point of the two bodies i in this way:

$$\boldsymbol{a}^i_\alpha = \frac{\partial \boldsymbol{x}^i}{\partial \xi_\alpha} = \boldsymbol{x}^i_{,\alpha}, \quad \boldsymbol{n}^i = \frac{\boldsymbol{a}^i_1 \times \boldsymbol{a}^i_2}{\|\boldsymbol{a}^i_1 \times \boldsymbol{a}^i_2\|}, \tag{4.1}$$

with $\alpha = 1, 2$ for the considered tangential direction within a three-dimensional setup. For the description of the normal contact, the normal gap $\bar{g}_N$ between slave and master is calculated as follows

$$\bar{g}_N = \left(\boldsymbol{x}^2 - \bar{\boldsymbol{x}}^1\right) \cdot \bar{\boldsymbol{n}}^1 \geq 0. \tag{4.2}$$

The bar indicates the projection of a chosen slave point onto the master surface, obtaining the minimal distance between point P and Q, see figure 4.1 a). The projection

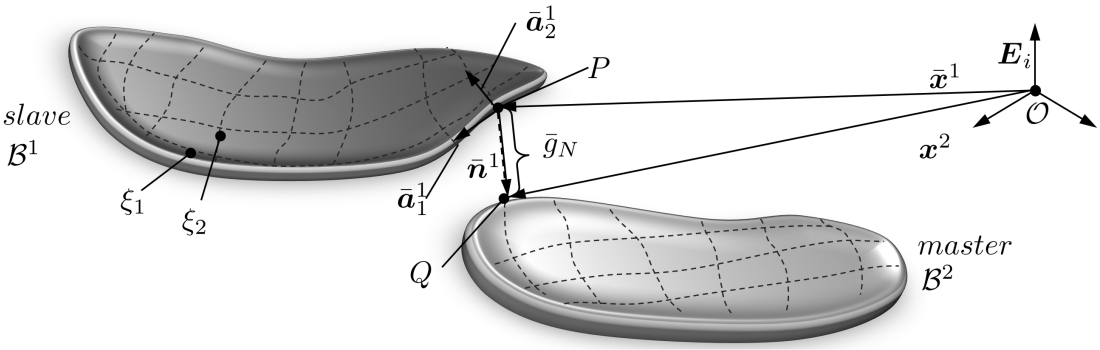

Figure 4.1: Contact quantities of two bodies coming into contact at point P and Q.

point is determined with the help of the parametrized distance function d

$$d\left(\xi_1, \xi_2\right) = \left\| \boldsymbol{x}^2 - \boldsymbol{x}^1\left(\xi_1, \xi_2\right) \right\| . \tag{4.3}$$

Since we are interested in the minimum of the distance function $d\left(\xi_1, \xi_2\right)$, its derivative must be equal to zero

$$\frac{\partial d\left(\xi_1, \xi_2\right)}{\partial \xi_\alpha} = \frac{\boldsymbol{x}^2 - \boldsymbol{x}^1\left(\xi_1, \xi_2\right)}{\left\|\boldsymbol{x}^2 - \boldsymbol{x}^1\left(\xi_1, \xi_2\right)\right\|} \cdot \boldsymbol{x}^1_{,\alpha}\left(\xi_1, \xi_2\right) = 0. \tag{4.4}$$

With the projected coordinates $\bar{\xi}_1$ and $\bar{\xi}_2$ on the master surface, the normal vector of the projection point $\bar{\boldsymbol{n}}^1$ is calculated with equation (4.1). During a contact situation, a relative movement between the bodies may occur with the result that the master point $\boldsymbol{x}^2$ moves relatively to the projected slave point $\bar{\boldsymbol{x}}^1$. The path of the master point is unknown *a priori* and therefore calculated with quantities defined on the slave surface at the projection point. Following Wriggers (2006), the total sliding distance $\bar{g}_T$ is determined by the integral of the incremental path of the slave point along the master surface, starting with the time t_0 until t:

$$\bar{g}_T = \int_{t_0}^{t} \|\dot{\boldsymbol{g}}_T\| \, \mathrm{d}t = \int_{t_0}^{t} \left\| \bar{\boldsymbol{a}}^1_\alpha \dot{\bar{\xi}}_\alpha \right\| \, \mathrm{d}t. \tag{4.5}$$

4.2 Contact Interface Constraints

Considering normal contact between two bodies, two possible states may occur. A closed gap results in the gap function ($g_N = 0$) and a negative pressure value ($p_N < 0$), whereas an open gap ($g_N > 0$) is accompanied by ($p_N = 0$). Combining both conditions leads to the well-known Hertz-Signorini-Moreau conditions

$$g_N \geq 0, \quad p_N \leq 0, \quad g_N p_N = 0. \tag{4.6}$$

Adding a constraint equation for the tangential part, the conditions are often summarized as Kuhn-Tucker-Karush conditions. Two states are distinguished for the tangential direction, stick and slip. The tangential velocity $\dot{\boldsymbol{g}}_T$ has to be equal to zero for the stick case, because no relative movement between the bodies occurs. A slip criterion f_s is used, being smaller than zero for the stick case ($f_s < 0$) and zero for slipping bodies ($f_s = 0$). For example the Coloumb-friction-law with the constant coefficient of friction μ, the tangential contact stress vector $\boldsymbol{t}_T$, and normal pressure p_N is widely used

$$f_s = \|\boldsymbol{t}_T\| - \mu\,|p_N| \leq 0. \tag{4.7}$$

Additionally, the so-called slip rate $\dot{\gamma}$ is introduced, being zero ($\dot{\gamma} = 0$) for the stick case and greater than zero for sliding bodies ($\dot{\gamma} > 0$). In the case of tangential movement, an evolution equation is used to calculate the tangential gap

$$\dot{\boldsymbol{g}}_T = \dot{\gamma}\frac{\boldsymbol{t}_T}{\|\boldsymbol{t}_T\|}. \tag{4.8}$$

It is derived from considering the dissipation introduced during sliding, see Wriggers (2006). Furthermore, it states the same direction for the tangential gap and the tangential contact stress vector. Similar to the constraints in normal direction, the combination of the conditions for the slip criterion and the slip rate are summarized as the tangential interface constraints

$$\dot{\gamma} \geq 0, \quad f_s \leq 0, \quad \dot{\gamma} f_s = 0. \tag{4.9}$$

4.3 Enforcement of Contact Constraints and Weak Forms

There exist different numerical methods for obtaining a solution of pure mechanical contact problems. For a detailed description of various methods see Wriggers (2006). In this work, weak forms for the contact contributions are introduced, adding the derived weak forms in a final step to the continuum-mechanical contributions for a mechanical contact problem.

Generally, the weak form for contact problems G^c can be formulated as a sum of the virtual contact work part G^c_u and a part for the enforcement of the contact constraints G^c_l

$$G^c = G^c_u + G^c_l. \tag{4.10}$$

Two methods are introduced in this work, the Lagrange-multiplier method and the penalty method. Within the Lagrange-multiplier method the contact constraints are enforced exactly by adding the additional unknowns λ_N in normal and $\boldsymbol{\lambda}_T$ in tangential direction. The penalty method introduces no further unknowns and provides just an approximated solution of the mechanical contact problem at hand. Nevertheless, it reduces the computational effort and will be used therefore throughout this work. The Lagrange-multiplier method is explained in a first step, since it provides the basis for the introduced mortar contact element in chapter 5. Afterwards, the main features of the penalty method are given.

Following WRIGGERS (2006), the potential energy function for the derivation of the weak contact form can be written as

$$\Pi_c^{LM} = \int\limits_{\partial_c \mathcal{B}_t} \left(g_N \lambda_N + \boldsymbol{g}_T \cdot \boldsymbol{\lambda}_T \right) \, \mathrm{d}a. \tag{4.11}$$

The variation of Π_c^{LM} leads to the virtual contact work part G_u^c for the LAGRANGE-multiplier method

$$G_u^c = \int\limits_{\partial_c \mathcal{B}_t} \left(\delta g_N \lambda_N + \delta \boldsymbol{g}_T \cdot \boldsymbol{\lambda}_T \right) \, \mathrm{d}a. \tag{4.12}$$

The weak forms for the enforcement of contact constraints differ for the cases of stick, slip and no contact. For the stick case, no penetration, no tangential movement and no incremental slip is assumed, leading to

$$G_l^c = \int\limits_{\partial_c \mathcal{B}_t} \left(\delta \lambda_N g_N + \delta \boldsymbol{\lambda}_T \cdot \Delta_t \boldsymbol{g}_T + \delta \gamma \frac{1}{c_C} \Delta_t \gamma \right) \, \mathrm{d}a = 0. \tag{4.13}$$

For detailed derivations of the terms to enforce the contact constraints the reader is referred to WEISSENFELS (2013). During slipping, the constitutive equation (see last section 4.2 is used and thus the tangential LAGRANGE-multiplier is identified as the tangential stress $\boldsymbol{t}_T$, cf. WRIGGERS (2006).

For the penalty method the weak form consists only of the part with regard to the virtual contact work. Since no additional unknowns are introduced, it reads

$$G_u^c = \int\limits_{\partial_c \mathcal{B}_t} \left(\delta g_N p_N + \delta \boldsymbol{g}_T \cdot \boldsymbol{t}_T \right) \, \mathrm{d}a. \tag{4.14}$$

The complete tangential gap splits in an elastic (e) and an irreversible slip part (s) for the penalty method

$$\boldsymbol{g}_T = \boldsymbol{g}_T^e + \boldsymbol{g}_T^s. \tag{4.15}$$

The normal pressure p_N is approximated by the product of a penalty factor c_N and the normal gap g_N. The same approximation is introduced for the tangential stress vector using the tangential penalty factor c_T and the elastic part of the tangential gap $\boldsymbol{g}_T^e$

$$p_N = c_N g_N, \quad \boldsymbol{t}_T = c_T \boldsymbol{g}_T^e. \tag{4.16}$$

The penalty parameters c_N and c_T have to be chosen carefully since a compromise between solution quality and stability has to be achieved. The solution quality increases with a penalty factor approaching the stiffness of the stiffer body in contact, loosing numerical stability since the equation system is becoming more ill-conditioned.

Similar to trial elastic steps in plasticity and the use of radial-return-mapping algorithms, a trial tangential stress vector $\boldsymbol{t}_T^{tr,n+1}$ is introduced. It is evaluated under the presumption of sticking and a pure elastic movement, completed by the corresponding trial slip criterion $f^{s,tr}$

$$\boldsymbol{t}_T^{tr,n+1} = c_T \left(\boldsymbol{g}_T^{n+1} - \boldsymbol{g}_T^{s,n}\right), \quad f^{s,tr} = \left\|\boldsymbol{t}_T^{tr,n+1}\right\| - \mu c_N \left|g_N\right|. \tag{4.17}$$

After the evaluation of the trial slip criterion, the node either sticks ($f^{s,tr} \leq 0$) without a change in the tangential gap, leading to an unchanged tangential stress ($\boldsymbol{t}_T = \boldsymbol{t}_T^{tr}$). For the slip case ($f^{s,tr} > 0$) the tangential gap and the tangential stress vector have to be updated using a radial-return-mapping algorithm:

$$\boldsymbol{g}_T^{s\,n+1} = \boldsymbol{g}_T^{s\,n} + \frac{f^{s,tr}}{c_T} \frac{\boldsymbol{t}_T^{tr}}{\|\boldsymbol{t}_T^{tr}\|}, \quad \boldsymbol{t}_T^{n+1} = -\mu c_N \left|g_N\right| \frac{\boldsymbol{t}_T^{tr}}{\|\boldsymbol{t}_T^{tr}\|}. \tag{4.18}$$

4.4 Thermal Contact Interface

The first law of thermodynamics (compare equation (3.24)) is reduced to an interface in a first step excluding all volume terms. Thus, all relevant interface terms are used, adding a surface source term r_a:

$$\int\limits_{\partial_c \mathcal{B}_t} \boldsymbol{t} \cdot \boldsymbol{v} \,\mathrm{da} - \int\limits_{\partial_c \mathcal{B}_t} \boldsymbol{q} \cdot \boldsymbol{n} \,\mathrm{da} + \int\limits_{\partial_c \mathcal{B}_t} r_a \,\mathrm{da} = 0. \tag{4.19}$$

The work of external forces $\tilde{\boldsymbol{t}}$ and the heat flux $\tilde{\boldsymbol{q}}$ on the contact interface are given as

$$\boldsymbol{t} \cdot \boldsymbol{v} - \tilde{\boldsymbol{t}} \cdot \tilde{\boldsymbol{v}} = 0 \text{ on } \partial_c \mathcal{B}_t, \quad \boldsymbol{q} \cdot \boldsymbol{n} - \tilde{\boldsymbol{q}} \cdot \tilde{\boldsymbol{n}} = 0 \text{ on } \partial_c \mathcal{B}_t. \tag{4.20}$$

Assuming traction- and heat flux-free behaviour in normal direction on the rest of the boundary, the contact quantities are directly inserted in equation (4.19). The source term r_a is neglected further on, since no external contact heat sources are applied in this work. Multiplying the whole equation (4.19) with a test function $\delta\theta$ leads to

$$\int\limits_{\partial_c \mathcal{B}_t} \tilde{\boldsymbol{t}} \cdot \tilde{\boldsymbol{v}} \delta\theta \,\mathrm{da} - \int\limits_{\partial_c \mathcal{B}_t} \tilde{\boldsymbol{q}} \cdot \tilde{\boldsymbol{n}} \delta\theta \,\mathrm{da} = 0. \tag{4.21}$$

Each interface integral is divided into a contribution of surface 1 and surface 2 of the two contact bodies

$$\int\limits_{\partial_c \mathcal{B}_t^1} \tilde{\boldsymbol{t}}_1 \cdot \tilde{\boldsymbol{v}}_1 \delta\theta_1 \,\mathrm{da} + \int\limits_{\partial_c \mathcal{B}_t^2} \tilde{\boldsymbol{t}}_2 \cdot \tilde{\boldsymbol{v}}_2 \delta\theta_2 \,\mathrm{da} - \int\limits_{\partial_c \mathcal{B}_t^1} \tilde{\boldsymbol{q}}_1 \cdot \tilde{\boldsymbol{n}}_1 \delta\theta_1 \,\mathrm{da} - \int\limits_{\partial_c \mathcal{B}_t^2} \tilde{\boldsymbol{q}}_2 \cdot \tilde{\boldsymbol{n}}_2 \delta\theta_2 \,\mathrm{da} = 0. \tag{4.22}$$

With $\tilde{\boldsymbol{n}}_2 = -\tilde{\boldsymbol{n}}_1 = \tilde{\boldsymbol{n}}_c$ and $\tilde{\boldsymbol{t}}_2 = -\tilde{\boldsymbol{t}}_1 = \tilde{\boldsymbol{t}}_c$ the equation is rewritten as

$$\int\limits_{\partial_c \mathcal{B}_t} \tilde{\boldsymbol{t}}_c \cdot \left[\tilde{\boldsymbol{v}}_2 \delta\theta_2 - \tilde{\boldsymbol{v}}_1 \delta\theta_1\right] \,\mathrm{da} - \int\limits_{\partial_c \mathcal{B}_t} \left[\tilde{\boldsymbol{q}}_2 \delta\theta_2 - \tilde{\boldsymbol{q}}_1 \delta\theta_1\right] \cdot \tilde{\boldsymbol{n}}_c \,\mathrm{da} = 0. \tag{4.23}$$

The distribution factor κ is introduced enabling arbitrary shares of the dissipative quantity $(\tilde{\boldsymbol{t}}_c \cdot \tilde{\boldsymbol{v}}_c)$ for both surfaces. The quantities $\tilde{\boldsymbol{v}}_2 = \tilde{\boldsymbol{v}}_1 = \tilde{\boldsymbol{v}}_c$ and $\tilde{\boldsymbol{q}}_2 = \tilde{\boldsymbol{q}}_1 = \tilde{\boldsymbol{q}}_c$ are introduced additionally simplifying equation (4.23)

$$\int\limits_{\partial_c \mathcal{B}_t} \tilde{\boldsymbol{t}}_c \cdot \tilde{\boldsymbol{v}}_c \underbrace{(\kappa \delta\theta_1 + (1-\kappa)\delta\theta_2)}_{\delta\theta_D} \, \mathrm{d}a - \int\limits_{\partial_c \mathcal{B}_t} \tilde{\boldsymbol{q}}_c \cdot \tilde{\boldsymbol{n}}_c \underbrace{(\delta\theta_2 - \delta\theta_1)}_{\delta g_\theta} \, \mathrm{d}a = 0. \tag{4.24}$$

With these transformations, the terms in brackets contain only the test functions for surfaces 1 and 2 and the introduced parameter κ. The first term $\delta\theta_D$ is often used with $\kappa = 0.5$ distributing the frictional heat equally to the surfaces. The second term is called variational thermal gap δg_θ.

The heat flux $\tilde{\boldsymbol{q}}_c \cdot \tilde{\boldsymbol{n}}_c$ is modelled with a constitutive equation including a thermal conductivity parameter h_c and the thermal gap g_θ

$$\tilde{\boldsymbol{q}}_c \cdot \tilde{\boldsymbol{n}}_c = h_c \cdot \underbrace{(\theta_2 - \theta_1)}_{g_\theta} \tag{4.25}$$

leading to the compact weak form for a thermal contact interface

$$G_\theta^c(\theta, \delta\theta) = \int\limits_{\partial_c \mathcal{B}_t} \tilde{\boldsymbol{t}}_c \cdot \tilde{\boldsymbol{v}}_c \delta\theta_D \, \mathrm{d}a + \int\limits_{\partial_c \mathcal{B}_t} h_c \cdot g_\theta \delta g_\theta \, \mathrm{d}a. \tag{4.26}$$

For rough surfaces, the macroscopic contact interface represents the nominal contact area $\partial_c \mathcal{B}_t$. Contributions of body interfaces that are not in direct macroscopic contact are not considered in this section. The real contact area, in which microscopic surface asperities are in direct contact, is only a portion of the nominal contact area. Thus, the heat transfer is split into a real contact (rc) part and a part with a microscopical gap (gc) (displayed in figure 4.2 b))

$$\tilde{\boldsymbol{q}}_c = \tilde{\boldsymbol{q}}_{rc} + \tilde{\boldsymbol{q}}_{gc}. \tag{4.27}$$

Direct heat transfer takes place between the contact spots and through the interface gap several effects can contribute to the heat transfer. In Persson et al. (2010),

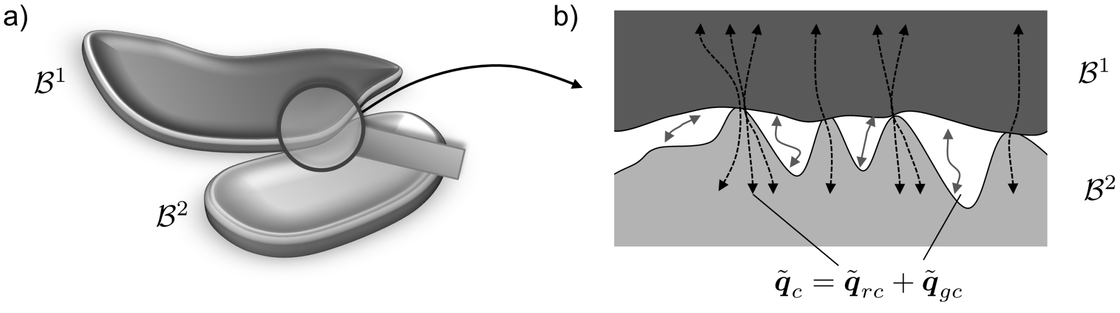

Figure 4.2: a) Two bodies in contact with heat transfer at the contact interface. b) Detailed heat transfer at a microscopic length scale. Heat flux $\tilde{q}_c$ is splitted into real contact part (rc) and gap contact part (gc).

for instance, different heat transfer mechanisms are studied, such as a radiative contribution, a contribution from surrounding gas or liquid and the heat transfer through capillary bridges. Especially the real contact area heat conductivity parameter will increase with increasing nominal pressure. More parts of the surface asperities get in contact with each other and the microscopic gap is closed with increasing pressure. A simple numerical description for the real contact contribution including a normal pressure dependency can be found in Wriggers & Miehe (1994). Experimental access to the single quantities and a separation of the physical contributions is quite complex. In this work a very simple model for the contact heat transfer described with the coefficient h_c will be introduced without any distinctions between different physical effects and without a normal pressure dependency. As a physical background a contribution from real microscopic contact spots and a contribution of the surrounding gas is assumed, neglecting all other effects. Detailed explanations and the underlying assumptions are explained in subsection 8.3.1.

Chapter 5

Finite Element Method

In this chapter, the general framework of finite elements is described in a first step. Afterwards, details regarding the implementation of a thermomechanical continuum finite element and a thermomechanical mortar contact finite element are explained.
Both elements are implemented in the software FEAP with the possibility to access all quantities. Within the software ABAQUS, thermomechanical continuum elements and different contact formulations are available based on the same principles although direct access to certain variables and intermediate results of the framework is limited. No differentiation between two-dimensional and three-dimensional formulations is applied in this chapter, since the FEAP elements are formulated in a three-dimensional setup. In chapter 6, further comments on the used elements are given.

5.1 Background

The idea of the finite element method (FEM) is based on a division of a continuous initial boundary value problem (IBVP) in a defined, finite number of elements approximating the solution of the IBVP, see Zienkiewicz & Taylor (2000a,c,b) and Wriggers (2008). Applying the methodology to solid mechanics means that a body $\mathcal{B}$ and its surface $\partial\mathcal{B}$ are approximated by a number n_e of elements Ω_e, see figure 5.1 a)-b)

$$\mathcal{B} \approx \mathcal{B}^h = \bigcup_{e=1}^{n_e} \Omega_e. \tag{5.1}$$

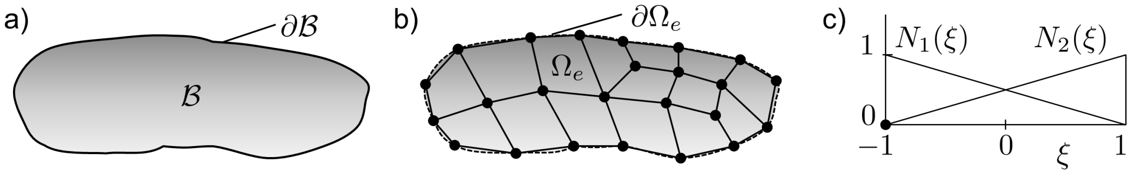

Figure 5.1: a) Solid two-dimensional body, b) discretized body, c) one dimensional linear ansatz functions.

The superscript h is used to declare an approximation, for example elements with four nodes (black dots) can be used for a two dimensional problem. Besides the geometry described by the position vector $\boldsymbol{x}$, the solution field (in the case of a solid body the displacement $\boldsymbol{u}(\boldsymbol{x})$ as well as the temperature $\theta(\boldsymbol{x})$) is approximated element-wise. The displacement solution field can be expressed by the nodal values $\boldsymbol{u}_I$ within the finite element method using so-called shape functions N_I to interpolate the solution for the whole element

$$\boldsymbol{u}\left(\boldsymbol{x}\right) \approx \boldsymbol{u}^h\left(\boldsymbol{x}\right) = \sum_{I=1}^{n_p} N_I\left(\boldsymbol{x}\right)\boldsymbol{u}_I. \tag{5.2}$$

This is achieved by summation of all nodal contributions n_p. The basic principles are derived exemplarily for the mechanical part of finite elements in this section and details with respect to the temperature field are described in section 5.2.

In order to simplify the construction of shape functions for arbitrary finite elements, the isoparametric concept is often used in finite element frameworks. The classical isoparametric concept uses the same shape functions for the geometry and the solution field on a reference element with the reference coordinates $\boldsymbol{\xi}$:

$$\boldsymbol{x}\left(\boldsymbol{\xi}\right) \approx \boldsymbol{x}^h\left(\boldsymbol{\xi}\right) = \sum_{I=1}^{n_p} N_I\left(\boldsymbol{\xi}\right)\boldsymbol{x}_I, \quad \boldsymbol{u}\left(\boldsymbol{\xi}\right) \approx \boldsymbol{u}^h\left(\boldsymbol{\xi}\right) = \sum_{I=1}^{n_p} N_I\left(\boldsymbol{\xi}\right)\boldsymbol{u}_I. \tag{5.3}$$

Furthermore, the virtual displacement $\delta\boldsymbol{u}$ is discretized throughout this work with the same shape functions N_I (Bubnov-Galerkin-Approach)

$$\delta\boldsymbol{u}\left(\boldsymbol{\xi}\right) \approx \delta\boldsymbol{u}^h\left(\boldsymbol{\xi}\right) = \sum_{I=1}^{n_p} N_I\left(\boldsymbol{\xi}\right)\delta\boldsymbol{u}_I. \tag{5.4}$$

For 3D simulations, a hexahedral reference element $\Omega_\square$ with local coordinates $\boldsymbol{\xi} = \{\xi, \eta, \zeta\}$ is often used, see figure 5.2. The shape functions N_I are constructed in the way that they equal one at node I and are zero at all other nodes J (Kronecker-Delta property). Furthermore, the partition of unity is applied ensuring that the sum of all shape functions in one element equals one at each position:

$$N_I\left(\boldsymbol{\xi}_J\right) = \delta_{IJ}, \quad \sum_{I=1}^{n_p} N_I(\boldsymbol{\xi}) = 1. \tag{5.5}$$

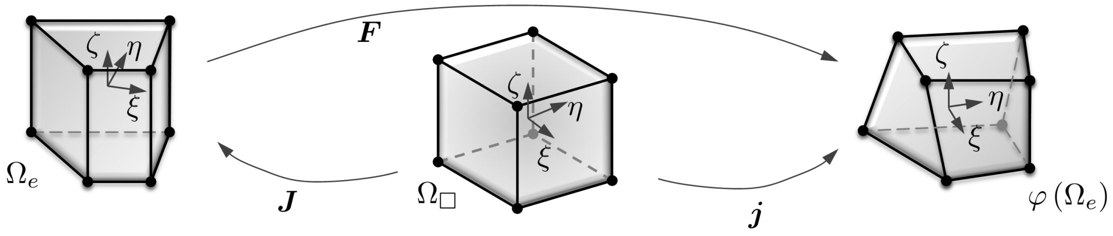

Figure 5.2: Isoparametric concept with initial, reference and current configuration.

A simple one-dimensional reference element and its shape functions are displayed in figure 5.1 c). The trilinear shape functions for a three-dimensional eight node element read

$$N_I(\boldsymbol{\xi}) = \frac{1}{2}(1+\xi_I\xi) \cdot \frac{1}{2}(1+\eta_I\eta) \cdot \frac{1}{2}(1+\zeta_I\zeta)\,. \tag{5.6}$$

A reduction by crossing the term with ζ leads to the bilinear two-dimensional shape functions for a four node element. Mappings (see figure 5.2) between the reference configuration $\Omega_\square$, the initial configuration, and the current configuration are derived as

$$\boldsymbol{J}(\boldsymbol{\xi}) = \frac{\partial \boldsymbol{X}(\boldsymbol{\xi})}{\partial \boldsymbol{\xi}} = \sum_I \boldsymbol{X}_I \otimes \frac{\partial N_I(\boldsymbol{\xi})}{\partial \boldsymbol{\xi}}, \quad \boldsymbol{j}(\boldsymbol{\xi}) = \frac{\partial \boldsymbol{x}(\boldsymbol{\xi})}{\partial \boldsymbol{\xi}} = \sum_I \boldsymbol{x}_I \otimes \frac{\partial N_I(\boldsymbol{\xi})}{\partial \boldsymbol{\xi}}. \tag{5.7}$$

The quantities $\boldsymbol{J}$ and $\boldsymbol{j}$ are called JACOBIAN matrix in the initial and the current configuration, respectively.

Using the mapping scheme described above, integrals can be transferred to the reference element $\Omega_\square$. These integrals can be solved in various ways, using for example a GAUSSIAN integration scheme, solving the integral approximately. This is done by introducing a summation over the function evaluated at a certain number of integration points n_g multiplied with the corresponding weight function w_g for each integration point. With functions $\boldsymbol{f}$ which depend on the current coordinate vector $\boldsymbol{x}$, the integration is given in the following form

$$\int\limits_{\Omega_e} \boldsymbol{f}(\boldsymbol{x})\,\mathrm{d}v = \int\limits_{\Omega_\square} \boldsymbol{f}(\boldsymbol{x}(\boldsymbol{\xi}))\det \boldsymbol{j}(\boldsymbol{\xi})\,\mathrm{d}v \approx \sum_{g=1}^{n_g} \boldsymbol{f}(\boldsymbol{x}(\boldsymbol{\xi}_g))w_g \det \boldsymbol{j}(\boldsymbol{\xi}_g). \tag{5.8}$$

The coordinates of the integration points ($\boldsymbol{\xi}_g$) are listed in various books, see for example WRIGGERS (2008).

In order to describe the whole process of solving partial differential equations using the finite element method, the weak form based on the balance of linear momentum is used as an example. The inner part of the weak form G_u^b is determined by the first term of equation (3.84) containing the CAUCHY stress and the gradient of the virtual displacement

$$\int\limits_{\mathcal{B}_t} \boldsymbol{\sigma} : \mathrm{grad}^s \delta\boldsymbol{u}\,\mathrm{d}v \approx \bigcup_{e=1}^{n_e}\sum_{I=1}^{n_p} \delta\boldsymbol{u}_I^T \cdot \int\limits_{\Omega_e} (\mathrm{grad}\, N_I)^T \cdot \boldsymbol{\sigma}\,\mathrm{d}v = \delta\widetilde{\boldsymbol{u}}^T \cdot R(\boldsymbol{u}). \tag{5.9}$$

The finite element formulation is introduced using the assembling operator $\bigcup$ over all elements n_e. Therefore, the volume integral over the whole domain is transferred to an integral over the element domain and a summation over all nodes. The same shape functions like for the displacement are used for the virtual displacement. The derived element contributions in equation (5.9) are integrated over the volume of the finite element, using the introduced GAUSSIAN integration scheme (cf. equation (5.8)). In a

next step, an assembled virtual displacement $\delta\widetilde{\boldsymbol{u}}$ is multiplied with an assembled vector of internal nodal forces $R(\boldsymbol{u})$, using the Gaussian integration scheme described above. The reader is referred to Zienkiewicz & Taylor (2000b,c,a) and Wriggers (2008) for further details regarding the assembly process.
In addition to the internal forces, external forces are applied as boundary conditions by body forces and tractions at the body surface. Since no body forces $\hat{\boldsymbol{b}}$ are considered in this work, only surface tractions $\hat{\boldsymbol{t}}$ are transferred in the same way as the internal nodal forces

$$\int\limits_{\partial\mathcal{B}_t} \hat{\boldsymbol{t}} \cdot \delta\boldsymbol{u}\, \mathrm{d}a \approx \bigcup_{e=1}^{n_e} \sum_{I=1}^{n_p} \delta\boldsymbol{u}_I^T \cdot \int\limits_{\partial\Omega_e} N_I \cdot \hat{\boldsymbol{t}}\, \mathrm{d}a = \delta\widetilde{\boldsymbol{u}}^T \cdot P_{ext}. \tag{5.10}$$

with the difference that a surface integral has to be evaluated and the resulting assembled vector of traction forces is named P_{ext} assuming an independence of the displacement. The whole system of equations is determined by the so-called residual vector $G(\boldsymbol{u})$

$$G(\boldsymbol{u}) = R(\boldsymbol{u}) - P_{ext} = 0. \tag{5.11}$$

An iterative solution of the non-linear equation system is often provided by the use of a Newton-Raphson scheme based on the use of a Taylor series aborted after the first derivative

$$G(\boldsymbol{u}^{k+1}) = G(\boldsymbol{u}^k) + \left.\frac{\partial G(\boldsymbol{u})}{\partial \boldsymbol{u}}\right|_{\boldsymbol{u}=\boldsymbol{u}^k} (\boldsymbol{u}^{k+1} - \boldsymbol{u}^k) = 0. \tag{5.12}$$

The solution for the next iteration step $k+1$ is calculated by

$$\boldsymbol{u}^{k+1} = \boldsymbol{u}^k - K_T^{-1} G(\boldsymbol{u}^k), \tag{5.13}$$

introducing the tangent stiffness matrix K_T

$$K_T = \left.\frac{\partial G(\boldsymbol{u})}{\partial \boldsymbol{u}}\right|_{\boldsymbol{u}=\boldsymbol{u}^k}. \tag{5.14}$$

The whole iterative procedure is interrupted in the case a certain convergence criterion is fulfilled, achieving a solution for the displacement vector, see Wriggers (2008) for details.

5.2 Thermomechanical Continuum Element

A three-dimensional thermomechanical continuum finite element is derived in this section. First, the mechanical part is derived, thereafter the thermal part is given. Both are combined in a last step. The displacement and virtual displacements are discretized by bilinear or trilinear ansatz functions as described in the previous subsection

$$\boldsymbol{u}(\boldsymbol{\xi}) = \sum_{I=1}^{n_p} N_I(\boldsymbol{\xi})\boldsymbol{u}_I, \quad \delta\boldsymbol{u}(\boldsymbol{\xi}) = \sum_{I=1}^{n_p} N_I(\boldsymbol{\xi})\delta\boldsymbol{u}_I. \tag{5.15}$$

The gradients of the displacement and virtual displacement are often described with so-called $\boldsymbol{B}$-matrices including the derivatives of the shape functions with respect to $\boldsymbol{x}$.

$$\operatorname{grad}\boldsymbol{u}(\boldsymbol{\xi}) = \sum_{I=1}^{n_p} \boldsymbol{B}_I^u(\boldsymbol{\xi})\boldsymbol{u}_I, \quad \operatorname{grad}\delta\boldsymbol{u}(\boldsymbol{\xi}) = \sum_{I=1}^{n_p} \boldsymbol{B}_I^u(\boldsymbol{\xi})\delta\boldsymbol{u}_I. \tag{5.16}$$

The internal part of the mechanical weak form is used as the basis for the derivation of the necessary internal nodal force vector and the tangent stiffness matrix. All quantities are considered on the element level using the integration over the element volume Ω_e

$$G_u^{b,int} = \int\limits_{\Omega_e} \boldsymbol{\sigma} : \operatorname{grad}^s\delta\boldsymbol{u}\,\mathrm{d}v = \delta\boldsymbol{u}_I^T \cdot \int\limits_{\Omega_e} (\operatorname{grad} N_I)^T \cdot \boldsymbol{\sigma}\,\mathrm{d}v. \tag{5.17}$$

The Voigt notation used for matrix operations is indicated by the superscript v. Using Gaussian integration with eight integration points ($n_g = 8$), the internal nodal force vector is given by

$$R_u^e = \sum_{g=1}^{n_g}\sum_{I=1}^{n_p} \boldsymbol{B}_I^{uT}(\boldsymbol{\xi}_g)\boldsymbol{\sigma}^v(\boldsymbol{\xi}_g)\det\boldsymbol{j}(\boldsymbol{\xi}_g)w_g. \tag{5.18}$$

The weak form is linearized with respect to the displacements $\boldsymbol{u}$ and after some transformations, cf. Wriggers (2008), an expression with the elasticity tensor $\mathbb{c}$ and the Cauchy stress tensor (see subsection 3.3.3) is derived

$$D_uG_u^{b,int} = \int\limits_{\Omega_e} \left(\operatorname{grad}^s\delta\boldsymbol{u} : \mathbb{c} : \operatorname{grad}^s\Delta\boldsymbol{u} + (\operatorname{grad}^s\delta\boldsymbol{u}\cdot\boldsymbol{\sigma}) : \operatorname{grad}^s\Delta\boldsymbol{u}\right)\,\mathrm{d}v. \tag{5.19}$$

The element stiffness matrix K_{uu}^e is again derived in Voigt notation transferring the elasticity tensor in square matrix $\boldsymbol{C}^v$

$$K_{uu}^e = \sum_{g=1}^{n_g}\sum_{I=1}^{n_p}\sum_{K=1}^{n_p} \left(\boldsymbol{B}_I^{uT}(\boldsymbol{\xi}_g)\boldsymbol{C}^v\boldsymbol{B}_K^u(\boldsymbol{\xi}_g) + \mathbf{1}G_{IK}\right)\det\boldsymbol{j}(\boldsymbol{\xi}_g)w_g, \tag{5.20}$$

with the first term being the non-linear material part. In addition to the index I for the virtual displacement, the index K is introduced for the linearized displacement. The non-linear geometrical part is written as

$$G_{IK} = N_{I,i}(\boldsymbol{\xi}_g)\sigma_{ij}N_{K,j}(\boldsymbol{\xi}_g). \tag{5.21}$$

After the mechanical part, the thermal part is described. For the temperature θ the same linear shape functions as in the mechanical part are used

$$\theta(\boldsymbol{\xi}) = \sum_{I=1}^{n_p} N_I(\boldsymbol{\xi})\theta_I, \quad \operatorname{grad}\theta(\boldsymbol{\xi}) = \sum_{I=1}^{n_p} \boldsymbol{B}_I^\theta(\boldsymbol{\xi})\theta_I. \tag{5.22}$$

The $\boldsymbol{B}$-matrices for the description of the gradient (marked with the superscript θ) have a different size compared to the mechanical part, because the temperature is described by one value at each node. Following the previous subsection, the virtual temperature $\delta\theta$ is described by the same shape function N_I and $\boldsymbol{B}_I^\theta$. The internal thermal weak form derived from the first law of thermodynamics and the heat equation can be expressed on element level as

$$G_\theta^{b,int}(\theta, \delta\theta) = \int_{\Omega_e} \left(\rho c\dot{\theta}\delta\theta + k\operatorname{grad}^T\theta\operatorname{grad}\delta\theta - D_{int}\delta\theta\right)\,\mathrm{d}v. \tag{5.23}$$

Following the described procedure according to the mechanical part, the element internal residual vector is derived as

$$R_\theta^e = \sum_{g=1}^{n_g}\sum_{I=1}^{n_p}\left(\rho c N_I(\boldsymbol{\xi}_g)\dot{\theta}^e + \boldsymbol{B}_I^{\theta T}(\boldsymbol{\xi}_g)k\operatorname{grad}\theta^e\right)\det\boldsymbol{j}(\boldsymbol{\xi}_g)w_g. \tag{5.24}$$

The included elemental time derivative of the temperature is approximated by an implicit Euler scheme

$$\dot{\theta}^e(t_{n+1}) = \sum_{K=1}^{n_p} N_K(\boldsymbol{\xi}_g)\frac{\theta_K(t_{n+1}) - \theta_K(t_n)}{\Delta t}. \tag{5.25}$$

Furthermore, the elemental gradient of the temperature reads

$$\operatorname{grad}\theta^e = \sum_{K=1}^{n_p} \boldsymbol{B}_K^\theta(\boldsymbol{\xi}_g)\theta_K. \tag{5.26}$$

The linearization of the thermal part of the internal weak form with respect to the temperature yields

$$D_\theta G_\theta^{b,int} = \int_{\Omega_e}\left(\rho c\Delta\dot{\theta}\delta\theta + \operatorname{grad}^T\Delta\theta k\operatorname{grad}\delta\theta\right)\,\mathrm{d}v. \tag{5.27}$$

The thermal tangent stiffness matrix is then computed by Gaussian integration and summation over nodes I and K

$$K_{\theta\theta}^e = \sum_{g=1}^{n_g}\sum_{I=1}^{n_p}\sum_{K=1}^{n_p}\left(\frac{\rho c}{\Delta t}N_I(\boldsymbol{\xi}_g)N_K(\boldsymbol{\xi}_g) + \boldsymbol{B}_I^{\theta T}(\boldsymbol{\xi}_g)k\boldsymbol{B}_K^\theta(\boldsymbol{\xi}_g)\right)\det\boldsymbol{j}(\boldsymbol{\xi}_g)w_g. \tag{5.28}$$

Direct modelling of thermomechanical terms originating from coupling effects like a temperature dependent stress vector or a displacement-induced internal dissipation are neglected in this work ($D_{int} = 0$). These terms could be gained by a linearization of the mechanical part with respect to temperature and vice versa

$$D_\theta G_u^{b,int} = \int\limits_{\Omega_e} \frac{\partial \boldsymbol{\sigma}}{\partial \theta} \Delta\theta : \operatorname{grad}^s \delta\boldsymbol{u} \, \mathrm{d}v = 0, \quad D_u G_\theta^{b,int} = -\int\limits_{\Omega_e} \frac{\partial D_{int}}{\partial \boldsymbol{u}} \cdot \Delta\boldsymbol{u} \delta\theta \, \mathrm{d}v = 0. \tag{5.29}$$

Therefore, the mechanical-thermal and thermomechanical stiffness matrices are not evaluated in this work. This leads consequently to a decoupled stiffness matrix K

$$K = \begin{bmatrix} K_{uu} & K_{u\theta} \\ K_{\theta u} & K_{\theta\theta} \end{bmatrix} = \begin{bmatrix} K_{uu} & 0 \\ 0 & K_{\theta\theta} \end{bmatrix}. \tag{5.30}$$

For a viscoelastic continuum, the described thermal effects are introduced in the hyperelastic part, see subsection 3.3.3 and 3.3.4.

Since the used rubber materials are nearly incompressible, special techniques are used within finite elements in order to avoid volume locking phenomena. One possibility is the Q1P0 formulation introduced in subsection 3.3.3 that will be later used for calculations with the software ABAQUS. In FEAP, a different possibility is available to avoid locking. The total stiffness matrix is decomposed in a constant part integrated by one Gauss point and an additional stabilization term

$$K = K_0 + K_{stab}. \tag{5.31}$$

The concept is based on the enhanced strain theory and the element is called Q1SP, see Reese (2001) for further details.

5.3 Thermomechanical Mortar Contact Element

In this work, finite deformations and a complex contact interaction between rubber material and the rough counter surface are expected. In contrast to other numerical contact approaches like the node-to-segment (NTS) strategy, the mortar method is robust for large deformations and sliding, avoiding locking phenomena or failing projections, cf. Laursen (2003); Wriggers (2006). In contrast to the NTS method, a weak coupling of the contact constraints is enforced, leading to a segment-to-segment based formulation. One main feature of the mortar method is to determine the contact area in an appropriate way with a projection plane. Another important feature is to average kinematical quantities providing smooth contact forces. The proposed thermomechanical mortar contact element is based on the formulation in Weissenfels (2013) and Dobberstein (2014).

The contact constraint using a Lagrange-multiplier is given in section 4.3 providing the basis for the mortar contact formulation

$$G_l^c = \int\limits_{\partial_c \mathcal{B}_t} \delta\boldsymbol{\lambda} \cdot \boldsymbol{g} \, \mathrm{d}a. \tag{5.32}$$

An appropriate integration over the contact interface $\partial_c \mathcal{B}_t$ is a crucial point in numerical contact mechanics algorithms. The idea of the mortar approach is to project the slave and master elements on an intermediate projection plane and to perform the integration on the emerging geometrical intersections, see figure 5.3 a). Following the isoparametric concept and GAUSSIAN integration introduced in section 5.1, the global contact interface is approximated by a summation over all slave nodes n^1_{sl} and all adjacent elements n^1_{ad} since the base vectors are averaged over these elements. Furthermore, the contact area is divided into segments n_{seg} and in a next step the arbitrary segments are divided into triangular pallets n_{pa} containing a certain number of integration points $\bar{\boldsymbol{x}}^p_g$ per pallet n^{pa}_{gp} as displayed in figure 5.3 b)

$$\int\limits_{\partial_c \mathcal{B}_t} \mathrm{d}a \approx \sum_{a=1}^{n^1_{sl}} \sum_{b=1}^{n^1_{ad}} \sum_{s=1}^{n_{seg}} \sum_{p=1}^{n_{pa}} \sum_{g=1}^{n^{pa}_{gp}} \det \boldsymbol{j}\, w_g = \sum_{a=1}^{n^1_{glob}} \sum_{g=1}^{n_{gp}} \det \boldsymbol{j}\, w_g. \tag{5.33}$$

Projected master and slave nodes $\bar{\boldsymbol{x}}^i_j$ and certain intersection points construct an intersection area, white area in figure 5.3 a)-b). Lines between all projected points on the projection plane are constructed in order to determine the intersection points $\bar{\boldsymbol{x}}_{int}$. Details regarding the segmentation, construction of pallets, and the positions of integration points can be found in PUSO & LAURSEN (2004a,b); WEISSENFELS (2013). The determinant of the JACOBIAN $\det \boldsymbol{j}$ is calculated as the area of the three $j = 1-3$ pallet points $\bar{\boldsymbol{x}}^p_j$. In order to simplify the notation, the summation over global slave nodes n^1_{glob} is used for the summation over slave nodes, adjacent elements, segments and pallets.
The slave and master coordinates $\boldsymbol{x}^1$ and $\boldsymbol{x}^2$ are discretized with linear shape functions based on the convective coordinates $\boldsymbol{\xi^i}$

$$\boldsymbol{x}^1\left(\boldsymbol{\xi^1}\right) = \sum_{B=1}^{n_s} N_B\left(\boldsymbol{\xi^1}\right) \boldsymbol{x}^1_B, \quad \boldsymbol{x}^2\left(\boldsymbol{\xi^2}\right) = \sum_{C=1}^{n_m} N_C\left(\boldsymbol{\xi^2}\right) \boldsymbol{x}^2_C. \tag{5.34}$$

The number of nodes for each contact element on the slave and master side is defined by n_s and n_m. Additionally, LAGRANGE-multipliers are introduced with the same linear shape functions at the slave side

$$\boldsymbol{\lambda}\left(\boldsymbol{\xi^1}\right) = \sum_{A=1}^{n_s} M_A\left(\boldsymbol{\xi^1}\right) \boldsymbol{\lambda}_A. \tag{5.35}$$

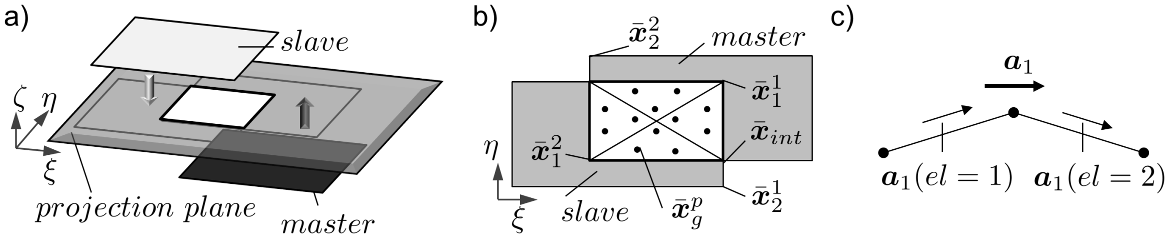

Figure 5.3: a) Mortar projection, b) construction of a segment and associated pallets including integration points, c) smoothing of base vectors.

In this work, for M_A the same linear shape functions are used as for the slave side. But, generally it is possible to use special dual shape functions for M_A (see WOHLMUTH (2000), POPP ET AL. (2009), POPP ET AL. (2010), POPP (2012)). Mortar approaches are based on smoothing the slave base vectors $\boldsymbol{a}^1$, tangential vectors $\boldsymbol{t}^1$ and normal vectors $\boldsymbol{n}^1$ by averaging over all adjacent elements n^1_{ad} (see figure 5.3 c) for an example),

$$\boldsymbol{a}^1_\alpha = \sum_{b=1}^{n^1_{ad}} \sum_{I=1}^{n_s} N_{I,\alpha} \left(\boldsymbol{\xi}^{1(b)}_\alpha \right) \boldsymbol{x}^{1(b)}_I, \quad \boldsymbol{t}^1_\alpha = \frac{\boldsymbol{a}^1_\alpha}{\|\boldsymbol{a}^1_\alpha\|}, \quad \boldsymbol{n}^1 = \boldsymbol{t}^1_1 \times \boldsymbol{t}^1_2. \tag{5.36}$$

In this way, jumps in contact forces are avoided leading to a robust algorithm.
The introduced discretizations for the slave surface, the master surface, and the LAGRANGE-multipliers are inserted in equation (5.32). In this way, the contact surface is approximated by the described summation, leading to

$$G^c_l = \sum_{a=1}^{n^1_{glob}} \delta \boldsymbol{\lambda}_A \sum_{g=1}^{n_{gp}} M_A \left(\boldsymbol{\xi}^1_g \right) \left(\sum_{C=1}^{n_m} N_C \left(\boldsymbol{\xi}^2_g \right) \boldsymbol{x}^2_C - \sum_{B=1}^{n_s} N_B \left(\boldsymbol{\xi}^1_g \right) \boldsymbol{x}^1_B \right) \det \boldsymbol{j} w_g. \tag{5.37}$$

A mean gap function between slave and master side is identified as

$$\bar{\boldsymbol{g}}_A = \sum_{g=1}^{n_{gp}} M_A \left(\boldsymbol{\xi}^1_g \right) \left(\sum_{C=1}^{n_m} N_C \left(\boldsymbol{\xi}^2_g \right) \boldsymbol{x}^2_C - \sum_{B=1}^{n_s} N_B \left(\boldsymbol{\xi}^1_g \right) \boldsymbol{x}^1_B \right) \det \boldsymbol{j} w_g, \tag{5.38}$$

which can be split into normal and tangential parts by multiplication with the corresponding normal or tangential vectors. Corresponding to equation (5.38), a virtual mean gap $\delta \bar{\boldsymbol{g}}_A$ and a gap including the old time step quantities o are defined. The penalty method introduced in section 4.3 is used to solve the contact part of the weak form introducing the approximations of the normal pressure and the tangential stress with the penalty factors c_N and c_T

$$\bar{t}_{NA} = c_N \bar{\boldsymbol{g}}_A \cdot \boldsymbol{n}_A, \tag{5.39}$$

$$\bar{t}_{T\alpha A} = -c_T \left[(\bar{\boldsymbol{g}}_A - \bar{\boldsymbol{g}}^o_A) \cdot \boldsymbol{t}_{A\alpha} + \Delta_t \bar{\gamma}_A \frac{\bar{\boldsymbol{t}}_A \cdot \boldsymbol{t}_{A\alpha}}{\|\bar{\boldsymbol{t}}_{TA}\|} \right] + \bar{t}^n_{T\alpha A}, \quad \|\bar{\boldsymbol{t}}_{TA}\| = \sqrt{(\bar{\boldsymbol{t}}_A \cdot \boldsymbol{t}_{A\alpha})^2}. \tag{5.40}$$

Using the penalty method, the only contribution to the contact weak form is formed by the virtual contact work (cf. section 4.3) which is divided into normal and tangential parts

$$G^{ch}_{uA} = \delta \bar{\boldsymbol{g}} \cdot (\boldsymbol{n}_A c_N \bar{\boldsymbol{g}}_A \cdot \boldsymbol{n}_A + \boldsymbol{t}_{A\alpha} \bar{t}_{T\alpha A}) = \sum_{s=1}^{n^A_{seg}} \delta \boldsymbol{d}^u_s \cdot \boldsymbol{R}^s_u. \tag{5.41}$$

The superscript h indicates the discretization and the index A is introduced as a node index, since the residual and stiffness matrix are derived nodal-wise, see also WEISSENFELS (2013) for details. The equation can be reformulated in a product of virtual displacements $\delta\boldsymbol{d}_s^u$ containing slave and master contributions of all involved segments n_{seg}^A and the residual for each segment $\boldsymbol{R}_u^s$

$$\boldsymbol{R}_u^s = \boldsymbol{G}_{\delta\boldsymbol{g}}^s \left(\boldsymbol{n}_a c_N \bar{\boldsymbol{g}}_A \cdot \boldsymbol{n}_A + \boldsymbol{t}_{A\alpha} \bar{t}_{T\alpha A}\right). \tag{5.42}$$

Parts of the linearization procedure in order to derive stiffness matrices for the mortar contact element are listed in equations (B.1)-(B.6). Moreover, the interested reader is referred to WEISSENFELS (2013) and DOBBERSTEIN (2014) for details regarding the complex linearization procedure for mortar contact elements.

The extension of the contact element towards a fully coupled thermomechanical element starts with the definition of slave and master temperatures

$$\theta^1\left(\boldsymbol{\xi}^{\boldsymbol{1}}\right) = \sum_{B=1}^{n_s} N_B\left(\boldsymbol{\xi}^{\boldsymbol{1}}\right)\theta_B^1, \quad \theta^2\left(\boldsymbol{\xi}^{\boldsymbol{2}}\right) = \sum_{C=1}^{n_m} N_C\left(\boldsymbol{\xi}^{\boldsymbol{2}}\right)\theta_C^2, \tag{5.43}$$

applying the same shape functions introduced in the mechanical part. A temperature gap $\bar{\boldsymbol{g}}_{\theta A}$ following equation (5.38) and a dissipative gap $\delta\theta_D$ (cf. equation (4.24)) are defined

$$\bar{\boldsymbol{g}}_{\theta A} = \sum_{g=1}^{n_{gp}} M_A\left(\boldsymbol{\xi}_g^1\right)\left(\theta^2\left(\boldsymbol{\xi}_g^2\right) - \theta^1\left(\boldsymbol{\xi}_g^1\right)\right)\det\boldsymbol{j}\, w_g, \quad \delta\theta_D = \kappa\delta\theta_1 + (1-\kappa)\delta\theta_2. \tag{5.44}$$

Similar to the mechanical part and with the use of equation (4.26), a nodal discretized weak form can be derived for the contact element

$$G_{\theta A}^{ch} = \delta\bar{g}_{\theta A}\left(\tilde{h}_c \bar{g}_{\theta A}\right) + \delta\theta_{GA}\left(\frac{\boldsymbol{g}_{TA} - \boldsymbol{g}_{TA}^o}{\Delta t}\cdot\boldsymbol{t}_{TA}\right) = \sum_{s=1}^{n_{seg}^A} \delta\boldsymbol{d}_s^\theta \cdot \boldsymbol{R}_\theta^s, \tag{5.45}$$

with the thermal residual vector $\boldsymbol{R}_\theta^s$. Details regarding the formulation, implementation and linearization of the thermomechanical contact contributions can be found e.g. in DITTMANN ET AL. (2014).

Chapter 6

Multiscale Approach for Hysteretic Friction

First, a review and summary of existing multiscale approaches for rubber friction is provided in section 6.1, accomplished by a review of some microscopic studies. Afterwards, a multiscale finite element approach for hysteretic rubber friction on rough surfaces based on contact homogenization is proposed in section 6.2. The approach is modified and enhanced in order to deal with real rough surfaces in section 6.3. Some features of the introduced method are studied in detail with single scale calculations in section 6.4. Finally, the introduced multiscale method for rough surfaces is validated with results of friction experiments in section 6.5.

6.1 Review of Previous Multiscale Approaches

Following subsection 2.3.2, two categories of numerical multiscale approaches for rubber friction are defined. The first approach is named multiscale projection method and is proposed in NITSCHE (2011). Frictionless behaviour is established on all scales and the solution is gained by a complex communication between the scales. For every macroscopic contact spot, a microscopic calculation starts, applying the current macroscopic displacement on the micro scale as a boundary condition. Afterwards, a projection of microscopic stresses and contact forces on the finite elements of the macroscopic scale is performed. This process is repeated until a defined convergence criterion of the residual norm is reached. An advantage of this method is that no information is lost because all quantities are transferred between the scales. However, a bad convergence rate of the macroscopic solution and instabilities due to the projection are a drawback. Additionally, an implementation of viscoelastic effects, which is elementary for the study of elastomer friction, is not demonstrated in NITSCHE (2011). The extension to viscoelasticity could be difficult, because the data structure and handling are complicated within such a framework. Therefore, approaches with a reduction of passed information promise a way to study the hysteretic effect of rubber friction.

Another method called multiscale contact homogenization technique was proposed by TEMIZER & WRIGGERS (2008) for the first time, dealing with contact between a macroscopic rubber block and moving micro particles. The scales are separated into a macroscopic scale without microscopic details and a microscopic scale containing in this case the micro particles. The local macroscopic contact pressure and velocity are used as spatially constant boundary conditions on the microscopic scale. That implies that the macroscopic length scale L has to be significant larger than the microscopic length scale l

$$L \gg l, \tag{6.1}$$

to allow for an application of this approach. Otherwise, the assumed constant boundary conditions would become inadequate. A periodic representative microscopic setup is constructed since the microscopic structure has repetitive character. Thus, the microscopic simulation setup is often called representative volume element or representative contact element (RVE/RCE). The resulting total reaction forces on top of the rubber block in x- and z-direction are calculated (cf. figure 2.3), transferred to a coefficient of friction and averaged over time in a homogenization step

$$\mu(t) = \frac{|F_x(t)|}{|F_z(t)|}, \quad \mu_{avg.} = \frac{1}{t_1 - t_0} \int\limits_{t_0}^{t_1} \mu(t)\, \mathrm{d}t. \tag{6.2}$$

For the force evaluation, dynamic and interlocking effects are considered in Temizer & Wriggers (2008), viscoelasticity is added in Temizer & Wriggers (2010a). The gained friction coefficient is incorporated in the macroscopic calculation and thus enhancing the contact calculation with the microscopic result. In Temizer & Wriggers (2008) this operation is repeated in every contact integration point with a different microscopic input for every time step resulting in a large calculation time. A similar scheme is used in FE-square methods for continuum setups, see Feyel (1999) and Zohdi & Wriggers (2008). This procedure is quite expensive from a computational point of view since many microscopic calculations with different velocity and pressure values are performed in each macroscopic time step.

The method was transferred to the contact of rubber including a viscoelastic material law with a rigid rough surface in Reinelt (2008) and Wriggers & Reinelt (2009). An important feature of this approach is that the rough surface is idealized by a certain number of sinusoidal waves increasing also the number of involved scales in contrast to two scales in Temizer & Wriggers (2008). The choice of these scales is based on an approximation of the rough surface HDC function (see subsection 2.3.1) by a sum of single HDC functions $\sum |C_{z_i}|$ of each scale i. This represents the most critical point of this approach since the self-affine rough surface is reproduced by periodic sinusoidal waves that are by definition not self-affine. Thus, the individual HDC functions are manipulated by an idealization introducing a constant value after the cut off point, although the HDC functions fluctuate after this point for sinusoidal functions, see Reinelt (2008). With the manipulated HDC functions, a problematic approximation of the HDC function of the rough surface is performed since the number of introduced sinusoidal scales is an uncertain parameter with unknown convergence properties. In Reinelt (2008) and Wriggers & Reinelt (2009), global results obtained with a three-scale or four-scale approximation of the rough surface are compared and a large influence on the global result is detected, although the HDC function of the rough surface is approximated in a similar manner. Adding a very small length scale or a completely different choice of intermediate scales could result in a very similar approximation quality with respect to the HDC function, but a complete different result for the final coefficient of friction could be obtained. Criteria how to choose the number of scales and the corresponding wavelengths and amplitudes remain an open and difficult question of this approach.

In contrast to the approach in TEMIZER & WRIGGERS (2008), pressure and velocity values for the microscopic calculations are not extracted during a macroscopic calculation in WRIGGERS & REINELT (2009). This procedure results in a reduced computational time and is therefore the basis of the later proposed multiscale approach in this work. Furthermore, the pressure values applied on the lower scales are determined by estimation of the true contact area before the calculation, see REINELT (2008) for details. Following TEMIZER & WRIGGERS (2008), the microscopic coefficient of friction is obtained by homogenization starting the whole framework with a frictionless calculation on the lowest scale. The resulting coefficient of friction depending on the contact pressure and velocity is then incorporated on the next larger scale followed by another homogenization step until the final macroscopic length scale is reached. The gained coefficient of friction is a result of the viscoelastic energy dissipation inside the material (cf. subsection 2.3.2) providing the chance to study the hysteretic contribution of rubber friction. Furthermore, in REINELT (2008) and WRIGGERS & REINELT (2009) the approach is also extended by an adhesive interaction on the lowest scale, see chapter 7 for more details.

An important factor which influences the outcome of the homogenization procedure is the appropriate choice of parameters like microscopic block size or boundary conditions among others. There exist various scientific publications dealing especially with the correct choice of these parameters in order to achieve converged results. In TEMIZER & WRIGGERS (2008) the influence of microscopic block height, block length and the number of involved micro particles is investigated since these quantities represent free parameters. Additionally, in TEMIZER & WRIGGERS (2010a) the difference between displacement boundary conditions and traction boundary conditions applied on the microscopic block are investigated. Dealing with viscoelastic solids, the compression time Δt_p for applying the pressure on top of a microscopic sinusoidal RCE is identified as an important parameter in DE LORENZIS & WRIGGERS (2013). The compression time influences the oscillations of the resulting coefficient of friction since the contact area is adjusted in this phase and a large difference to the stationary contact area during the dragging phase results in large oscillations. As a consequence, the compression time has to be adopted for different velocities and pressures in the way that the contact area of the compression phase approaches the contact area of the dragging phase, see subsection 6.2.2. In SCARAGGI ET AL. (2016) the influence of geometrical and material non-linearities on a sinusoidal RCE is studied and compared to analytical approaches.

The description of the rough surface is a crucial and important point for the modelling of a sliding rubber block on a rough surface. Some microscopic studies take complex geometries into account, for example micro particles with non-circular shapes are investigated in Temizer (2013). In Temizer (2014) and Stupkiewicz et al. (2014), microscopic rough surfaces for the rubber block bottom as well as for the counter surface are introduced in order to study geometrical effects and surface anisotropy.

6.2 Multiscale Contact Homogenization

In contrast to the already introduced multiscale approach for hysteretic rubber friction on rough surfaces in Wriggers & Reinelt (2009), the proposed algorithm incorporates the rough surface directly without a transformation to sinusoidal functions, see Wagner et al. (2015). It is based on splitting the surface into separate scales and contact homogenization techniques like proposed in Temizer & Wriggers (2008). The focus of this section is to describe the main idea of the contact homogenization multiscale framework, providing the basis for a detailed description of the surface treatment and extension of the method in section 6.3.

6.2.1 General Framework

The proposed multiscale framework of this section is only universally applicable for separated length scales, because it is based on introduced homogenization multiscale approaches of section 6.1. Therefore, the range of application is limited to problems with separated scales. An extension and modification of the approach towards rough road surfaces which are naturally not separated is introduced in the next section.

In order to reduce the computational costs for the multiscale method, the numerical calculations on all scales are reduced to two-dimensional setups throughout this work. Furthermore, a plane strain approach is applied in this work calculating sections of the plane in sliding direction (x-z-plane in figure 2.3). It is used because the dimension of the rubber block in y-direction is comparatively large, leading to a relative small strain component in this direction. The difference between two-dimensional and three-dimensional setups with respect to results and calculation time is discussed in subsection 6.4.3 in detail.

The framework of a multiscale homogenization approach is divided in the most important steps and features in figure 6.1. In a first step A) the rough surface is decomposed in macroscopic (1) and microscopic (2) parts. This step is very essential for real rough road surfaces and requires therefore special techniques which will be described in subsection 6.3.1 and are excluded in this subsection. The global input parameters are the material properties of the rubber material, the rough surface, the global pressure p_1 and the velocity v_1 (bold letters in step A) of figure 6.1). The whole approach starts with a frictionless macroscopic calculation including a viscoelastic material law (see subsection 3.3.4). Following the previous chapters the complete weak form, neglecting body forces $\hat{\boldsymbol{b}}$, can be constructed by a continuum part and contact part (see equation (3.84) and (4.14))

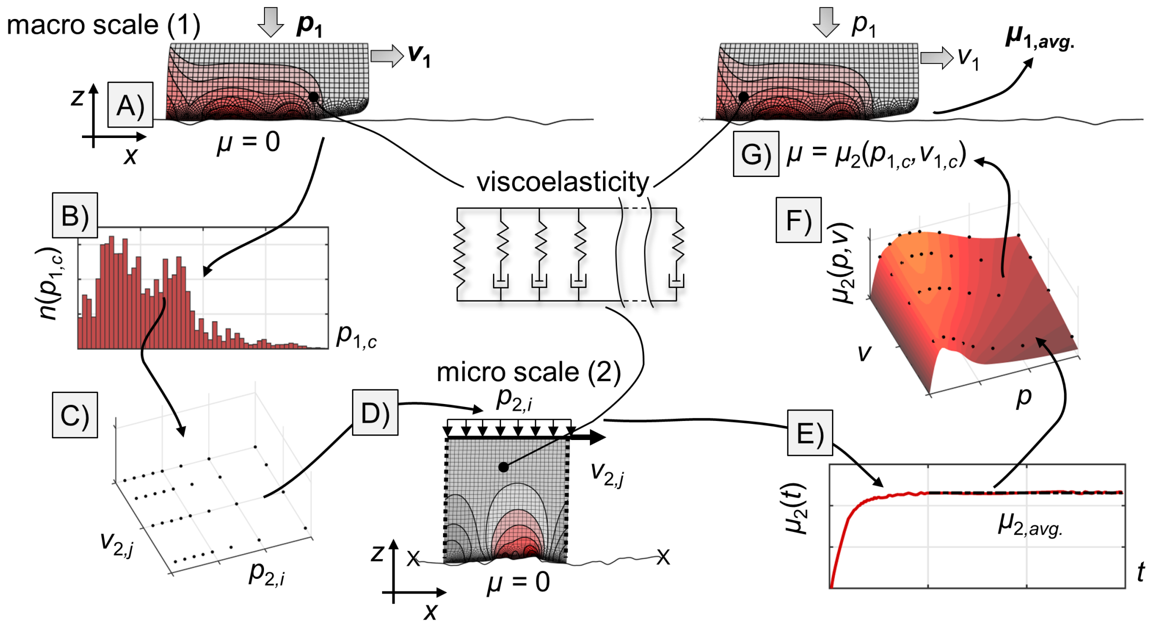

Figure 6.1: A) Surface split. B) Contact pressure evaluation. C) Definition of microscopic boundary values. D) Calculation of representative microscopic sample. E) Homogenization. F) Micro friction law. G) Macroscopic calculation with microscopic friction law.

$$G_u^{0,n}(\boldsymbol{u}, \delta\boldsymbol{u}) = \int\limits_{\mathcal{B}_t^n} \boldsymbol{\sigma} : \operatorname{grad}^s \delta\boldsymbol{u} \, \mathrm{d}v - \int\limits_{\partial_t \mathcal{B}_t^n} \hat{\boldsymbol{t}} \cdot \delta\boldsymbol{u} \, \mathrm{d}a + \int\limits_{\partial_c \mathcal{B}_t^n} \delta g_N p_N \, \mathrm{d}a = 0. \tag{6.3}$$

The weak form is superscripted with a 0 to indicate frictionless behaviour and the superscript n represents the considered scale. No tangential contact contribution is considered for the frictionless case and the penalty method is used, introducing a normal pressure p_N, see section 4.3 for details. This first macroscopic calculation is used to determine contact pressure values $p_{1,c}$ of all time steps and contact elements, see step B), in order to estimate the pressure distribution $n(p_{1,c})$. Following the idea of scale separation, the information is used to construct a field of spatially constant boundary conditions in step C) for the microscopic representative setup by dividing the whole pressure range in a finite number of pressure values $p_{2,i}$. The high pressure range occurs less often than the lower pressure range, see figure 6.1, and is therefore divided with fewer points than the lower range in the sketched example. This procedure has to be repeated for large changes in the global parameter set p_1, v_1 since the local contact pressure distribution may differ. Furthermore, the velocity field $v_{2,j}$ can be divided through the definition of velocities between the highest applied macroscopic velocity v_1 and a small velocity close to 0m/s.

In step D) a periodic microscopic representative finite element setup is constructed and various calculations with the defined pressures $p_{2,i}$ and velocities $v_{2,j}$ are performed. The periodicity is introduced since the microscopic length scale represents a cutout of the full problem with rubber material on each side of the cutout. Wihout periodic boundary conditions the microscopic rubber samples would start to buckle at the left and right side. The calculations are again frictionless and the same viscoelastic material law from the macroscopic scale is applied. By the use of a rough surface and a viscoelastic material an energy dissipation is caused that can be evaluated through balancing the reaction forces on top of the rubber block leading to a generated coefficient of friction, see equations (2.8) and (6.2). This effect is known as hysteretic friction (cf. section 2.2). Furthermore, it has to be remarked that the pure hysteretic response can be evaluated by an analysis of the dissipated energy, whereas an evaluation of the reaction forces includes automatically geometric effects, such as interlocking (see figure 6.3). After a transition phase, the applied periodic boundary conditions lead to a stationary response of the coefficient of friction. Following the concept of contact homogenization and based on equation (6.2), the time dependency is removed by time homogenization in step E), leading to $\mu_{2,avg.}$, see Temizer & Wriggers (2008) and Wriggers & Reinelt (2009). The boundary conditions of the microscopic calculation and some important details regarding the homogenization procedure are discussed in subsection 6.2.2.

After all microscopic calculations were executed, a pressure- and velocity-dependent friction law $\mu_2(p, v)$ is constructed in step F). This friction law can be directly inserted in the macroscopic contact formulation, evaluating the law for the macroscopic contact pressure and velocity, see step G). The weak form for the frictional case is indicated with the superscript f. Introducing also a tangential contribution of the contact virtual work, results in

$$G_u^{f,n}(\boldsymbol{u}, \delta\boldsymbol{u}) = \int\limits_{\mathcal{B}_t^n} \boldsymbol{\sigma} : \operatorname{grad}^s \delta\boldsymbol{u} \, \mathrm{d}v - \int\limits_{\partial_t \mathcal{B}_t^n} \hat{\boldsymbol{t}} \cdot \delta\boldsymbol{u} \, \mathrm{d}a + \int\limits_{\partial_c \mathcal{B}_t^n} (\delta g_N p_N + \delta \boldsymbol{g}_T \cdot \boldsymbol{t}_T) \, \mathrm{d}a = 0. \quad (6.4)$$

The friction law obtained by homogenization is considered in every contact element and time step and can additionally be linearized with respect to contact pressure and velocity. Details on how to construct the microscopic friction law with splines can be found in subsection 6.2.2. Finally, the frictional macroscopic calculation generates a hysteretic contribution in the same way as the microscopic calculation. The resulting coefficient of friction is then containing also the interlocking response. The macroscopic response is evaluated again by balancing the reaction forces. The final result $\mu_{1,avg.}$ (marked with bold letters in step G) of figure 6.1), which is the stationary coefficient of friction, is gained through time homogenization following equation (6.2). In general, the method could be extended to more than two scales by applying a further loop between step D) and E).

6.2.2 Homogenization and Micro Friction Law

The most important features of the microscopic scale calculation and boundary conditions are explained in this subsection. Afterwards, remarks and comments on the homogenization procedure and on the micro friction law generation are given.

An exemplary microscopic setup is displayed in figure 6.2 a). As already explained in the last sections, a frictionless setup with a periodic rough surface is constructed.

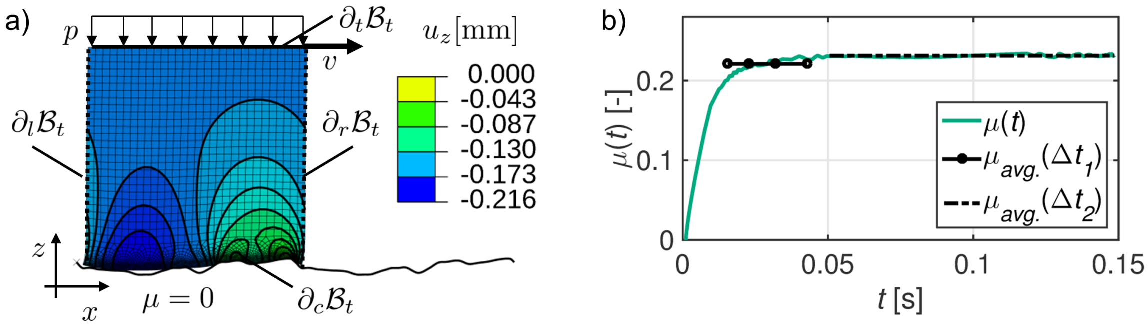

Figure 6.2: a) Periodic microscopic setup with boundary conditions and exemplary solution, b) resulting coefficient of friction and exemplary homogenized values.

A finite linear viscoelastic material law is used to generate the hysteretic response, see subsection 3.3.4. The contact calculation between the rubber block and the rough surface on $\partial_c\mathcal{B}_t$ is based on the derived equations of chapters 3, 4 and the finite element formulation provided in chapter 5.

The applied boundary conditions are motivated by the explained multiscale setup, a constant pressure p is applied on the top of the rubber block at $\partial_t\mathcal{B}_t$ distributed to equivalent nodal forces by the finite element software. Before the pressure is applied a first simulation step is calculated with a constant displacement $\bar{u}$ on $\partial_t\mathcal{B}_t$ in order to establish a very small contact area between the rubber block and the rough surface. After the initial contact step and the compression phase, in which the pressure is applied in a certain time interval t_p, a dragging or sliding phase is started keeping the pressure constant on the upper part of the body, cf. TEMIZER & WRIGGERS (2008), DE LORENZIS & WRIGGERS (2013) or WAGNER ET AL. (2015). The dragging velocity v is applied on the same edge like the pressure $\partial_t\mathcal{B}_t$ indicated by an arrow in figure 6.2 a). It has to be remarked that the z-displacements of the element nodes of the upper edge $\partial_t\mathcal{B}_t$ are linked following WAGNER ET AL. (2015). This procedure is motivated by more stable simulations for this setup without remarkable differences in the later evaluated coefficient of friction.

As already mentioned, periodic microscopic surface samples are used for the introduced multiscale method. This setup has to be completed by periodic boundary conditions on the outer left boundary $\partial_l\mathcal{B}_t$ and the outer right boundary $\partial_r\mathcal{B}_t$ of the rubber block, see figure 6.2 a), by the following conditions

$$\boldsymbol{x}_r - \boldsymbol{x}_l = \boldsymbol{X}_r - \boldsymbol{X}_l, \quad \boldsymbol{t}_r = -\boldsymbol{t}_l \quad on\ \partial_l\mathcal{B}_t \cup \partial_r\mathcal{B}_t, \tag{6.5}$$

ensuring periodicity of the position vector $\boldsymbol{x}$ and anti-periodicity of the tractions $\boldsymbol{t}$. The position vector in the initial configuration is given by $\boldsymbol{X}$.

After a solution is obtained, see for example the displacement in z-direction in figure 6.2 a), the total reaction forces are evaluated with the described microscopic setup. This step is performed by evaluating the reaction forces on top of the rubber block, see WAGNER ET AL. (2015). Afterwards, the time dependent coefficient of friction originating from hysteretic and interlocking effects is calculated using equation (6.2) and transferred to a homogenized coefficient of friction $\mu_{avg.}$.

The homogenized solution depends on several parameters like homogenization interval Δt, compression time t_p, finite element mesh and discretization level, block dimensions and further aspects. Discretization studies are for example discussed in de Lorenzis & Wriggers (2013) and Wagner et al. (2015). The rubber block height is set equal to the block length throughout this work, avoiding a free parameter. Additionally, the surface wavelengths are in contrast to approaches with sinusoidal functions (Wriggers & Reinelt (2009); de Lorenzis & Wriggers (2013)) not freely chosen and therefore also excluded from an intensive analysis. Nevertheless, the homogenization time (indicated in figure 6.2 b)) is identified as an important parameter in Wagner et al. (2015) due to an insufficient separation of time and length scales for the studied examples. Thus, this effect is discussed in the next subsection in a numerical validation study. The importance of the compression time is already mentioned and explained in section 6.1. Following de Lorenzis & Wriggers (2013), this parameter is adopted manually for different global simulation parameters throughout this work, avoiding large oscillations of the frictional response, see for example figure 6.2 b).

Next to the homogenization procedure, a micro friction law can be constructed with the calculated microscopic coefficients of friction used as a raw data field. In order to circumvent a special shape of the friction law like proposed in Wriggers & Reinelt (2009), that may fail for different surfaces or rubber materials, a spline surface with piecewise polynomial functions is fitted to the generated raw data

$$\mu(p, v) = \sum_{i=1}^{n_p} \sum_{j=1}^{n_v} c_{ij} \cdot (p - \xi_p)^{n_p - i} \cdot (v - \xi_v)^{n_v - j}. \tag{6.6}$$

The spline coefficients c_{ij}, break points ξ_p, ξ_v and spline dimensions n_p, n_v are determined within the software MATLAB. The smoothness of the spline surface provides good properties for the linearization within a mortar contact element, see Wagner et al. (2015) and equations (B.7)-(B.9) in appendix B.

6.2.3 Numerical Validation

The ability to solve complex contact interactions with the proposed multiscale method as well as the performance of the method is demonstrated for a simple test case with

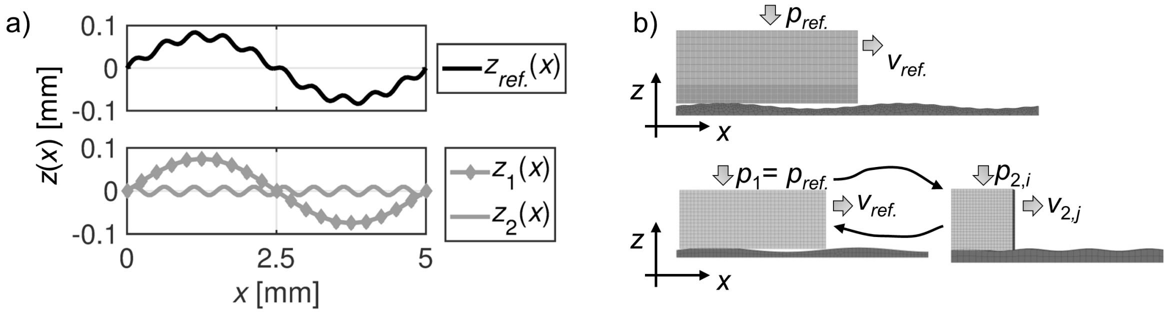

Figure 6.3: a) Surface profiles for reference setup and multiscale setup, b) reference setup (top) and multiscale setup (bottom) with $p_{ref.} = 0.3$MPa, $v_{ref.} = 500$mm/s.

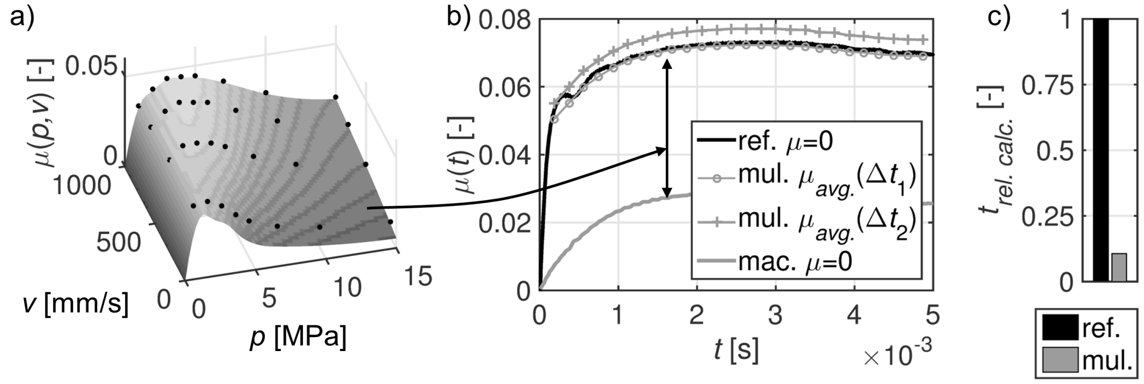

Figure 6.4: a) Microscopic friction law, black dots indicate raw data. b) Coefficient of friction for reference setup and multiscale setup. c) Relative calculation time for reference and multiscale setup.

sinusoidal functions, cf. Wagner et al. (2015). The framework described in the last subsections is implemented in the finite element software FEAP. The available three-dimensional code is reduced to a quasi-two-dimensional setup by linking the nodes of one used element in y-direction to each other in the x-z-plane. A deformation-based finite linear viscoelastic material model is used for the rubber samples (see subsection 3.3.4) within the described continuum finite element framework of 5.2. The rough surface is modelled with a linear elastic material model and fixed elements at the bottom of the body, since almost no deformations are expected for the rough surface. The reader is referred to Wagner et al. (2015) for all material parameters. Within FEAP the described mortar contact element (cf. section 5.3) is used to solve the mechanical contact interaction of the two deformable bodies.

An artificial reference problem represented by the summation of two defined sinusoidal functions is constructed

$$z_{ref.}(x) = z_1(x) + z_2(x), \tag{6.7}$$

$$z_1(x) = 0.075 \sin(2\pi/5x), \quad z_2(x) = 0.01 \sin(2\pi/0.5x). \tag{6.8}$$

Furthermore, a multiscale setup consisting of a macroscopic simulation on $z_1(x)$ and a microscopic simulation on $z_2(x)$ are conducted, see figure 6.3. In a first step, a micro friction law on the microscopic setup is calculated, following the procedure of the previous subsections, see figure 6.4. Further on, the resulting friction law is inserted into a macroscopic calculation and the resulting global coefficient of friction is compared to the reference solution.

This simple test case reveals that the multiscale result (mul.) approaches the reference solution (ref.), see figure 6.4 b), by reducing the calculation time drastically, see figure 6.4 c). The reference solution is approached, if the starting process of the microscopic rubber block is included in the homogenization step, see figure 6.4 b). The exemplary outcome of different homogenization times ($\mu_{avg.}(\Delta t_1)$, $\mu_{avg.}(\Delta t_2)$) is demonstrated in figure 6.2 b). The surface scales and time scales for macroscopic and microscopic interactions are not fully separated in this test case and the reference solution contains microscopic run-in effects that are neglected by homogenization of the stationary response $\mu_{avg.}(\Delta t_2)$. Therefore, the homogenization time is chosen as $\Delta t_1 = 0.75 \cdot 10^{-3}$s (equals 1.5 wavelenghts of the surface profile) in order to include these run-in effects.

6.3 Extension to Rough Road Surfaces

This section provides an overview of surface descriptions and decomposition techniques for real rough road surfaces, being necessary for numerical multiscale frameworks. In order to incorporate rough road surfaces with non-separated length scales and arbitrary shape, the introduced multiscale framework of the last section is extended and certain steps of the framework are modified. Finally, details regarding implementation and automation of the multiscale method are explained in the last subsection.

6.3.1 Surface Description

The incorporation of a real rough road surface into multiscale approaches can be performed by different approximations. Reconstructions based on HDC functions and all resulting difficulties are mentioned and discussed in section 6.1.
In order to avoid the problematic reconstruction by sinusoidal functions, see approach 1) in figure 6.5, a new method is proposed in Wagner et al. (2015). It is based on a reconstruction using a PSD function $C_{PSD}(q)$, see subsection 2.3.1, and generates rough surface profiles for all considered scales. First of all, equally to the HDC-based approach, a rough surface measurement is performed and then transformed into a PSD function of the measured rough surface (step 2a in figure 6.5). In step 2b, the rough surface is reconstructed by a sum over a large number of sinusoidal functions i

$$z(x) = \sum_{i=1}^{N} 2\sqrt{\frac{2\pi}{X} C_{PSD}(q_i)} \sin(q_i x + \phi_i), \tag{6.9}$$

with a random shift angle ϕ_i and the largest wavelength X. Based on the derived equations in Persson et al. (2005), this procedure is used in Wagner et al. (2015) to reconstruct a real rough road surface. Furthermore, the reconstructed surface can be split into macroscopic and microscopic parts by dividing the introduced sum at a certain split frequency. In figure 6.5 (approach 2) a PSD function and the corresponding macroscopic and microscopic surface parts are displayed, see Wagner et al. (2015). A continuous spectrum is used and a problematic choice of certain frequencies for each scale is avoided, revealing a benefit in contrast to HDC-based approaches. Afterwards, representative cutouts of the reproduced surface parts are chosen, exhibiting directly periodic structure due to the reconstruction procedure. Nevertheless, the choice of a representative cutout reveals a drawback of the PSD-based reconstruction because it is very difficult to define a scientific criterion for an adequate choice. Therefore, in the following subsection 6.3.2 an extension of the multiscale approach is proposed, avoiding this difficulty.

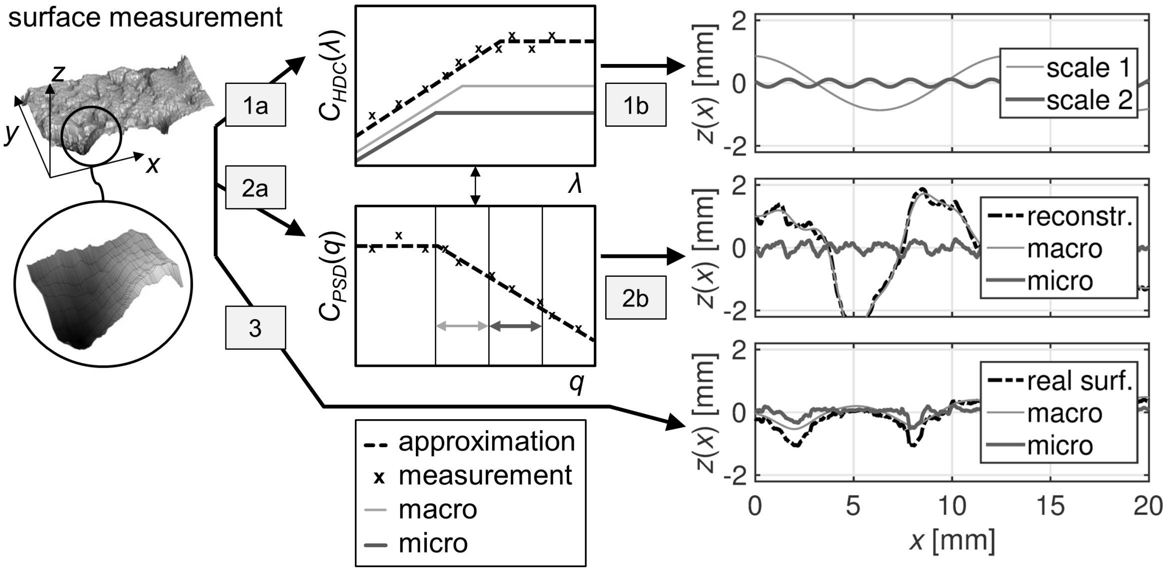

Figure 6.5: Three approaches for processing and decomposition of a rough surface measurement: 1) HDC-based approximation, 2) PSD-based reconstruction, 3) Direct filtering of the rough surface.

Another drawback of the PSD-based approach is the introduction of the random phase shift angle ϕ_i, leading to a loss of surface characteristics. This is illustrated in figure 6.5 by displaying the real rough surface profile in approach 3. Unfortunately, the reconstruction of the same rough surface in step 2b overestimates for example the amplitude of the surface profile. Furthermore, the reconstructed shape is also quite different compared to the measurement.

Thus, this work proposes, following Wagner et al. (2017), to use the rough surface measurement directly for setting up the multiscale method without loss of any surface characteristics and without any transformation or reconstruction, see figure 6.5 with approach 3. The necessary decomposition of the rough surface measurement for applying a multiscale setup is performed by the use of band-pass filters. A two-scale problem can be for example defined by three wavelengths $\lambda_{max}, \lambda_{split}, \lambda_{min}$ and two band-pass

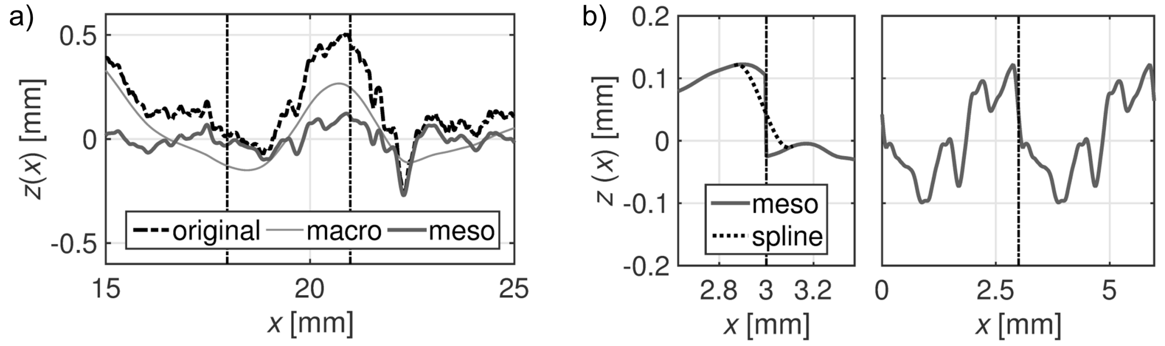

Figure 6.6: a) Choice of mesoscopic cutout for the construction of a representative finite element setup. b) Manipulation of the cutout to ensure a periodic surface sample by using a connecting spline.

filters $\mathcal{F}$, one defining the macroscopic surface and the other the microscopic surface part

$$\mathcal{F}_{macro}(\lambda_{max} - \lambda_{split}), \quad \mathcal{F}_{micro}(\lambda_{split} - \lambda_{min}). \tag{6.10}$$

By choosing the same split wavelength λ_{split} for both filters, a continuous spectrum is ensured and the surface characteristics are captured by this approach. Similar to the PSD-based approach, cutouts of the rough surface have to be chosen to construct numerical setups for microscopic scales. This leads to the same difficulties regarding the choice of a representative surface part for the whole rough surface structure. Therefore, an extension to include surface statistics is presented in the next subsection 6.3.2. Additionally, no periodicity is achieved for chosen surface parts, if the rough surface is used directly, see for instance the mesoscopic surface part in figure 6.6 a). Therefore, chosen surface samples are manipulated at the ends by introducing a smooth spline function that enforces a periodic surface sample because it represents a cutout of a long rough surface profile, cf. figure 6.6 b).

It has to be remarked that all proposed surface decompositions (HDC, PSD, filtering) violate the assumption of scale separation since no significant offset between the scales is applied. Furthermore, the approaches in Wriggers & Reinelt (2009) and Wagner et al. (2015) (cf. section 6.2) introduce a certain amount of scale separation, since the sinusoidal and rough surface profiles for the scales differ significantly in amplitude. Thus, the contact homogenization of section 6.2 is applied revealing that the methodology works in principle. Nevertheless, the assumptions of scale separation are not completely fulfilled. Therefore, a way to adopt the multiscale approach of the last section is discussed in the next subsection 6.3.2.

6.3.2 Multiscale Framework

Dealing with real rough road surfaces, a few critical points of the multiscale framework for separated length scales of section 6.2 are encountered. First of all, the choice of a representative cutout for macroscopic and microscopic surface scales is rather problematic since a real rough surface consists of profiles fluctuating in amplitude and frequency, cf. figure 6.5. Hence, an adequate choice of a single profile representing all rough surface characteristics of the considered scale remains a very challenging task and no profound criteria are defined in literature. In order to circumvent this problem, a certain number of surface profiles is introduced in Wagner et al. (2017), enhancing the multiscale framework with surface characteristics on each scale, see step A) in figure 6.7. In principle, a different number of surface samples k and j can be used to determine pressure values for the microscopic scale (k) and microscopic coefficients of friction for the upscaling part (j). How to proceed with the additional information of a few surface samples is discussed after a modification of the multiscale contact homogenization approach is introduced.

The assumption of scale separation fails for the complex contact problem at hand, including real rough road surfaces. Road surfaces are self-affine and rough over many length scales including a continuous spectrum, see subsection 2.3.1 and subsection 6.3.1.

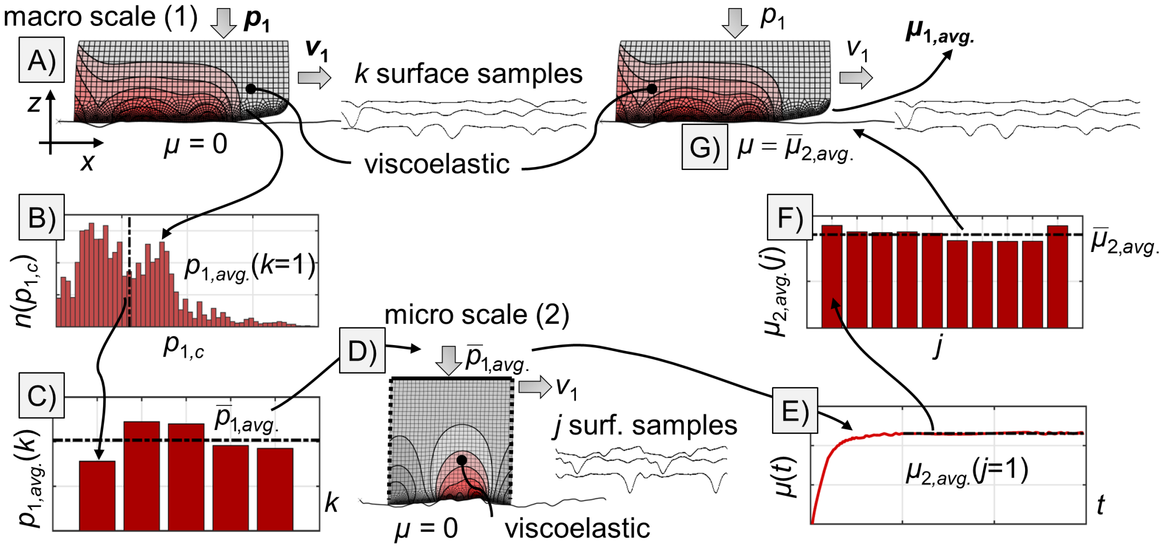

Figure 6.7: Modified multiscale approach with a certain number of surface samples and expanded averaging between the scales.

Thus, scale separation could only be enforced for rough road surfaces by neglecting intermediate scales and fulfilling for that reason equation (6.1). Since the contribution of intermediate scales is very essential for the final result of rubber friction problems (see Persson (2001)), the smallest wavelength of the macroscopic length scale is automatically the largest surface wavelength of the microscopic length scale, comparable to the PSD-based decomposition in Wagner et al. (2015). Consequently, the choice of local contact pressures as constant input parameters for the smaller scale becomes inadequate. Moreover, a fluctuating pressure field motivated from the macroscopic contact pressures would be an accurate boundary condition for the microscopic scale. Avoiding a complex procedure with fluctuating boundary conditions, an averaged contact pressure is introduced in Falk et al. (2016) or Wagner et al. (2017) representing the characteristics of the macroscopic pressure field, see step B) in figure 6.7. This averaged contact pressure $p_{1,avg.}(k)$ is determined by using all (n_c) local macroscopic contact pressures $p_{1,c,i}$ of all time steps and for each introduced surface profile k

$$p_{1,avg.}(k) = \frac{\sum\limits_{i=1}^{n_c} \left(\int\limits_{A_{1,c,i}} p_{1,c,i}(k)\,\mathrm{d}a \right)}{\sum\limits_{i=1}^{n_c} A_{1,c,i}} = \frac{1}{n_c} \cdot \sum_{i=1}^{n_c} p_{1,c,i}(k). \tag{6.11}$$

The element contact area surrounding each contact node is given as $A_{1,c,i}$ and the evaluation can be simplified for meshes with equidistant nodes (see second part of the equation (6.11)). Accordingly to this procedure, high and low pressure values are excluded from the analysis introducing a simplification. Due to the fact that these pressures occur with less frequency (see figure 6.7 B)) and the mean pressure value is used rather often in a multiscale procedure (cf. contact pressure histogram in Wagner

ET AL. (2015)), the approach provides an acceptable approximation. Moreover, it has to be remarked that for pressure values around the mean pressure $p_{1,avg.}(k)$ the gained coefficient of friction behaves nearly constant in a certain range (comparable to the peak plateau in figure 6.1) and therefore more calculations in order to gain the mean pressure value could not enhance the result. Therefore, the number of surface samples (k) for pressure evaluation can be reduced for the proposed multiscale setup compared to the number of surface samples j for the evaluation of the coefficient of friction $(k < j)$.

In a next step, the dependency of the surface profiles is removed by averaging, see step C) in figure 6.7,

$$\bar{p}_{avg.} = \frac{1}{n_k} \sum_{k=1}^{n_k} p_{avg.}(k). \tag{6.12}$$

As a consequence, a defined pressure value is transferred as a constant pressure boundary condition on the microscopic scale. Following this procedure, the computational costs are reduced in comparison to the approach calculating the microscopic setup for various pressure and velocity values (see section 6.2). In addition and based on the fact that only the stationary response is considered in this work, a full slip condition for the microscopic scale is assumed revealing the possibility to apply only the considered macroscopic velocity v_1 on the microscopic scale. Consequently, this procedure is an adequate way to reduce the computational effort once again. Only the global velocities of interest are calculated with the whole setup.

The calculated microscopic coefficients of friction are homogenized $\mu_{avg.}(j)$ in step E) following the already explained homogenization technique. Comparable to the approach for the resulting pressures, the same averaging operation over all calculated surface samples j is executed in step F)

$$\bar{\mu}_{avg.} = \frac{1}{n_j} \sum_{j=1}^{n_j} \mu_{avg.}(j). \tag{6.13}$$

Due to this step, the incorporation of the homogenized microscopic friction response simplifies, in contrast to section 6.2, to a setting of the macroscopic coefficient of friction to $\bar{\mu}_{avg.}$, see step G) in figure 6.7.

The proposed multiscale method is extended by the incorporation of more than two length scales, cf. WAGNER ET AL. (2017). It is necessary to expand the approach for a treatment of rubber friction on rough road surfaces (centimeter to micrometer length scale) since a division into only two scales would lead to immense calculation times for each scale. Each scale would involve a lot of surface details and the necessary finite element meshes to resolve the rough surface would introduce a lot of degrees of freedom and a large active set of contact points. Hence, the approach is expanded to more length scales with less details for each scale leading to acceptable calculation times. Therefore, equation (6.10) is adopted to more than two scales by introducing further splitting wavelengths $\lambda_{split,i}$ between the upper and lower limit $\lambda_{max}, \lambda_{min}$,

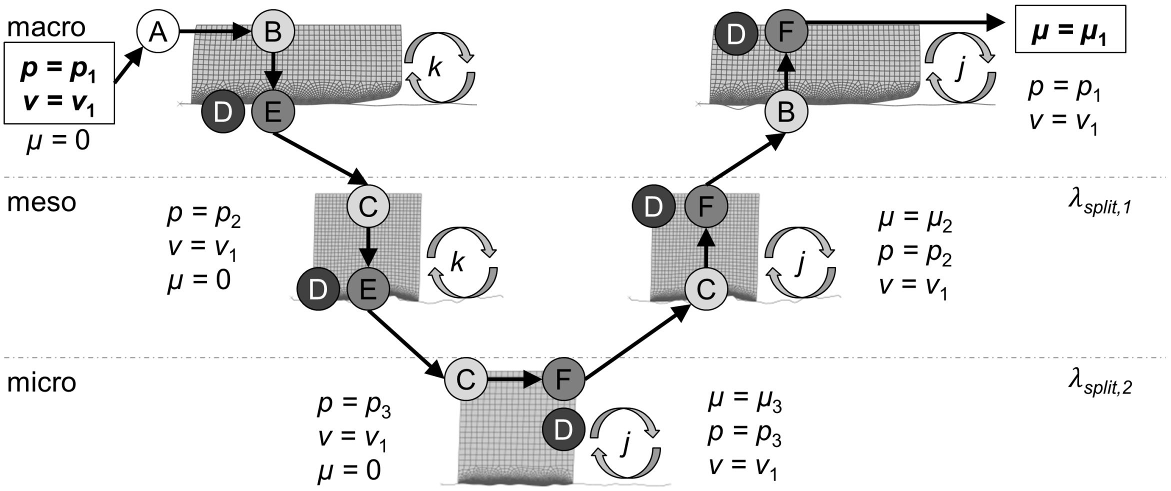

Figure 6.8: Exemplary expanded multiscale setup to three scales. Capital letters belong to the automation process and are explained in subsection 6.3.3

$$\mathcal{F}_{macro}(\lambda_{max} - \lambda_{split,1}), \quad \mathcal{F}_{meso}(\lambda_{split,1} - \lambda_{split,2}) \quad \ldots \quad \mathcal{F}_{micro}(\lambda_{split,n-1} - \lambda_{min}), \qquad (6.14)$$

introducing for example a mesoscopic length scale ($meso$) between $\lambda_{split,1}$ and $\lambda_{split,2}$. Further scales are indicated by dots (...) and for n possible scales a total number of $n-1$ splitting wavelengths would be introduced. Based on the description in subsection 6.3.1, the decomposing band-pass filters $\mathcal{F}$ are used between the defined wavelengths, ensuring that no surface wavelengths are neglected and a continuous spectrum is calculated.

An exemplary decomposition in three scales with an intermediate mesoscopic length scale (meso) is shown in figure 6.8. All passed quantities between the scales represent averaged values (subscripts are excluded in the figure) and the loops for averaging pressures and coefficients of friction are indicated by arrows. The capital letters A-F are introduced to describe the automated ABAQUS-script and all necessary subroutines in the next subsection. In principle, the setup is extended by introducing further pressure and friction homogenization steps starting with a frictionless branch that is used to downscale the pressure. Afterwards, the gained coefficient of friction is upscaled from the smallest length scale to the largest scale following the procedure described above.

6.3.3 Implementation and Automation

The introduced multiscale method offers large potential for automation, because a lot of finite element calculations and repeating operations have to be started deriving the simulation parameters from a global input. For this reason, an automated version of the multiscale setup is developed in the software package ABAQUS using Python-scripts, see SIMULIA (2014b) for an introduction. ABAQUS offers with the possibility to use Python-scripts for preprocessing and postprocessing an advantageously environment for the implementation of the extended multiscale method. All necessary modules for the modelling of hysteretic rubber friction that were implemented in FEAP (see last section 6.2) are also available in ABAQUS.

The main differences between FEAP and ABAQUS elements are explained and henceforth ABAQUS is used for all calculations in this work. The elements are based accordingly to the FEAP elements on the described continuum and contact mechanical background and the introduced finite element methodology of chapters 3, 4 and 5. Nevertheless, some small differences exist. Therefore, a brief overview on the most important features and chosen settings for the elements and differences to FEAP elements are provided.

In contrast to reduced three-dimensional elements in FEAP, two dimensional plane strain elements are used within ABAQUS. The hyperelastic material response is modelled by a MOONEY-RIVLIN material and a stress based finite linear viscoelastic material model, see subsection 3.3.4. In order to avoid volume locking, quadrilateral four node hybrid elements based on a Q1P0 formulation are used for the rubber material, see subsection 3.3.3. The formulation is based on linear shape functions for the displacement and constant shape function for the element pressure. Within ABAQUS, two different contact formulations can be chosen: node to surface (NTS) or surface to surface (STS) contact elements. As already mentioned in section 5.3, NTS contact elements are less stable in the context of large sliding distances and large deformations in the contact zone. Additionally, the contact patch test is not passed by NTS elements and the calculated contact pressure values may be less accurate, see SIMULIA (2014a). As a consequence and to ensure stable simulations, the STS contact element is chosen for the multiscale calculations. Nevertheless, aborting simulations with a bad convergence rate are checked and are sometimes recalculated by applying the NTS contact formulation or automatic stabilization. Furthermore, calculations with NTS-elements are less time consuming since the integration procedure for the contact area is less expensive. In order to reduce the calculation time, the rough counter surface is modelled by linear one-dimensional rigid elements within ABAQUS.

Before an automated script is executed (master script in figure 6.9), all global parameters m are defined, for example the used surface(s), the rubber compound(s), macroscopic pressure and velocity values. The number of scales n and the amount of surface samples k/j for the downpassing and uppassing branch of the multiscale framework are also defined in advance. Both quantities present important input parameters for the whole framework. Especially the number of surface samples used for the homogenization procedure is an important free parameter and thus addressed in subsection 6.4.2 in more detail. Further explanations regarding the choice of calculated scales are provided in section 6.5 with the experimental validation of the method. Prior to the automated script, also a scripted surface evaluation is performed that generates data files (*.csv files) for all chosen scales and surface samples from a rough surface measurement.

A short description of the automated multiscale framework and the executing master script is provided henceforward. First of all, the global parameters m are set, see script A) in figure 6.8 and figure 6.9. The work flow of the multiscale framework is extendable to different materials or velocities for example, indicated by the loop over m

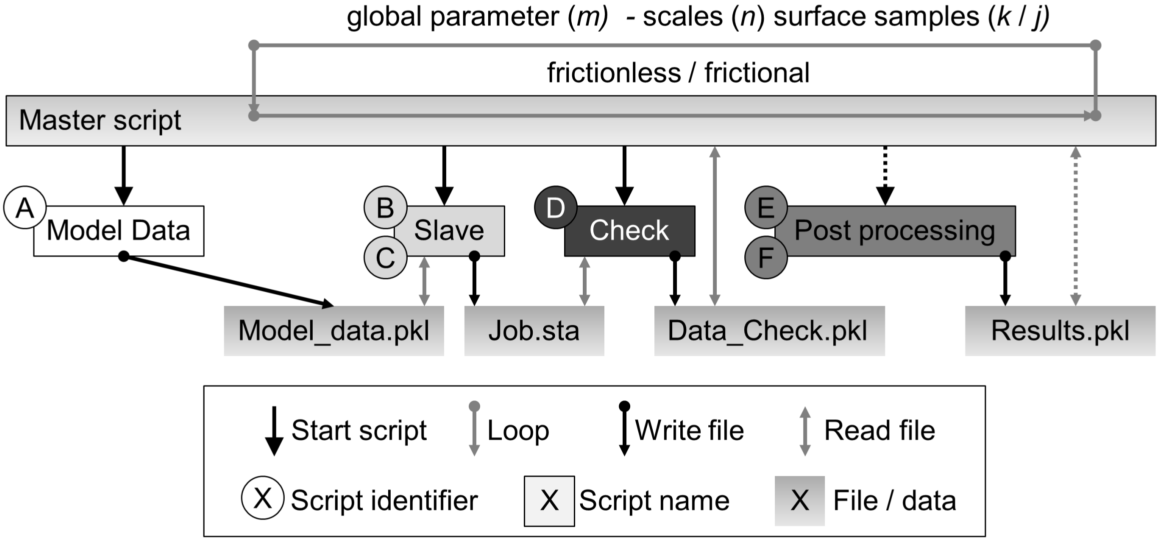

Figure 6.9: Workflow of automated multiscale framework using Python scripts within ABAQUS.

in figure 6.9. Further on, these parameters are saved globally by using a pickle format, see SIMULIA (2014b) for details, together with the geometrical information for the surface scales, hyperelastic and viscoelastic material parameters and some options for the simulation setups.

In a next step, this information is used and slave scripts for the macroscopic length scale (B) and all smaller length scales (C) are started from the master script. Since the boundary conditions (non-periodic or periodic) and the appearance of the leading edge differ for the macroscopic and all other smaller scales (cf. figure 6.8), separate scripts have to be used. Alongside with the saved global information, the generated surface data files are called within the slave scripts for the automated construction of finite element calculations with all necessary options and boundary conditions following the already given descriptions of the setups. The ABAQUS calculations are furthermore directly started from the slave scripts generating an output and statistic file (*.sta) with information about the performed time steps of the simulation. After the started simulation finished, the script D (check) inspects the number of performed time steps to see if enough time steps for a homogenization are available or if the simulation failed.

The post processing scripts are separated for the pressure evaluation (E) and homogenization of the coefficient of friction (F), see figure 6.8 and figure 6.9. Based on the information saved in the data-check pickle (failed or successful calculation) the post-processing is started (saving the results in the results pickle) or skipped (possible skipping is indicated by dotted lines in figure 6.9). This step is included to ensure that the whole framework is able to continue, if single calculations fail. The master script performs later on the averaging over surface samples, the processing to the next scale and the transition from the frictionless to the frictional branch of the multiscale framework, compare subsection 6.3.2. Finally, the global results are saved in *.csv-files.

6.4 Single Scale Numerical Studies

In a first step, the ability of the introduced surface processing to capture surface anisotropy is demonstrated on the basis of a single scale macroscopic calculation. Furthermore, two important micromechanical aspects with impact on the homogenization result are investigated in detail. First, a large number of microscopic rough surface samples is calculated, providing conclusions for the choice of surface samples within the multiscale framework. Second, a three-dimensional calculation on a rough surface is compared to two-dimensional calculations on profiles from the same surface substrate.

6.4.1 Anisotropy on Macroscopic Rough Surfaces

An interesting property of the introduced direct modelling of rough surfaces is that surface anisotropy can be modelled and predicted. The described analytical approaches of subsection 2.3.2 would use the same PSD function for a mirrored surface profile and predict hence the same coefficient of friction for both profiles. A modified analytical approach that is able to capture the results of friction measurements for different sliding directions is introduced in Carbone et al. (2009).

A simple macroscopic test case with two mirrored sawtooth profiles for the counter surface and an introduced initial coefficient of friction $\mu = 0.2$ is calculated, see figure 6.10. The first orientation is called smooth profile and the second orientation (lower profile in figure 6.10 a)) is named sharp profile. The names of the profiles are directly attributed to the expected and calculated hysteretic response. In figure 6.11 the resulting coefficient of friction over time for both profiles, and the time averaged response, as well as the relative difference for the generated coefficient of friction are presented. As already mentioned, this work does not differentiate between hysteretic and interlocking phenomena and therefore the generated coefficient of friction evaluated by the reaction forces contains both effects. The sharp sawtooth profile reveals an approximately 40% larger generated coefficient of friction revealing how large the influence of surface anisotropy might be. Another interesting fact is that two geometrical effects can be distinguished by numerical simulations. First, a large interlocking peak in figure 6.10 a) is caused by the impact of the leading edge of the rubber block on the rough surface. The second effect that can be detected is a higher coefficient of friction over the remaining time interval, excluding an interlocking peak for the smooth profile. Concluding, this

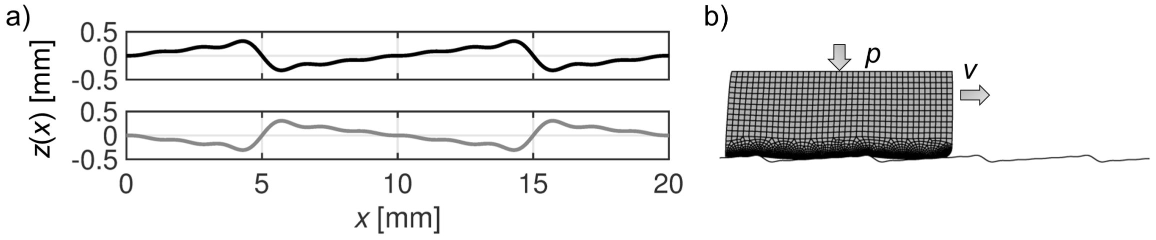

Figure 6.10: a) Smooth profile (top) and sharp profile (bottom), b) exemplary finite element setup for smooth profile with parameters p =0.3 MPa, v =0.5m/s, height h = 8mm, length l =20mm, applied μ=0.2 and material m2 (see appendix C for the used material parameter).

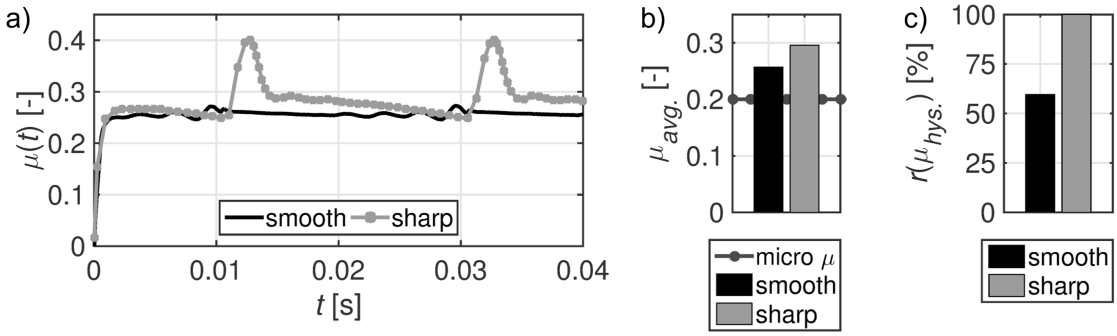

Figure 6.11: a) Coefficient of friction over time, b) averaged coefficient of fricion, c) relative difference of generated coefficient of friction.

means that also during sliding without leading edge impacts, a higher frictional force is generated for the sharp profile. Surface anisotropy might therefore be an important effect on all scales, see Stupkiewicz et al. (2014) for a microscopic numerical study, and the proposed rough surface treatment incorporates this effect directly. In Tiwari et al. (2016), also an anisotropy in the frictional response is observed introduced by changing the sliding direction of a preconditioned rubber sample after each sliding experiment. This effect arises from the conditioned profile of the macroscopic rubber sample and is not modelled in this work, although it would be in principle possible to capture this effect by introducing different sliding directions and the rubber profiles in the simulation.

6.4.2 Microscopic Rough Surface Statistics

The smallest length scale of the later calculated multiscale setup is chosen for this study, because large fluctuations in frequency and amplitude of the rough surface samples are expected on this scale, cf. Wagner et al. (2017). A microscopic rough surface measurement is filtered between the measurement resolution of $\lambda_{min} = 0.003$mm and the size of a microscopic rubber block with a length of $l = 0.04$mm. Thus, the upper cutoff of the band-pass filter is set to $\lambda_l = 0.04$mm. Afterwards, three hundred different cutouts are chosen and periodicity is enforced by the procedure described in subsection 6.3.1. Finite element setups are created with all surface samples choosing the same settings for the microscopic rubber block, for example a viscoelastic material and frictionless behaviour at the interface. An exemplary finite element setup and four further surface samples are displayed in figure 6.12. The microscopic input parameters are $p = 3$MPa, $v = 0.01$m/s.

As a result, the homogenized hysteretic coefficient of friction μ of 287 simulations is obtained since 13 calculations failed due to large element distortions. Nevertheless, the large amount of information is used to perform an analysis of two features: microscopic statistics with the frequency of occurrence $m(\mu)$ and convergence properties of surface sample average $\mu^k_{avg.}$ are studied.

The distribution of the microscopic coefficients of friction plotted for an increasing number of calculations n (cf. figure 6.13 a)) demonstrates that the overall result of the

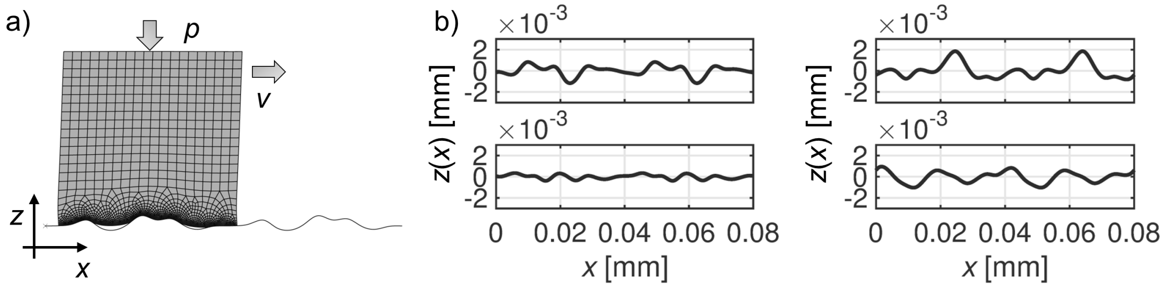

Figure 6.12: a) Exemplary finite element setup with $p = 3\text{MPa}$, $v = 0.01\text{m/s}$, $h = l = 0.04\text{mm}$, rubber compound A (cf. subsection 7.4 for all material parameters), $\mu = 0$. b) Four of three hundred surface representations.

microscopic scale approaches an asymmetric distribution. Consequently, by the use of a large amount of surface samples the complete statistical distribution is approximated. Despite this interesting property, it is not recommended to use such a large number of samples for each scale in a multiscale setup due to an immense resulting calculation time.

The calculated 287 coefficients of friction provide the basis for an evaluation of the averaged coefficient of friction. This quantity is analyzed, because the sample average is of high importance for the multiscale method. The coefficient of friction obtained from averaging over all results is used as the reference solution $\mu^{ref.}_{avg.}$ assuming that this value represents the rough surface response properly. Furthermore, different evaluation orders k with a random choice of the calculated surface samples are analyzed over an increasing number of surface samples n for the calculation of the average. For example for ten surface samples $n = 10$, the first or last ten results can be averaged providing different results. Since it is not known *a priori* which surface samples have to be

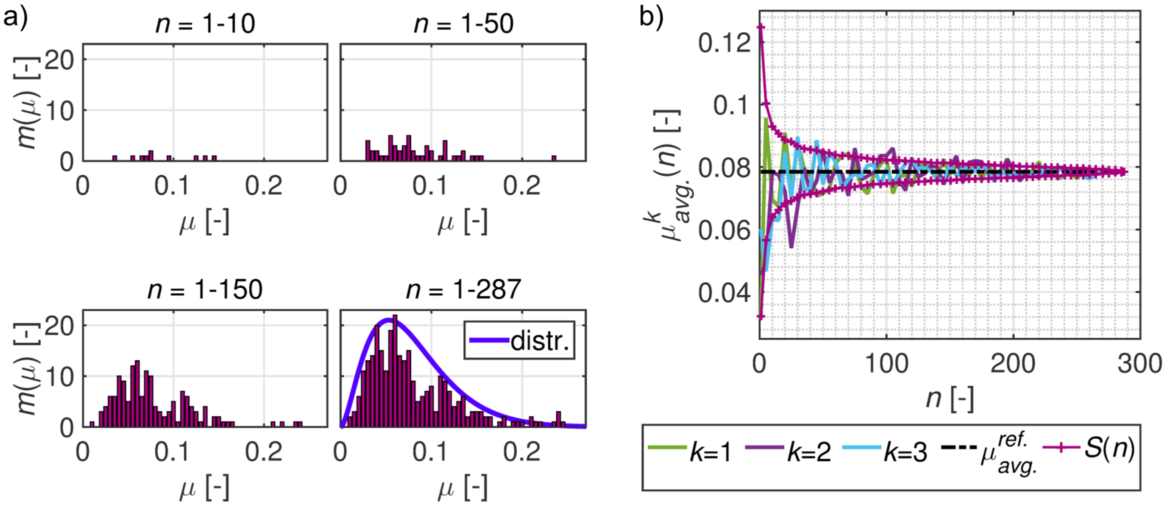

Figure 6.13: a) Frequency of occurrence $m(\mu)$ of calculated μ with increasing set of calculations. b) Averaged coefficient of friction over number of surface samples n for three random evaluation orders k. Standard deviation $S(n)$ is added for 1000 evaluation orders.

chosen, this procedure is applied. With an increasing surface sample number n the reference solution is approached in the limit case, since it is of less importance which surface samples are chosen for the evaluation. In figure 6.13 b) three random evaluation orders ($k = 1, k = 2, k = 3$), the reference value and a standard deviation value $S(n)$ are displayed. This standard deviation is gained by the evaluation of 1000 random evaluation orders k, providing an idea how fast the surface sample average decreases with arbitrary choice of microscopic surface samples n. In conclusion, the average over ten surface samples already causes a significant decrease of the standard deviation from $S(1) = +/-0.047$ down to $S(10) = +/-0.015$ and therefore the reliability of the homogenized result. This result is of course linked to the considered surface characteristics, input parameters and further details. Nevertheless, the number of ten surface samples is used in later performed calculations with the multiscale method since it allows for a good compromise between result quality and affordable calculation time.

6.4.3 Comparison of 2D and 3D Micromechanical Solutions

A comparison of two-dimensional (2D) and three-dimensional (3D) setups is executed in this subsection in order to quantify the difference with respect to the homogenized coefficient of friction and the calculation times. Since different surface cutouts are used on each scale within the multiscale setup, surface characteristics are already included. Nevertheless, the contact of a real rubber block with a rough surface remains a 3D problem and a reduction to a 2D setup introduces an error that is analyzed in this subsection. This remaining error is induced by different contact conditions and surface asperities that support certain rubber parts excluding meanwhile rough surface parts from the contact patch. These effects and also complicated deformation states are excluded from a 2D analysis causing a different frictional response.

The calculated 2D and 3D setups, their parameters and an exemplary solution are displayed in figure 6.14. All seventeen 3D surface profile lines l_y in 3D y-direction (distance between the lines $\Delta y = 0.01875$mm), that get into contact with the rubber block, are calculated also with a 2D setup. The same boundary conditions are applied accomplished by a non periodic setup in this case. The gained homogenized coefficients of friction for all lines l_y are displayed in figure 6.15 a).

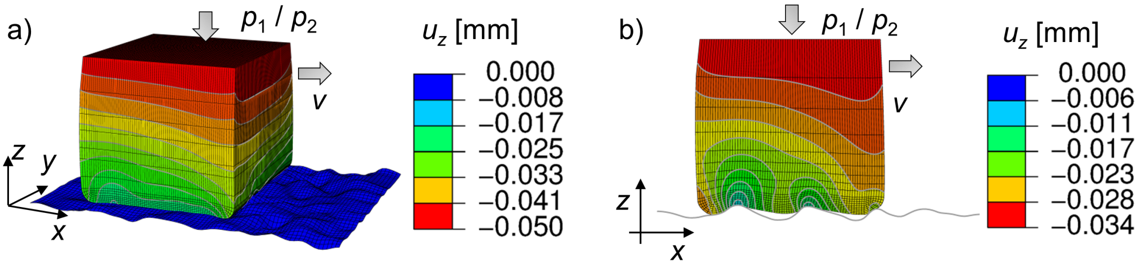

Figure 6.14: a) 3D setup, b) exemplary 2D setup with displacement solution in z-direction. Used parameters $v = 1$m/s, $p_1 = 0.3$MPa, $p_2 = 2$MPa, material m1 (see appendix C for all viscoelastic material parameters), $h = l = 0.3$mm, $\mu = 0$.

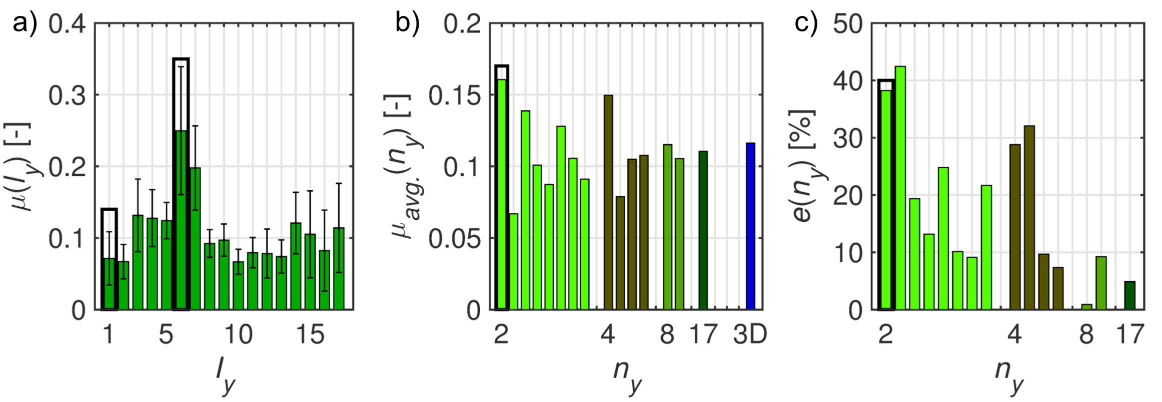

Figure 6.15: Results for $p_2 = 2\text{MPa}$. a) 2D coefficients of friction for lines l_y, b) combined averages $\mu_{avg.}(n_y)$ of n_y lines, c) relative error with respect to 3D solution for combined averages.

In a next step, random combinations of n_y lines are averaged and this procedure is repeated seven times for $n_y = 2$, four times for $n_y = 4$ and twice for $n_y = 8$. For example the first and sixth line (indicated by a black box in figure 6.15 a)) are averaged resulting in the first combined value $\mu_{avg.}(n_y)$ of figure 6.15 b). Afterwards, the relative error $e(n_y)$ of these combined line averages with respect to the 3D solution is calculated and displayed in figure 6.15 c). Depending on the choice of surface profiles for the combined average, the error to the 3D solution may become quite large. Especially, if only two lines are considered for the combined averaging procedure. Nevertheless, a decrease for an increasing number of averaged lines is detected.

The results for both applied pressure values are summarized in figure 6.16. In figure 6.16 a) the resulting contact areas are displayed. Obviously, the higher pressure causes a larger contact area and more profile lines get into contact with the rubber block. The results of figure 6.15 c) are averaged once again ($e_{avg.}(n_y)$) in order to derive a unique plot of the relative error for both pressure values, see figure 6.16 b). During the increase of averaged lines, the relative error decreases for both pressures. Nevertheless, the error becomes smaller for the larger pressure value p_2 approaching five percent

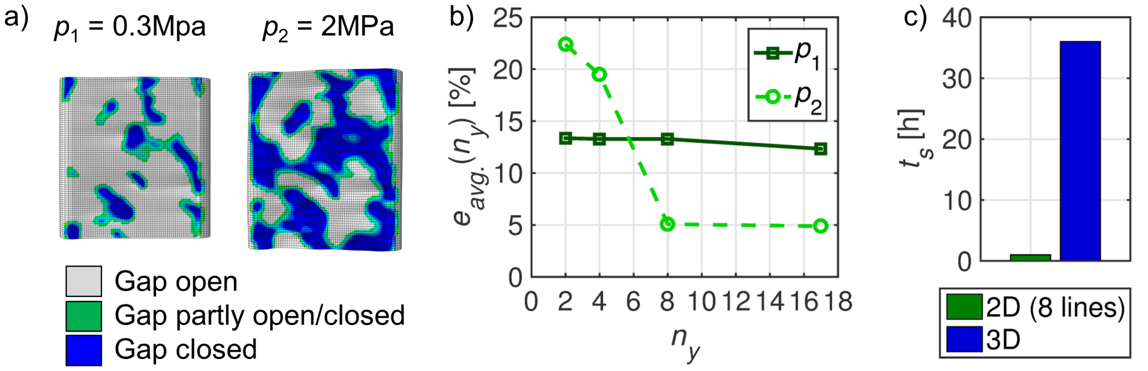

Figure 6.16: a) Rubber contact area with displayed gap for p_1 and p_2. b) Averaged relative error for different random choices of n_y random 2D lines. c) Calculation time for 8 lines in a 2D setup and the full 3D calculation.

deviation in the limit of averaging over all possible 17 lines. This fact can directly be linked to the larger contact area: for the small pressure p_1 some profiles are not in contact in the 3D setting, but come into contact for the 2D setting. In consequence, this leads to the incorporation of false values into the calculated average value for the 2D setup. Since the pressure value p_2 is in the range of used microscopic pressures within the multiscale method, the impact on the result is expected to be rather small, if enough surface lines are incorporated (this property was already investigated in the last subsection 6.4.2).

This conclusion is in accordance with the result of the micromechanical statistics of the last subsection. Moreover, the enforcement of periodic boundary conditions become very complicated for 3D setups, since the introduced manipulation with splines at the end of surface cutouts has to be performed in two dimensions (cf. 6.3.1). Additionally, the comparison of calculation times in figure 6.16 c) reveals the large effort that is enforced with 3D setups, making it rather difficult to use 3D setups in the proposed multiscale method. Therefore, all following studies are performed with two-dimensional setups.

6.5 Experimental Validation

In this section, the multiscale method for hysteretic friction of section 6.3 is validated with experiments on wet surfaces. Wet surface experiments are chosen because a partly suppressed adhesive contribution is assumed, see also chapter 7 for a detailed discussion. The focus of the section is to study the ability of the method to predict the influence of a global parameter change (velocity and pressure) on performances of different rubber compounds, cf. subsection 6.5.1. The differentiation between rough surfaces is investigated in subsection 6.5.2. Furthermore, the surface polishing effect (changing rough surface properties) is modelled with the introduced methodology, see subsection 6.5.3. Finally, exemplary interesting quantities gained by the multiscale method are displayed in subsection 6.5.4.

6.5.1 Material Comparison

The multiscale method needs two main experimental inputs for an appropriate modelling of hysteretic effects: a measurement of the rough surface used for the friction experiments and a measurement of the viscoelastic material properties of the considered rubber compounds. The rough surface is measured with two optical profilometers by the use of 3D scanning in this work. The first device measures the macroscopic details of the surface with a nominal lateral resolution of 0.019mm, see upper surface measurement in figure 6.17 a). Besides, the second device measures the microscopic details with a nominal lateral resolution of 0.003mm, see lower surface measurement in figure 6.17 a). Both measurements make it possible to include details of the rough surface in the multiscale analysis, i.e. from macroscopic asperities down to microscopic roughness.

The contact of the rubber block with the rough surface is assumed on the top asperities of the rough surface and therefore the upper parts of the rough surface measurement are evaluated for the choice of surface samples included later in the multiscale setup. Furthermore, two geometrical dimensions for the surface evaluation and the construction of the multiscale setup for the validation are determined by the executed friction experiments: based on the macroscopic dimensions of the rubber block (20mm x 8mm, see top of figure 6.17 c)) and the lowest captured surface detail with a resolution of 0.003mm, four scales are chosen for the construction of the multiscale setup.

Using four scales for the multiscale setup leads to the possibility to divide each surface measurement into two scales. Each measurement (coarse and fine resolution) is decomposed into two scales to keep the single calculation time of the finite element simulations in an acceptable range. Furthermore, using one scale for the macroscopic rough surface measurement and including all surface asperities, would result in approximately 1000 necessary contact elements on the rough surface, because the lowest wavelength of 0.2mm has to be resolved with at least a few elements. In addition, the rubber block represents the slave body in the contact algorithm. For this surface it is recommended to use at least twice more elements, leading to a lot of finite elements for the whole problem. Even in a two-dimensional setup, such a finite element calculation leads to enormous simulation times since a lot of sliding steps with an embedded contact search are performed during a single finite element analysis, see also subsection 6.2.2. A comparison of calculation times between a few fast solvable two-dimensional setups and a three-dimensional setup with a very high calculation time is given in subsection 6.4.3. Since a few surface samples have to be included in the multiscale analysis, a very large calculation time for single calculations increases the effort drastically. Therefore, four scales deliver a compromise between the increasing effort for the multiscale setup with

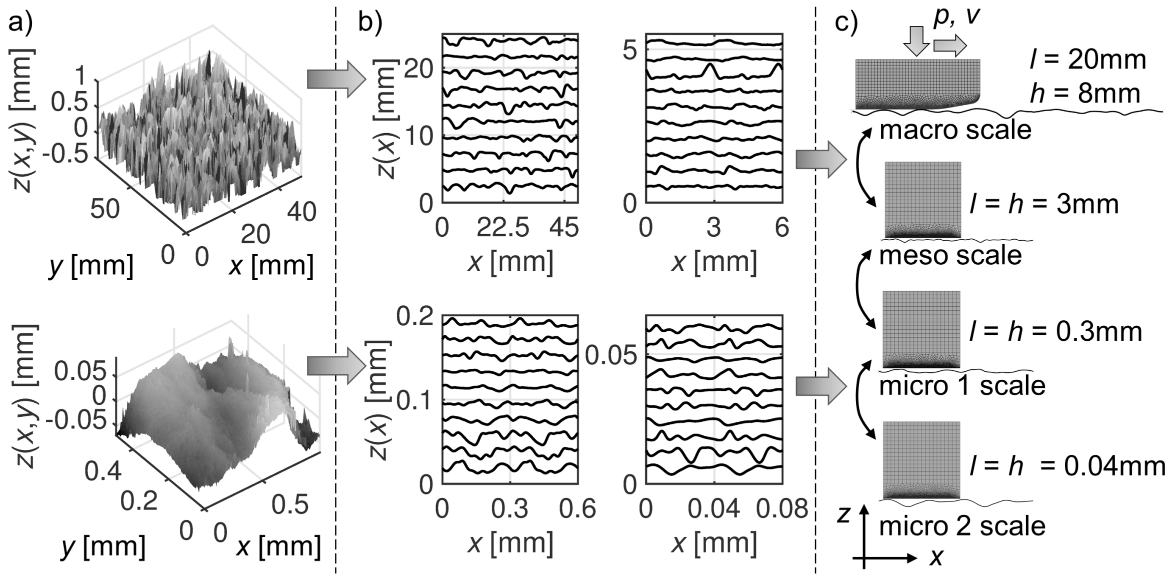

Figure 6.17: Surface 1: a) Macroscopic and microscopic surface measurements. b) Ten extracted surface samples on each scale for the construction of four scales. c) Four-scale setup with rubber block dimensions.

Table 6.1: Physical properties of rubber compounds c1-c6: filler amount f in parts per hundred rubber, shore hardness A h, glass transition temperature T_g, Mooney-Rivlin parameters C_{10}, C_{01}, D_1.

Comp.	f (Phr)	h (ShA)	T_g (°C)	C_{10} (MPa)	C_{01} (MPa)	D_1 (MPa)
c1	$f_0 + 35$	$h_0 + 10$	T_{g0}	0.136	0.518	0.031
c2	f_0	$h_0 + 10$	T_{g0}	0.246	0.489	0.027
c3	$f_0 + 35$	h_0	T_{g0}	0.174	0.309	0.042
c4	$f_0 + 35$	$h_0 + 10$	T_{g0} - 20	0.150	0.623	0.026
c5	f_0	$h_0 + 10$	T_{g0} - 20	0.327	0.613	0.021
c6	f_0	h_0	T_{g0}	0.219	0.318	0.038

an increasing number of scales and the decreasing calculation time of each single finite element setup, cf. calculation times for undivided scales and multiscale approach in subsection 6.2.3.

The second set parameter of the multiscale setup, the use of ten surface samples on each scale, is motivated by the study in subsection 6.4.2. This study provides a quantitative proof that the variance of the homogenized coefficient of friction is reduced if ten samples are used for averaging. The resulting and chosen surface samples for the two measurements are displayed in figure 6.17 b). Following subsection 6.3.1, band-pass filters are used to extract the wavelength ranges for all scales: for the macroscopic scale the range is 20mm-3mm, followed by 3mm-0.3mm for the mesoscopic scale. Furthermore, the two microscopic scales are defined as follows: The range of micro 1 scale is given by 0.3mm-0.04mm and micro 2 by 0.04mm-0.003mm. The chosen edge wavelengths and the scale names for the multiscale setup are displayed in figure 6.17 c). In general, a ratio around $r = 10 : 1$ between the block lengths of two following scales is chosen to provide the possibility to include microscopic details with an acceptable calculation time, cf. subsection 6.2.3.

Defined physical properties of different rubber compounds are investigated in this subsection: filler amount (f), hardness (h) and glass transition temperature (T_g) of six rubber compounds are varied around initial values f_0, h_0, T_{g0}. The values for all characteristics of the six rubber compounds are listed in table 6.1, see also IGNATYEV ET AL. (2015). Furthermore, MOONEY-RIVLIN parameters and PRONY parameters are necessary for the calculation using a viscoelastic material model in ABAQUS, see subsection 3.3.4. A preconditioned rubber sample is loaded with compression and tension providing the hysteretic response to which the MOONEY-RIVLIN parameters are fitted for each rubber compound, the resulting values are listed in table 6.1. Moreover, the viscoelastic material parameters are determined by a dynamic mechanical analysis (DMA), see subsection 3.3.1 for details. A prestrained rubber sample is exposed to a harmonically oscillating load with a small strain amplitude used to generate the frequency-dependent storage- and loss-modulus, i.e. $E'(\omega)$ and $E''(\omega)$. Following the description in subsection 3.3.1, the measured data in the temperature range of -40°C up to $+70$°C and the frequency range of 0.01Hz up to 50Hz are mastered for a large frequency range by the use of the time-temperature superposition principle, eliminating the temperature dependency (master temperature of $T = 20$°C). Afterwards, a fitting

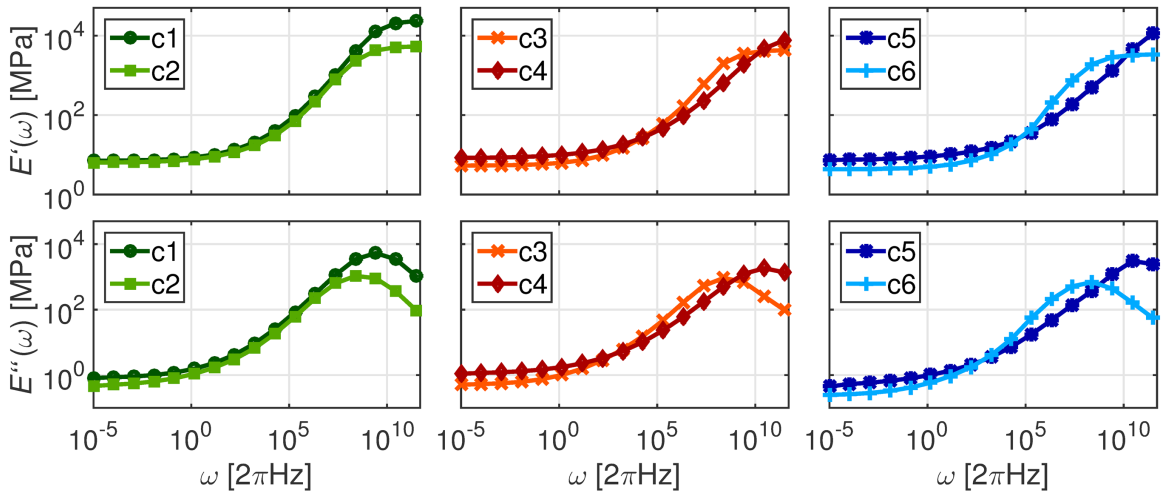

Figure 6.18: Storage- (upper part of figure) and loss-moduli (lower part of figure) for six different rubber compounds c1-c6.

is applied to adapt the moduli E_i and relaxation times τ_i of the MAXWELL elements in order to reproduce the measured curves of $E'(\omega)$ and $E''(\omega)$, displayed in figure 6.18 for all compounds.

A picture of the used experimental setup for the friction experiment is displayed in figure 2.2 a) accompanied by a description of the test rig in subsection 2.1.2. The macroscopic size of the rubber sample (20mm x 8mm) is already shown in figure 6.17, including a rounded front generated by a run-in procedure, see also subsection 2.1.2. All experiments are performed for a global temperature of $T_0 = 20°\text{C}$, velocities between $v = 0.1\text{m/s} - 3\text{m/s}$ and pressures between $p = 2\text{MPa} - 8\text{MPa}$ on a surface covered with water. Therefore, it is assumed that the adhesive contribution is partly suppressed and the frictional response is dominated by the hysteretic response, see also section 7.2. Furthermore, all experimental values of the coefficient of friction are gained by time averaging over the part of stationary sliding, see also figure 2.2 b). The simulated values are gained by the hysteretic multiscale setup of section 6.3 with the introduced four scales for the six materials.

First of all, a closer look on the velocity- and pressure-dependency of one exemplary rubber compound (c2) is provided in figure 6.19. In figure 6.19 a) an increasing trend over global velocity of the simulated coefficient of friction is revealed, whereas the experimental values decrease for increasing velocity. This incorrect reproduction of the global trend is attributed to the physical effects that are not considered in the multiscale simulation, mainly adhesive interactions and temperature effects. An adhesive contribution $\mu_A(v)$ could increase the global coefficient of friction especially for low velocities, cf. LORENZ ET AL. (2015). Additionally, for wet surfaces also a flash temperature effect (lower than for dry surfaces due to cooling) is expected. This temperature effect generates a lower frictional response, especially for large velocities. The direction of both effects (adhesion and temperature) are indicated in figure 6.19. Due to water filling the cavities of the rough surface and also in the large velocity range a viscous contribution of shearing a thin water film could influence the response.

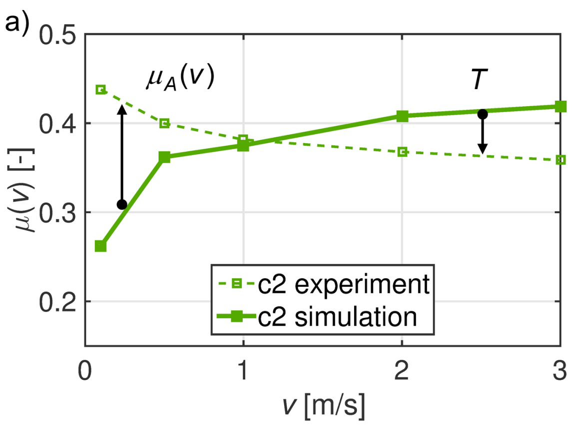

Figure 6.19: Experimental and simulated coefficient of friction for rubber compound c2. a) Macroscopic pressure $p = 0.3\text{MPa}$, b) velocity $v = 1\text{m/s}$.

For the pressure dependency, an increasing value is at least reproduced for the low pressure values, whereas the prediction does not reproduce the large pressure range correctly, see figure 6.19 b). This observation can again be attributed to the not considered adhesive contributions that would increase proportionally to the contact area the coefficient of friction, see chapter 7. Nevertheless, the gained simulated hysteretic results are used to compare different responses for materials with the above defined characteristics.

The first studied physical parameter is the glass transition temperature T_g of the rubber compounds that indicates at which temperature the material begins to behave softly and flexibly in contrast to a brittle and hard (therefore called glassy) behaviour beneath this temperature. A lower glass transition temperature is used for rubber compounds of winter tires since the material stays flexible in a larger range of cold temperatures. At room temperature (used in the friction experiments) a summer tire reveals a better frictional performance since the dissipation behaviour is optimal in a higher temperature range (higher T_g). The introduced rubber materials make it possible to study

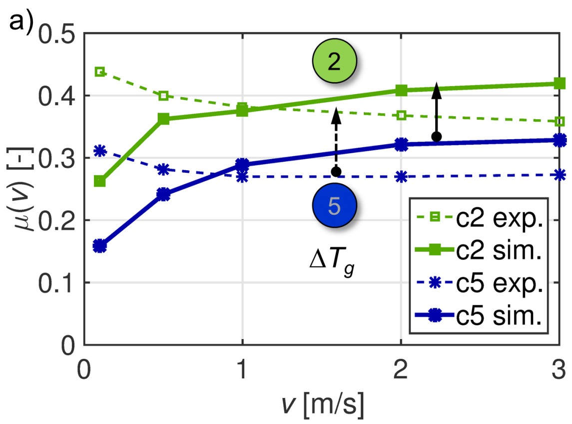

Figure 6.20: Comparison of compound pairs over velocity with different glass transition temperature (T_g) for a) low filler level and b) high filler level. Global pressure $p = 0.3\text{MPa}$.

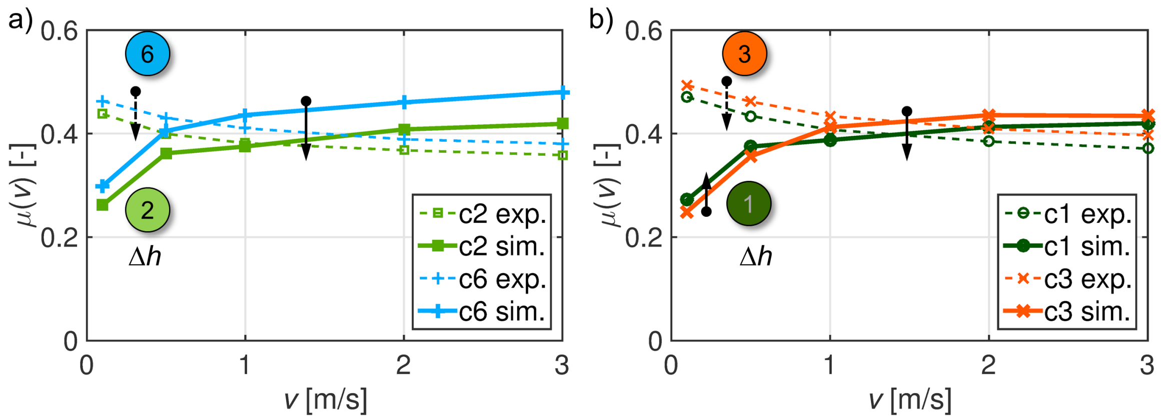

Figure 6.21: Comparison of compound pairs over velocity with different hardness (h) and same high T_{g0} for a) low filler level and b) high filler level. Global pressure $p = 0.3$MPa.

this effect for two material combinations, one at a low (c5-c2) and the other at a high filler level (c4-c1), both with the same hardness $h_0 + \Delta h$, cf. table 6.1. In figure 6.20, the experimental and simulated coefficients of friction over velocity are compared for the two compound combinations, revealing that the difference between the materials is predicted correctly. The expected higher coefficient of friction for high T_g compounds is achieved for both filler levels, indicated by arrows in figure 6.20.

The next physical property that is studied is the material hardness h. A shift of the frictional response to a lower level for an increasing hardness is expected, because a softer compound undergoes larger deformations and therefore more hysteresis is generated in a certain range. This effect is reproduced for the low filler level (c6-c2) over the whole velocity range and for the high filler level (c3-c1) at least for velocities above $v = 0.5$m/s, see figure 6.21.

The last material property of the six compound setup is the variation of filler level that can be studied for three compound combinations, expecting a higher frictional response for the high filler level. The ranking for a filler variation at a high hardness and high

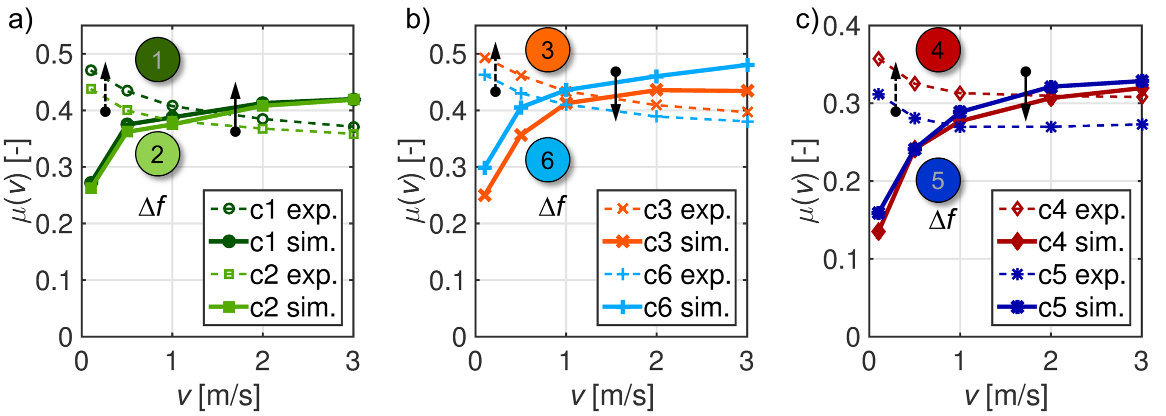

Figure 6.22: Comparison of compound pairs over velocity with different filler level (f) for a) high h, high T_g, b) low h, high T_g and c) high h, low T_g. Global pressure $p = 0.3$MPa.

T_g (c2-c1) level is captured properly with the method, see figure 6.22 a). Nevertheless, the prediction of the ranking for changing filler levels in the other two cases is not predicted, cf. figure 6.22 b)-c). This gap is attributed to the used viscoelastic material model which is based on a finite linear viscoelastic theory and therefore unable to capture for example the Payne-Effect. Especially, this effect may be very important for material responses with different filler levels.

6.5.2 Surface Comparison

In this subsection, the response of two different rough surfaces is analyzed with the hysteretic multiscale method of section 6.3. Therefore, a second rough surface (surf. 2) is introduced and decomposed in the same manner like the rough surface (surf. 1) in the previous subsection 6.5.1. As a consequence, the same band-pass filter edge wavelengths are used to construct four scales with ten surface samples on each scale, see figure 6.23. The texture of the displayed surface is rougher than the one of the previous surface, compare also figure 6.17. This observation is also outlined in figure 6.24 which displays two exemplary surface samples for each of the two lowest scales of both surfaces. Although surface 2 consists of some surface samples with higher amplitudes than surface 1, similar surface samples can also be found in the whole setup for both surfaces. Hence, it is very important to include more than one surface sample for each scale in order to capture surface characteristics in a correct manner.
The same experimental setup as described in the previous subsection is used for a friction experiment on both surfaces. Rubber compound c3 (see previous subsection for the material parameters) is used for the study on a surface covered with water and the global velocity $v = 0.5\text{m/s}$, pressure $p = 0.3\text{MPa}$ and temperature $T_0 = 20°\text{C}$.

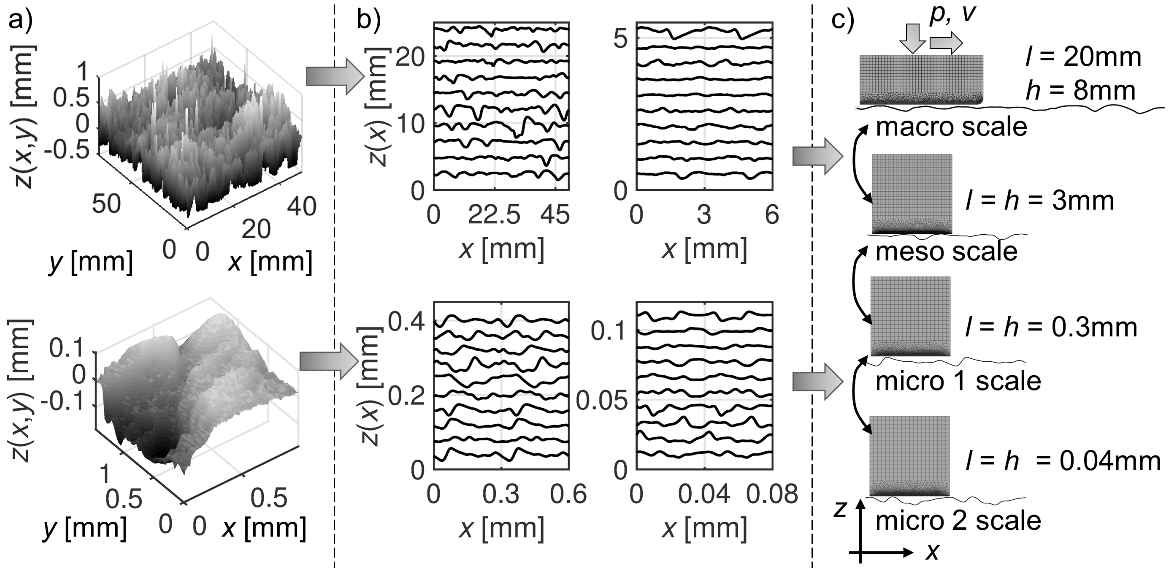

Figure 6.23: Surface 2: a) Macroscopic and microscopic surface measurements. b) Ten extracted surface samples on each scale for the construction of four scales. c) Four-scale setup with rubber block dimensions.

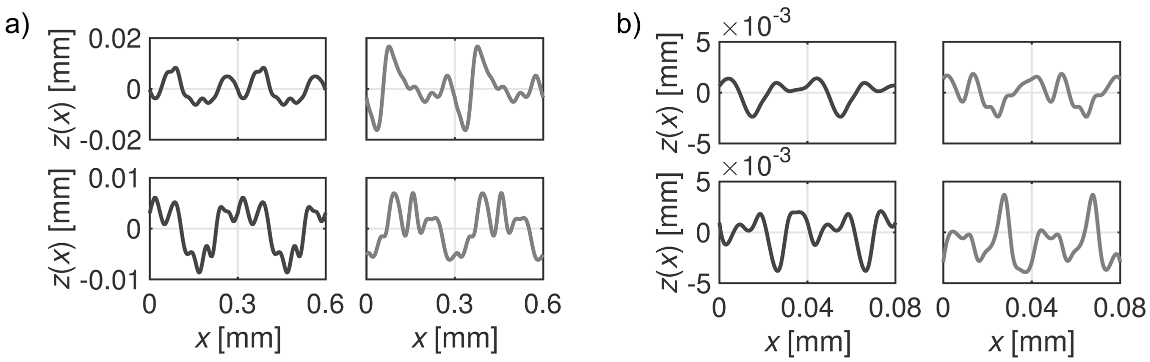

Figure 6.24: Exemplary surface samples of surface 1 (dark profiles) and surface 2 (bright profiles) for a) micro 1 scale and b) micro 2 scale.

The experimental and simulated results are displayed in figure 6.25, the absolute values in a) and the relative values using the result of the second surface as a reference in b). First of all, the simulated absolute values are lower than the experimental values, because again adhesive effects are neglected in a pure hysteresis study. Second, the correct prediction of the surface ranking is achieved with the simulation. Thus, the proposed multiscale method is able to capture different surface textures that may for example become more difficult with the approaches proposed in Wriggers (2008), Wagner et al. (2015) or Falk et al. (2016).

6.5.3 Surface Polishing Effects

The rough surface is modelled as a rigid body in all previous simulations, because it does not change its shape strongly during a few friction experiments. However, a lot of experimental studies observe the effect of flattening rough road surface asperities during a large number of sliding or polishing cycles (called runs n in this work). This effect is often called surface polishing effect, see Knill (1960) for an early description, Do et al. (2009), Wang et al. (2013), Wang et al. (2015), Chen et al. (2016) for more recent studies providing experimental results. In Wang et al. (2015), a

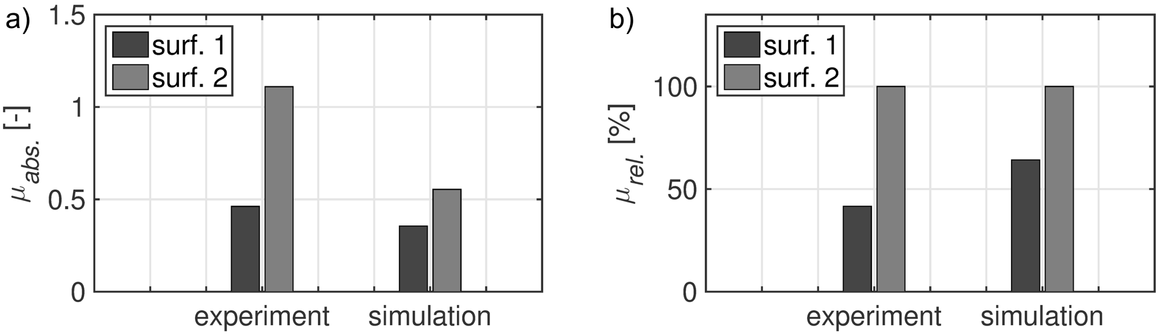

Figure 6.25: a) Absolute values of the experimental (wet) and simulated coefficient of friction for $v = 0.5\text{m/s}$, $p = 0.3\text{MPa}$, $T_0 = 20°\text{C}$, material c3. b) Relative values of experimental and simulated coefficient of friction, reference surf. 2.

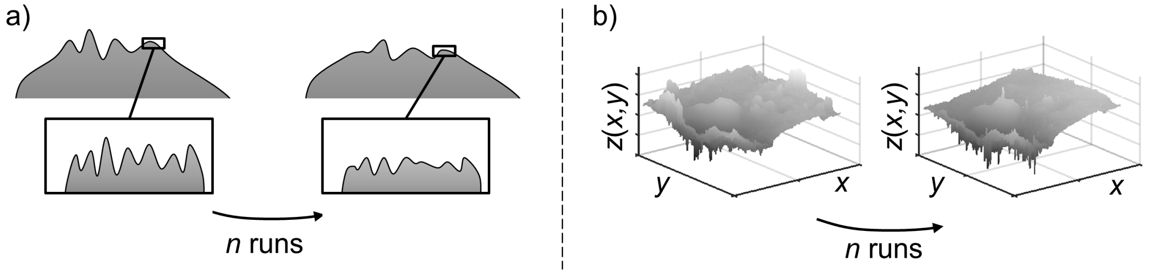

Figure 6.26: a) Schematic overview of surface polishing effects on two length scales. b) Exemplary microscopic surface measurements between n wet experimental runs.

schematic overview of the effect is given and also the effect of an increasing coefficient of friction for the first polishing cycles is described, attributing it to the removal of binder material on top of the surface revealing the rough surface aggregates. After a peak value is reached, a decreasing coefficient of friction due to polishing of the surface asperities is observed, converging to a final value, often called μ_{end}. The effect of removed binder material is not studied in this subsection concentrating on the polishing behaviour of wet road surfaces.

In order to study geometrical surface polishing effects, often a detailed analysis of single road surface stones is performed revealing that the surface polishing can be observed at different length scales, see results in Chen et al. (2016). On the one hand, the single stone asperities are polished on a macroscopic level. On the other hand, the microscopic roughness is decreased during n runs of a sliding rubber block, see figure 6.26 a) for a schematic overview. In this subsection, only the evolution of microscopic surface texture is studied, exemplary surface measurements are displayed in figure 6.26 b). The experimental results are provided in normalized form by the industrial partner, but nevertheless the data is sufficient to study the observed trends of surface polishing (rubber compound m2 is used for the study, see appendix C for the material parameters).

In this study, a hysteretic two-scale setup is constructed out of microscopic surface measurements that are performed and repeated after a certain number of runs n. The principle procedure is displayed in figure 6.27. The microscopic pressure values and dimensions of the two microscopic scales are according to the previous multiscale simulations, see subsection 6.5.1 and 6.5.2. Similar to the multiscale setup, a frictionless

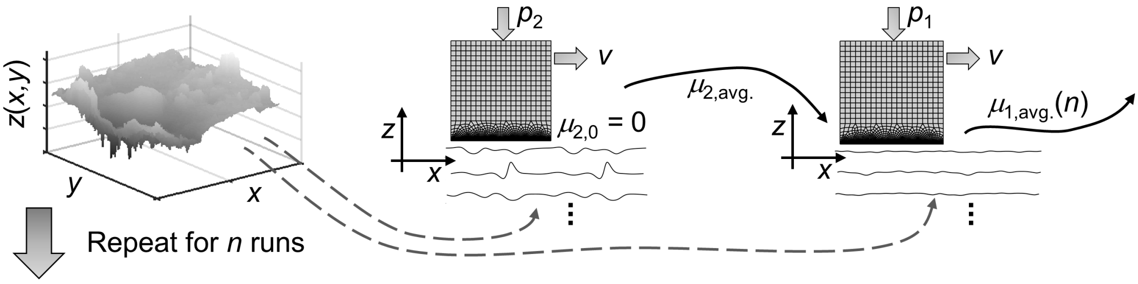

Figure 6.27: Construction of the two-scale setup for every measurement point after n runs. Parameters $v = 0.5$m/s, $p_1 = 2.5$MPa, $h_1 = l_1 = 0.3$mm, $p_2 = 4.5$MPa, $h_2 = l_2 = 0.04$mm, rubber compound m2.

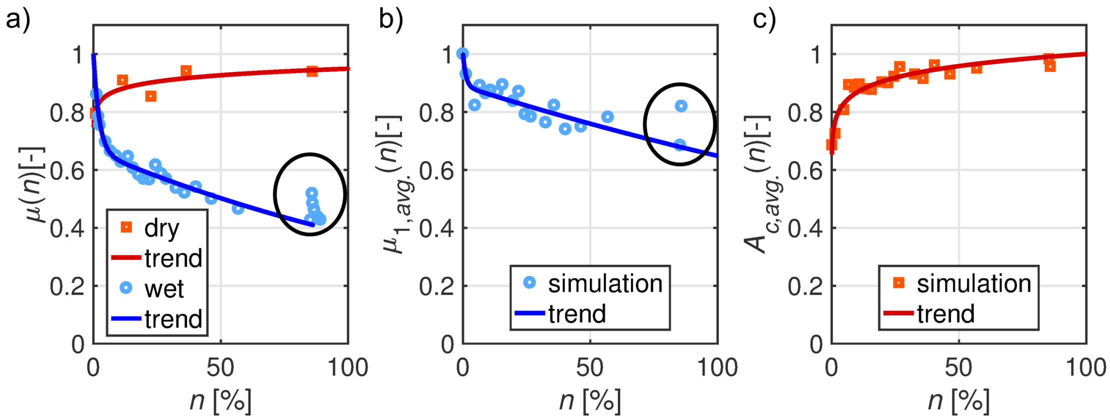

Figure 6.28: a) Normalized experimental results for wet and dry experiments after n runs. b) Normalized simulated coefficient of friction (averaged). c) Normalized simulated contact area (averaged).

behaviour is assumed on the lowest scale (micro 2) and the resulting hysteretic coefficient of friction is passed to the next scale (micro 1). In order to capture the surface characteristics in an appropriate way, 100 surface samples are introduced for each scale and all resulting time averaged coefficients of friction are averaged afterwards over the number of surface samples. Consequently, 200 single calculations are performed for each run n leading to the final result in form of the coefficient of friction $\mu_{1,avg.}(n)$.

In figure 6.28 a) the normalized results of the coefficient of friction over the normalized number of friction experiment runs n are displayed. Whereas a decreasing coefficient of friction is observed for wet conditions, a few dry experiments are performed in between, revealing an increasing trend over the number of runs n. On a wet surface, the dominant physical effect is assumed to be hysteresis. And thus, due to the surface polishing effect, less microscopic deformation is induced through the rough surface leading to the observed decreasing trend of $\mu(n)$. Meanwhile, the microscopic contact area is assumed to increase and therefore the expected larger effect of adhesion for dry surfaces is assumed to increase. This is the explanation for a slight increase of the measured coefficient of friction under dry conditions. Trend lines for wet and dry measurements are added to figure 6.28 a).

Figure 6.28 b) displays the normalized numerical results for the pure hysteretic coefficient of friction gained with the described two-scale setup. First of all, through the direct incorporation of the rough surface, the decreasing trend of the coefficient of friction for the wet measurement is reproduced. Furthermore, an evaluation of the normalized relative contact area over runs n confirms the assumption of an increasing microscopic contact area, cf. 6.28 c). This surface property is linked to the slightly increasing dry coefficient of friction, since adhesive effects would increase with a larger contact area, see also chapter 7.

Another effect is observed in the experiment and highlighted with a black circle at the end of the wet measurements in figure 6.28 a). After a dry measurement point, a run-in effect is observed for the wet condition, starting with a coefficient of friction above the general trend for the wet measurement. The effect is just displayed for the last dry measurement point, cf. figure 6.28 a). During the following wet measurements, again a decreasing coefficient of friction is observed reaching the trend line after a while. This effect is attributed to wear effects, that are more present for dry surfaces, inducing a roughening of the rubber surface and maybe also the road surface. In summation, this effects may lead to a temporary increased hysteretic response. Furthermore, remaining wear products at the rough road surface may also increase the wet frictional response for a while. The temporary increase of the wet coefficient of friction after the dry measurement is demonstrated with one additional simulation near the dry measurement point, cf. black circle in figure 6.28 b). This result indicates that the surface roughness (tracked with a surface measurement) is increased for that point, confirming the formulated assumptions of introduced roughening.

6.5.4 Quantities from Multiscale Calculations

In subsections 6.5.1 and 6.5.2, the global coefficient of friction was presented as the output of the multiscale method and validated with experimental results in order to investigate the prediction quality of global trends. Nevertheless, also different quantities like the contact area (see subsection 6.5.3) can be evaluated with the multiscale method and provide further results that are not accessible with experimental methods. Furthermore, a detailed analysis of the distribution of certain quantities over the introduced length scales can be performed with the multiscale method.

For the setup of subsection 6.5.1 and the global parameters $p = 0.3$MPa, $v = 1$m/s and material c3, the evaluated quantities for the pressure, the coefficient of friction, and the contact area are displayed for each scale in figure 6.29 a). The quantities

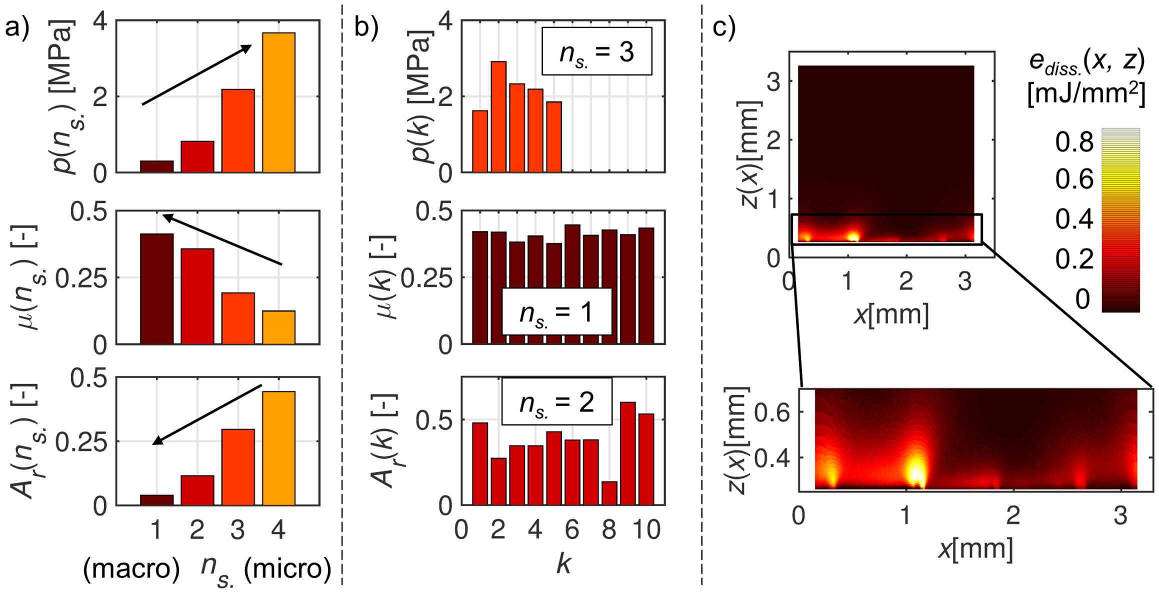

Figure 6.29: Global parameters: $p = 0.3$MPa, $v = 1$m/s, material c3. Scale n_s: 1 = macro, 2 = meso, 3 = micro1, 4 = micro2. a) Overall pressure p, overall coefficient of friction μ and overall relative contact area A_r over number of scales $n_{s.}$. b) p, μ, A_r over calculated surface samples k for certain exemplary scales n_s. c) Local relative dissipated energy at mesoscopic scale.

are displayed as the overall result including the previous responses of the other scales, e.g. the combined coefficient of friction is displayed for each scale. The analysis of the down-scaled pressure, the up-scaled coefficient of friction and the contact area can reveal interesting information how the quantities are distributed over length scales, for example how much friction is generated on certain scales.

In addition, closer looks on all quantities can be performed by displaying the quantities over surface samples k before averaging is applied, see figure 6.29 b) for examples. Consequently, also the statistical distribution of the quantities can be evaluated, revealing maybe interesting differences between used rubber compounds or surfaces that can be used to improve future tires, cf. formulated goals in section 1.1. Beyond quantities over scales and surface samples, various local quantities like stresses, strains or dissipated energy can be evaluated locally for each finite element calculation, see figure 6.29 c). As an example, the dissipated energy over height could provide additional valuable information how a certain material reacts on a defined surface.

Summarizing, a lot of quantities that are not reachable in experiments can be evaluated with the proposed multiscale setup revealing the chance to tune material properties to improve tire relevant properties of the rubber compounds.

Chapter 7

Multiscale Approach including Adhesive Friction

The chapter provides a short overview of existing numerical approaches for adhesion of rubber on various surfaces. Further, the assumed prevailing physical mechanism is described in the second section providing the basis for a multiscale finite element framework including adhesive effects. The multiscale framework is explained in section 7.3 following Wagner et al. (2017). Afterwards, the multiscale approach is validated with experimental results provided by the German Institute of Rubber Technology (DIK), cf. subsection 2.1.2. Based on the achieved results, a modification of the assumptions and a consequently slightly different multiscale procedure is introduced in section 7.5. This approach is again validated with the same experimental results.

7.1 Preliminary Numerical Approaches for Adhesion

A brief overview of adhesion models incorporated in finite element frameworks is provided in this section. The overview is limited to adhesion models that are already coupled to multiscale analyses of rubber friction on rough surfaces and the methods these approaches are based on. Beyond these particular models, a lot of numerical approaches for adhesive contact are developed, see Sauer (2015) and the therein provided references for an overview.

The most common approach to include adhesion in a numerical contact analysis is the use of a traction-separation model, also often referred to as cohesive zone modelling, cf. Xu & Needleman (1994); Rahulkumar et al. (2000). In addition to the standard contact algorithms of chapter 4, the normal and tangential mechanical interaction is enhanced with a gap-dependent adhesive force with inverse algebraic signs allowing also positive contact stresses. Furthermore, this force increases with an increasing gap until a certain adhesive limit is reached, followed by a decreasing branch of the traction-separation curve. In Raous et al. (1999) a thermodynamically consistent pseudo-potential is introduced for the interface leading to a modification of the Karush-

Kuhn-Tucker conditions (see section 4.2) with an adhesive force. The theory is accomplished by an adhesion intensity factor β being one for full adhesion and zero if full separation of the bodies is reached. In order to complete the set of equations, an evolution equation for β is introduced. Finally, a constitutive law has to be chosen for the method, leading to the problem of parameter identification.

The model of Raous et al. (1999) is used and applied to multiscale frameworks for rubber friction in Wriggers & Reinelt (2009) and Falk et al. (2016) introducing in both studies six parameters for the adhesive law. The adhesive interaction is added on the smallest length scale enhancing the coefficient of friction on this scale. Despite the motivation of some parameters by physical considerations in Wriggers & Reinelt (2009), the choice of the adhesive parameters remains a very challenging task, because the range of adhesive interaction forces is a few nanometers. Furthermore, no link to repeatable and defined laboratory tests is provided, leading to a more or less large range of possible parameters. In Reinelt (2008), the difficulties of parameter choice and the large impact on the final coefficient of friction are discussed.

Further studies that provide interesting approaches for finite element adhesion models are developed e.g. in Dobberstein (2014), Sauer & Li (2007) or Sauer & Wriggers (2009). In Dobberstein (2014), a complex traction-separation law based on the theory of Talon & Curnier (2003) with tangential contact is incorporated in a three-dimensional mortar contact element to simulate a demolding process of rubber on a macroscopic length scale. In Sauer & Li (2007) and Sauer & Wriggers (2009), an interatomic interaction potential is coupled to finite elements on a continuum level, providing the chance to describe van-der-Waals interactions. These formulations provide a more direct access to the adhesive interaction than traction-separation approaches. Nevertheless, the determination of appropriate model parameters for a rubber material on a rough surface with an additional complex tangential interaction remains an open question.

Because of the unknown and hard to measure adhesive parameters for all introduced numerical adhesion models, a direct modelling of adhesion is omitted in this work. Instead, a phenomenological model based on physical assumptions, experimental observations and analytical theories is introduced in the following sections, cf. Wagner et al. (2017). The assumptions link the nanoscopic mechanism to a macroscopic adhesion law providing the possibility to fit it to macroscopic friction experiments and validate the theory in this chapter.

7.2 Adhesion Model and Assumptions

In subsection 2.2.1, a brief overview of possible origins for adhesion of sliding rubber on a rough surface is listed. Following the analytical studies adding adhesive interactions to sliding rubber on a rough surface, adhesion is considered to be generated by the interaction of rubber molecules with atoms of the rough counter surface, see Persson & Volokitin (2006) or Lorenz et al. (2015). The rubber molecules are assumed to be elastic chains undergoing bonding-stretching-debonding cycles at a nanometer length scale, see figure 7.1 a)-b). Whenever a chain sticks to the rough surface a

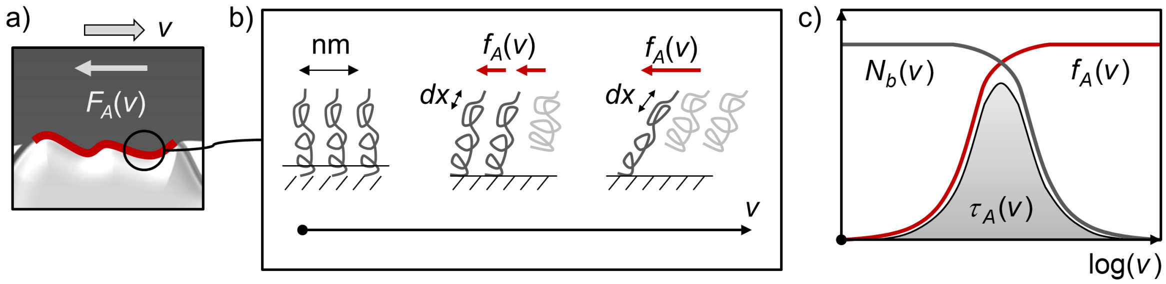

Figure 7.1: a) Rubber friction with adhesive contribution at the interface. b) Chain dynamics at the interface on a nanometer length scale. c) Qualitative shape of adhesive shear stress.

velocity-dependent adhesive force $f_A(v)$ for this single chain is built up

$$f_A(v) = c \cdot dx(v), \tag{7.1}$$

with the spring stiffness c and elongation $dx(v)$ of the chain. For an increasing macroscopic velocity v the single chains are stretched more at the interface, indicated in figure 7.1 b). Simultaneously, the number of bonded chains $N_b(v)$ decreases for an increasing velocity as a result of less time for bonding and less resistance to a debonding cycle. Multiplying both quantities, the number of bonded chains and the single chain force $f_A(v)$, the local mechanism of adhesion can be transferred to the macroscopic shear force $F_A(v)$

$$F_A(v) = N_b(v) \cdot f_A(v), \quad \tau_A(v) = \frac{F_A(v)}{A_c(v)}. \tag{7.2}$$

By dividing the total adhesive shear force by the current contact area, also depending on the macroscopic velocity, a global adhesive shear stress is derived, cf. Lorenz et al. (2015). As a consequence of the combination of the single shear force and the number of bonded chains, the global shear stress has a bell-shaped appearance over velocity, see figure 7.1 c). A mathematical description of the bell-shaped curve is provided

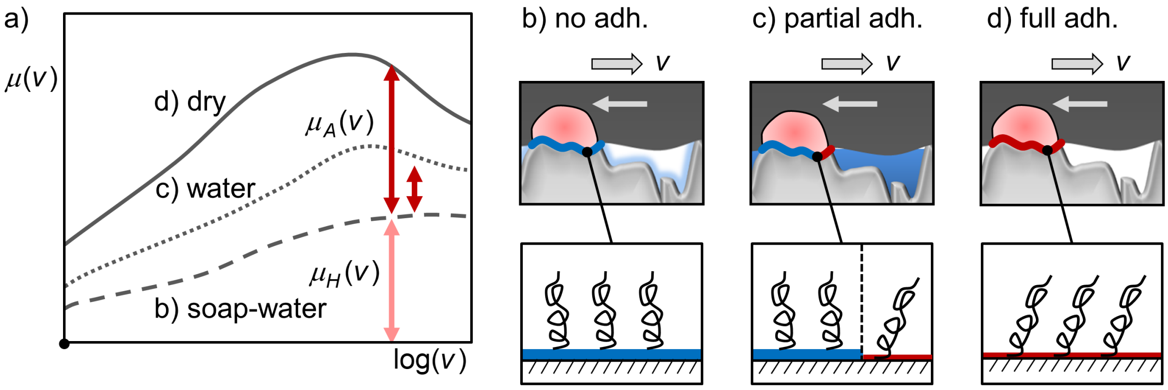

Figure 7.2: a) Qualitative result of friction experiments over a large range of global velocities for different surface conditions. b) Rough surface with soap-water mixture, no adhesion (adh.) assumed. c) Rough surface with water, partial adhesion. d) Dry surface with full adhesive contribution.

among others in Le Gal et al. (2005), Le Gal & Klüppel (2008) and Lorenz et al. (2015). To summarize, the global adhesive shear stress is motivated by physical assumptions on the nanoscopic length scale for the adhesion mechanism of sliding rubber samples. The concrete parameters to describe the shear stress quantitatively can be obtained by fitting to experimental results. Details are provided in the next section.

In addition to the derived chain dynamics, further common assumptions for rubber friction and the global coefficient of friction $\mu(v)$ are introduced in this section. Following section 2.2 and the observations of friction studies with rubber samples on rough road surfaces, the decomposition of the global coefficient of friction and a link to adhesive and hysteretic interactions for different surface conditions is provided. Three different surface states are considered in this work: a surface covered with a soap-water mixture (figure 7.2 b)), a surface covered with water (figure 7.2 c)), and a completely dry surface (figure 7.2 d)). First of all, for moderate global pressure values the same amount of hysteresis $\mu_H(v)$ is assumed for different surface conditions on the same rough surface, see red shaded areas in figure 7.2 b)-d). In general, the rubber sample is able to follow the top surface asperities under all surface conditions, since the surface is covered with thin liquid layers on the top asperities.

Additionally, certain amounts of the liquid can be wiped away from the surface asperities, leading to dry contact regions. Under large macroscopic pressures some surface asperities may be suppressed by water, because the rubber block is not able to remove the incompressible water from the surface valleys, leading in consequence to a different hysteretic contribution in comparison to a dry surface. This case is not considered in this work and thus hysteresis provides the basic contribution with the same magnitude for all surface conditions.

The differences of the global coefficient of friction for different surface states (see figure 7.2 a)) are attributed to a changing adhesive contribution, cf. Wagner et al. (2017),

$$\mu(v) = \mu_H(v) + \alpha\mu_A(v), \quad \alpha \in [0,1]\,. \tag{7.3}$$

In order to represent different amounts of the adhesive contribution, a coefficient α indicating the share of adhesion is introduced, being zero for no adhesion and taking the value of one for the largest adhesive contribution. Accordingly to experimental studies (cf. Le Gal et al. (2005)), the lowest global coefficient of friction is measured for a rough surface covered with a soap-water mixture, see figure 7.2 a). This observation is linked to the physical properties of the used liquid. Since a soap-water mixture provides a very low surface tension, it is assumed that the whole surface is covered with the liquid. Hence, a separation medium may be provided on the whole surface, figure 7.2 b). This separation medium prevents the rubber chains from bonding to the surface, avoiding a significant contribution of adhesion for this surface condition. Therefore, regarding this assumptions the coefficient α equals zero for a rough surface covered with a soap-water mixture.

For dry surfaces, no suppression of the bonding-stretching-debonding cycles of the rubber molecules is present and hence the coefficient α is set to one. This choice is based on the largest measured coefficient of friction for dry conditions, cf. figure 7.2

a). The measured coefficient of friction for a surface covered with water is higher than for a soap-water covered surface, but lower than on a dry surface. In particular, it is assumed that water is wiped away from the surface asperities revealing dry parts of the rough surface where bonding cycles of rubber molecules occur. Thus, the coefficient α takes a value between zero and one for a rough surface covered with water, leading to a combination of a hysteretic and an adhesive contribution.

It has to be remarked, that wiping of the interface liquid may also occur for a soap-water mixture. However, the amount of liquid wiped away may be less than for a water covered surface. This circumstance is addressed in section 7.5 in more detail.

7.3 Multiscale Framework including Adhesion

Based on the assumptions of the last section and the introduced adhesion mechanism, the multiscale framework for hysteretic friction (cf. chapter 6) is enhanced with an adhesion part. The adhesive interaction is incorporated through a phenomenological model at the macroscopic length scale and fitted to experimental data, cf. Wagner et al. (2017). Following the last section, a bell shaped adhesive shear stress with free fitting parameters is introduced and coupled to the current contact area calculated by the numerical multiscale setup of the hysteretic part, see figure 7.3.

The framework starts as described in section 6.3 with the pressure down-passing branch on frictionless finite element setups, see step A) in figure 7.3. Three scales ($n = 3$) are exemplarily displayed, although in general the method is extendable to more scales. Additionally to the homogenization of the coefficient of friction in the up-passing branch, the current contact area of each surface sample j is evaluated. Correspondingly to the

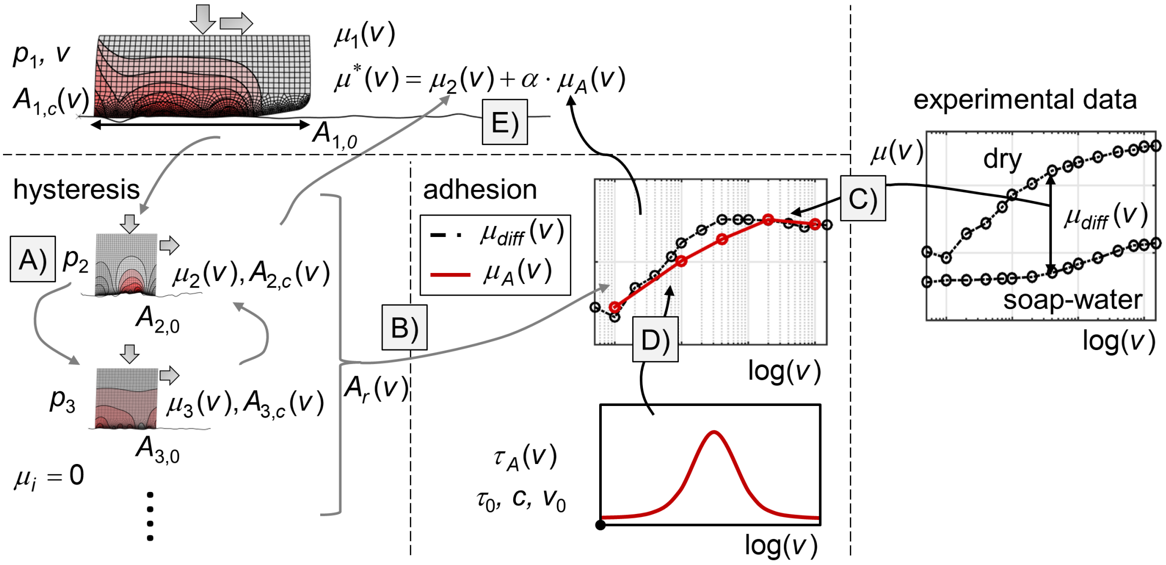

Figure 7.3: Multiscale framework coupling hysteretic and adhesive contributions. A) Down-scaling of pressure. B) Calculation of the contact area. C) Calculation of $\mu_{diff}(v)$. D) Adoption of adhesive parameters. E) Combination of hysteretic and adhesive coefficients of friction.

procedure for the time homogenization and surface sample averaging of the coefficient of friction (see section 6.1 and section 6.3), the same operations are performed for the current contact area of each scale

$$A_{n,c,avg.} = \frac{1}{t_1 - t_0} \int_{t_0}^{t_1} A_{n,c}(t)\,\mathrm{d}t, \quad \bar{A}_{n,c} = \frac{1}{n_j} \sum_{j=1}^{n_j} A_{n,c,avg.}(j). \tag{7.4}$$

These values, named for simplification $A_{n,c}$ from now on, depend on the global applied velocity. Moreover, the contact area also depends on the global pressure. This dependency is not indicated in the equations and in figure 7.3, since a validation for a large velocity range without varying the global pressure is performed in section 7.4. The whole framework is interrupted before the calculation of the frictional macroscopic scale, providing the possibility to impose an adhesive contribution, see figure 7.3. The global relative contact area is calculated by all evaluated current contact areas and the nominal contact areas (step B))

$$A_r(v) = \frac{A_{1,c}(v)}{A_{1,0}} \cdot \left(\prod_{n=2}^{n_s} \frac{A_{n,c}(v)}{A_{n,0}} \right). \tag{7.5}$$

Since the current contact area of the macroscopic frictional calculation is not available at this moment, the evaluated current contact area of the frictionless calculation is used in equation (7.5). The error introduced by this evaluation is only marginal.

Correspondingly to the introduced assumptions, experimental results enter the whole framework in step C), see figure 7.3. The difference $\mu_{diff}(v)$ between friction experiments on a dry surface and on a rough surface covered with a soap-water mixture is calculated. The whole difference is assumed to be generated by adhesive interactions. Therefore, $\mu_{diff}(v)$ is approximated by the bell shaped shear stress introduced in section 7.2.

A law for the bell shaped shear stress $\tau_A(v)$ is chosen from the analytical literature, following the proposal of Lorenz et al. (2015)

$$\tau_A(v) = \tau_0 \exp\left(-c \left[\log\left(\frac{v}{v_0} \right) \right]^2 \right), \tag{7.6}$$

with the parameter τ_0 defining the curve amplitude, parameter c describing the width, and parameter v_0 determining the position of the peak value. This parameter set provides the possibility to fit macroscopic responses for different materials or rough surfaces. In order to fit the difference of the coefficient of friction provided by the experimental results, the shear stress is transferred to an adhesive coefficient of friction $\mu_A(v)$ with the use of the global pressure and the relative contact area (cf. Le Gal et al. (2005), Le Gal & Klüppel (2008) and Lorenz et al. (2015))

$$\mu_A(v) = \frac{\tau_A(v)}{p_1} \cdot A_r(v). \tag{7.7}$$

Modifying the parameters τ_0, c, v_0, the experimental response is approximated, see step D) in figure 7.3. The adhesive response is expected to depend on the relative contact area, because with a larger contact area the number of adhesive bonds increases, cf. Le Gal & Klüppel (2008). Thus, the relative contact area enters the formulation in step D). It has to be remarked that the numerically calculated contact area including geometrical and material non-linearity may differ from the area calculated by analytical approaches.

The last step of the framework determines the macroscopic coefficient of friction by the addition of the hysteretic response $\mu_2(v)$ of all scales underneath the macroscopic scale and the adhesive contribution $\mu_A(v)$, step E) in figure 7.3.

$$\mu^*(v) = \mu_2(v) + \alpha \cdot \mu_A(v), \quad \alpha \in [0,1]\,. \tag{7.8}$$

Following section 7.2, the coefficient α is introduced to differentiate dry results with $\alpha = 1$ or further experimental results using different liquids, especially water, by setting α between zero and one. Finally, the global coefficient of friction μ_1 containing also the hysteretic effects of the macroscopic scale is gained by time homogenization. By the proposed incorporation of adhesive effects at the macroscopic scale a recalculation of the lower scales is omitted, revealing another benefit with respect to time efficiency of the multiscale framework.

7.4 Experimental Validation

In this section, the multiscale method for hysteretic and adhesive rubber friction of chapter 6 and chapter 7 is validated with experimental results, see Wagner et al. (2017). First, the validation setup with a rough surface is introduced and different rubber compounds are calculated with the multiscale method.

The setup for the validation of adhesive friction combined with hysteresis is introduced: three different rubber compounds are used for the validation in order to study different adhesive contributions dependent on the individual rubber compound. The storage- and loss-moduli for the three compounds are displayed in figure 7.4 and in table 7.1 the Mooney-Rivlin-parameters are listed. Furthermore, surface 3 is used for this validation study, shown in figure 7.5. For the mulitscale setup four scales with ten surface samples are applied, compare setup in subsection 6.5.1.

The global parameter range is defined by a global pressure of $p = 0.2$MPa and very low sliding velocities between $v = 10^{-5} - 10^{-2}$m/s. The low velocity range is used because it is important to exclude temperature effects in this study and this is ensured with

Table 7.1: Mooney-Rivlin parameters of compounds A, B and C.

Compound	C_{10} (MPa)	C_{01} (MPa)	D_1 (MPa)
A	0.382	0.300	0.029
B	0.113	0.581	0.029
C	0.374	0.266	0.031

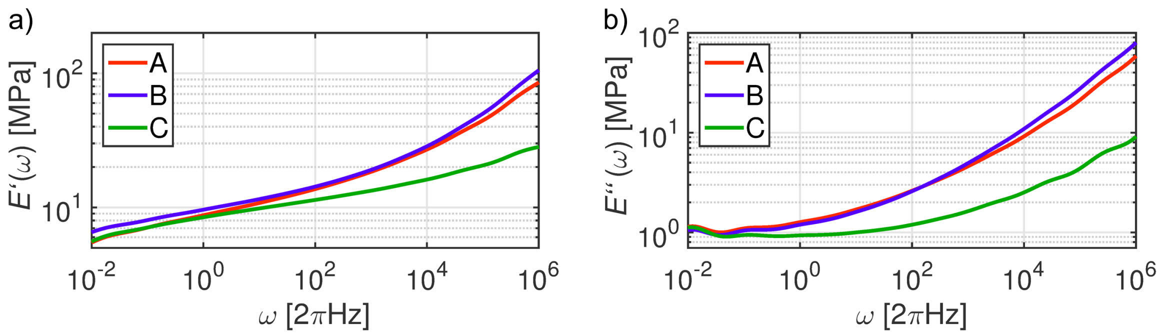

Figure 7.4: a) Storage modulus E‘ and b) loss modulus E“ for three different rubber compounds A, B, and C in the relevant excited frequency range.

these values for the global velocity, compare the velocity threshold derived in Persson (2006) for which temperature effects get important. The rough surface is used in a dry experimental setup and also covered with a soap-water mixture, repeating the experiment to exclude the adhesive contribution, see section 7.2 for detailed explanations. The results of the friction experiment are used to calculate the difference between the dry and soap-water coefficient of friction $\mu_{diff}(v)$.

In a first step, the hysteretic multiscale setup is calculated following the description of section 7.3 and stopping before the final macroscopic calculations are started. Then, the effect of adhesion can be included in a final step. The whole procedure is performed for the described three materials on surface 3. The resulting relative contact areas over velocity calculated by equation (7.5) are displayed for all three compounds in the upper part of figure 7.6.

In a next step, equation (7.7) is used to fit $\mu_{diff}(v)$ with the use of the gained rela-

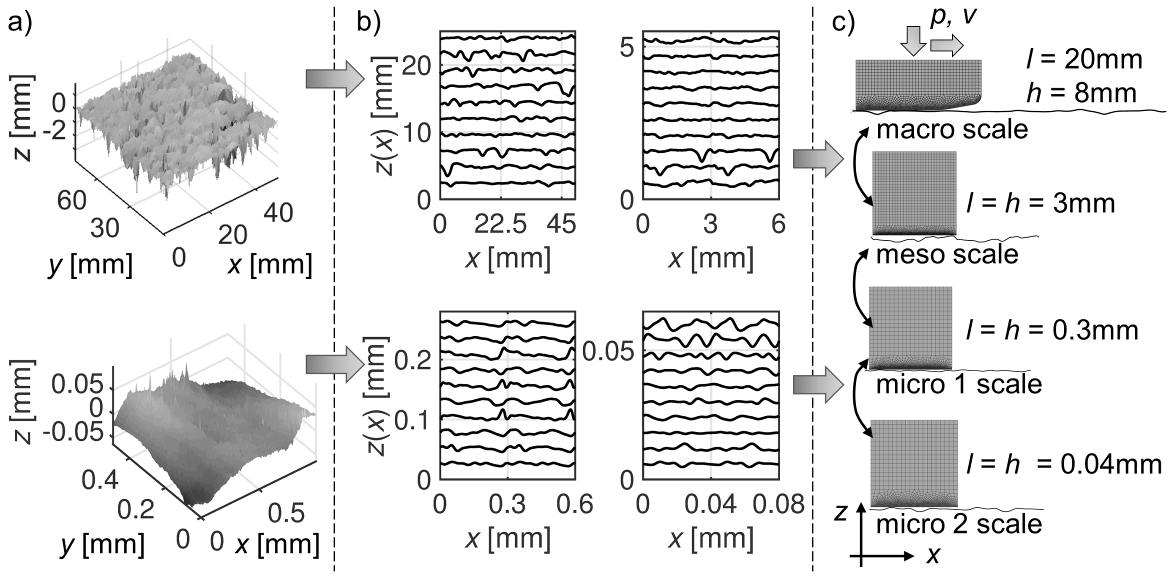

Figure 7.5: Surface 3: a) Macroscopic and microscopic surface measurements. b) Ten extracted surface samples on each scale for the construction of four scales. c) Four-scale setup with rubber block dimensions.

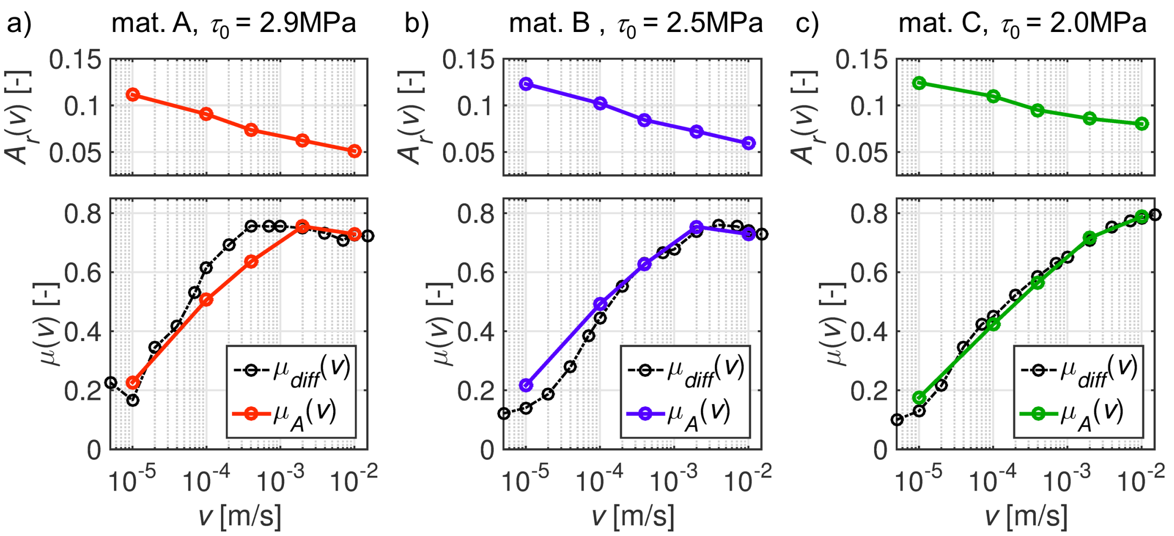

Figure 7.6: Relative contact areas A_r calculated with the multiscale framework for all materials (top). Fitted adhesive coefficients of friction with the experimental input $\mu_{diff}(v)$ (bottom). Parameters $c = 0.18$ and $v_0 = 0.02\text{m/s}$ for all materials.

tive contact area and the adhesion law for the shear stress (see equation (7.6)). The parameters c, v_0 and τ_0 are adopted to reproduce the experimental difference between the dry and soap-water measurement $\mu_{diff}(v)$, see lower part of figure 7.6. Similar to LORENZ ET AL. (2015), the parameter $\tau_0 = 2.9/2.5/2.0\text{MPa}$ is assumed to be material dependent and the values for $c = 0.18$ and $v_0 = 0.02\text{m/s}$ are fixed for all rubber compounds, providing a good approximation of the experimental results including the

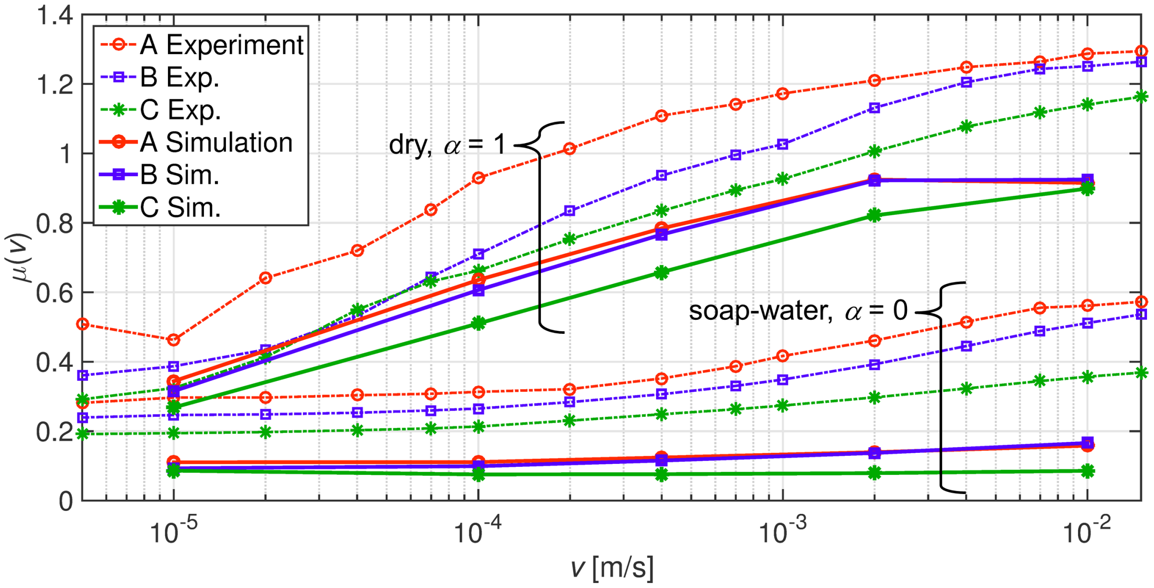

Figure 7.7: Experimental results (dashed lines) for dry and soap-water surface conditions. Numerical results (solid lines) calculated with the multiscale finite element framework for three materials A, B and C.

contact area in this procedure.

In a next step, the fitted adhesive coefficient of friction is added to the hysteretic coefficient of friction and two macroscopic setups are calculated, one with α set to zero and another one with α set to one, resulting in the full adhesive contribution, see also equation (7.8). The final results are displayed together with the experimental results in figure 7.7.

Until now, in section 7.3 a pure hysteretic contribution for a surface covered with a soap-water mixture is expected. However, this assumption may be incorrect, since a gap between the experimental curve for a soap-water measurement and the pure hysteretic simulation is detected. This gap is consequently not closed with the addition of the adhesive coefficient of friction (comparing it now to the dry experimental result). But, nevertheless the correct trend over velocity and the ranking of the materials can be predicted with the method (except for the last velocity point). A contribution of adhesion is already introduced for a surface covered with soap-water in the next subsection in order to close the detected gap.

7.5 Modified Approach and Validation

The assumption of no adhesive interaction on a rough surface covered with a soap-water mixture may be to some extent questionable. Soap-water may also be wiped away from the top surface asperities like in the case of a rough surface covered with water. This effect would result in partly dry surface asperities where consequently bonding of rubber molecules to the rough surface could occur. Thus, for a water covered surface, larger dry contact areas are expected, cf. experimental observations of figure 7.2. This modified assumption is supported by the numerical results of the last section 7.4.

All in all, a purely hysteretic multiscale simulation for low velocities $v = 10^{-5} - 10^{-2}$m/s reveals a discrepancy between the calculated response and a soap-water measurement,

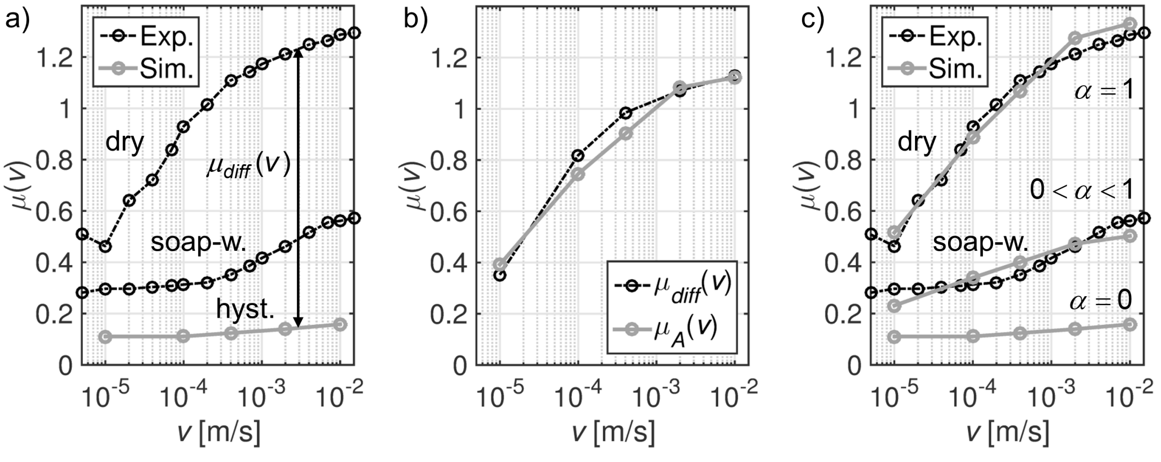

Figure 7.8: a) Difference between simulated hysteretic response and dry experiment. b) Fitting of $\mu_A(v)$ to $\mu_{diff}(v)$. c) Exemplary simulation results by adoption of $\alpha = 0.3$ for the soap-water result.

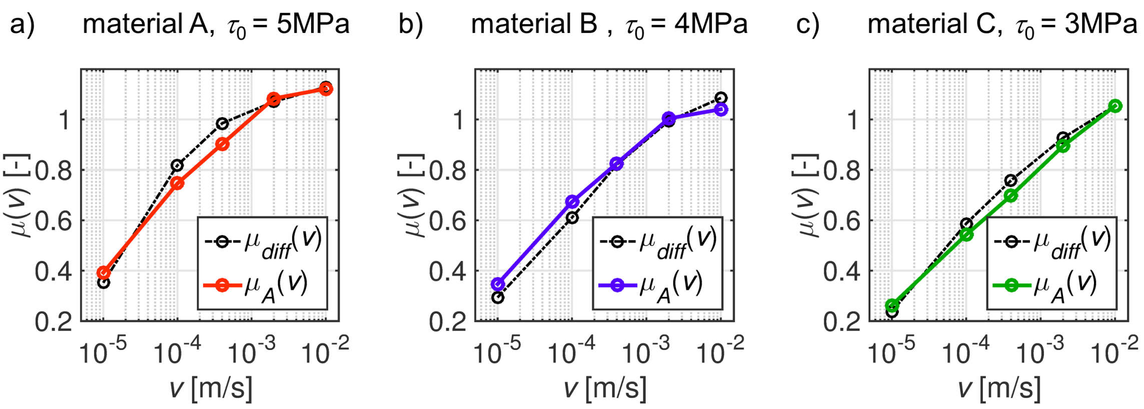

Figure 7.9: Fitted adhesive coefficients of friction. Input $\mu_{diff}(v)$ from dry experimental measurement and pure hysteresis calculation. Parameters $c = 0.12$ and $v_0 = 0.11\mathrm{m/s}$ determined for all materials.

see figure 7.8 a). This gap is attributed to an already present adhesive interaction and therefore the calculation of the adhesive contribution compared to section 7.3 is modified slightly, following Wagner et al. (2017).

The purely hysteretic multiscale framework is calculated as a first step and afterwards the difference $\mu_{diff}(v)$ between this result and the dry experiment is evaluated, see figure 7.8 a). The fitting procedure is kept unchanged following the description provided in section 7.3, see equations (7.6), (7.5) and (7.7) , using the relative contact area and the shear stress law, see figure 7.8 b).

In the last step of the modified approach, two macroscopic simulations are executed. Following the changed assumptions, the coefficient α is adopted between zero and one achieving an approximation of the soap-water result, see figure 7.8 c) and equation (7.8). Finally, the full adhesive contribution $\mu_A(v)$ is added to the hysteretic result by simulations on the macroscopic scale with $\alpha = 1$.

Similar to the last subsection, the same relative contact area is used based on a hysteretic calculation (see top of figure 7.6). The difference $\mu_{diff.}(v)$ is now calculated by an experimental and simulated input and the variation of τ_0 is used to approximate different compound responses. The parameters of the adhesion law are adopted revealing again the possibility to adjust the parameters $c = 0.12$ and $v_0 = 0.11\mathrm{m/s}$ and to change the parameter $\tau_0 = 5/4/3\mathrm{MPa}$ material dependent, see figure 7.9.

In a next step, the gained adhesive coefficient of friction $\mu_A(v)$ is added in contrast to the last subsection with a variation of the parameter α to the purely hysteretic result in order to reproduce the soap-water and dry measurement. The full adhesive contribution is again assumed for the dry surface and hence α is set to one, see figure 7.10. The dry experimental result is reproduced quantitatively and qualitatively better than in the last subsection by the original procedure. Furthermore, the increasing trend over velocity is reproduced and the ranking of the materials is correct for all velocity values. The next macroscopic setup is calculated to approximate the soap-water measurement by setting the parameter α to a value between one and zero. By setting α to 0.3 for all rubber compounds, the experimental results are approximated quite well, reproducing the trend over velocity and the correct ranking of the materials. Following the new

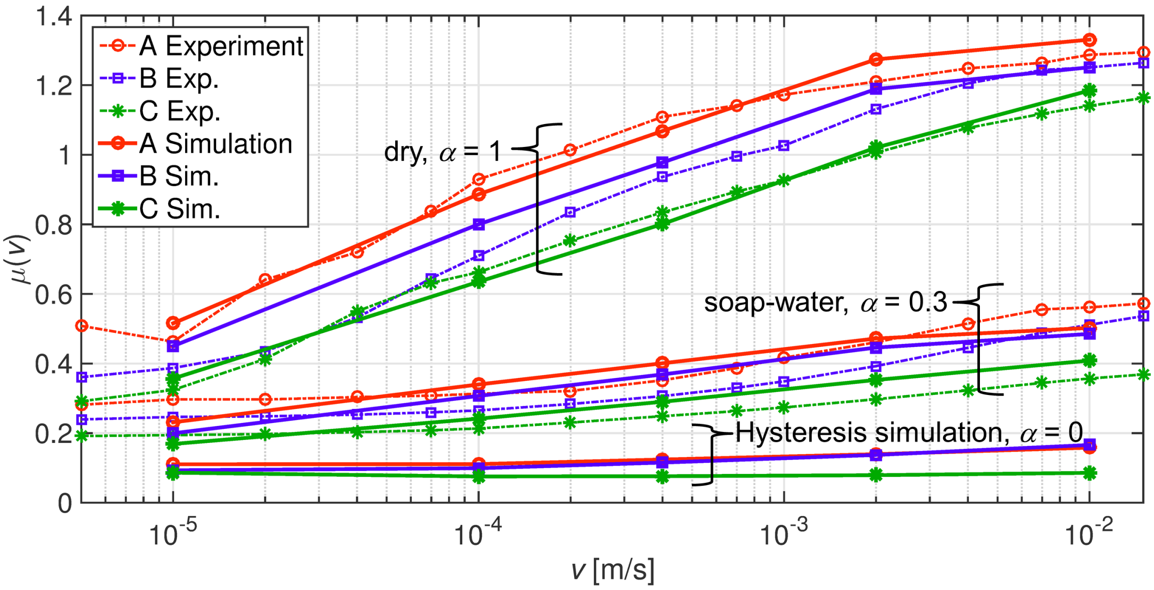

Figure 7.10: Experimental results (dashed lines) for dry and soap-water surface conditions. Numerical results (solid lines) calculated with the multiscale finite element framework for three materials A, B and C with adapted coefficient α for different surface conditions.

assumption, an adhesive share of 30% is assumed for this particular rough surface covered with soap-water.

Nevertheless, it has to be mentioned that for example also different effects are used in literature to close the gap between pure hysteretic calculations to the experimental results on a surface covered with soap-water. For instance, in LORENZ ET AL. (2015) the assumption of filler-road interaction is introduced, adding a constant coefficient of friction to the hysteretic response. The measured velocity-dependency of the soap-water response in this work would be captured less accurate with an added constant. Furthermore, certain measured input parameters may influence the absolute level of the coefficient of friction. For instance, the correct choice of fitted material parameters may change the hysteretic response. The exclusion of surface polishing effects and the use of an appropriate surface measurement may also influence the result if a lot of friction experiments are performed on the same surface (see subsection 6.5.3). In addition, a higher lateral measurement resolution for the microscopic surface could introduce further microscopic surface details increasing the absolute level of the pure hysteretic simulation. Consequently, also a combination of all effects could contribute to the gap between soap-water measurement and hysteresis simulation. In this work the introduced assumption of adhesive interactions being already present on soap-water covered surfaces is checked, revealing a good possibility to close the detected gap.

Chapter 8

Thermomechanical Extension of the Multiscale Approach

The chapter starts with an overview of numerical approaches dealing with temperature effects of sliding rubber samples and thermomechanical interactions which are modelled with multiscale approaches. In the second section, the flash temperature effect observed for sliding rubber samples is described in detail, completing the descriptions of chapter 2. Based on this description, a new approach to include thermomechanical coupling in the proposed multiscale setup is introduced in section 8.3. Afterwards, the most important parameters, effecting the results achieved with this method, are analyzed with numerical studies in section 8.4. In the last subsection the multiscale method and single aspects of it are validated with experimental results.

8.1 Review of Numerical Approaches

A brief overview of numerical approaches addressing thermomechanical coupling for rubber friction and multiscale approaches will be given in this section. In principle, two categories of studies are available: single scale approaches and multiscale methods. Important features of the numerical studies are summarized starting with single scale approaches.

In HOFSTETTER ET AL. (2006b), a thermomechanical analysis is used for a macroscopic sliding rubber block with the coefficient of friction in the contact formulation, leading to heating of the rubber block. In contrast to the introduced multiscale method in this work, no rough surface profiles are modelled in HOFSTETTER ET AL. (2006b). The analysis studies a different number of sipes (cuts) in a rubber block, the resulting pressure under the rubber block, temperature distribution, and wear of the macroscopic rubber block. A pressure and velocity dependent macroscopic friction law with six parameters is used for the study and a temperature dependency is additionally introduced by a WLF-transformation. Moreover, an empirical law for the contact heat transfer coefficient h_c (compare section 4.4) with further parameters is applied and the heat distribution parameter κ is assumed to be pressure dependent with two additional fitting parameters. Summarizing, in HOFSTETTER ET AL. (2006b) a large set of fitting parameters is introduced that depends on the used rubber material, rough surface, and further quantities. In contrast, in this work it is tried to use the minimal amount of fitting parameters for the thermal interaction. Furthermore, hysteretic effects are modelled directly and adhesion is added by a phenomological adhesion law, see chapters 6 and 7, providing already fewer parameters and a more direct modelling approach.

In Temizer & Wriggers (2010b), a complex multiscale setup based on contact homogenization techniques (see section 6.1) is proposed. The aim of the approach is to provide an accurate procedure to identify the thermal contact heat conductance (expressed by the parameter h_c in this work) based on micromechanical properties of the introduced rough surface. Similar to the multiscale approaches for sliding rubber samples, macroscopic contact variables such as surfacial stretch, contact pressure and heat flux are applied on a representative periodic microscopic RVE with rough surface details in a thermomechanical analysis. A dissipation analysis leads to the prediction of the macroscopic temperature and consequently to the heat conductance parameter. Further studies exploring the response of microscopic random rough surfaces can be found in Temizer (2011), and an extension to isogeometric contact algorithms is explored in Temizer (2014). In Sadowski & Stupkiewicz (2010), an effective contact heat conductance parameter is determined by homogenization of micromechanical finite element setups with rough surfaces, describing the quantity for different real contact area fractions. Moreover, in Temizer (2016) also a complex approach for the determination of the distribution parameter κ for the dissipative frictional interaction for two rough interfaces is developed.

The cited thermomechanical multiscale approaches are often limited to intensive miromechanical studies providing interesting features with respect to macroscopic variables, for example the pressure dependency of the thermal contact conductance. Nevertheless, a real coupling with communicating scales and simulations on all introduced scales (like in Temizer & Wriggers (2008); Wagner et al. (2015, 2017)) is not established so far. Therefore, this work concentrates on the proposal of a multiscale framework for sliding rubber samples that is suitable to describe large sliding distances and the most important thermomechanical effects. In order to achieve this goal, less attention is paid to the identification of the parameters h_c and κ in this work.

8.2 Flash Temperature Effect

During sliding of a rubber sample on a dry rough counter surface, a significant heating is observed above a sliding velocity of $v = 1\text{mm/s}$, see Persson (2006) and Persson (2014) for an analytical forecast of this velocity bound, and Linke et al. (2014) or Fortunato et al. (2015) for experimental values. A decreasing global coefficient of friction for high velocity values is predicted by analytical theories that incorporates temperature effects, cf. Persson (2006). In contrast, theories neglecting temperature effects overestimate the frictional response for high velocities. Therefore, thermal effects are added to the already proposed numerical multiscale framework. Since the interface temperature rises locally to a high level after very small sliding distances, thermal effects for sliding rubber samples are in literature often named flash temperature effects, cf. Persson (2006). Being already present for very small sliding distances, the flash temperature effect can be separated from a rise of the internal rubber temperature (often called background temperature) due to very long sliding or rolling distances.

Mainly, two physical effects contribute to the frictional heating of sliding rubber samples. First of all, hysteresis induced by rough surface asperities and its associated energy dissipation causes an internal heating of the rubber block, see section 2.2. The second heat source is attributed to adhesion at the rubber road interface on a nanometer length scale and is referred to as frictional heating. Combined, both effects induce a significant temperature increase inside the rubber block and on the contact surface. Consequently, the temperature dependent viscoelastic properties of the rubber material change (see subsection 3.3.1), shifting the spectrum of the loss-modulus to higher frequencies. This results in a more elastic and less viscous response for the considered excitation frequencies of the rough surfaces. Consequently, this leads to the described decrease of the global frictional response.

Furthermore, wear of the rubber sample may influence the whole thermal response since energy is dissipated in a wear process and less heat build up of the contact surface due to removed rubber material could change the thermal behaviour as well. Like in the previous chapters, wear is not considered in this work and postponed to future studies. Due to this fact, rubber samples after a run-in phase with a stationary profile and a worn down leading edge are used for validation.

8.3 Extension of the Multiscale Framework

In this section, the general framework of the extended multiscale method is explained in detail introducing a thermomechanically coupled calculation at the macroscopic length scale. Before the general framework is outlined in subsection 8.3.2, some important model assumptions are introduced in subsection 8.3.1. The descriptions are followed by details regarding the evaluation procedure for the quantities which have to be transferred between the scales in subsection 8.3.3. Finally, a few implementation aspects within the finite element software ABAQUS are given in subsection 8.3.4.

8.3.1 Model Assumptions

In order to solve the problem at hand in an acceptable calculation time, a simplification is introduced. An important feature of hysteresis is that most of the energy dissipation and generation of the hysteretic friction occurs close to the rubber contact surface in micrometer range since small length scales contribute most to the whole response, see Persson (2001) and cf. section 2.2. Thus, the hysteretic contribution is reduced to a surface contribution for the later described coupling via the coefficient of friction and added to the adhesive friction component. This treatment reveals some advantages with respect to the proposed multiscale setup, since the hysteretic interaction is already available by the homogenization steps in the shape of a coefficient of friction and therefore directly usable in this way, compare chapter 6. In principle, an appropriate coupling would be created by a transfer of the microscopically dissipated energy into the bulk of the macroscopic length scale predicting a correct temperature gradient inside the rubber block. It has to be remarked that the highest temperature could be reached a few micrometers inside the rubber block using such a coupling strategy, see Fortunato et al. (2015) for instance. Such a coupling strategy would need a very finely resolved thermomechanically coupled mesh on the macroscopic length scale. Due to this fact, it would be rather difficult to solve such a problem in reasonable calculation times with finite elements embedded in a multiscale framework.

Following section 8.1, a complex multiscale approach to determine the constitutive contact parameters for the contact heat conductivity h_c and the dissipation factor κ is omitted, cf. section 4.4. Furthermore, no experimental values are provided in the validation program to set these parameters. Hence, a simplified treatment is proposed and the parameters are not used to fit experimental temperatures or friction forces, see section 8.1. Since hysteresis and adhesion can be attributed to the rubber block, the dissipation factor is set to $\kappa = 1$ distributing the heat in a first step directly to the rubber block. Meanwhile, the contact heat conductivity h_c is assumed to be very large, ensuring almost the same surface temperature for both bodies in very short time intervals. In the validation program the road and the rubber surface temperatures are observed to be similar which supports the chosen conditions. A parametric study of the contact heat conductivity h_c using an analytical approach can be found in Persson (2014). Some measurements of h_c for normal contact of rubber with rough surfaces can be found in Persson et al. (2010), listing for example air gap heat transfer coefficients above $h_c = 1000\mathrm{W/m^2K}$ for pressures around $p = 50\mathrm{kPa}$. The proposed assumptions exclude both parameters as fitting values from the analysis providing consistency to those experimental observations.

8.3.2 General Framework

The proposed multiscale method of chapter 6 is extended towards the incorporation of thermomechanical effects providing the ability to predict a decreasing coefficient of friction for large sliding velocities, cf. section 8.2. The extension focuses on the most important aspect of the coupled thermomechanical problem at hand: the changing viscoelastic material properties due to an increased temperature inside the rubber block near the contact surface causing the decrease of the coefficient of friction. The relaxation times are modelled temperature dependent to achieve the shift in the frequency range of the material (see subsection 3.3.1), influencing directly the dissipation behaviour on all scales.

The main idea of the proposed extension of the multiscale method is to calculate the macroscopic length scale with a full thermomechanical coupling. The hysteretic part of the coefficient of friction is gained by the approach introduced in chapter 6 and a constant adhesive part is added at the macroscopic scale, omitting the fitting procedure of chapter 7. At the contact interface frictional energy is generated depending on the applied friction coefficient. This frictional energy causes a heat build up at the contact interface in this coupled calculation, following the assumptions of the previous subsection 8.3.1. Consequently, this heat source generates a temperature gradient inside the rubber material and the relaxation times of the used viscoelastic material model have to be changed accordingly. All lower scales below the macroscopic scale are calculated with a pure mechanical setup, but with changed material properties with respect to the macroscopic temperature gradient. This procedure generates a different hysteretic coefficient of friction induced by the rough surface. Afterwards, this changed frictional response is coupled back to the macroscopic calculation by inserting the coefficient of friction in the contact formulation. In contrast to a temperature independent multiscale setup, the whole procedure is repeated a few times during one macroscopic sliding process. Consequently and in contrast to chapters 6 and 7, the whole procedure is made time-dependent at the macroscopic scale. Furthermore, the very fast changes of the flash temperature during the beginning of the sliding process can be considered.

The extended method is displayed in figure 8.1, showing all details for two exemplary scales, although the method is extendable to more scales and more surface samples, cf. chapter 6. In detail, the multiscale setup starts with the described hysteretic mechanical setup of section 6.3 for the global parameters p_1 and v_1, generating the homogenized coefficient of friction for the used background temperature T_0. This temperature is set to 20°C in most studies. The resulting coefficient of friction $\mu(T_0)$ is then applied in step A) shown in figure 8.1 and enters directly the contact formulation of the thermomechanically coupled macroscopic simulation. It is used as a dissipative heat source generating a high temperature at the contact interface distributed by heat conduction inside the rubber block.

The mechanical weak form for the macroscopic scale of chapter 6 is completed by the introduction of a thermal part and solved for both bodies $i = 1, 2$ using the contribution for solid bodies G_θ^b (see equation (3.89)) and the thermomechanical contact part G_θ^c (see equation (4.26)).

An adiabatic setup concentrating on the temperature effects at the contact interface is introduced with external heat fluxes set to $\hat{\boldsymbol{q}} \cdot \hat{\boldsymbol{n}} = 0$. The start temperature is T_0 in the whole domain (for the rubber and road block $\mathcal{B}_0^1$ and $\mathcal{B}_0^2$) and the rubber temperature is kept constant at T_0 on top of the rubber block $\partial_t \mathcal{B}_t$, cf. subsection 6.2.2.

On the macroscopic scale both bodies are modelled, in contrast to the mechanical calculations of the last chapters, with two-dimensional thermomechanical finite elements, see chapter 5 for details. On the lower scales pure mechanical calculations are performed and thus the road surface is modelled like in the previous chapter with discrete linear line elements. The multiscale method including temperature effects, all numerical studies and the experimental validation are calculated within ABAQUS. The thermomechanically coupled elements of the macroscopic scale require additional material parameters, i.e. heat capacities c_i, heat conductivities k_i and mass density values ρ_i for both materials, rubber (1) and road material (2). Additionally, a temperature dependent viscoelastic response can be included in the analysis. This effect can be added by setting the parameters of the WLF-transformation, see subsection 3.3.1, including a shift of the relaxation times. Furthermore, an internal dissipation D_{int} is neglected in the introduced solution for the macroscopic scale, since the contribution on this scale is in contrast to the microscopic contribution negligible. Thermal effects

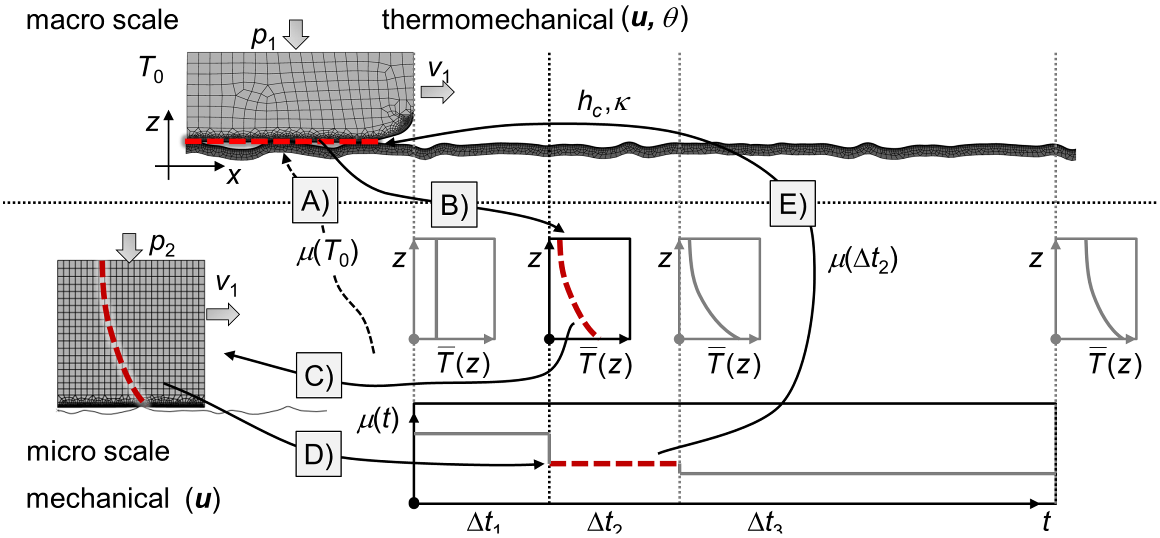

Figure 8.1: Extended multiscale framework with two exemplary scales. A) First thermomechanically coupled macroscopic simulation. B) Evaluation of macroscopic temperature gradient. C) Application of temperature gradient on microscopic length scale. D) Microscopic Homogenization. E) Application of microscopic coefficient of friction at the macroscopic scale in the second time interval.

at the contact interface are included by activating the thermal contact parameters in the analysis, see section 4.4. The parameters h_c and κ for dissipation and heat conductivity need to be defined for the two thermal interactions at the contact surface, see subsection 8.3.1 for the choice of these parameters.

During a few sliding steps of the coupled macroscopic simulation, the surface temperature increases drastically and the simulation is stopped to start a new set of calculations on the lower scales with adapted material properties, see step B) in figure 8.1. Thus, the temperature distribution near the contact surface inside the rubber block is evaluated. The temperature gradient changes along the sliding direction. In order to provide a defined value for all microscopic scales, a spatial homogenization over the x-direction is performed resulting in an averaged gradient $\overline{T}(z)$. This procedure is described in subsection 8.3.3 in detail. This representative temperature gradient for the macroscopic sliding interval is used to modify the relaxation times of the rubber material over block height on all lower scales by a WLF-transformation, see step C) in figure 8.1 and the following subsection 8.3.3 for details.

The pure mechanical microscopic setups with adopted material properties result in a reduced coefficient of friction that is evaluated by time homogenization in step D), following subsection 6.2.2. This value is then applied to the frictional dissipation in the next macroscopic time interval (step E)) until the simulation is stopped again, because the temperature gradient increased. All steps are repeated until the final sliding distance of the macroscopic rubber block is achieved. Since the temperature gradient changes very fast at the beginning of the sliding distance, it is recommended to use more time intervals at this state and less later on.

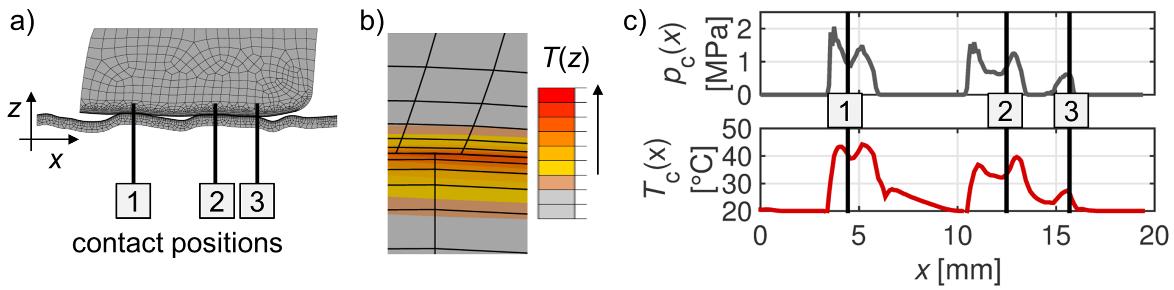

Figure 8.2: a) Macroscopic thermomechanical calculation with three exemplary contact positions. b) Exemplary temperature field at the contact interface. c) Contact pressure and contact temperature distribution along the rubber surface.

8.3.3 Temperature Gradient

The spatial averaging and evaluation of a defined temperature gradient for the lower scale simulations and the setup of mechanical calculations with changed material properties are explained in this subsection in detail.

First of all, the thermomechanically coupled macroscopic simulation provides a spatial resolved temperature field θ for the rubber block. Since a high gradient of the temperature is expected with very high local temperatures $T_c(x)$ at the contact interface caused by the frictional dissipation, the macroscopic finite element mesh is resolved much finer in z-direction than in sliding direction, see figure 8.2 a)-b). Due to the irregular appearance of the rough surface and locally different sliding conditions, different temperature distributions occur over the x-direction of the macroscopic rubber block.

The macroscopic pressure distribution $p_c(x)$ is evaluated in order to determine the positions of active contact nodes, cf. figure 8.2 c). In figure 8.2, three exemplary contact positions with different surface temperatures are marked. In order to define the temperature gradient for the lower scales, the temperature gradients for all active contact nodes n_a are evaluated, see figure 8.3 a) for the gradients of the mentioned

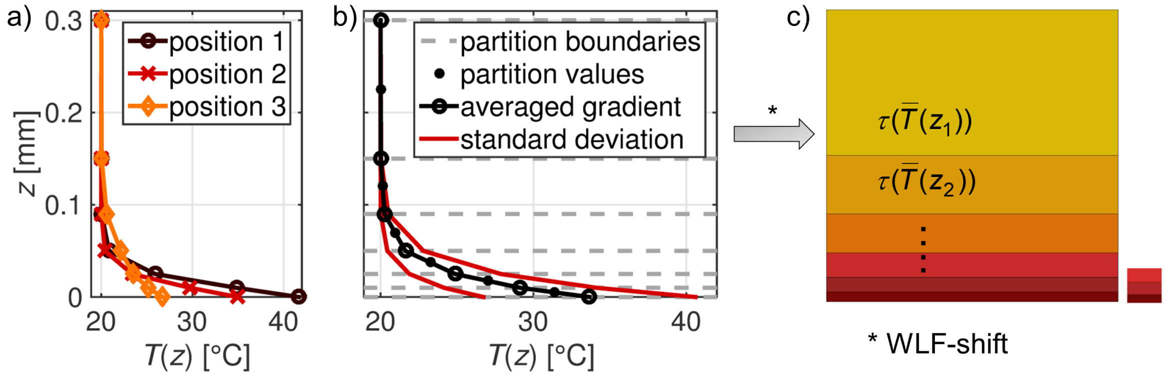

Figure 8.3: a) Temperature gradients at three exemplary contact positions and averaged temperature gradient for lower scales. b) Applied partitions with changed relaxation times. c) Visualization of the material parameter adaption on two exemplary microscopic scales.

three contact positions providing an example.
Accordingly to the evaluation of the macroscopic pressure values of section 6.3, it offers an advantage in calculation time if the passed information to the lower scales is reduced. Furthermore, the reduction of information becomes necessary for a setup with several scales accomplished by a certain number of surface samples on each scale. Hence, the evaluated temperature gradients are averaged over x-direction

$$\overline{T}(z) = \frac{1}{n_a} \sum_{k=1}^{n_a} T(x_k, z). \tag{8.1}$$

The spatially averaged and summarized value $\overline{T}(z)$ is applied to the lower scales, see figure 8.3 b). Since the temperature gradients differ locally, also a standard deviation is calculated and displayed providing bounds for the most frequent values.
In the finite element setup, linear shape functions are used to solve the temperature field. For the smaller scales the stepwise linear macroscopic temperature gradient is transferred to a stepwise constant representation of the temperature gradient. This step simplifies the transformation of the obtained macroscopic information to the lower scales, since a defined number i of a few partitions over height is introduced and the material parameters just need to be adopted for every partition, see figure 8.3 b). The microscopic scales are constructed with different material properties over the height of the rubber block according to the calculated temperature values, using the resolution provided by the macroscopic mesh in z-direction. The boundary values of each partition are averaged to obtain a defined constant partition value.
In figure 8.3 c), two exemplary lower scales with the introduced partitions are displayed. According to the partition temperature $\overline{T}(z_i)$ the relaxation time of the viscoelastic material is shifted with the WLF-transformation, cf. equation (3.37) and subscetion 3.3.1 for details. These modified material properties lead to a different hysteretic response which results in a changed and here decreasing coefficient of friction, cf. section 8.2. The influence of the chosen partitioning and the necessary resolution to approximate the macroscopic temperature gradient sufficiently are studied in subsection 8.4.2.

8.3.4 Implementation

In order to achieve results without a very complex implementation and development of various Python scripts in ABAQUS, a simple procedure is established in this work to perform the homogenization steps. Furthermore, the work focuses on the achievement of first results with the extended multiscale method, demonstrating the ability of the method to reproduce the most important physical temperature effects.
The macroscopic simulation is stopped after each time interval t_i and the simulations on all lower scales are performed after the macroscopic temperature gradient is evaluated. The gradient is used to define partitions with modified material properties for the finite element models on all lower scales, see last subsection 8.3.3. This part offers large potential for automation, because after every interruption of the macroscopic calculation, a few scales and a certain number of surface samples are calculated on each scale. After the first homogenization step (step 1 in upper right part of figure 8.4 b)),

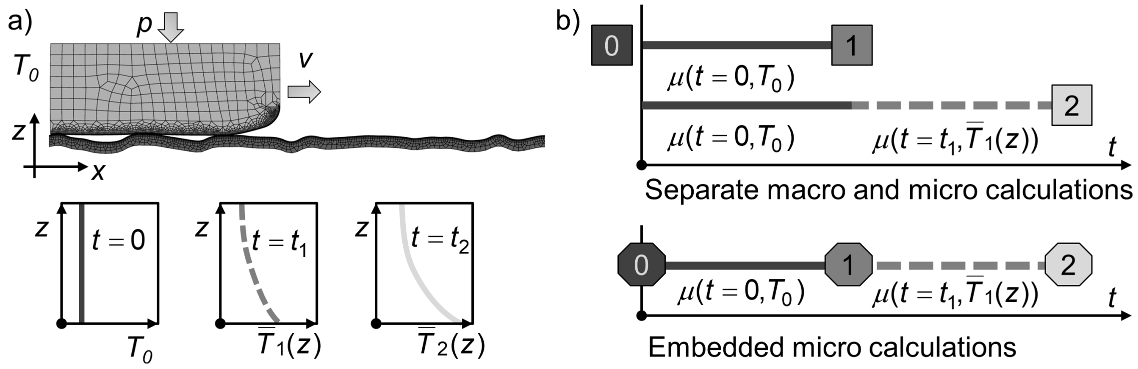

Figure 8.4: a) Exemplary macroscopic simulation with averaged temperature gradients at times t_1 and t_2. b) Possible procedures to implement the proposed multiscale method.

a second macroscopic calculation is started due to the fact that the first macroscopic calculation was stopped after the first time interval. With this procedure, additional computational effort is introduced by recalculating the first time interval until the simulation is stopped again to evaluate the behaviour of all lower scales and so forth. Nevertheless, the implementation is kept rather simple and the recalculation of the macroscopic scale requires less effort than the homogenization procedure on all lower scales. Therefore, the implementation displayed at the upper right part of figure 8.4 b) is used in this work.

In contrast to the approach for hysteretic and adhesive friction, the thermomechanically coupled approach is not yet fully automated with Python scripts. Since the macroscopic calculation is interrupted a few times, a direct evaluation of the temperature gradient (compare subsection 8.3.2) and automated down-passing to all lower scales would provide an appropriate solution for the problem at hand. Also the up-scaling part and the incorporation of the modified microscopic coefficient of friction offer a lot of potential for a completely automated solution. Such a procedure would result in a macroscopic calculation that is interrupted for the evaluation of all lower scales and continued after the result is incorporated in the macroscopic contact formulation, compare subsection 8.3.2. The possible procedure is displayed schematically in the lower right part of figure 8.4 b).

8.4 Numerical Studies

Sensitive quantities exerting influence on the global results of the extended multiscale method are identified in this section and studied in detail. The first quantity, the resolution of the macroscopic finite element mesh in z-direction, is analyzed in subsection 8.4.1. Afterwards, a microscopic example and the convergence of the frictional homogenization with respect to the level of partition refinement in z-direction is studied in subsection 8.4.2. A very important quantity determining the solution of the whole multiscale setup is the choice of points in time in a homogenization loop on all lower scales. This quantity is studied in subsection 8.4.3.

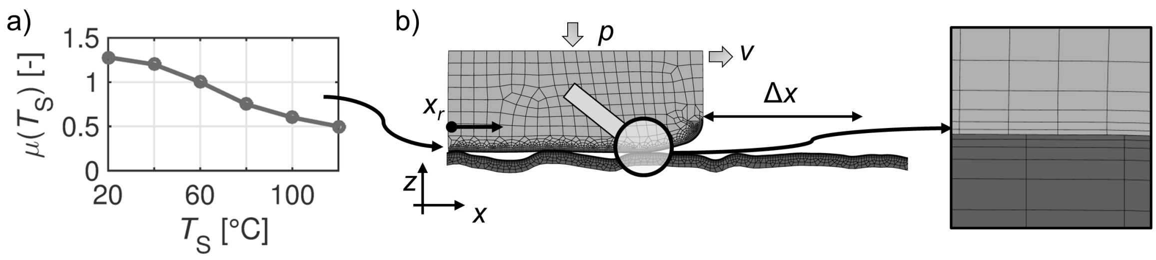

Figure 8.5: a) Applied coefficient of friction depending on surface temperature T_S. b) Simulation setup with interface details. Conditions: $p = 0.3\text{MPa}$, $v = 1\text{m/s}$, $l = 20\text{mm}$, $h = 8\text{mm}$, $\Delta x = 10\text{mm}$, $h_c = 10\text{mW/mm}^2\text{K}$, $\kappa = 0.9$, rubber compound m1, road material r1.

8.4.1 Macroscopic Mesh Study

At the contact interface, a high temperature gradient is expected for a thermomechanically coupled simulation of rubber sliding on a rough surface. A macroscopic single scale simulation is performed in this subsection to determine the convergence for local mesh refinement at the interface. The setup for the study is displayed in figure 8.5. In order to generate high temperatures at the interface, a high coefficient of friction is applied within the contact formulation, $\mu = 1.28$ at 20°C surface temperature. In addition, the coefficient of friction depends on the surface temperature T_S, see figure 8.5 a). This dependency is introduced to imitate the expected macroscopic behaviour described in section 8.3. The trend over temperature is extracted from the example in 8.5.3. To provide a high interface temperature, also a large global velocity of $v = 1\text{m/s}$ is used in this setup. All used parameters are listed in figure 8.5 and detailed thermomechanical material parameters are provided in appendix C. The finite element meshes of both bodies, rubber block and road surface, are refined equally in z-direction, see figure 8.5 b), although the slave mesh (rubber side) is discretized finer in x-direction. The introduced node distribution near the contact interface ($0\text{mm} - 0.09\text{mm}$) is displayed for three meshes n_m in figure 8.6 a). In figure 8.6 b)-d) the results of three

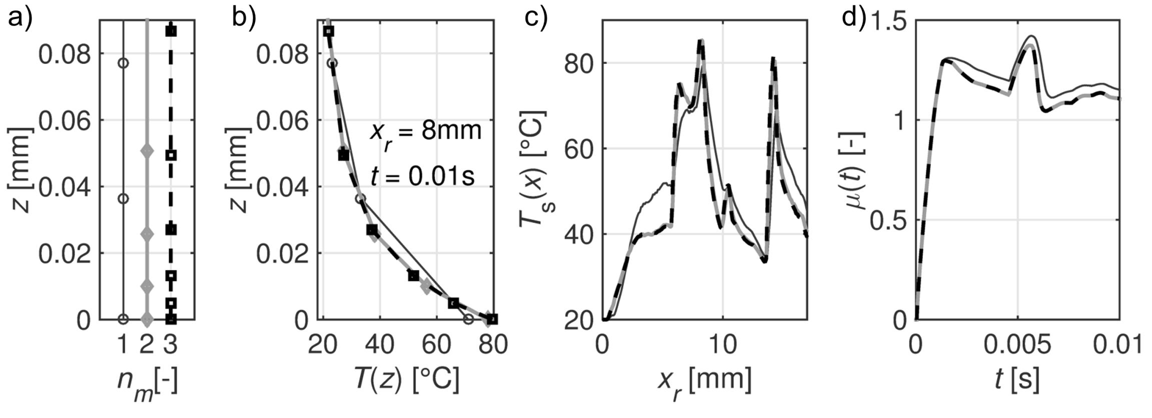

Figure 8.6: a) Mesh resolution near the interface for three different meshes. b) Resulting temperature gradient at rubber $x = 8\text{mm}$. c) Surface temperature after $\Delta x = 10\text{mm}$, d) Coefficient of friction over time.

different resulting quantities are displayed: an exemplary temperature gradient, the surface temperature for 17mm of the rubber block which are in contact for the last time step and the resulting macroscopic coefficient of friction. The results reveal that with the second discretization, converged results for all quantities are achieved, whereas the first mesh predicts incorrect temperature gradients, surface temperatures and consequently different coefficients of friction. Other global parameters, like higher sliding velocities, may change the needed level of mesh refinement. But as described above, particularly large values for μ and v were chosen in order to provide large heating at the interface. The second mesh with the position of the first macroscopic node at $z = 0.01$mm is used as a reference for later calculations in order to resolve high temperature gradients.

8.4.2 Homogenization Study

The temperature gradient has to be resolved on the microscopic scales, similar to the macroscopic level, with a sufficient accuracy by the introduced partitions with different material properties. The effect of the partition refinement on the homogenization result of an exemplary microscopic calculation on a rough surface sample is studied in this subsection, see figure 8.7 a). Two arbitrary macroscopic temperature gradients are introduced, see figure 8.7 b), and approximated by four different representations of partitions, see figure 8.7 c). Since the gradients are averaged over the macroscopic block length in a multiscale study, the surface temperatures are on a lower level compared to the local values. The number of partitions n_p below $z = 0.09$mm is used as the identifying number for the level of refinement. The material values for each partition are determined for all four representations (shifted relaxation time) via a WLF-shift, see subsection 8.3.3 for a description of the procedure and appendix C for the used material parameters of compound m2.

The frictionless microscopic calculation is performed for both temperature gradients and with all partition refinement levels leading to the coefficients of friction displayed in figure 8.8 a). First of all and in correspondence to the described qualitative expectations

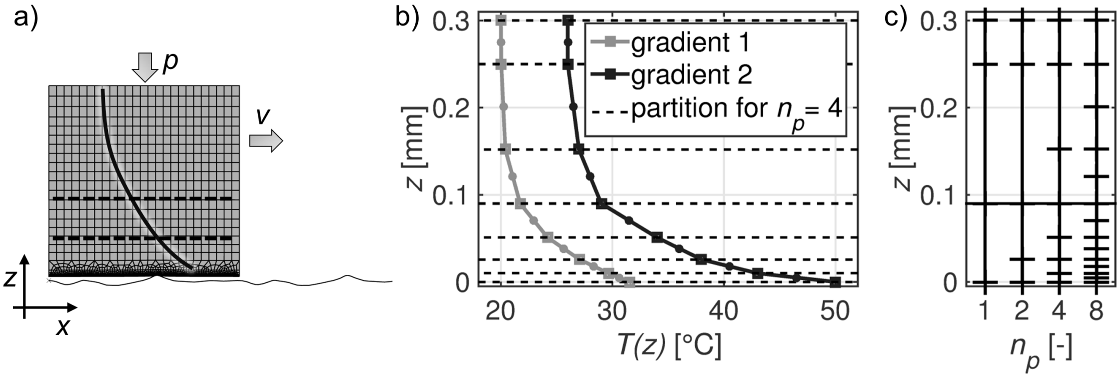

Figure 8.7: a) Microscopic setup with $p = 1.5$MPa, $v = 0.5$m/s, $l = h = 0.3$mm, $\mu = 0$, rubber compound m2, b) Applied temperature gradients. c) Used partition representations for the rubber block

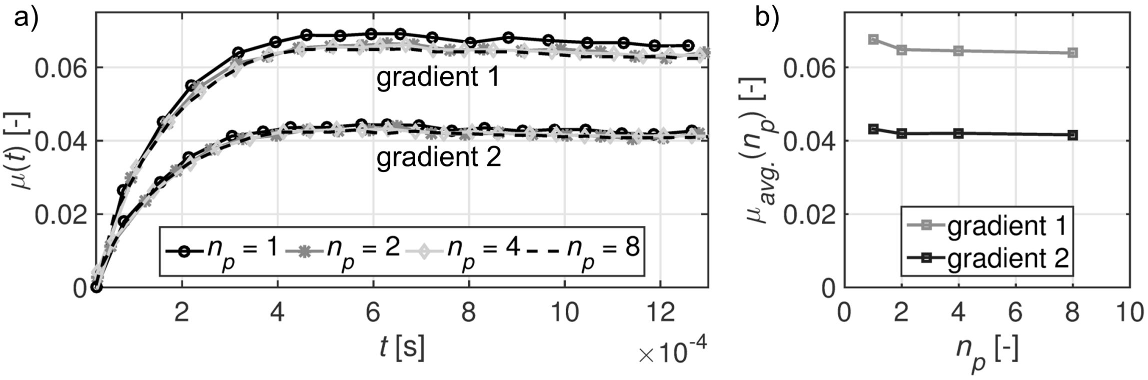

Figure 8.8: a) Resulting coefficient of friction for both temperature gradients over time. b) Homogenized coefficient of friction over number of partitions.

of sections 8.2 and 8.3, the gradient with higher temperature values (gradient 2) results in a lower level of the gained coefficient of friction. Second, no large deviations for different partition refinement levels are observed. This is displayed with the time averaged values $\mu_{avg.}$ in figure 8.8 b). Consequently, also large temperature gradients can be approached with a rather low number of rubber partitions for the microscopic scales in a multiscale setup.

8.4.3 Choice of Multiscale Homogenization Points

Within the proposed thermomechanical multiscale method a free model parameter is introduced: certain points in time have to be chosen for which the macroscopic calculation is interrupted and a temperature gradient is passed down to the microscopic length scales. For each interruption, a homogenization loop is applied on all lower scales.

In order to study this parameter, a two-scale setup with a macroscopic and a microscopic scale is constructed, see figure 8.9 and appendix C for the used material parameters. With the intention to examine the influence of the chosen homogenization points, the macroscopic time interval $\Delta t = 0.02s$ is divided with an increasing number of divisions n_d for which the temperature gradient is evaluated and passed to the microscopic scale. The time interval Δt is divided in $n_d = 1, 2, 4, 8$ divisions and the

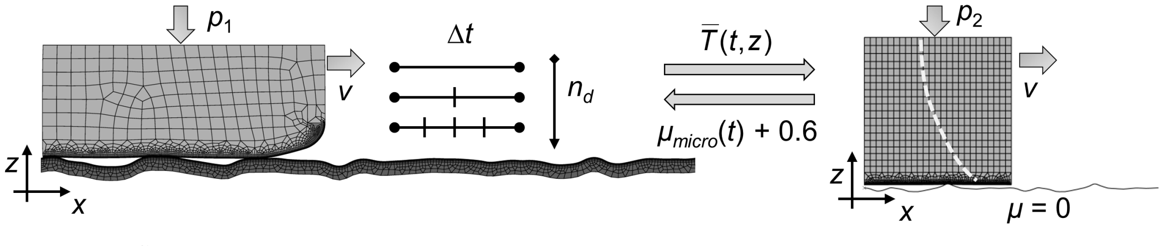

Figure 8.9: Setup with macroscopic values $p_1 = 0.3\text{MPa}$, $l_1 = 20\text{mm}$, $h_1 = 8\text{mm}$, $\kappa = 1$, $h_c = 10^6\text{mW/mm}^2\text{K}$, road material r1. Microscopic values $p_2 = 2\text{MPa}$, $l_2 = h_2 = 0.3\text{mm}$. Common velocity $v = 0.5\text{m/s}$ and rubber compound m2.

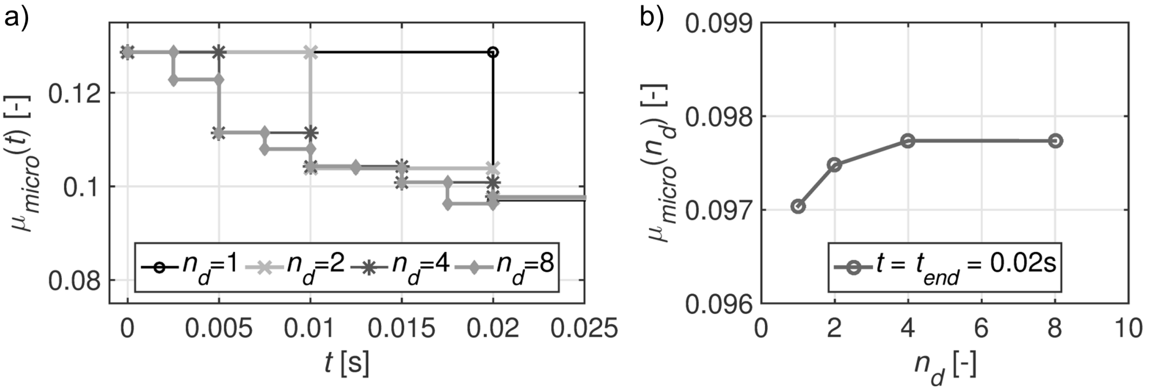

Figure 8.10: a) Microscopic coefficient of friction over time for different divisions. b) Final microscopic coefficient of friction for different division numbers n_d.

two-scale simulation is performed for each division number, see figure 8.9.

The averaged temperature gradient $\overline{T}(t, z)$ of the macroscopic calculation is passed to the microscopic scale after each division in time. Afterwards, the homogenized coefficient of friction $\mu_{micro}(t)$ from a frictionless calculation on the microscopic scale is passed back to the macroscopic contact formulation, see subsection 8.3.2 for details. It has to be remarked that the temperature gradient and the homogenized coefficient of friction depend on the macroscopic time t, whereas the microscopic time dependency is removed by homogenization. A constant part of $\mu_{const.} = 0.6$ is added on the macroscopic scale to the homogenized microscopic coefficient of friction to imitate the contributions of the neglected lower scales and to enforce higher temperatures at the macroscopic scale. Further simulation parameters are listed in figure 8.9.

The results of the calculated microscopic coefficients of friction for all four applied divisions of Δt are displayed over the macroscopic time interval in figure 8.10 a). These values are passed to the macroscopic length scale. First of all, the method is not able to predict the real temporal evolution of the microscopic and macroscopic coefficient of friction, since the time interval is divided in pieces and the frictional response is approximated with piecewise constant values. Thus, a lot of time intervals would be needed for an appropriate reproduction of the *a priori* unknown temporal evolution of μ. The results of figure 8.10 a) support this statement. More divisions ($n_d = 8$ for example) lead to smaller steps in the evaluation and with an increasing number of divisions convergence of the temporal evolution is reachable.

Nevertheless, the introduced study focuses on statements regarding the relative prediction quality that is achieved with different divisions n_d of the macroscopic time interval with respect to the resulting coefficient of friction after Δt. Therefore, figure 8.10 b) displays the last value at $t_{end} = 0.02s$ over the applied number of divisions n_d. For an increasing number of divisions, the considered value of the microscopic coefficient of friction converges to a defined value.

By application of the high reference microscopic coefficient of friction ($\mu = 0.6 + \mu(t = 0)$) for a longer time interval with $n_d = 1$, more frictional heating is induced at the macroscopic scale than for higher division numbers n_d. This leads at the end of Δt to a higher macroscopic temperature gradient, causing vice versa a lower resulting

coefficient of friction at t_{end}, see $n_d = 1, 2$ in figure 8.10 b).
For the introduced example, the absolute difference of the resulting coefficient of friction with respect to the division number is rather low. This may change for different global conditions and by consideration of all microscopic length scales. However, this study shows that with an appropriate choice of divisions in time, a converged result can be achieved. Especially at the beginning of the sliding process, large changes of the surface temperature and the temperature gradient are expected, compare subsection 8.3.2. Thus, shorter time intervals should be used in this range in order to capture these large changes properly with the method.

8.5 Experimental Validation

Beyond the global coefficient of friction, temperatures can be measured during friction experiments. In order to verify the assumptions of chapter 8 single scale calculations are performed to validate the method. Especially, macroscopic road surface temperatures and rubber bulk temperatures measured by the Continental Reifen Deutschland GmbH and the Institute of Dynamics and Vibration Research (IDS) in Hanover are evaluated, see subsections 8.5.1 and 8.5.2. Although an exact experimental validation remains an open point, a multiscale setup with rough surfaces is calculated in the last subsection to demonstrate the global behaviour of the method with respect to the coefficient of friction over velocity.

8.5.1 Surface Temperature

In this subsection, the surface temperature generated by a friction experiment is studied and a thermomechanically coupled single scale simulation on the macroscopic length scale is validated with the experimental results. It is in general possible to predict the overall coefficient of friction of a sliding rubber block with the thermomechanical multiscale method of chapter 8, but the adequate introduction of a temperature dependent adhesive contribution remains a challenging task. Therefore, every thermal multiscale analysis would suffer from the unknown thermal adhesion properties, providing a large range of possible fitting parameters for the overall coefficient of friction. In order to

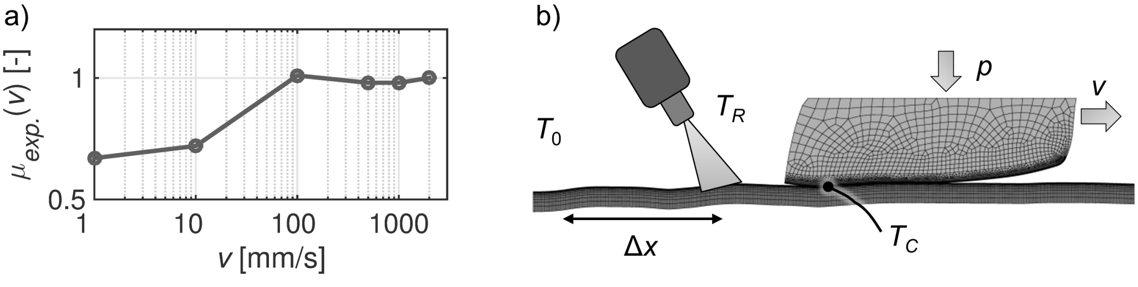

Figure 8.11: a) Measured coefficient of friction over velocity for $p = 0.3$MPa, material m3. b) Simulation setup with rubber block dimensions $l = 20$mm, $h = 7$mm and thermal contact parameters $\kappa = 1$, $h_c = 10^6$mW/mm^{2}K, $T_0 = 20$°C, road material r1 (see appendix C).

validate the prediction accuracy of surface temperatures occurring at the sliding interface, the measured coefficient of friction is used as an input for the simulation, instead of simulating it on the lower scales. Viscoelastic effects are already considered in the provided frictional response. Thus, a thermo-hyperelastic material model is used for the rubber block, neglecting the viscoelastic contribution.

In subsection 8.3.1, assumptions with respect to the coupled thermomechanical simulation at the macroscopic length scale were introduced. Especially, the assumptions of a very high heat conductance parameter in the contact zone, the total assignment of the frictional distribution parameter to the slave rubber surface, and the boundary conditions of the simulation (see also subsection 8.3.2) are validated with surface temperature measurements in this subsection.

The same temperature is observed at the sliding interface during the experiments for both bodies, rubber and road surface, see also subsection 8.3.1. A direct access to temperatures at the sliding interface is provided by a measurement of the rough road surface temperature behind the sliding rubber sample, cf. FORTUNATO ET AL. (2015). Two sets of temperature measurements are provided by experiments that are carried out at the Institute of Dynamics and Vibration Research (IDS). The first one evaluates the road temperature (T_R exp.) with a thermo-camera. The other measurement technique uses a pyrometer that measures the surface temperature of the rubber block. This is the so-called contact temperature (T_C exp). The second measurement is performed directly after the friction experiment trough a hole in the rough road surface.

The macroscopic simulation setup and its parameters are listed in figure 8.11 b). Since hysteretic effects are not modelled directly in this setup, just the thermo-hyperelastic rubber material m3 is used (see appendix C for the thermomechanical material parameters). Furthermore, the road surface is modelled with a linear elastic material with the elastic and thermal parameters also according to appendix C. Following subsection 8.3.1, a very high thermal contact conductance $h_c = 10^6\text{mW/mm}^2\text{K}$ and a dissipation factor $\kappa = 1$ are used for the thermomechanical contact interface. The thermomechanical setup of the calculation assuming a start temperature $T_0 = 20°\text{C}$, the full conversion of friction into heat (see figure 8.11 a) for the values of μ, and adiabatic conditions at all outer surfaces follow the detailed description provided in subsection 8.3.2.

An exemplary temperature distribution near the contact interface provided by the simulation is displayed in figure 8.12 a), revealing that the flash temperature is concentrated at the interface. Another phenomenon observed in experiments is that the flash temperature is already high after a very short sliding distance. Therefore, the road and rubber temperatures of the simulation are evaluated after a very short sliding interval of $\Delta x = 15\text{mm}$. The maximal road temperature is evaluated at the top of the surface asperity directly behind the rubber block with a short time delay of $\Delta t = 10^{-3}\text{s}$ for all velocities. The contact temperature is extracted a few time steps before the rubber block leaves the surface asperity at the back of the rubber block, because the contact temperature is maximal in this phase. Since already very large calculation times are reached with the fine thermomechanically coupled finite element mesh, the sliding interval of the simulation is limited to 25mm. Nevertheless, the temperatures

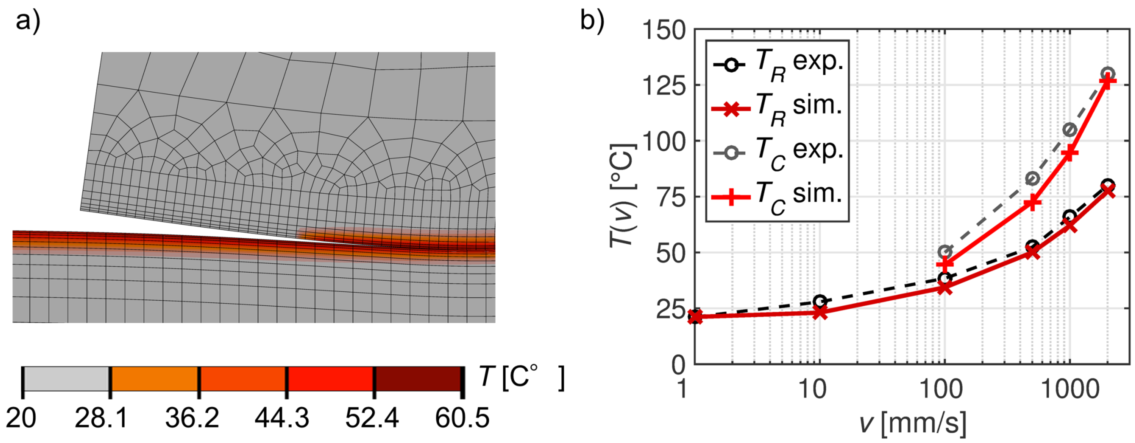

Figure 8.12: a) Simulated temperature distribution for $v = 1000\text{mm/s}$, $\Delta x = 15\text{mm}$. b) Experimental and simulated values for road and contact temperature over velocity.

are approaching their final values very fast during the simulation and therefore the gained values are compared directly to the experimental results, although these values are measured after longer sliding distances up to 200mm.

In figure 8.12 b), the evaluated simulation results are compared to the experimental values, revealing that the magnitude of the macroscopic temperatures is reached with all introduced assumptions. Furthermore, the increasing temperature trends over velocity at the contact interface T_C and on the road track T_R are captured correctly by the simulation setup, revealing that the setup is in principle able to reproduce the measured trend. Nevertheless, a gap between simulation and experiment is observed. This is attributed to the different sliding distances for the evaluation of simulated and experimental temperatures, since a longer sliding distance in experiments should cause higher temperatures at the interface. Moreover, wear effects may also change the whole thermomechanical balance at the interface being not represented by the current approach. However, the whole setup was used to validate the trend over velocity and the magnitude of the temperature values, revealing that the presented setup of a simulation on a rough surface is able to reproduce both.

8.5.2 Rubber Bulk Temperature

In this subsection, a setup for measuring rubber bulk temperatures during a friction experiment is introduced and explained. Later on, a single macroscopic scale simulation with thermomechanical coupling for long sliding distances is introduced and the temperatures inside the rubber block are calculated and compared with the measured values.

In order to be able to measure temperatures inside the rubber block, in addition to the coefficient of friction, thermocouples are placed inside the rubber block before vulcanization of the rubber specimens in a mold, see figure 8.13 a). Six thermocouples are placed at different positions along the rubber block width and over height inside the rubber block. Furthermore, the thermocouples are led through a hole in the upper metal plate of the mold, ensuring that they are not cut during vulcanization and usable

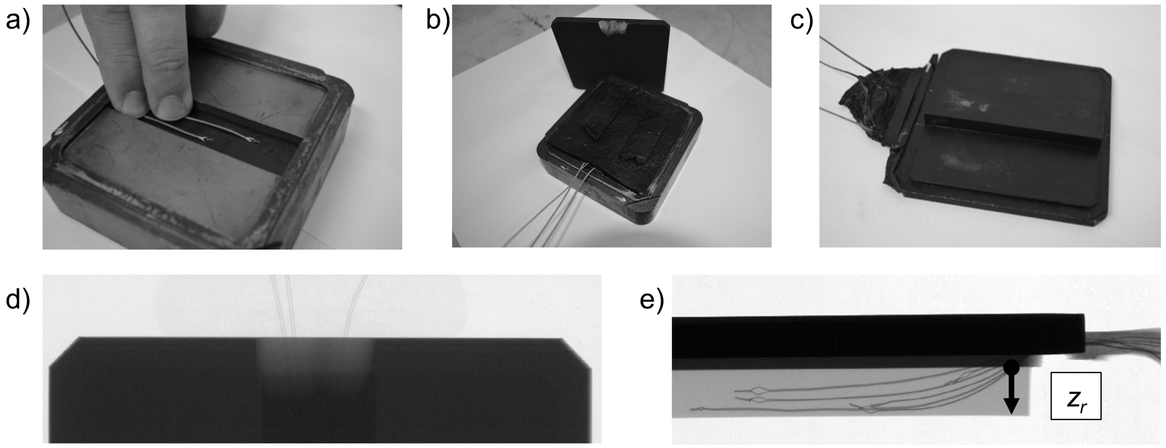

Figure 8.13: a)-b) Thermocouples inside the rubber block before vulcanization. c) Final rubber sample with thermocouples after vulcanization. d)-e) Computer tomography images of rubber block providing the positions of the thermocouples after vulcanization.

afterwards, see figure 8.13 b). In a next step, the positions of the thermocouples inside the rubber block are checked by computer tomography providing the relative coordinates over height z_r of the thermocouple ends inside the rubber block measured from top of the rubber block, see figure 8.13 d)-e). The larger z_r the closer the thermocouple is placed to the rubber surface coming in contact with the road. Furthermore, three thermocouples are placed near the leading edge in sliding direction of the rubber block (front) and three are adjusted to the backside of the rubber block (back).

These prepared rubber samples are used in a friction experiment with a sliding distance of $\Delta x = 350$mm. The friction experiment is repeated a couple of times in order to generate a temperature increase inside the bulk material. All other global parameters are listed in figure 8.14. In addition to the bulk temperatures, the temperature of

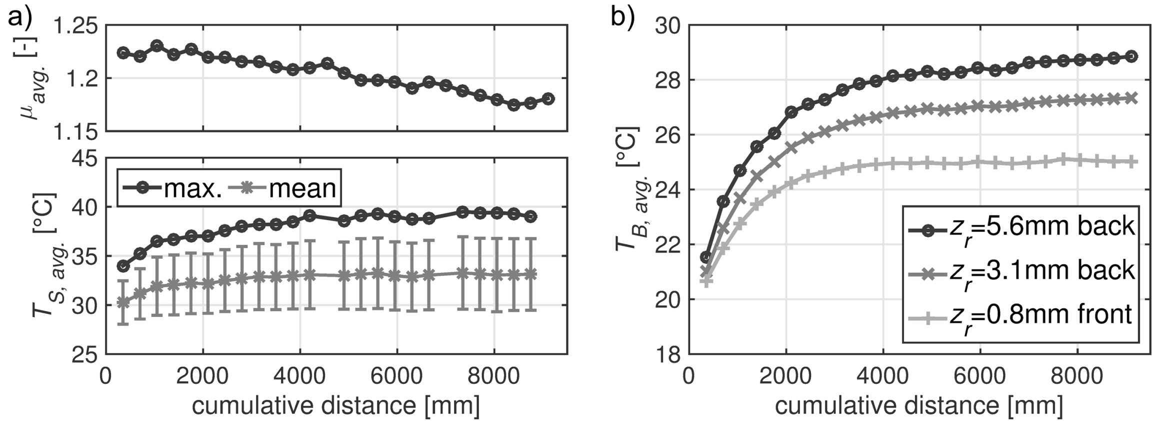

Figure 8.14: Global parameters $p = 0.3$MPa, $v = 0.5$m/s, $T_0 = 20$°C, rubber compound m2. a) Measured coefficient of friction and averaged measured surface temperature over cumulative distance. b) Averaged bulk temperature response of three thermocouples at different position z_r and different positions in sliding direction.

the rubber block bottom is measured approximately five seconds after the sliding is completed, cf. figure 2.2 c) for an exemplary measurement. The results of the coefficient of friction are averaged over sliding time for each measurement and listed over the cumulative sliding distance in figure 8.14 a). Additionally, the information provided by the surface measurement, maximal and space averaged values, are listed in figure 8.14 a). In figure 8.14 b), the averaged bulk temperature over sliding time for different positions of the thermocouples is displayed over cumulative sliding distance.

The bulk temperature changes just slightly over the sliding distance, the biggest increase inside the bulk material is noticed during the preparation for the next run of the friction experiment (duration $\Delta t = 30\text{s} - 40\text{s}$), see lower part of figure 8.16. This observation is illustrated by the plot of the bulk temperature over time for the first three friction experiments.

A thermomechanical macroscopic calculation is chosen to simulate and compare the temperatures inside the rubber bulk to the experimental values. The hysteretic effects are not considered with a multiscale setup in this subsection following the explanations of the last subsection. Thus, the whole setup is reduced to a single scale simulation on a rough surface using the experimental coefficient of friction (see figure 8.14 a)) as the input at the contact layer, causing frictional heating. Since the direct modelling of hysteresis is neglected, a thermo-hyperelastic rubber material (m2) and thermo-elastic road material (r1) are used, see appendix C for applied thermomechanical material parameters. Following the last subsection and the descriptions of subsection 8.3.2, the thermomechanical boundary conditions are set applying a start temperature, adiabatic conditions at the free edges and the same choice for the thermal contact parameters.

The main challenge of the coupled simulation is to reproduce the experimental sliding distance of $\Delta x = 350\text{mm}$, avoiding one large simulation setup with a very long rough surface, because such a setup is difficult to handle with respect to the calculation time. More elements and an extended contact search increase the calculation time drastically. Hence, a special procedure for the macroscopic simulation is introduced calculating a macroscopic setup with a sliding distance of $\Delta x = 50\text{mm}$ seven times after each other, see figure 8.15. In this way an appropriate calculation time for the single calculations and the resulting whole setup is achieved. The single separate calculations are connected by transferring the final temperature field of the rubber block $T_R(x, z)$ from the last ABAQUS odb-file as a start condition to the next macroscopic simulation resetting the temperature of the rough surface meanwhile. Consequently, the temperature inside the rubber bulk increases after each single calculation until the

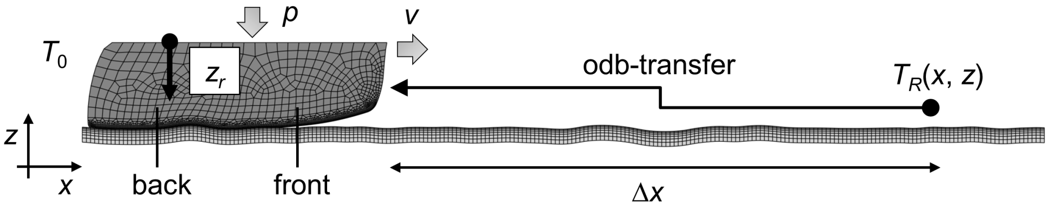

Figure 8.15: Simulation setup with global parameters $p = 0.3\text{MPa}$, $v = 0.5\text{m/s}$, $T_0 = 20°\text{C}$. Simulated sliding distance $\Delta x = 50\text{mm}$, rubber compound m2, road material r1, $\kappa = 1$, $h_c = 10^6\text{mW/mm}^2\text{K}$.

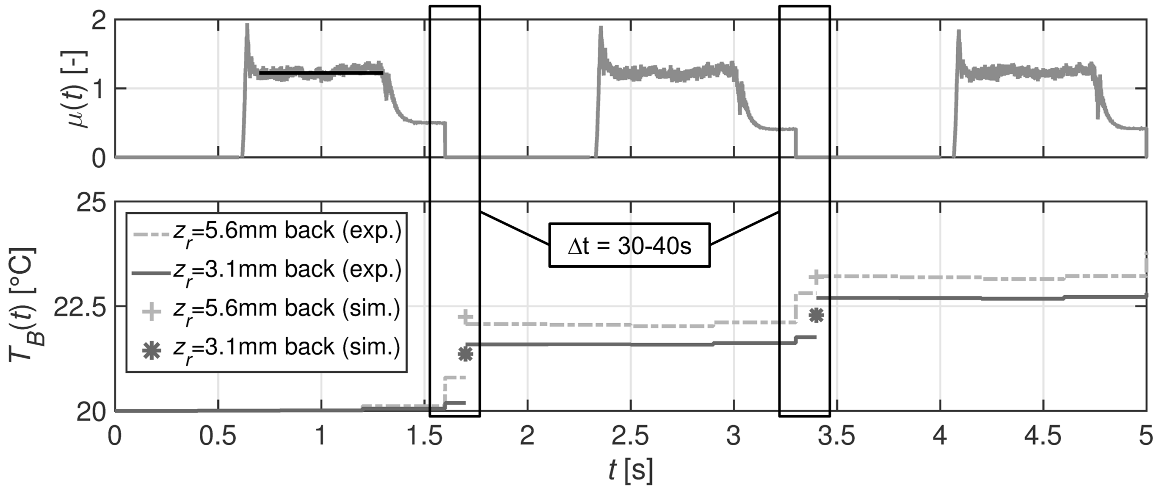

Figure 8.16: Measured coefficient of friction over sliding time (top). Measured bulk temperature over time with added simulation results (bottom). Time delay Δt represents preparation time for next experiment.

sliding distance of the experimental setup is reached.

Two experimental runs are simulated with the described setup by fourteen macroscopic simulations and the temperatures over height at the back of the rubber block can be compared to the experimental values after the first and second run. Following the conditions of the friction experiment, also a time delay of $\Delta t = 35$s after a sliding distance of $\Delta x = 50$mm is introduced in the simulation setup. In accordance to the steps at the experimental setup, the rubber block is lifted at this step and only heat conduction inside the rubber block is calculated.

In figure 8.16, the simulated values, including the time delay, are displayed revealing that these values fit quite well to the starting values of the next friction experiment measured with the thermocouples for two positions. To sum up, the time delay after the experiment causes the generated heat at the contact interface that is distributed inside the rubber block. Furthermore, this effect and the resulting temperatures are reproduced with the introduced simulation setup. In addition to the last subsection, the simulation reveals that the assumed boundary conditions for the thermomechanical setup and especially the assumptions for the interface are able to capture the internal thermal effects for sliding rubber samples in an adequate way. Nevertheless, longer sliding distances beyond the analyzed 700mm total sliding length are not examined in this work. Such long sliding distances introduce a stronger change of the rubber background temperature in the bulk, whereas flash temperature effects happen on much smaller length and time scales, cf. subsection 8.5.1.

8.5.3 Global Coefficient of Friction

In this subsection, a reduced multiscale setup based on the approach of section 8.3 is evaluated. The example is used to demonstrate the behaviour of the global coefficient of friction for a thermomechanically coupled multiscale simulation and a multiscale setup

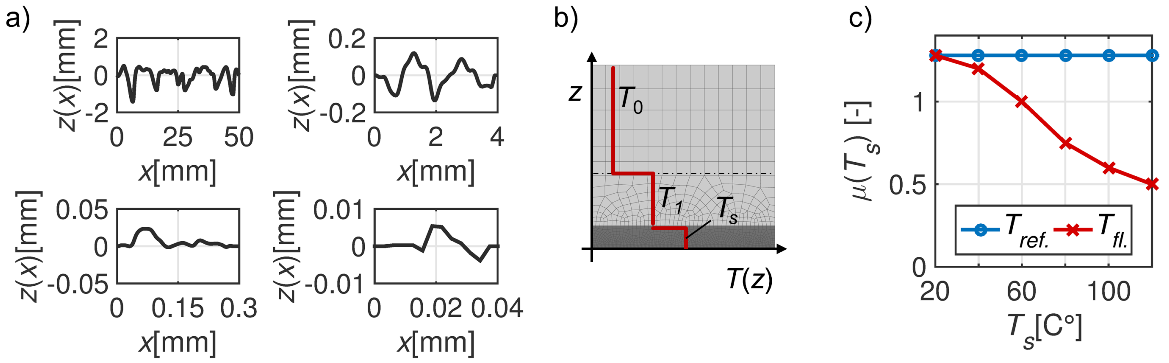

Figure 8.17: a) Surface profiles of four scale setup, thermomechanical parameters for macroscopic scale: $\kappa = 0.8$, $h_c = 1.6\text{mW}/\text{mm}^2\text{K}$. b) Hot layer model for microscopic length scales. c) Overall microscopic coefficient of friction (with and without hot layer) after homogenization for $p = 0.3\text{MPa}$, $v = 1\text{m/s}$, $T_0 = 20°\text{C}$, rubber compound m1, road material r1 (see appendix C).

without temperature effects over velocity. At this stage, no experimental validation of the approach is possible and therefore just a qualitative prediction is conducted and compared to analytical theories. Nevertheless, it is listed within the experimental validation section since measured input data was used: rough surface profiles and viscoelastic rubber properties.

The used multiscale setup is displayed in figure 8.17, simplifying the simulation procedure of section 8.3. However, the approach is still able to reproduce the main thermal effect with respect to the coefficient of friction. Similar to section 6.5 four scales are used, see figure 8.17 a), but only one surface sample is introduced on each scale for this qualitative study, reducing the computational effort.

The concentration on the qualitative global behaviour motivates the introduction of another simplification: the macroscopic temperature gradient is not passed from the macroscopic simulation downwards as proposed in section 8.3. Instead, the calculation of the hysteretic microscopic coefficient of friction is performed decoupled from the macroscopic calculation, revealing the opportunity to calculate the whole microscopic response before the thermomechanically coupled macroscopic simulation. Therefore, the assumption of a hot layer with the height of five micrometer is introduced at the lowest length scale, figure 8.17 b). This layer is also introduced at the second and third scale and the layer temperature is considered as the macroscopic surface temperature T_S, whereas the rubber background temperature is T_0. In order to ensure a smoother transition of the changed material properties for very high surface temperatures, a second partition on the first twenty micrometers is introduced with an averaged temperature T_1 between the very high surface temperature and background temperature, cf. temperature profile in figure 8.17 b).

Following subsection 8.3.3, according to the surface temperature T_S, different mechanical properties are set for the microscopic layers and the temperature T_1 by the WLF-transformation and the coefficient of friction is gained by homogenization. The calculated microscopic friction law for different surface temperatures is displayed in figure 8.17 c) for $v = 1\text{m/s}$ and attributed to flash temperature effects $T_{fl.}$. Furthermore, in

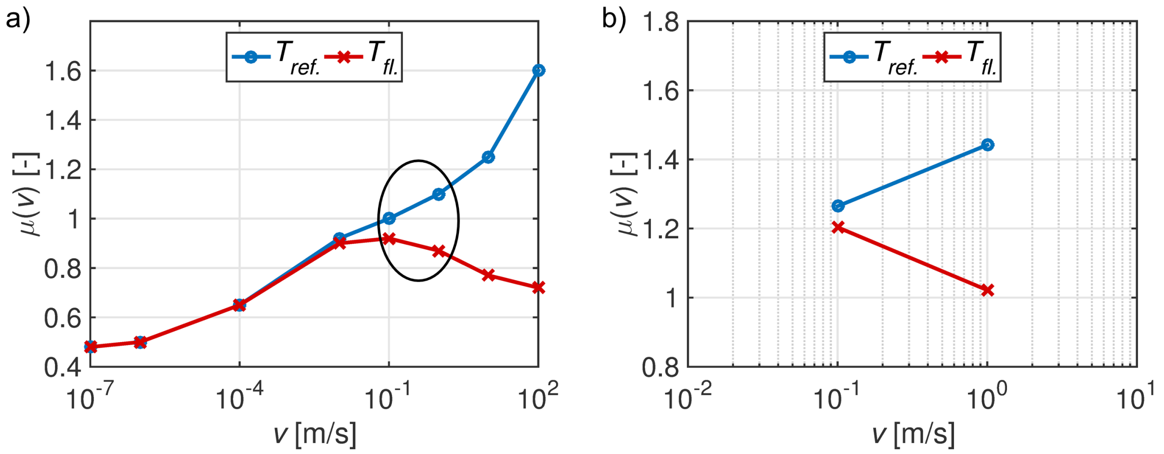

Figure 8.18: a) Calculated coefficient of friction by analytical approach with and without flash temperature effects, extracted from PERSSON (2006). b) Simulated coefficient of friction by multiscale approach with and without flash temperature effects.

the same figure also the reference microscopic coefficient of friction for $T_{ref.} = 20°C$ is displayed.

The absolute level of the coefficient of friction is rather high, this may change if more surface samples would be added, compare results of subsection 6.5.2. For example the lowest scale is calculated on a very rough surface sample ensuring that after all scales the absolute level of the coefficient of friction approaches the values of a dry measurement. This leads to the right order of magnitude of the resulting temperatures in the thermomechanically coupled macroscopic simulation. By the proposed choice of a very high hysteretic contribution, the adhesive interaction is excluded from the current analysis.

In the last step of the setup, a mechanical macroscopic simulation with the microscopic coefficient of friction without temperature effects ($T_{ref.}$) is performed for two macroscopic velocities, $v = 0.1\text{m/s}$ and $v = 1\text{m/s}$. The same two simulations are performed with a thermomechancially coupled simulation using the velocity-dependent microscopic coefficient of friction including the surface temperature dependency ($T_{fl.}$) as the input for frictional heating, see figure 8.17 c). Depending on the macroscopic surface temperature, the coefficient of friction is adopted during the thermomechanical calculation without downpassing the macroscopic temperature gradient in this simplified setup. This procedure leads to a decreasing coefficient of friction over time. All other boundary conditions are set as described in subsections 8.5.1 and 8.5.2.

In figure 8.18 b), the final results of the multiscale setup are displayed, applying time homogenization after a stationary coefficient of friction was reached in the macroscopic simulation. The most important effect for the considered velocity range is reproduced with the proposed setup: an increasing coefficient of friction over velocity without thermal effects is converted to a decreasing trend if thermal effects are included in the multiscale setup. This global behaviour corresponds qualitatively to an analytical solution over a wide velocity range, cf. figure 8.18 a). See PERSSON (2006) for details regarding the setup and boundary conditions of the analytical approach. Nevertheless, a full experimental validation of the thermomechanical multiscale approach with the full coupling of the temperature gradient is postponed to future studies.

Chapter 9

Summary, Conclusion and Outlook

In this work, a novel multiscale FEM approach for hysteretic friction representing an important friction mechanism for sliding rubber samples is developed. A viscoelastic material model is used to model the energy dissipation inside the rubber bulk material. The direct inclusion of the rough surface without any transformations, that may lead to an incorrect representation of the surface characteristics, is a key feature of the method. The potential of this approach to cover surface anisotropy and interlocking effects is demonstrated with examples. Furthermore, the multiscale method is based on a continuous decomposition of the rough surface into certain length scales via filtering and the scales are coupled with the coefficient of friction gained by time homogenization. For separated length scales, the generation of a pressure and velocity-dependent friction law is proposed and its ability to reproduce a solution obtained with a unseparated model simulation is demonstrated.

Nevertheless, the length scales of a real rough road surface cannot be separated in orders of magnitude, since all surface details contribute to the hysteretic excitation of the viscoelastic rubber material. Therefore, an extended version of the multiscale approach is introduced using also a homogenization of the pressure values for the lower scales, applying the relevant slip velocity for one macroscopic evaluation point. Moreover, several length scales are introduced for real rough surfaces to include asperity details in acceptable calculation times and every scale is enhanced by the use of a certain number of rough surface profiles. By the evaluation of micromechanical studies it is demonstrated that at least ten surface samples should be introduced in a two-dimensional multiscale setup, because the statistical properties of the surface are approximated in this way with the desired accuracy. The whole framework with its various communications between the length scales is automated within the software package ABAQUS.

The prediction quality of the hysteretic multiscale approach is evaluated with experimental results on wet surfaces, revealing that large global changes of velocity and pressure values are not fully reproducible with the method since not all possibly relevant physical effects are coupled at this stage of the method. However, the multiscale approach is used to study different rubber compounds and various surface characteristics with respect to their hysteretic response, demonstrating that fundamental changes can be predicted with the method. Especially, the effects on the global coefficient of friction by changing the glass transition temperature of the rubber compounds and the rubber hardness are captured with the method. The insufficient prediction of the response for rubber compounds with different filler levels in two of three cases is attributed to the viscoelastic material model and the measured data that is used for it. The expansion of the test procedure to different strain and frequency levels, the inclusion of the PAYNE-effect, and a modification to a finite viscoelastic model instead of a finite linear one are some exemplary promising ways to improve the prediction quality in future studies. In contrast and additional to experiments, the dynamic contact area can be calculated with the method as well as further quantities. For example, the dissipated energy on a local level or the distribution of chosen quantities over surface samples or length scales can be studied with the multiscale method, enabling an interesting analysis of these quantities.

Adhesion is added to the proposed multiscale method on the macroscopic length scale by the introduction of a physically motivated phenomenological law for the shear stress coupled to the calculated contact area of all length scales. Details regarding the assumed mechanism of rubber molecule chains undergoing bonding-debonding cycles are given. Moreover, the experimental separation of hysteresis and adhesion by the introduction of a soap-water film in contrast to a dry surface is explained.

The multiscale method enhanced with the adhesive law reveals the ability to capture the global trend of the coefficient of friction over velocity for low sliding speeds, excluding temperature effects for this parameter range. The correct ranking of different rubber compounds is predicted for dry and wet (soap-water mixture on the surface) measurements by adopting the three fitting parameters of the formulation. Furthermore, an absolute gap between hysteretic simulation and wet measurement is closed by a modification of the approach, assuming that dry friction occurs locally even on a surface covered with soap-water. The proposed procedure requires results of a macroscopic friction experiment as an input at the moment. Additionally, no connection of the introduced fitting parameters to physical properties is established in this work and thus providing a topic for future studies. Moreover, further validation studies could be performed with the approach and the temperature dependence of adhesion should be added in order to be able to apply the approach to larger velocities. Direct microscopic modelling of adhesion with separate experimental input remains a challenging task since the link of the introduced parameters to experiments is quite difficult.

In a last step, the multiscale method is extended towards flash temperature effects by introducing a thermomechanically coupled macroscopic simulation using the complete microscopic coefficient of friction (hysteretic and adhesive part) for frictional heating. The generated temperature gradient inside the rubber bulk is used to modify the viscoelastic material properties of the microscopic length scales via a WLF-transformation. In contrast to the approach for hysteresis and adhesion, a homogenization loop over all lower length scales is introduced after certain macroscopic time intervals, because a high temperature increase at the interface is observed. Therefore, the microscopic response changes very fast over time and this behaviour is reproduced with the extended multiscale setup. The behaviour of critical model parameters is checked in numerical studies, revealing converging properties for the macroscopic mesh resolution, the introduced resolution of the shifted material parameters at the lower scales and the refinement of introduced time intervals.

The simple choice of the thermal contact parameters without direct measurements of the heat conductivity is validated with single scale macroscopic simulations comparing surface and bulk temperature measurements with the calculated values. Finally, a four scale multiscale setup is used to demonstrate the global decreasing trend of the coefficient of friction if temperature effects are activated. Instead, a pure mechanical response predicts an increasing hysteretic response with increasing velocity above 0.1m/s. In a next step, a validation of the setup with experimental results would be advantageous after a thermomechanical description and estimation of adhesive friction is added to the approach.

In general, the separation of the physical effects in experiments is difficult, but could provide better validation options for the simulation. Thus, further experimental investigations remain an open topic. In contrast to the separation of effects in experiments, the combination of all physical effects in the simulation setup, adding e.g. wear effects or water interaction, reveals many possibilities for future studies. Furthermore, the assumption of smooth rubber surfaces can be revised and the simulation could be enhanced by taking the rubber roughness into account. The transformation of the two-dimensional setup to a fully three-dimensional multiscale calculation remains a challenging topic for rough surfaces and could be studied in future. Another topic is to include advanced kinematics (e.g. rolling) into the multiscale approach, making the results comparable to tire test results.

Appendix A

Material Models

The invariants in terms of principal stretches are given as

$$I_C = \operatorname{tr} \boldsymbol{C} = \operatorname{tr} \boldsymbol{b} = \lambda_1^2 + \lambda_2^2 + \lambda_3^2, \tag{A.1}$$

$$II_C = \frac{1}{2}\left((\operatorname{tr} \boldsymbol{C})^2 - \operatorname{tr} \boldsymbol{C}^2\right) = \frac{1}{2}\left((\operatorname{tr} \boldsymbol{b})^2 - \operatorname{tr} \boldsymbol{b}^2\right) = \lambda_1^2\lambda_2^2 + \lambda_2^2\lambda_3^2 + \lambda_3^2\lambda_1^2, \tag{A.2}$$

$$III_C = \det \boldsymbol{C} = \det \boldsymbol{b} = \lambda_1^2\lambda_2^2\lambda_3^2. \tag{A.3}$$

The derivatives of the invariants with respect to the right Cauchy-Green tensor (identical derivation for the left Cauchy-Green tensor) are expressed by

$$\frac{\partial I_C}{\partial \boldsymbol{C}} = \boldsymbol{1}, \quad \frac{\partial II_C}{\partial \boldsymbol{C}} = I_C \cdot \boldsymbol{1} - \boldsymbol{C}, \tag{A.4}$$

$$\frac{\partial III_C}{\partial \boldsymbol{C}} = \frac{\partial J^2}{\partial \boldsymbol{C}} = III_C \cdot \boldsymbol{C}^{-1} = J^2 \cdot \boldsymbol{C}^{-1}, \tag{A.5}$$

$$\frac{\partial \ln J}{\partial \boldsymbol{C}} = \frac{\partial \ln \sqrt{III_C}}{\partial \boldsymbol{C}} = \frac{1}{\sqrt{III_C}} \frac{1}{2\sqrt{III_C}} III_C \cdot \boldsymbol{C}^{-1} = \frac{1}{2}\boldsymbol{C}^{-1}. \tag{A.6}$$

The Lamé constants μ, λ and the bulk modulus K can be expressed by the material parameters Young's modulus E and Poisson's ratio ν. The parameters used for the Mooney-Rivlin-model in ABAQUS (see SIMULIA (2014a)) are linked to the Lamé constants. Furthermore, the connection to the Blatz-Ko model is established via a non-linearity factor f (see Blatz & Ko (1962); Horgan (1996)).

$$\mu = \frac{E}{2(1+\nu)}, \quad \lambda = \frac{E\nu}{(1+\nu)(1-2\nu)}, \quad K = \frac{E}{3(1-2\nu)}, \tag{A.7}$$

$$\mu = 2(C_{10} + C_{01}), \quad K = \frac{2}{D_1}, \tag{A.8}$$

$$C_{10} = \frac{\mu}{2} f, \quad C_{01} = \frac{\mu}{2}(1-f). \tag{A.9}$$

A strain energy function without a volumetric-deviatoric split is listed for a Neo-Hookean material with the material constants μ and λ. Furthemore, the corresponding equilibrium and non-equilibrium stresses are given:

$$\Psi_{EQ}^{NH}(J, I_C) = \frac{\mu}{2}\left(I_C - 3 - 2\ln J\right) + \frac{\lambda}{4}\left(J^2 - 1 - 2\ln J\right), \tag{A.10}$$

$$\boldsymbol{\sigma}_{EQ}^{NH} = \frac{\mu}{J}\left(\boldsymbol{b} - \mathbf{1}\right) + \frac{\lambda}{2J}\left(J^2 - 1\right)\mathbf{1}, \tag{A.11}$$

$$\boldsymbol{\sigma}_{NEQ}^{NH,k} = \frac{\mu_k}{J}\left(\boldsymbol{b}_e^k - \mathbf{1}\right) + \frac{\lambda_k}{2J}\left(\left(J_e^k\right)^2 - 1\right)\mathbf{1}. \tag{A.12}$$

Appendix B

Mechanical Contact Linearization

The linearization of the mechanical contact weak form G is derived introducing the matrices $\bar{D}^c_{A\alpha\beta}$ and $\bar{L}^c_{A\alpha}$. The matrices are distinguished for the stick case $c = st$ and for the slip case $c = sl$. The solution vector $\boldsymbol{d}_s$ is defined afterwards, introducing the mechanical tangent matrices for the contact element $\boldsymbol{K}^s_{uu}$ and $\boldsymbol{K}^s_{uu\,r}$. The linearizations of the base vectors are neglected and not further considered, see Weissenfels (2013) and Dobberstein (2014) for details. The reader is also referred to these works for a detailed description of the complex linearization procedure leading to matrices like $\boldsymbol{G}^s_{\delta\boldsymbol{g}}$ or $\boldsymbol{G}^r_{\Delta\boldsymbol{g}^{(o)}}$.

$$\begin{aligned} DG^{ch}_{uA} = {} & \Delta\delta\bar{\boldsymbol{g}} \cdot (\boldsymbol{n}_A c_N \bar{\boldsymbol{g}}_A \cdot \boldsymbol{n}_A + \boldsymbol{t}_{A\alpha}\bar{t}_{T\alpha A}) \\ & + \delta\bar{\boldsymbol{g}} \cdot (\Delta\boldsymbol{n}_A c_N \bar{\boldsymbol{g}}_A \cdot \boldsymbol{n}_A + \boldsymbol{n}_A c_N \Delta\bar{\boldsymbol{g}}_A \cdot \boldsymbol{n}_A + \boldsymbol{n}_A c_N \bar{\boldsymbol{g}}_A \cdot \Delta\boldsymbol{n}_A \\ & + \Delta\boldsymbol{t}_{A\alpha}\bar{t}_{T\alpha A} + \boldsymbol{t}_{A\alpha}\bar{D}^c_{A\alpha\beta}\left[(\Delta\bar{\boldsymbol{g}}_A - \Delta\bar{\boldsymbol{g}}^o_A) \cdot \boldsymbol{t}_{\alpha\beta} + (\bar{\boldsymbol{g}}_A - \bar{\boldsymbol{g}}^o_A) \cdot \Delta\boldsymbol{t}_{\alpha\beta}\right] \\ & + \boldsymbol{t}_{A\alpha}\bar{L}^c_{A\alpha}\left[\Delta\bar{\boldsymbol{g}}_A \cdot \boldsymbol{n}_A + \bar{\boldsymbol{g}}_A \cdot \Delta\boldsymbol{n}_A\right]), \end{aligned} \tag{B.1}$$

$$\bar{D}^{st}_{A\alpha\beta} = -c_T 1_{\alpha\beta}, \quad \bar{L}^{st}_{A\alpha} = 0_\alpha, \tag{B.2}$$

$$\bar{D}^{sl}_{A\alpha\beta} = -\mu|\bar{t}_{NA}|\left[\frac{1_{\alpha\beta}}{\|\bar{\boldsymbol{t}}_{TA}\|} - \frac{\bar{t}^{tr}_{T\alpha A}\bar{t}^{tr}_{T\beta A}}{\|\bar{\boldsymbol{t}}_{TA}\|^3}\right] c_T, \quad \bar{L}^{sl}_{A\alpha} = \mu\,\mathrm{sign}(\bar{t}_{NA})\frac{\bar{t}^{tr}_{T\alpha A}}{\|\bar{\boldsymbol{t}}^{tr}_{TA}\|}. \tag{B.3}$$

$$DG^{ch}_{uA} = \delta\boldsymbol{d}_s \cdot \sum_{s=1}^{n^A_{seg}}\left(\boldsymbol{K}^s_{uu}\boldsymbol{d}_s + \sum_{r=1}^{n^A_{seg}}\boldsymbol{K}^s_{uu\,r}\boldsymbol{d}_r\right), \tag{B.4}$$

$$\boldsymbol{K}^s_{uu} = \boldsymbol{G}^s_{\Delta\delta\boldsymbol{g}}\left[\boldsymbol{n}_A c_N \bar{\boldsymbol{g}}_A \cdot \boldsymbol{n}_A + \boldsymbol{t}_{A\alpha}\bar{t}_{T\alpha A}\right], \tag{B.5}$$

$$\begin{aligned} \boldsymbol{K}^s_{uu\,r} = {} & \boldsymbol{G}^s_{\delta\boldsymbol{g}}\boldsymbol{n}_A\left[c_N\boldsymbol{G}^r_{\Delta\boldsymbol{g}}\boldsymbol{n}_A\right] + \boldsymbol{G}^s_{\delta\boldsymbol{g}}\boldsymbol{t}_{A\alpha}[\bar{D}_{A\alpha\beta}\left(\boldsymbol{G}^r_{\Delta\boldsymbol{g}} - \boldsymbol{G}^r_{\Delta\boldsymbol{g}^o}\right)\boldsymbol{t}_{A\beta} \\ & + \bar{L}_{A\alpha}\boldsymbol{G}^r_{\Delta\boldsymbol{g}}\boldsymbol{n}_A]. \end{aligned} \tag{B.6}$$

If a velocity and pressure dependent coefficient of friction $\mu^*(\|\boldsymbol{v}_A\|, \bar{p}_{NA})$ is used in the frictional macroscopic contact formulation, additional linearization terms have to be derived, $\bar{C}^{c*}_{TA\alpha\beta}$ and $\bar{C}^{c*}_{NA\alpha}$, whereas the coefficient of friction is inserted in the already derived matrices $\bar{D}^{c*}_{A\alpha\beta}$ and $\bar{L}^{c*}_{A\alpha}$, cf. Wagner et al. (2015) for further details.

$$\Delta\bar{t}^{c*}_{T\alpha A} = \left(\bar{D}^{c*}_{A\alpha\beta} + \bar{C}^{c*}_{TA\alpha\beta}\right)\left(\Delta\bar{\boldsymbol{g}}_A - \Delta\bar{\boldsymbol{g}}^o_A\right)\cdot\mathbf{t}_{A\beta} + \left(\bar{L}^{c*}_{A\alpha} + \bar{C}^{c*}_{NA\alpha}\right)\Delta\bar{\boldsymbol{g}}_A\cdot\mathbf{n}_A, \tag{B.7}$$

$$\bar{C}^{st\ *}_{NA\alpha} = 0_\alpha, \quad \bar{C}^{sl\ *}_{NA\alpha} = \frac{\partial\mu}{\bar{p}_{NA}}|\bar{p}_{NA}|\frac{\bar{t}_{T\alpha A}}{\|\bar{\boldsymbol{t}}^{tr}_{TA}\|}, \tag{B.8}$$

$$\bar{C}^{st\ *}_{TA\alpha\beta} = 0_{\alpha\beta}, \quad \bar{C}^{sl\ *}_{TA\alpha\beta} = \frac{\partial\mu}{\bar{\boldsymbol{v}}_A}\frac{1}{dt}|\bar{p}_{NA}|\frac{\bar{t}_{T\alpha A}1_\beta}{\|\bar{\boldsymbol{t}}^{tr}_{TA}\|}. \tag{B.9}$$

Appendix C

Material Parameters

Table C.1: Mechanical and thermal material parameters of the used road surface material r1.

E (MPa)	ν (-)	ρ (t/mm^3)	c (mJ/tK)	k (mW/mmK)
40.000	0.15	$2.19 \cdot 10^{-9}$	$0.92 \cdot 10^{9}$	0.7

Table C.2: Mooney-Rivlin parameters of rubber compounds m1, m2 and m3.

Compound	C_{10} (MPa)	C_{01} (MPa)	D_1 (MPa)
m1	0.174	0.300	0.0208
m2	0.174	0.309	0.0417
m3	0.347	0.810	0.0174

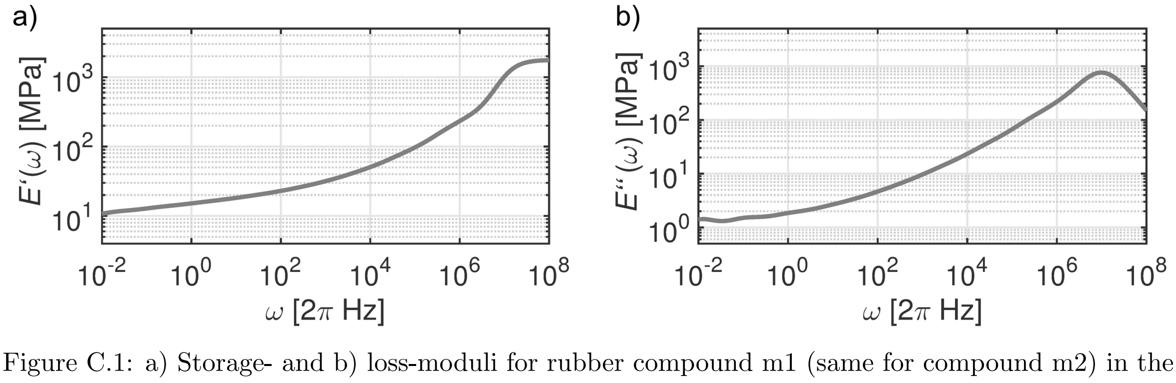

Figure C.1: a) Storage- and b) loss-moduli for rubber compound m1 (same for compound m2) in the relevant exited frequency range.

Table C.3: Thermal material parameters of rubber compounds m1, m2 and m3.

Compound	ρ (t/mm^3)	c (mJ/tK)	k (mW/mmK)	T_{ref} ($^\circ C$)	c_1 (-)	$c_2 (-)$
m1	$1.208 \cdot 10^{-9}$	$1.67 \cdot 10^{9}$	0.2553	20	7,95	109,32
m2	$1.208 \cdot 10^{-9}$	$1.4 \cdot 10^{9}$	0.2553	20	7,95	109,32
m3	$1.208 \cdot 10^{-9}$	$1.4 \cdot 10^{9}$	0.2553	-	-	-

Bibliography

ALTENBACH H. *Kontinuumsmechanik: Einführung in die materialunabhängigen und materialabhängigen Gleichungen*. Springer, Berlin, 2012, 2nd edition.

BARQUINS M. & ROBERTS A.D. Rubber friction variation with rate and temperature: some new observations. *Journal of Physics D: Applied Physics*, 19 (1986) (4): 547–563.

BLATZ P.J. & KO W.L. Application of Finite Elastic Theory to the Deformation of Rubbery Materials. *Journal of Rheology*, 6 (1962) (1): 223–251.

BOEHM J. *Der Payneeffekt: Interpretation und Anwendung in einem neuen Materialgesetz für Elastomere*. Ph.D. thesis, Universität Regensburg (2001).

CARBONE G., LORENZ B., PERSSON B.N.J. & WOHLERS A. Contact mechanics and rubber friction for randomly rough surfaces with anisotropic statistical properties. *The European Physical Journal E*, 29 (2009) (3): 275–284.

CHADWICK P. *Continuum mechanics: Concise theory and problems*. Dover Publications, Mineola, N.Y., 1999, 2nd corr. and enl. edition.

CHEN X., DAI S., GUO Y., YANG J. ET AL. Polishing of Asphalt Pavements: From Macro- to Micro-Scale. *Journal of Testing and Evaluation*, 44 (2016) (2): 885–894.

COLEMAN B.D. & NOLL W. The thermodynamics of elastic materials with heat conduction and viscosity. *Archive for Rational Mechanics and Analysis*, 13 (1963) (1): 167–178.

DITTMANN M., FRANKE M., TEMIZER İ. & HESCH C. Isogeometric Analysis and thermomechanical Mortar contact problems. *Computer Methods in Applied Mechanics and Engineering*, 274 (2014): 192–212.

DO M.T., TANG Z., KANE M. & DE LARRARD F. Evolution of road-surface skid-resistance and texture due to polishing. *Wear*, 266 (2009) (5-6): 574–577.

DOBBERSTEIN J.H. *Interaction between rubber material and model during demolding*. Ph.D. thesis, Leibniz Universität Hannover (2014).

FALK K., LANG R. & KALISKE M. Multiscale Simulation to Determine Rubber Friction on Asphalt Surfaces. *Tire Science and Technology*, 44 (2016) (4): 226–247.

Feyel F. Multiscale FE2 elastoviscoplastic analysis of composite structures. *Computational Materials Science*, 16 (1999) (1-4): 344–354.

Fletcher W.P. & Gent A.N. Nonlinearity in the Dynamic Properties of Vulcanized Rubber Compounds. *Rubber Chemistry and Technology*, 27 (1954) (1): 209–222.

Flory P.J. Thermodynamic relations for high elastic materials. *Transactions of the Faraday Society*, 57 (1961): 829–838.

Fortunato G., Ciaravola V., Furno A., Lorenz B. et al. General theory of frictional heating with application to rubber friction. *Journal of Physics: Condensed Matter*, 27 (2015) (17): 175 008.

Gäbel G.S. *Beobachtung und Modellierung lokaler Phänomene im Reifen/Fahrbahn-Kontakt*. Ph.D. thesis, Leibniz Universität Hannover (2009).

Gent A.N. *Engineering with rubber: How to design rubber components*. Hanser Publishers, Munich and Cincinnati, 2012, 3rd edition.

Greenwood J.A. & Williamson J.B.P. Contact of nominally flat surfaces. *Proceedings of the Royal Society A: Mathematical, Physical and Engineering Sciences*, 295 (1966) (1442): 300–319.

Grosch K.A. The relation between the friction and visco-elastic properties of rubber. *Proceedings of the Royal Society A: Mathematical, Physical and Engineering Sciences*, 274 (1963) (1356): 21–39.

Harwood J.A.C., Mullins L. & Payne A.R. Stress softening in natural rubber vulcanizates. Part II. Stress softening effects in pure gum and filler loaded rubbers. *Journal of Applied Polymer Science*, 9 (1965) (9): 3011–3021.

Harwood J.A.C. & Payne A.R. Stress softening in natural rubber vulcanizates. Part III. Carbon black-filled vulcanizates. *Journal of Applied Polymer Science*, 10 (1966a) (2): 315–324.

Harwood J.A.C. & Payne A.R. Stress softening in natural rubber vulcanizates. Part IV. Unfilled vulcanizates. *Journal of Applied Polymer Science*, 10 (1966b) (8): 1203–1211.

Haupt P. *Continuum Mechanics and Theory of Materials*. Advanced Texts in Physics. Springer, Berlin, Heidelberg, 2000.

Höfer P. & Lion A. Modelling of frequency- and amplitude-dependent material properties of filler-reinforced rubber. *Journal of the Mechanics and Physics of Solids*, 57 (2009) (3): 500–520.

Hofstetter K., Eberhardsteiner J. & Mang H.A. Efficient treatment of rubber friction problems in industrial applications. *Structural Engineering and Mechanics*, 22 (2006a) (5): 517–539.

HOFSTETTER K., GROHS C., EBERHARDSTEINER J. & MANG H.A. Sliding behaviour of simplified tire tread patterns investigated by means of fem. *Computers & Structures*, 84 (2006b) (17-18): 1151–1163.

HOLZAPFEL G.A. *Nonlinear Solid Mechanics: A Continuum Approach for Engineering*. Wiley, Chichester and New York, 2000.

HOLZAPFEL G.A. & SIMO J.C. Entropy elasticity of isotropic rubber-like solids at finite strains. *Computer Methods in Applied Mechanics and Engineering*, 132 (1996a) (1-2): 17–44.

HOLZAPFEL G.A. & SIMO J.C. A new viscoelastic constitutive model for continuous media at finite thermomechanical changes. *International Journal of Solids and Structures*, 33 (1996b) (20-22): 3019–3034.

HORGAN C.O. Remarks on ellipticity for the generalized Blatz-Ko constitutive model for a compressible nonlinearly elastic solid. *Journal of Elasticity*, 42 (1996) (2): 165–176.

IGNATYEV P.A., RIPKA S., MUELLER N., TORBRUEGGE S. ET AL. Tire ABS-Braking Prediction with Lab Tests and Friction Simulations. *Tire Science and Technology*, 43 (2015) (4): 260–275.

KLÜPPEL M. & HEINRICH G. Rubber Friction on Self-affine Road Tracks. *Rubber Chemistry and Technology*, 73 (2000) (4): 578–606.

KNILL D.G. Petrographical aspects of the polishing of natural roadstones. *Journal of Applied Chemistry*, 10 (1960) (1): 28–35.

KUMMER H.W. *Unified Theory of Rubber and Tire Friction*. University Park : Pennsylvania State University, College of Engineering, Pennsylvania, 1966.

LAHAYNE O. & EBERHARDSTEINER J. Investigation of the temperature behaviour of sliding rubber materials. In DE HOSSON J.T.M., BREBBIA C.A. & NISHIDA S.I., eds., *Computer Methods and Experimental Measurements for Surface Effects and Contact Mechanics VIII*, pages 155–164. 2007.

LAURSEN T.A. *Computational Contact and Impact Mechanics: Fundamentals of Modeling Interfacial Phenomena in Nonlinear Finite Element Analysis*. Springer, Berlin, Heidelberg, 2003.

LE GAL A. & KLÜPPEL M. Investigation and modelling of rubber stationary friction on rough surfaces. *Journal of Physics: Condensed Matter*, 20 (2008) (1): 015 007.

LE GAL A., YANG X. & KLÜPPEL M. Evaluation of sliding friction and contact mechanics of elastomers based on dynamic-mechanical analysis. *The Journal of Chemical Physics*, 123 (2005) (1): 014 704.

LINDNER M. *Experimentelle und theoretische Untersuchungen zur Gummireibung and Profilklötzen und Dichtungen*. Ph.D. thesis, Leibniz Universität Hannover (2005).

LINKE T., WANGENHEIM M., LIND H. & RIPKA S. Experimental Friction and Temperature Investigation on Aircraft Tires. *Tire Science and Technology*, 42 (2014) (3): 116–144.

LION A. A physically based method to represent the thermo-mechanical behaviour of elastomers. *Acta Mechanica*, 123 (1997): 1–25.

LORENZ B., OH Y.R., NAM S.K., JEON S.H. ET AL. Rubber friction on road surfaces: Experiment and theory for low sliding speeds. *The Journal of Chemical Physics*, 142 (2015) (19): 194 701.

LORENZ B., PERSSON B.N.J., DIELUWEIT S. & TADA T. Rubber friction: Comparison of theory with experiment. *The European Physical Journal E*, 34 (2011) (12): 1–11.

DE LORENZIS L. & WRIGGERS P. Computational homogenization of rubber friction on rough rigid surfaces. *Computational Materials Science*, 77 (2013): 264–280.

MANDELBROT B.B. *The fractal geometry of nature: (formerly: Fractals)*. Freeman, New York, 1983, updated & augm. edition.

MARSDEN J.E. & HUGHES T.J.R. *Mathematical foundations of elasticity*. Dover, New York, 1994.

MOONEY M. A Theory of Large Elastic Deformation. *Journal of Applied Physics*, 11 (1940) (9): 582–592.

MULLINS L. Effect of Stretching on the Properties of Rubber. *Rubber Chemistry and Technology*, 21 (1948) (2): 281–300.

NITSCHE R. *A Multiscale Projection Method for Contact on Rough Surfaces*. Ph.D. thesis, Leibniz Universität Hannover (2011).

OGDEN R.W. *Non-linear elastic deformations*. Ellis Horwood series in mathematics and its applications. E. Horwood and Halsted Press, Chichester and New York, 1984.

PAYNE A.R. The dynamic properties of carbon black-loaded natural rubber vulcanizates. Part I. *Journal of Applied Polymer Science*, 6 (1962a) (19): 57–63.

PAYNE A.R. The dynamic properties of carbon black loaded natural rubber vulcanizates. Part II. *Journal of Applied Polymer Science*, 6 (1962b) (21): 368–372.

PERSSON B.N.J. *Sliding Friction: Physical Principles and Applications*. Springer, Berlin, 2000.

PERSSON B.N.J. Theory of rubber friction and contact mechanics. *The Journal of Chemical Physics*, 115 (2001) (8): 3840–3861.

PERSSON B.N.J. Adhesion between an elastic body and a randomly rough hard surface. *The European Physical Journal E*, 8 (2002) (4): 385–401.

PERSSON B.N.J. Rubber friction: role of the flash temperature. *Journal of Physics: Condensed Matter*, 18 (2006) (32): 7789–7823.

PERSSON B.N.J. Role of Frictional Heating in Rubber Friction. *Tribology Letters*, 56 (2014) (1): 77–92.

PERSSON B.N.J., ALBOHR O., TARTAGLINO U., VOLOKITIN A.I. ET AL. On the nature of surface roughness with application to contact mechanics, sealing, rubber friction and adhesion. *Journal of Physics: Condensed Matter*, 17 (2005) (1): R1–R62.

PERSSON B.N.J., LORENZ B. & VOLOKITIN A.I. Heat transfer between elastic solids with randomly rough surfaces. *The European Physical Journal E*, 31 (2010) (1): 3–24.

PERSSON B.N.J. & TOSATTI E. Qualitative theory of rubber friction and wear. *The Journal of Chemical Physics*, 112 (2000) (4): 2021–2029.

PERSSON B.N.J. & VOLOKITIN A.I. Rubber friction on smooth surfaces. *The European Physical Journal E*, 21 (2006) (1): 69–80.

POCIUS A.V. *Adhesion and Adhesives Technology: An Introduction*. Hanser Publishers and Hanser/Gardner Publications, Munich and Cincinnati, 2002, 2nd edition.

POPOVA E. & POPOV V.L. The research works of Coulomb and Amontons and generalized laws of friction. *Friction*, 3 (2015) (2): 183–190.

POPP A. *Mortar Methods for Computational Contact Mechanics and General Interface Problems*. Ph.D. thesis, Technische Universität München (2012).

POPP A., GEE M.W. & WALL W.A. A finite deformation mortar contact formulation using a primal-dual active set strategy. *International Journal for Numerical Methods in Engineering*, 79 (2009) (11): 1354–1391.

POPP A., GITTERLE M., GEE M.W. & WALL W.A. A dual mortar approach for 3D finite deformation contact with consistent linearization. *International Journal for Numerical Methods in Engineering*, 83 (2010) (11): 1428–1465.

PUSO M.A. & LAURSEN T.A. A mortar segment-to-segment contact method for large deformation solid mechanics. *Computer Methods in Applied Mechanics and Engineering*, 193 (2004a) (6-8): 601–629.

PUSO M.A. & LAURSEN T.A. A mortar segment-to-segment frictional contact method for large deformations. *Computer Methods in Applied Mechanics and Engineering*, 193 (2004b) (45-47): 4891–4913.

Rahulkumar P., Jagota A., Bennison S.J. & Saigal S. Cohesive element modeling of viscoelastic fracture: Application to peel testing of polymers. *International Journal of Solids and Structures*, 37 (2000) (13): 1873–1897.

Raous M., Cangémi L. & Cocu M. A consistent model coupling adhesion, friction, and unilateral contact. *Computer Methods in Applied Mechanics and Engineering*, 177 (1999) (3-4): 383–399.

Reese S. *Thermomechanische Modellierung gummiartiger Polymerstrukturen*. Habilitationsschrift, Leibniz Universität Hannover, Hannover (2001).

Reese S. & Govindjee S. Theoretical and Numerical Aspects in the Thermo-Viscoelastic Material Behaviour of Rubber-Like Polymers. *Materials of Time-Dependent Materials*, 1 (1998a): 357–396.

Reese S. & Govindjee S. A theory of finite viscoelasticity and numerical aspects. *International Journal of Solids and Structures*, 35 (1998b) (26-27): 3455–3482.

Reinelt J. *Frictional Contact of Elastomer Materials on Rough Rigid Surfaces*. Ph.D. thesis, Leibniz Universität Hannover (2008).

Rendek M. & Lion A. Strain induced transient effects of filler reinforced elastomers with respect to the Payne-Effect: Experiments and constitutive modelling. *ZAMM*, 90 (2010) (5): 436–458.

Ripka S. *Experimental investigation and modeling of tire tread block friction on ice*, volume IDS 01/2013 of *Berichte aus dem IDS*. PZH Verlag, Garbsen, 2013.

Ripka S., Gäbel G. & Wangenheim M. Dynamics of a Siped Tire Tread Block - Experiment and Simulation. *Tire Science and Technology*, 37 (2009) (4): 323–339.

Rivlin R.S. Large Elastic Deformations of Isotropic Materials. IV. Further Developments of the General Theory. *Philosophical Transactions of the Royal Society A: Mathematical, Physical and Engineering Sciences*, 241 (1948) (835): 379–397.

Roberts A.D. Theories of dry rubber friction. *Tribology International*, 9 (1976) (2): 75–81.

Roberts A.D. & Thomas A.G. The adhesion and friction of smooth rubber surfaces. *Wear*, 33 (1975) (1): 45–64.

Röthemeyer F. & Sommer F. *Kautschuk-Technologie: Werkstoffe, Verarbeitung, Produkte*. Hanser, München, 2013, 3rd edition.

Rust W. *Nichtlineare Finite-Elemente-Berechnungen: Kontakt, Geometrie, Material*. Studium. Vieweg+Teubner Verlag / Springer Fachmedien Wiesbaden GmbH, Wiesbaden, 2011, 2nd edition.

Sadowski P. & Stupkiewicz S. A model of thermal contact conductance at high real contact area fractions. *Wear*, 268 (2010) (1-2): 77–85.

Sauer R.A. A Survey of Computational Models for Adhesion. *The Journal of Adhesion*, 92 (2015) (2): 81–120.

Sauer R.A. & Li S. An atomic interaction-based continuum model for adhesive contact mechanics. *Finite Elements in Analysis and Design*, 43 (2007) (5): 384–396.

Sauer R.A. & Wriggers P. Formulation and analysis of a three-dimensional finite element implementation for adhesive contact at the nanoscale. *Computer Methods in Applied Mechanics and Engineering*, 198 (2009) (49-52): 3871–3883.

Scaraggi M., Comingio D., Al-Qudsi A. & de Lorenzis L. The influence of geometrical and rheological non-linearity on the calculation of rubber friction. *Tribology International*, 101 (2016): 402–413.

Schallamach A. The Load Dependence of Rubber Friction. *Proceedings of the Physical Society. Section B*, 65 (1952) (9): 657–661.

Schallamach A. The Velocity and Temperature Dependence of Rubber Friction. *Proceedings of the Physical Society. Section B*, 66 (1953) (386): 386–392.

Schallamach A. How does rubber slide? *Wear*, 17 (1971) (4): 301–312.

Simo J.C. On a fully three-dimensional finite-strain viscoelastic damage model: Formulation and computational aspects. *Computer Methods in Applied Mechanics and Engineering*, 60 (1987) (2): 153–173.

Simo J.C. & Hughes T.J.R. *Computational Inelasticity*, volume 7 of *Interdisciplinary applied mathematics*. Springer, New York, 1998.

SIMULIA. *Abaqus Analysis User's Guide (6.14)*. Dassault Systèmes SIMULIA Corp., Providence Rhode Island USA, 2014a.

SIMULIA. *Abaqus Scripting User's Manual (6.14)*. Dassault Systèmes SIMULIA Corp., Providence Rhode Island USA, 2014b.

SIMULIA. *Abaqus Theory Guide (6.14)*. Dassault Systèmes SIMULIA Corp., Providence Rhode Island USA, 2014c.

Stupkiewicz S., Lewandowski M.J. & Lengiewicz J. Micromechanical analysis of friction anisotropy in rough elastic contacts. *International Journal of Solids and Structures*, 51 (2014) (23-24): 3931–3943.

Talon C. & Curnier A. A model of adhesion coupled to contact and friction. *European Journal of Mechanics - A/Solids*, 22 (2003) (4): 545–565.

Temizer İ. Thermomechanical contact homogenization with random rough surfaces and microscopic contact resistance. *Tribology International*, 44 (2011) (2): 114–124.

TEMIZER İ. Granular contact interfaces with non-circular particles. *Tribology International*, 67 (2013): 229–239.

TEMIZER İ. Multiscale thermomechanical contact: Computational homogenization with isogeometric analysis. *International Journal for Numerical Methods in Engineering*, 97 (2014) (8): 582–607.

TEMIZER İ. Sliding friction across the scales: Thermomechanical interactions and dissipation partitioning. *Journal of the Mechanics and Physics of Solids*, 89 (2016): 126–148.

TEMIZER İ. & WRIGGERS P. A multiscale contact homogenization technique for the modeling of third bodies in the contact interface. *Computer Methods in Applied Mechanics and Engineering*, 198 (2008) (3-4): 377–396.

TEMIZER İ. & WRIGGERS P. Inelastic analysis of granular interfaces via computational contact homogenization. *International Journal for Numerical Methods in Engineering*, 84 (2010a) (8): 883–915.

TEMIZER İ. & WRIGGERS P. Thermal contact conductance characterization via computational contact homogenization: A finite deformation theory framework. *International Journal for Numerical Methods in Engineering*, 83 (2010b) (1): 27–58.

TIWARI A., DOROGIN L., STEENWYK B., WARHADPANDE A. ET AL. Rubber friction directional asymmetry. *EPL (Europhysics Letters)*, 116 (2016) (6): 66 002.

TRUESDELL C., NOLL W. & ANTMAN S.S. *The Non-Linear Field Theories of Mechanics*. Springer, Berlin, Heidelberg, 2004, 3rd edition.

WAGNER P., WRIGGERS P., KLAPPROTH C., PRANGE C. ET AL. Multiscale FEM approach for hysteresis friction of rubber on rough surfaces. *Computer Methods in Applied Mechanics and Engineering*, 296 (2015): 150–168.

WAGNER P., WRIGGERS P., VELTMAAT L., CLASEN H. ET AL. Numerical multiscale modelling and experimental validation of low speed rubber friction on rough road surfaces including hysteretic and adhesive effects. *Tribology International*, 111 (2017): 243–253.

WALLASCHEK J. & WIES B. Tyre tread-block friction: modelling, simulation and experimental validation. *Vehicle System Dynamics*, 51 (2013) (7): 1017–1026.

WANG D., CHEN X., XIE X., STANJEK H. ET AL. A study of the laboratory polishing behavior of granite as road surfacing aggregate. *Construction and Building Materials*, 89 (2015): 25–35.

WANG D., CHEN X., YIN C., OESER M. ET AL. Influence of different polishing conditions on the skid resistance development of asphalt surface. *Wear*, 308 (2013) (1-2): 71–78.

Weissenfels C. *Contact methods integrating plasticity models with application to soil mechanics*. Ph.D. thesis, Leibniz Universität Hannover (2013).

Williams M.L., Landel R.F. & Ferry J.D. The Temperature Dependence of Relaxation Mechanisms in Amorphous Polymers and Other Glass-forming Liquids. *Journal of the American Chemical Society*, 77 (1955) (14): 3701–3707.

Willner K. *Kontinuums- und Kontaktmechanik: Synthetische und analytische Darstellung*. Springer, Berlin Heidelberg, 2012.

Wohlmuth B.I. A Mortar Finite Element Method Using Dual Spaces for the Lagrange Multiplier. *SIAM Journal on Numerical Analysis*, 38 (2000) (3): 989–1012.

Wriggers P. *Computational contact mechanics*. Springer, Berlin and New York, 2006, 2nd edition.

Wriggers P. *Non Linear Finite Element Methods*. Springer, Berlin Heidelberg, 2008.

Wriggers P. & Miehe C. Contact constraints within coupled thermomechanical analysis - A finite element model. *Computer Methods in Applied Mechanics and Engineering*, 113 (1994) (3-4): 301–319.

Wriggers P. & Reinelt J. Multi-scale approach for frictional contact of elastomers on rough rigid surfaces. *Computer Methods in Applied Mechanics and Engineering*, 198 (2009) (21-26): 1996–2008.

Xu X.P. & Needleman A. Numerical simulations of fast crack growth in brittle solids. *Journal of the Mechanics and Physics of Solids*, 42 (1994) (9): 1397–1434.

Zeng H. *Polymer Adhesion, Friction, and Lubrication.* John Wiley & Sons, Inc, Hoboken, NJ, USA, 2013.

Zienkiewicz O.C. & Taylor R.L. *The basis*, volume 1 of *The finite element method*. Butterworth-Heinemann, Oxford, 2000a, 5th edition.

Zienkiewicz O.C. & Taylor R.L. *Fluid dynamics*, volume 3 of *The finite element method*. Butterworth-Heinemann, Oxford, 2000b, 5th edition.

Zienkiewicz O.C. & Taylor R.L. *Solid mechanics*, volume 2 of *The finite element method*. Butterworth-Heinemann, Oxford, 2000c, 5th edition.

Zohdi T.I. & Wriggers P. *An Introduction to Computational Micromechancis*, volume 20 of *Lecture notes in applied and computational mechanics*. Springer, Berlin, 2008.

Curriculum Vitae

Name:	Paul Wagner
Date of Birth:	18. August 1987
Place of Birth:	Ziegenhals, Poland
Nationality:	German
Marital status:	married

Occupation

since 03/2017	Development engineer, Contact and Friction Physics, Continental Reifen Deutschland GmbH
11/2012 - 02/2017	Research assistant at the Institute of Continuum Mechanics, Gottfried Wilhelm Leibniz Universität Hannover

Study

10/2007 - 10/2012	Study of Mechanical Engineering, Gottfried Wilhelm Leibniz Universität Hannover
10/2008 - 09/2010	Student assistant at the Institute of Continuum Mechanics, Gottfried Wilhelm Leibniz Universität Hannover

School Education

2000 - 2007	Secondary school, Hannah-Arendt-Gymnasium, Barsinghausen
1998 - 2000	Middle school, Ganztagsgymnasium, Barsinghausen
1994 - 1998	Primary school, Wilhelm-Stedler-Schule, Barsinghausen

Awards and Scholarships

2013	Award of the Dr. Jürgen and Irmgard Ulderup Stiftung (Final Exam)
2009	Award of the Dr. Jürgen and Irmgard Ulderup Stiftung (Intermediate Exam)
2007 - 2012	Scholarship of the Konrad-Adenauer-Stiftung